Ministry of High Education and Sientific Research
Hassiba Benbouali University of Chlef
Faculty of Civil Engineering and Architecture
Departement of Civil Engineering

A THESIS

Submitted in partial fulfillment of the requirements for the degree of

DOCTOR

In Civil Engineering

Option : Structures

by

SENDJASNI Sarra

Title :

INVESTIGATION OF STRUCTURAL BEHAVIOR OF CONCRETE COLUMNS WITH INTERNAL AND/OR EXTERNAL FRP CONFINEMENT

Defended on 07/04/2026, in front of :

AIT ATMANE Hassen	**Professor**	**University HB Chlef**	**President**
BENNAI Riadh	**Professor**	**University HB Chlef**	**Examiner**
ZIDOUR Mohamed	**Professor**	**University IK Tiaret**	**Examiner**
HASSAINE DAOUADJI Tahar	**Professor**	**University IK Tiaret**	**Examiner**
BERRADIA Mohammed	**MCA**	**University HB Chlef**	**Supervisor**
BENZAID Riad	**Professor**	**University MSB Jijel**	**Invited**
HOLSCHEMACHER Klaus	**Professor**	**University AS Leipzig**	**Invited**

Ministère de l'Enseignement Supérieur et de la Recherche Scientifique

Université Hassiba Benbouali de Chlef

Faculté de Génie Civil et d'Architecture

Département de Génie Civil

THÈSE

Présentée pour l'obtention du diplôme de

DOCTORAT

Filière : Génie Civil

Spécialité : Structures

Par

SENDJASNI Sarra

Thème :

INVESTIGATION DU COMPORTEMENT STRUCTUREL DES COLONNES EN BETON AVEC CONFINEMENT INTERNE ET/OU EXTERNE EN PRF

Soutenue le 07/04/2026, devant le jury composé de :

AIT ATMANE Hassen	**Professeur**	**Université HB Chlef**	**Président**
BENNAI Riadh	**Professeur**	**Université HB Chlef**	**Examinateur**
ZIDOUR Mohamed	**Professeur**	**Université IK Tiaret**	**Examinateur**
HASSAINE DAOUADJI Tahar	**Professeur**	**Université IK Tiaret**	**Examinateur**
BERRADIA Mohammed	**MCA**	**Université HB Chlef**	**Rapporteur**
BENZAID Riad	**Professeur**	**Université MSB Jijel**	**Invité**
HOLSCHEMACHER Klaus	**Professeur**	**Université AS Leipzig**	**Invité**

ACKNOWLEDGMENT

I would like to express my deepest gratitude to all those who contributed, directly or indirectly, to the completion of this doctoral research.

First and foremost, I extend my sincere thanks to my thesis supervisor, ***Dr. Mohammed BERRADIA****, Senior Lecturer (Class A) at Hassiba Benbouali University of Chlef, for his trust, availability, wise guidance, and for the rigorous and supportive supervision he provided throughout the course of this work.*

My heartfelt appreciation also goes to my co-supervisors: ***Professor Riad BENZAID****, from Mohamed Seddik Ben Yahia University of Jijel, and* ***Professor Klaus HOLSCHEMACHER****, from the Leipzig University of Applied Sciences in Germany, for their valuable scientific input, continuous support, and thoughtful guidance, which greatly enriched my research.*

I would like to sincerely thank ***Professor Riadh BENNAI*** *from the University of Chlef,* ***Professor ZIDOUR Mohamed*** *from the University of Tiaret, and* ***Professor HASSAINE DAOUADJI Tahar*** *from the University of Tiaret, for the honor of accepting to review this thesis and for their constructive remarks, which helped improve the quality of the work.*

Special thanks are extended to ***Professor AIT ATMANE Hassen*** *from the University of Chlef for graciously accepting to chair the defense committee. His presence was a great honor for me.*

I also wish to warmly thank ***Dr. Bilel ZAROUALI****, from the Department of Hydraulic Engineering at Hassiba Benbouali University of Chlef, and* ***Dr. Asmaa YASSEN HAMED****, from the Higher Institute of Engineering and Technology in Luxor, Egypt, for their support, enriching scientific discussions, and constant encouragement throughout my doctoral journey.*

To ***Dr. Nafissa BELKACEM*** *from the Department of Mechanics Engineering at Hassiba Benbouali University of Chlef, I express my sincere gratitude for her continuous support, inspiration, and kind belief in my potential. Your encouragement has been a true source of motivation.*

I am also deeply thankful to all the faculty members of the Department of Civil Engineering and the Department of Science and Technology for their dedication, guidance, and the valuable knowledge they generously shared over the years.

Finally, to all those who have crossed my path and contributed, in one way or another, to the completion of this thesis thank you, from the bottom of my heart.

DEDICATION

I dedicate this work to all those who have shaped my path with love, strength, and unwavering support,

To my dear brother ***Fares SENDJASNI****, the anchor of my life your constant presence, encouragement, and belief in me gave me the strength to persevere. This achievement carries your name in every step,*

To my beloved sister ***Nadia SENDJASNI****, whose kindness, wisdom, and warm heart have always brought me comfort and confidence. Your love is a gentle force that lifts me up every day,*

To my cherished father ***Slimane SENDJASNI****, a man of great wisdom and quiet strength your sacrifices, guidance, and calm presence have been a foundation upon which I have built my dreams,*

To my loving mother ***ElAlia TORCHI****, whose boundless love and endless prayers have carried me through every challenge you are the soul of my success and the heart of my courage,*

To all ***my brothers*** *and* ***my sisters****, and their children,*

To my entire ***SENDJASNI*** *family, thank you for the strong roots, the values, and the unwavering support you've always given me,*

To my best friends and fellows PhD students ***Manel ABDOUN*** *and* ***Asma DJILALI BOUZINA*** *your friendship and constant encouragement have been a true gift on this journey,*

To ***Dr. Nadia DIBOUNE****, with heartfelt thanks for your valuable help, guidance, and the generous support you have provided your presence made a real difference in this work,*

To ***Mr. Elhouari DJILALI AYAD****, head of the road marking company thank you for your valuable support and trust, which have meant a great deal to me;*

To his entire team, especially my dear friend ***Selatena Nour El-Houda****, thank you for your encouragement and kindness throughout this journey.*

With all my love and gratitude, I dedicate this work to each and every one of you.

Abstract

The objective of this thesis is to develop new predictive models for the compressive load-carrying capacity of concrete columns confined using composite materials, either as internal reinforcements and/or external fiber-reinforced polymer (FRP) wraps, under various axial load eccentricity levels. To achieve this, general regression approaches and advanced machine learning models, such as XGBoost and Random Forest (RF), were employed. We also used deep learning models, such as BiLSTM and CNN-BiLSTM, to predict the axial compressive capacity of concrete-filled steel tubes confined with fiber-reinforced polymers. The proposed confinement models were developed using a bibliographic database composed of 308 reinforced concrete specimens strengthened with FRP bars, and 250 reinforced concrete specimens confined by external FRP wraps or steel tubes. The results showed that the proposed models, particularly those based on XGBoost and Random Forest (RF), achieved high accuracy with a coefficient of determination (R^2) of 0.98, along with minimal values for the root mean square error (RMSE) and mean absolute error (MAE), thus outperforming conventional empirical models. The CNN-BiLSTM model also demonstrated better performance than the BiLSTM model. Furthermore, finite element analysis using ABAQUS showed that the predicted axial loads and deformations closely matched the experimental results, thereby confirming the accuracy and conservativeness of the finite element model employed.

Keywords: load-carrying capacity; FRP bars; FRP wraps; steel tube; machine learning; deep learning; concrete columns; finite elements

Résumé

L'objectif de cette thèse est de développer de nouveaux modèles de prédiction de la capacité portante en compression des colonnes en béton confiné avec l'utilisation des matériaux composites sous forme d'armatures internes et/ou des enveloppes externes en polymères renforcés de fibres à différents niveaux d'excentricité de la charge axiale. Pour ce faire, nous avons utilisé des approches de régression générale et des modèles d'apprentissage automatique avancés, tels que l'XGBoost et la forêt aléatoire (RF). Nous avons aussi, utilisés des modèles d'apprentissage profond, tels-que BiLSTM et CNN-BiLSTM, pour prédire la capacité portante en compression axiale des tubes en acier remplis de béton confinés avec des polymères renforcés de fibres. Les modèles de confinement proposés ont été développés en utilisant une base de données bibliographiques composées de 308 spécimens en béton armé renforcé avec des barres en polymères renforcés de fibres et 250 spécimens en béton armé confiné par des enveloppes externes en polymères renforcés de fibres ou des tubes en acier. Les résultats obtenus ont montré que, les modèles proposés notamment ceux basés sur XGBoost et la forêt aléatoire (RF), permettent d'avoir une bonne précision avec un coefficient de détermination (R^2) de 0,98 en plus des valeurs minimes de la racine de l'erreur quadratique moyenne (RMSE) et la moyenne des différences absolues (MAE), dépassant ainsi, les modèles empiriques usuels. Le modèle CNN-BiLSTM a également donné une meilleure performance que celle du modèle BiLSTM. En outre, une analyse par éléments finis avec l'usage d'ABAQUS a montré que les prédictions charge et déformation axiales approchaient les valeurs des résultats expérimentaux, ce qui permet de confirmer la précision et la conservativité du modèle éléments finis ici utilisé.

Mots clés : capacité portante ; barres en PRF ; enveloppes en PRF ; tube en acier ; apprentissage automatique ; apprentissage profond ; colonnes en béton ; éléments finis.

ملـــــــــخص

تهدف هذه الأطروحة إلى تطوير نماذج جديدة للتنبؤ بالقدرة التحميلية الانضغاطية للأعمدة الخرسانية المحصورة باستخدام المواد المركبة، سواءً كتعزيزات داخلية و/أو أغلفة خارجية من البوليمرات المسلحة بالألياف (FRP)، وفق مستويات مختلفة من لا مركزية الحمولة المحورية. ولتحقيق ذلك، تم استخدام مناهج الانحدار العام ونماذج التعلم الآلي المتقدمة، مثل XGBoost والغابة العشوائية (RF). كما استخدمنا كذلك نماذج التعلم العميق، مثل BiLSTM و-CNN BiLSTM، للتنبؤ بالقدرة التحميلية الانضغاطية المحورية للأنابيب الفولاذية المملوءة بالخرسانة والمحصورة خارجيا بواسطة البوليمرات المسلحة بالألياف. تجدر الإشارة أن نماذج الحصر المقترحة تم تطويرها باستخدام قاعدة بيانات مستخلصة من المراجع العلمية ذات الصلة بموضوع البحث، والتي تشمل 308 عينة من الخرسانة المسلحة بقضبان من البوليمرات المسلحة بالألياف، و250 عينة من الخرسانة المسلحة المحصورة بواسطة أغلفة خارجية من البوليمرات المسلحة بالألياف أو أنابيب فولاذية. أظهرت نتائج البحث أن نماذج الحصر المقترحة، خاصةً تلك المبنية على XGBoost والغابة العشوائية (RF)، حققت دقة عالية في تقدير القيم المتوقعة مع معامل تحديد (R^2) بلغ 0.98، بالإضافة إلى قيم منخفضة لكل من الجذر التربيعي للخطأ المتوسط (RMSE) ومتوسط الخطأ المطلق (MAE)، متجاوزة بذلك النماذج التجريبية التقليدية. كما قدم نموذج CNN-BiLSTM أداءً أفضل مقارنةً بنموذج BiLSTM. علاوة على ذلك، أظهرت تحليلات العناصر المحددة باستخدام برنامج ABAQUS أن القيم المتوقعة للحمولة والتشوه المحوريين كانت قريبة من النتائج التجريبية، مما يؤكد دقة ومحافظة نموذج العناصر المحددة المستخدم.

الكلمات المفتاحية: القدرة التحميلية؛ قضبان FRP؛ أغلفة FRP؛ أنبوب فولاذي؛ التعلم الآلي؛ التعلم العميق؛ أعمدة خرسانية؛ العناصر المحددة.

TABLE OF CONTENTS

CHAPTER I: An Overview On Strengthening Of The Reinforced Concrete Columns

CHAPTER II: Integration of Training Sciences as Analytical Methods for Predicting the Behavior of Structural Elements Reinforced with Internal or External FRP Materials

CHAPTER III: Predicting The Load-Carrying Capacity Of Concrete Columns Internally Confined With Fiber Reinforced Polymer Bars

CHAPTER IV: High-Fidelity Simulation of Externally FRP-Confined CFST Columns: The Synergy of Hybrid Deep Learning

CHAPTER V: Finite Element Analysis of Axially Loaded FRP-Confined Concrete Filled Steel Tube Columns

LIST OF FIGURES

LIST OF SYMBOLS, ABBREVIATIONS

Abbreviations

AAE	Average Absolute Error
ACI	American Concrete Institute
AI	Artificial intelligence
ALCC	Axial load carrying capacity
ANN	Artificial neural network
BFRP	Basalt fiber-reinforced polymer
CFRP	Carbon fiber-reinforced polymer
GFRP	Glass fiber-reinforced polymer
RC	Reinforced Concrete
FRP	Fiber Reinforced Polymer
R^2	Coefficient of determination
RMSE	Root mean square error
MAE	Mean Absolute Error
ML	Machine learning
NSC	Normal Strength Concrete
SD	Standard Deviation
GFRP	Glass fiber-reinforced polymer
GMDH	Group Method of Data Handling
XGBoost	EXtreme Gradient Boosting
RF	Random forest
CFST	Concrete-Filled Steel Tube
CFDST	Configurations Filled with Sandwich Concrete
NSC	Normal-strength concrete
HSC	high-strength concrete
UHSC	Ultra-high-strength concrete
NSS	Normal-strength steel
HSS	High-strength steel
DL	Deep learning
FEM	Finite element modeling
CNNs	Convolutional Neural Networks
BiLSTM	Bidirectional Long Short-Term Memory
AVG	Average
S4R	4-node shell elements
C3D8R	8-node brick elements
NSE	Nash-sutcliffe efficiency
R	Correlation coefficient
KGE	Kling-gupta efficiency
SD	standard deviation
CV	coefficient of variation

Symbols

H	Height of the specimen
A_{frp}	Cross-sectional area of FRP reinforcing bar
A_g	Gross cross-sectional area
a, a_o	Regression coefficient
l_{type}	Type of FRP reinforcement
S_{type}	Cross-section type of concrete
CS	Configuration of stirrups
C_{type}	Type of concrete
d_m	Diameter of main FRP bar
d_s	Diameter of stirrups
e	Eccentricity
E_{frp}	Elastic modulus of FRP
f_c'	Compressive strength of concrete
f_{frp}	Tensile strength of FRP
n	No. of FRP bars
N	Total number of datasets
$N_{normalized}$	Normalized value
ρ_{frp}	Percentage of FRP reinforcement
P_u	Ultimate axial capacity
P_{cond}	Axial load condition
$P_{u,pred}$	Predicted values of ultimate axial capacity
$P_{u,exp}$	Experimental values of ultimate axial capacity
X_i	Experimental value
Y_i	Prediction value
X	Input parameters
Y	Output parameter
S_v	Spacing of stirrups
T_{type}	Type of tie bar
U_i	Predicted value
ε_{reg}	Axial strain in The FRP Bar
α_{frp}	Strength of the FRP bars
$\hat{y}_i$	Predicted output for the i-th instance
$L^{(t)}$	The total loss function at the t-th iteration
$f_l(X_i)$	The output of the t-th base model for input X_i
$\Omega(f_k)$	Regularization term that penalizes the complexity of the base mode
γ	Parameter that controls the penalty for adding additional leaves to the tree
T	The number of leaves in the tree
λ	Regularization parameter that controls the penalty on the leaf weights
w_j	Weight of the j-th leaf
L/D	Height-to-diameter
N_u	Ultimate axial load-carrying capacity of FRP-confined (CFST)
ξ_s	Confinement index of the steel tube

ξ_f	Confinement index of the PRF
A_s	Steel tube section area
f_y	Yield strength of the steel tube
A_c	Area of the core concrete
f_{co}	Compressive strength of unconfined concrete
A_f	FRP section area
f_f	Tensile strength of FRP
f'_{cc}	Compressive strength of confined concrete
f_l	Lateral confining pressure provided by FRP and steel tube
A_{sc}	Cross-sectional area of the specimens
N_s	Ultimate load of steel tube
N_{co}	Ultimate load of unconfined concrete
N_{cs}	Ultimate load of concrete under the circumferential constrain of steel tube
N_{cf}	Ultimate load of concrete under the circumferential constrain of FRP
k	Confinement stiffness of the FRP
E_f	Elastic modulus of the FRP
$\sigma_{r,c}$	Circumferential banding force of concrete
$\sigma_{\theta,s}$	Perimeter stress provided by the steel tube
f_{cf}	Tensile strength of CFRP
ρ	Steel ratio is defined as the ratio of the cross-sectional area of the steel tube to the sum of the cross-sectional areas of both the steel tube and the concrete core
ρ_1	CFRP ratio is described as the proportion of the combined cross-sectional area of CFRP and the concrete core to the total cross-sectional areas of both the steel tube and the concrete core
$\sigma_{L,s}$	Axial stress of steel tube
f_{cu}	Compressive strength of cube concrete
η_{cap}	Index of capacity
N	Unconfined concrete filled stainless steel tube columns
f_u	Ultimate tensile strength of the steel tube
f_{co}	Compressive strength of unconfined concrete
D	Diameter of the specimen cross section
t_s	Thickness of steel tube
f_y	Yield strength of steel tube
n	Number of FRP layers
f_f	Ultimate tensile strength of FRP
t_f	Thickness of FRP
ε_f	Ultimate tensile strain of FRP
H/D	Height-to-diameter ratio
D/t_s	Diameter-to-thickness ratio
U_{Rx}	Displacements in the X direction
U_{Ry}	Displacements in the Y direction
U_{Rz}	Rotational
E_s	Modulus of elasticity of steel

ν_c	Concrete's Poisson's ratio
f_{bo}/f_{co}	Ratio of concrete strength under biaxial compression to uniaxial strength
k_c	Strength ratio of concrete under equal biaxial compression to triaxial compression
e	Eccentricity parameter
ψ	Dilation angle
f and ε_x	Stress and strain of the confined concrete
f_o and ε_o	Peak stress and strain of the confined concrete
T	Where is the sequence length
x_t	Input feature vector at time step t
F	Number of features
w_f	Are the convolutional filters (weights)
b	Bias term
$h_t^{(c)}$	Output of the convolutional layer at position
ReLU	Activation function
k	Pooling size
$h_t^{(p)}$	Pooled feature at position t
W_d.	Weight matrix for the dense layer
b_d	Bias term
σ	Activation function
θ	Model parameters
η	Learning rate
$J(\theta)$	Loss function
∇_θ	Gradient of the loss function with respect to θ
$N_{uo,i}$ $N_{us,i}$	Observed and simulated observations, respectively.

General Introduction

1. Backgroud

1.1. Internal confinement with FRP bars

The primary function of a reinforced concrete compressive member is to support axial loads, regardless of whether they are accompanied by bending moments. However, the ability of steel bar reinforced concrete compressive members to carry axial loads diminishes over the design life of concrete structures due to corrosion of the steel bars. This problem is especially pronounced in coastal areas or harsh environmental conditions, presenting a major drawback of using steel reinforced concrete in construction. As a result, the expenses associated with retrofitting and repairing deteriorated concrete structures are notably high. The review of the literature found that fiber-reinforced polymer (FRP) composites have been widely used as internal reinforcement (FRP reinforcing bars) in reinforced concrete structures due to their excellent corrosion resistance, high strength-weight ratio resistance to harsh environmental conditions (Sun 2024, Jabbar and Farid 2018, Ye et al. 2022). In this context, several studies have been carried out on the performance of FRP bars reinforced concrete columns under concentric compression. The investigated parameters included the concrete compressive strength, gross cross-sectional area, cross-sectional area of FRP reinforcing bar, number of FRP bars, form of tie bar, type of longitudinal FRP reinforcement, type of transverse FRP reinforcement, diameter of stirrups, diameter of the main FRP bar, the elastic modulus of FRP bar and tensile strength of FRP bar, and spacing of stirrups. Experimental studies have shown that FRP bar-reinforced concrete compressive members exhibit lower load-carrying capacities under concentric axial loads than steel bar-reinforced concrete compressive members of identical size and reinforcement configuration. This disparity is mainly attributed to the reduced ultimate compressive strength and modulus of elasticity of FRP bars in compression, as compared to conventional steel bars. Additionally, neglecting the contribution of FRP bars will underestimate the axial capacity. According to Tobbi et al. (2014), the load-carrying capacity of concrete compressive members increases with considering the contribution of FRP bars. Similar to Tobbi et al. (2014), Elmessalami et al. (2019) concluded also that FRP bars can offer from 3%-14% of axial capacity. Theoretical models such as ACI 440.1R-15, CSA S806-02, CSA S806-12, AS-3600, Tobbi et al. (2012), Tobbi et al. (2014), Afifi et al. (2014a), Afifi et al. (2014b), Maranan et al. (2016), Xue et al. (2018), Mohammed et al. (2014a, b), Samani and Attard (2012), Khan et al. (2016), Hadhood et al. (2017) were established to predict the peak axial capacity of FRP bars reinforced concrete compressive members. The developed formulas were based on three main approaches: ignoring the contribution of FRP bars in compression, considering the contribution of FRP bars based on reduced tensile strength, and considering the contribution of FRP bars based on axial strain. Most of these models were suggested using regression analysis and based on limited test

results. The difficulties of these models are that they cannot predict the peak axial capacity of FRP bars-reinforced concrete compressive members accurately. However, investigations on the performance of FRP bars reinforced concrete compressive members under eccentric compression are still limited and no suggested formulas existing in the literature considered the eccentricity effect.

1.2. External confinement with FRP wraps

The adoption of Concrete-Filled Steel Tube (CFST) columns has seen a notable rise in recent years, attributed to their structural efficiency and capacity to support substantial loads. Investigations have been directed towards various cross-sectional configurations of CFST columns, including circular, square, rectangular, and elliptical shapes, as well as the exploration of different wrapping materials. Among these innovations are dual steel tube Configurations Filled with Sandwich Concrete (CFDST) and Concrete-Filled Steel Tubes (CFST) enhanced with additional materials such as Fiber-Reinforced Polymers (FRP) to augment their performance (Ding et *al*. 2018, Zhang et *al*. 2023). FRP-confined CFST columns are frequently employed in construction applications, including bridges and buildings. Their popularity stems from their superior strength-to-weight ratio, resistance to fatigue, and protection against corrosion. FRP, a composite material, consists of a polymer matrix reinforced with fibers. Various types of FRP, such as carbon fiber-reinforced polymers (CFRP), glass fiber-reinforced polymers (GFRP), and basalt fiber-reinforced polymers (BFRP), are selected for specific applications based on their distinct characteristics (Liu et *al*. 2018, Shen et *al*. 2019). The literature provides a comprehensive examination of FRP-confined CFST columns subjected to concentric loading, encompassing both experimental and numerical analyses. Key variables investigated include the numbers, thickness, and type of FRP layers (e.g., Ma et *al*. 2023, Sun et al. 2009 and Wang et al. 2006), concrete grades (normal-strength concrete (NSC), high-strength concrete (HSC), and ultra-high-strength concrete (UHSC)) (Cao et al. 2020, Ma et al. 2023, Li et al. 2008 and Shao et al. 2024), the strength of the steel tube (including normal-strength steel (NSS), high-strength steel (HSS), or stainless steel) (Zhao et *al*. 2021 and Zhang et al. 2023), and the ratio of the outer diameter to the thickness of the steel tubes (Shen et *al*. 2019, Zeng et *al*. 2021, Cao et *al*. 2020, Hassanein et *al*. 2023a, Hassanein et *al*. 2023b, Ma et *al*. 2023, Shao et *al*. 2024). Accurately estimating a column's final axial load-bearing capacity under axial loading is the main focus of engineering design for load-bearing capacity. In general, experimental techniques are preferred when evaluating the performance of composite columns. To examine the behavior of circular CFST columns enclosed with FRP under axial loading, numerous experiments were conducted. Many researchers have developed empirical design formulas to forecast the ultimate axial load of FRP-confined CFST circular columns under axial loading, as a result of extensive testing on these columns, such as Tao et *al*. (2007), Park et *al*. (2011), Che et *al*. (2012) and Lu et *al*. (2014) Dong et *al.* (2017), Ding et *al*. (2018), Tang et *al*. (2020) and Ma

et *al*. (2022). Most of these models were developed based on regression analysis and have been validated against their limited own or collected sets of experimental data. However, the drawback of these models is their limitations to predict the axial load-bearing capacity of FRP-wrapped CFST circular columns accurately. So, the expressions proposed using the regression technique are unable to estimate load capacity properly.

2. Research objectives

The thesis reports research carried out by the candidate over the last few years aimed at developing an improved understanding of the structural behavior of concrete columns internally and/or externally confined with FRP material. The work has been carried out with static application in mind, so enhancement in strength and ductility are considered.

For columns, the compressive behavior is obviously the most important, as it underpins studies into their behavior under other loading conditions. In addition, columns are normally also subjected to bending due to load eccentricity. This thesis therefore first discusses the behavior of concrete columns internally confined with FRP bars and subjected to both concentric and eccentric compression loads. The behavior of concrete columns confined by both FRP wraps and steel tubes and subjected to axial compression load is dealt with as the next subject. The research work presented in this thesis was carried out with the following objectives:

1. The first part of work proposes application of the eXtreme Gradient Boosting (XGBoost) and Random Forest (RF) algorithms to predict the axial capacity of FRP-reinforced compressive members having different levels of eccentricity. These approaches are unique, as they examine the development of an interpretable machine-learning model for capturing the axial load capacity of FRP-reinforced compressive members with different levels of eccentricity (e/h ranges from 0 to 1), an area that has not been extensively investigated before. Further, the proposed XGBoost and RF models offer a potential alternative to available mechanics-based models for practical engineering design purposes. In addition, an empirical model was also developed using regression analysis. A comprehensive dataset containing experimental data of 308 FRP-reinforced concrete samples was collected from the previous studies. The efficiency and accuracy of the proposed models were compared with those fifteen empirical models. Five statistical indicators including coefficient of determination (R^2), root mean square error (RMSE), mean absolute error (MAE), average absolute error (AAE), and standard deviation (SD) are calculated to assess the performance of those predictive models.
2. The second part of work suggests that the machine learning (ML) models now in use, which were created to forecast the axial load-carrying capacity of FRP-confined concrete-filled steel tube (CFST) columns, are mostly applicable to short columns.

Moreover, there are currently no finite element (FE) or hybrid deep learning (DL) models that can reliably forecast the axial load-carrying capacities of these columns. The approach used for this investigation is presented in this section and is broken down into four main parts. Examining current design models created to forecast the axial load-carrying capacities (N_u) of columns is the initial step in the process. The second stage involves gathering experimental data from pertinent studies and publications about the axial load-carrying capability of FRP-confined CFST columns. In the third step, ABAQUS software is used to simulate the axial load-axial deformation behavior of FRP-confined CFST columns. The FE results are then compared to experimental data from 40 FRP-confined CFST samples. The last section focuses on using CNN-BiLSTM and BiLSTM, two deep learning-based regression models, to forecast the axial load-carrying capability of FRP-confined CFST columns. The performance of the proposed models is compared with that of some models developed by other researchers.

3. Thesis outline

The thesis comprises five chapters. It begins with a general introduction in which the research problem is defined and the objectives are outlined. Chapters I and II provide an overview of the existing literature that is pertinent to the present research. Chapters III, VI and V present analytical and numerical investigations on various aspects of the behavior of concrete columns confined with internal and/or external FRP materials. Details of these chapters are summarized below.

Chapter I presents a review of the existing literature covering the topic related to the present study. The deterioration caused by reinforcement steel corrosion and seismic forces are discussed first. Somme common column retrofit methods are then reviewed and compared in order to highlight the advantages of FRP jacketing. The existing experimental studies on both internally and externally FRP-confined concrete columns are also presented.

In Chapter II, analysis methods covering approaches related to the present investigation are presented. First, a brief review of general regression analysis is provided. Then, machine learning-based regression approaches for predicting design models are reviewed. Finally, deep learning-based regression approaches for predicting design models are reported.

Chapter III presents the results of a study in which the benefit of FRP bars confinement of concrete columns under both concentric and eccentric compression load was examined. First, current design approaches for FRP-RC columns are reviewed. Next, a dataset consisting of 377 experimental results sourced from existing literature is compiled. The performance of existing models was evaluated using five statistical metrics: the coefficient of determination (R^2), root-mean-square error (RMSE), mean absolute error (MAE), average absolute error (AAE), and standard deviation (SD). Additionally, three load-carrying capacity (LCC)

prediction models were developed; one using a general regression technique and two employing machine learning algorithms, specifically eXtreme Gradient Boosting (XGBoost) and Random Forest (RF) regression methods. Finally, the proposed models were benchmarked against existing design standards and previously suggested empirical equations to assess their accuracy and reliability.

In chapter IV, the benefit of FRP confinement on concrete filled steel tube (CFST) columns under axial compression load is examined through an analytical study. Eight existing design models and 250 experimental data points were reviewed through the literature. Advanced hybrid deep learning (BiLSTM and CNN-BiLSTM) predictive models were proposed to accurately predict the axial load-carrying capacity (ALCC) of FRP-confined CFST columns under compression loads. Finally, a comparison of the accuracy between the proposed models and previously suggested empirical equations was conducted.

Chapter V is concerned with the finite element modeling of the monotonic axial compression behavior of FRP-confined concrete-filled steel tube (CFST) columns. First, a total of 40 experimental tests on FRP-confined CFST columns, collected from previous studies, were simulated using the ABAQUS software package. The FEA results were then compared with experimental data from the 40 FRP-confined CFST specimens. In addition, a detailed parametric study was conducted using the FEA model to investigate the effects of two parameters such as diameter-to-thickness ratio (D/t_s) and height-to-diameter ratio (H/D) ratio on the load-carrying capacity and ductility of the columns.

The thesis ends with the conclusions, where the findings drawn from the previous chapters are reviewed, and areas in need of further research are highlighted.

CHAPTER I:

AN OVERVIEW ON STRENGTHENING OF THE REINFORCED CONCRETE COLUMNS

I.1. INTRODUCTION

Reinforced concrete (RC) structures often require repair and strengthening due to changes in load or support conditions, material deterioration, or structural damage caused by earthquakes or extreme loading events. This chapter provides an overview of the existing literature pertinent to the present research. The discussion begins with deterioration caused by reinforcement steel corrosion and seismic forces. Subsequently, common column retrofit methods are reviewed and compared to highlight the advantages of FRP jacketing, considered a promising modern retrofit technique. Finally, existing experimental studies on both internally and externally FRP-confined concrete columns are briefly reviewed.

I.2. DEFICIENCIES IN REINFORCED CONCRETE COLUMNS

Reinforced concrete (RC) structures are widely used in civil engineering due to their strength, durability, and adaptability, consisting of concrete, which provides compressive strength, and embedded steel reinforcement, which enhances tensile capacity (Neville & Brooks 2010). Among the critical components of RC structures, columns play a fundamental role as the primary load-bearing elements, transferring loads from the superstructure to the foundation. The stability and overall performance of buildings and infrastructure heavily depend on the integrity of these columns (MacGregor & Wight 2016). However, RC columns are susceptible to deterioration due to various environmental and structural factors, with corrosion of reinforcement steel and seismic forces being two of the most severe challenges (Figure I.1).

Figure I.1: Failure of concrete columns due to corrosion and earthquakes (Paultre et *al*. 2013)

I.2.1. Corrosion

Corrosion of reinforcement steel (Figure I.2) significantly impacts the longevity and safety of RC columns, especially in aggressive environments such as coastal or industrial areas. Exposure to chloride ingress, carbonation, and moisture penetration leads to the loss of steel cross-section, cracking, and spalling of the concrete cover, ultimately weakening the load-

bearing capacity and reducing ductility (Broomfield 2007). Over time, this degradation makes the structure more vulnerable to external loads, particularly dynamic forces such as those induced by earthquakes (Andrade & Alonso 2001).

Figure I.2: Steel corrosion in concrete columns (Pellizzer & Leonel 2020).

I.2.1.1. Mechanisms of Corrosion in RC Columns

Corrosion of reinforcement is a frequent cause of deterioration in reinforced concrete (Figure I.3), and numerous researchers have investigated its mechanisms and impact on the structural behavior of deteriorated RC elements. This process is primarily driven by various environmental and chemical factors that degrade the embedded steel reinforcement over time, compromising the structural integrity of RC columns through different mechanisms (Broomfield 2007; Andrade & Alonso 2001).

1. **Chloride Ingress**: Exposure to de-icing salts or marine environments leads to chloride-induced corrosion, causing localized pitting that weakens steel reinforcement.

How does chloride penetrate the material?

- Chloride (Cl^-) enters the material from de-icing salts or marine environments;
- The ingress is non-uniform due to variations in porosity, cracks, and chloride binding on hydrated phases (Rodrigues et *al.* 2021);
- Local depassivation occurs through Cl^- adsorption, along with the formation and diffusion of iron (Fe) and oxygen (O) vacancies (not depicted in the figure).

Figure I.3: Chloride Ingress of Steel corrosion in concrete columns (Al-Haddad & Jokhio 2024).

There are two cases:

- **Low Chloride Content:** The passive layer undergoes cycles of breakdown and repair as CP precipitates on the remaining film;
- **High Chloride Content:** Pitting corrosion occurs, leading to the formation and persistence of an aggressive microenvironment (Figure I.4).

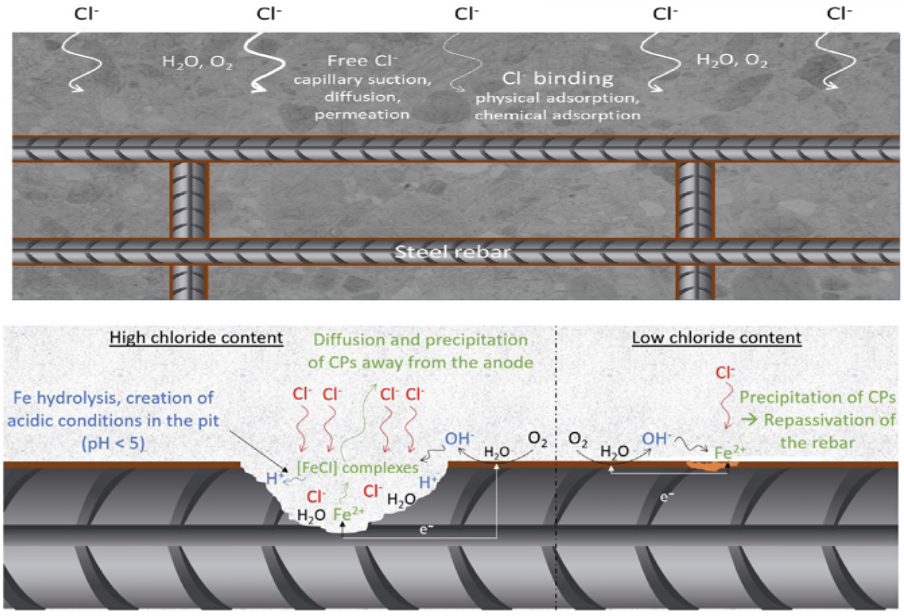

Figure I.4: Schematic representation of the mechanism of Chloride Ingress corrosion of steel in concrete (Rodrigues et *al*. 2021).

2. **Carbonation**: The ingress of carbon dioxide into concrete reduces the pH of the pore solution, breaking down the passive protective layer on the steel surface, leading to generalized corrosion (Figure I.5).

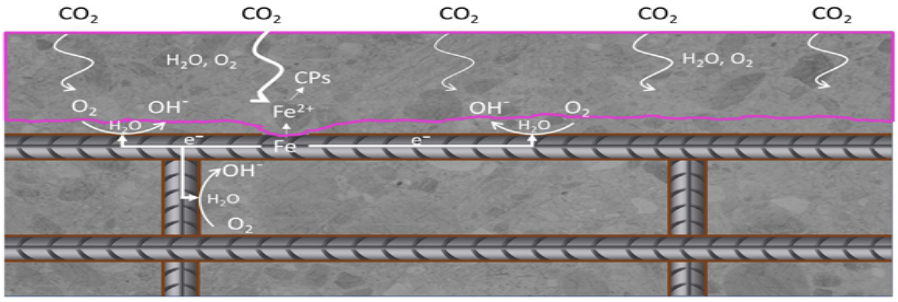

Figure I.5: Schematic representation of the mechanism of carbonation-induced corrosion of steel in concrete (Rodrigues et *al*. 2021).

3. **Moisture Penetration**: Water ingress through cracks or inadequate concrete cover accelerates corrosion by providing an electrolyte for electrochemical reactions. The presence of moisture enhances the migration of chloride ions and CO_2, further exacerbating the deterioration process.

4. **Oxygen Availability**: Variations in oxygen concentration contribute to differential aeration corrosion. Areas with restricted oxygen supply become anodic, while regions with higher oxygen availability act as cathodes, creating corrosion cells that accelerate steel degradation.

I.2.1.2. Effects of Corrosion on Structural Performance

The deterioration caused by corrosion affects the mechanical behavior and durability of RC columns in multiple ways (Figure I.6):

- **Reduction in Load-Bearing Capacity**: As steel reinforcement corrodes, its cross-sectional area decreases, reducing the column's ability to carry axial and lateral loads.
- **Cracking and Spalling**: The expansion of corrosion products induces internal stresses, leading to cracking and spalling of the concrete cover, which further accelerates deterioration.
- **Loss of Bond Strength**: The adhesion between steel and concrete weakens, compromising structural integrity and leading to premature failure under loads.
- **Reduction in Ductility**: Corrosion diminishes the ductility of RC columns, increasing their brittleness and making them more vulnerable to seismic forces.

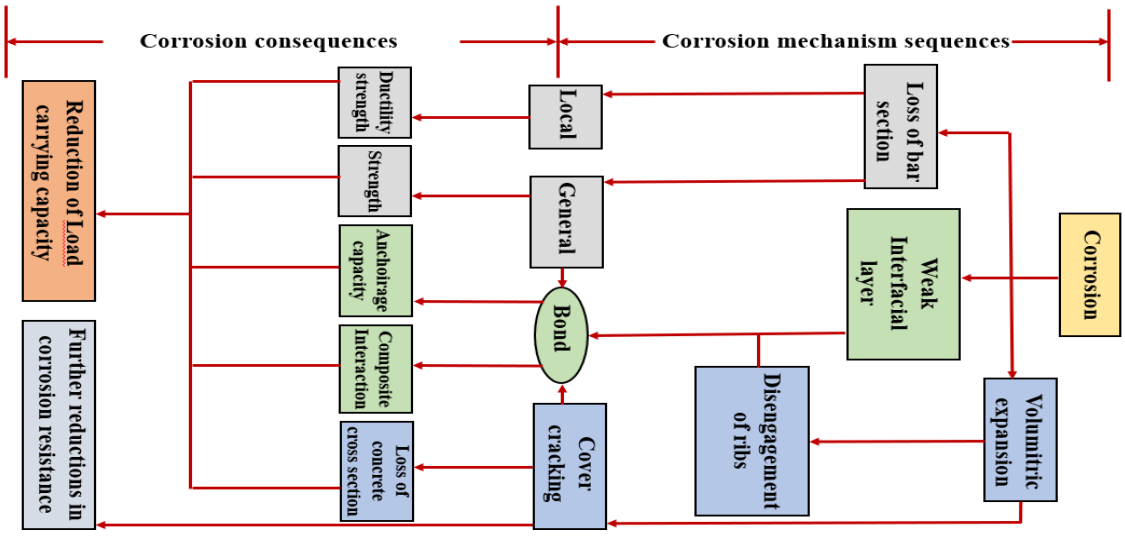

Figure I.6: Sequences and consequences of corrosion on reinforcements.

I.2.2. Corrosion and Seismic Performance of RC Columns

RC columns affected by corrosion exhibit a significant decline in seismic performance due to:

- **Weakened Confinement**: Corrosion reduces the effectiveness of transverse reinforcement (stirrups), impairing the column's ability to resist lateral seismic loads;
- **Brittle Failure Modes**: Loss of ductility leads to brittle failure, reducing the column's energy dissipation capacity during cyclic loading;
- **Degradation of Hysteretic Behavior**: Studies have shown that corroded RC columns experience severe stiffness and strength degradation under cyclic loading (Figure I.7), making them more susceptible to collapse during earthquakes (Oreb 2023).

Figure I.7: Concrete column destruction (Oreb 2023).

I.2.3. Experimental findings on corroded RC columns

I.2.3.1. Experimental study of Ma et al.

Ma et *al*. (2012) investigated the impact of reinforcement corrosion on the seismic behavior of RC columns. Their study involved 13 circular RC columns (see Figure I.8), which were subjected to accelerated corrosion tests, followed by cyclic lateral loading under a constant axial load. The key variables were corrosion loss (0% to 15.1%) and axial load ratio (0.15 to 0.9). The results showed that corrosion significantly reduces load capacity, stiffness, ductility, and energy dissipation. Higher corrosion levels and axial loads led to greater strength degradation and less stable hysteretic loops. When corrosion loss exceeded 14%, energy dissipation remained similar to non-corroded specimens, but strength degradation worsened. Additionally, stirrups were more vulnerable to corrosion, increasing the risk of brittle failure. The study highlights the need for corrosion prevention and retrofitting to maintain seismic resilience.

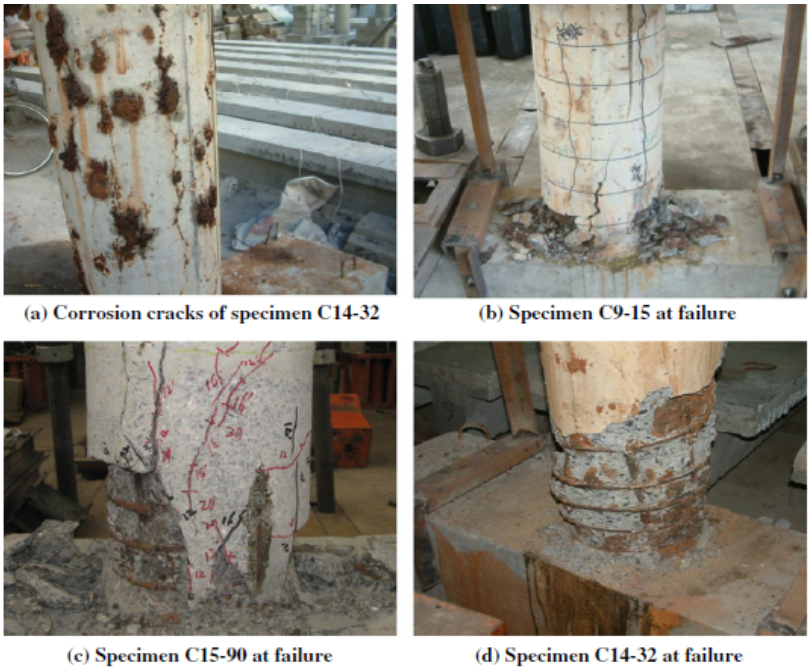

Figure I.8: Illustrations of corrosion and column failure (Ma et *al*. 2012).

I.2.3.2. Experimental study of Vu and Lu

The study of Vu and Lu (2018) examined the effects of reinforcement corrosion on the seismic performance of six full-scale RC short columns (Figure I.9), including both corroded and uncorroded specimens. Corrosion was induced using an electrochemical method, applying an external current to the reinforcement while immersing the columns in a 5% NaCl solution, and cyclic lateral loading was applied under constant axial force. Key variables included corrosion levels and axial load ratios (0.1f'cAg and 0.25f'cAg). The columns were designed with a 350×350 mm cross-section and a shear span-to-depth ratio of 1.5. The obtain results showed that corrosion significantly reduced seismic performance, with corroded columns losing up to 20% of shear strength and up to 57.9% of energy dissipation capacity. Higher axial loads worsened degradation, leading to increased stiffness loss, pinching effects, and brittle failure. Crack patterns differed, with corroded columns exhibiting additional vertical cracks due to bond deterioration. Drift capacity also declined, with axial failure drift ratios decreasing by up to 56.2% in highly corroded columns.

The study found that initial stiffness increased under high axial loads due to altered load transfer mechanisms. Overall, the findings highlight the severe impact of corrosion on RC columns, emphasizing the need for corrosion prevention and retrofitting to maintain structural resilience in seismic environments.

Figure I.9: Failure crack patterns observed in the test specimens under axial loading (Vu and Lu 2018).

I.3. SEISMIC RETROFITTING STRATEGIES OF RC BUILDINGS

Earthquakes cause sudden and severe devastation, leading to extensive structural damage ranging from minor to complete destruction. This, in turn, results in significant loss of life, making occupants hesitant to return unless assured of the building's safety. Research indicates that many damaged buildings can be safely reused through seismic retrofitting, which strengthens structures against future earthquakes. This method is often a more cost-effective and practical solution compared to demolition and reconstruction, even in cases of severe

damage. Seismic retrofitting plays a crucial role in reducing earthquake risks, especially in vulnerable regions. Various terms, such as repair, strengthening, and rehabilitation, are used in this context, though their definitions may vary.

Seismic retrofitting of buildings is necessary in two cases: (i) structures already damaged by earthquakes and (ii) buildings vulnerable to future seismic events. Engineers face challenges in retrofitting due to the lack of standardized methods, limited data on effectiveness, and no consensus on appropriate techniques for varying structural conditions and damage levels. A comprehensive catalogue of feasible retrofitting methods is essential, along with further research to improve techniques.

For existing earthquake-vulnerable buildings, retrofitting may be required for several reasons, such as updated seismic codes, design or construction deficiencies, the need to strengthen essential structures like hospitals and historic buildings, or changes in building use and renovations. Engineers must gather extensive records, including architectural plans, material properties, and structural details, to properly assess and strengthen these buildings while considering the effects of increased stiffness.

In Algeria, retrofitting and structural safety have not received sufficient attention, with no established guidelines or codes. While developed countries have advanced research on repair and retrofitting over the past decades, Algeria still lacks standardized assessment methods. Seismic retrofitting techniques focus on three key principles: (a) enhancing lateral strength, (b) improving ductility, and (c) increasing both strength and ductility, as illustrated in Figure I.10.

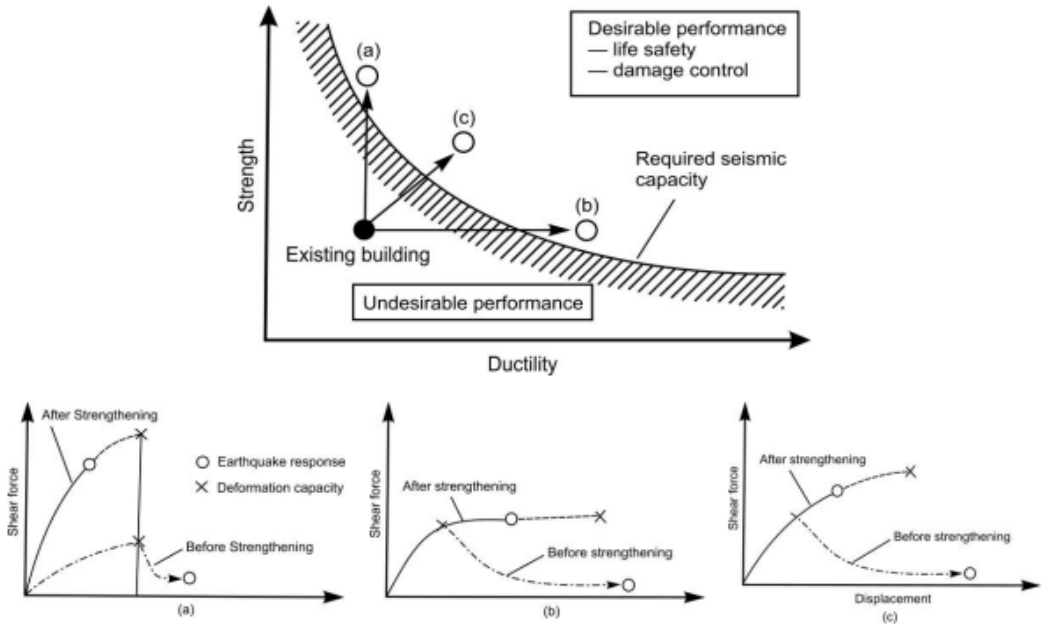

Figure I.10: Aim of seismic strengthening (Selemon et *al*. 2023).

The decision to repair and strengthen a structure depends not only on technical considerations as mentioned above but also on a cost/benefit analysis of the different possible

alternatives. It is suggested that the cost of retrofitting of a structure should remain below 25% of the replacement as major justification of retrofitting.

The following section will discuss the different reinforcement techniques as well as their limitations. The information presented in this section comes from the existing literature.

I.3.1. Classification of retrofitting techniques

Seismic capacity enhancement of existing structures can be achieved through two main approaches. The first is a global retrofitting strategy, which involves modifying the overall structural system. The second is a localized retrofitting method, focusing on improving the ductility of individual components to ensure they meet their specific performance requirements (Kam & Pampanin 2008, Bournas 2018). Based on this concept, the various retrofitting techniques for reinforced concrete buildings can be categorized as shown in Figure I.11.

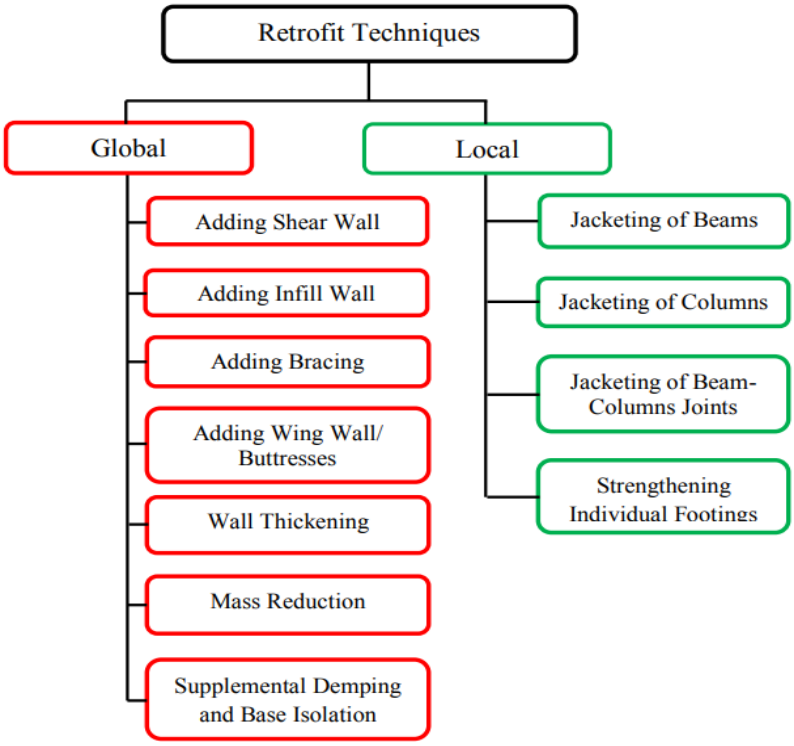

Figure I.11: Global and local retrofit techniques.

After presenting the global and local rehabilitation approaches for reinforced concrete structures, it is now appropriate to examine the specific strengthening techniques applied to individual structural elements, particularly reinforced concrete columns.

I.3.2. Local retrofit techniques

The member-level or local retrofitting approach aims to enhance the strength of structural components that lack adequate seismic resistance. This technique is more economical compared to retrofitting the entire structure. One of the most common methods for reinforcing

individual elements is jacketing, which consists of applying additional layers of concrete, steel, or fiber-reinforced polymer (FRP) to reinforce columns, beams, joints, and foundations in reinforced concrete structures. The next section presents a concise overview of jacketing and its applications to different structural elements.

I.3.3. Reinforced concrete jacketing

Concrete jacketing is a widely used technique for strengthening reinforced concrete elements, especially columns, to reduce lateral deformation and increase their strength and load-bearing capacity. This method consists of applying a reinforced concrete jacket to the existing element, incorporating longitudinal steel reinforcement and transverse ties around its perimeter. The jacket can be formed using either cast-in-place concrete or shotcrete (Figure I.12). It is typically applied to columns that are failing due to overload, material deterioration, poor maintenance, or inadequate construction practices. Additionally, it can be used to increase a column's load-bearing capacity when structural modifications or changes in the building's usage require it (Raza et *al*. 2019).

Figure I.12: Typical cross-sections of reinforced concrete jackets prior to concrete casting (www.quantity-takeoff.com).

The application of cast-in-place concrete jacketing involves setting up formwork around the existing column, ensuring it is firmly anchored to resist the pressure generated during concrete placement. Generally, a jacket thickness greater than 10 cm is adopted to enable effective casting and minimize the risk of void formation. In contrast, shotcrete enables the use of thinner jackets, with a minimum thickness of 5 cm. However, most jackets are at least 7.5 cm thick to ensure adequate concrete cover, accommodate reinforcement, and maintain sufficient spacing between the new rebars and the original structure.

Concrete jacketing enhances the column's dimensions as well as its longitudinal and transverse steel reinforcement. Establishing a strong interface between the original and the newly cast concrete is essential to ensure the repair's effectiveness. The primary goal of this method is to reinforce the column's axial-moment capacity, shear resistance, or overall

stiffness. While increased stiffness improves the building's resistance to lateral deformation, it also leads to greater strain due to the higher lateral load demand. This presents a trade-off, and the engineer must carefully calculate the jacket thickness to avoid overestimation. Concrete jackets are also effective in addressing buckling problems in slender columns.

Although widely used, concrete jacketing presents certain drawbacks. One major concern is the increase in the column's dimensions after repair, which reduces available space within the building-potentially posing challenges for architects and property owners. The process also involves extensive drilling into the existing column, which may already be weakened, as well as into the slabs, beams, and foundations. Moreover, ensuring monolithic casting of the concrete is both time-consuming and requires high level of accuracy, especially in the upper regions of the jacket.

The effectiveness of a jacketed structural element is primarily influenced by the strength of the jacket itself and the additional reinforcement achieved through the confinement of the original member (Figure I.13). Ideally, the column should be fully enclosed on all four sides to maximize confinement; however, this is not always feasible, particularly for columns positioned at the edges or corners of buildings. Additionally, confinement proves to be more effective for smaller columns compared to larger ones. (Abdelrahman 2023).

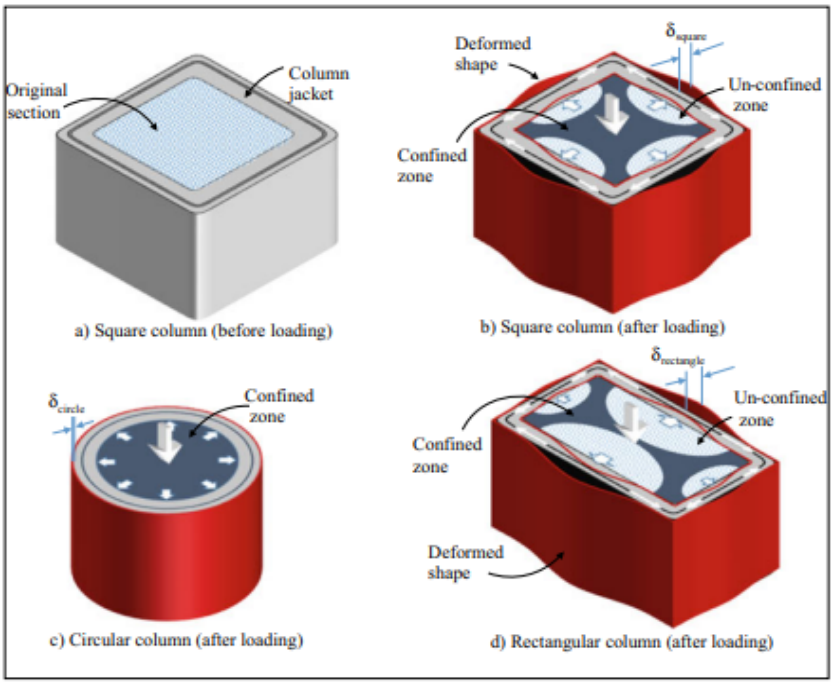

Figure I.13: Confinement of the columns induced by the jacket (Abdelrahman 2023).

I.3.3.1. Procedure for the construction of concrete jacket

The following steps can be followed for the construction of column jacketing, as depicted in Figures I.14a and I.14b:

1. Propping the slabs: Temporary supports are installed around the column and at other floor levels to create an alternative load path to the foundation. This is essential, as the column's load-bearing capacity is significantly reduced during the jacketing process.
2. Elimination of the existing concrete cover: The outer concrete layer is carefully removed until sound concrete is reached, provided there is no steel corrosion. Sandblasting is recommended to roughen the surface, as pneumatic hammering may cause microcracks in the substrate. If the reinforcement in the existing column is corroded, the concrete cover should be fully removed until the longitudinal steel bars are exposed. The steel bars are then cleaned and coated with anti-corrosion paint, or, if the corrosion is severe, they are replaced with new reinforcement.

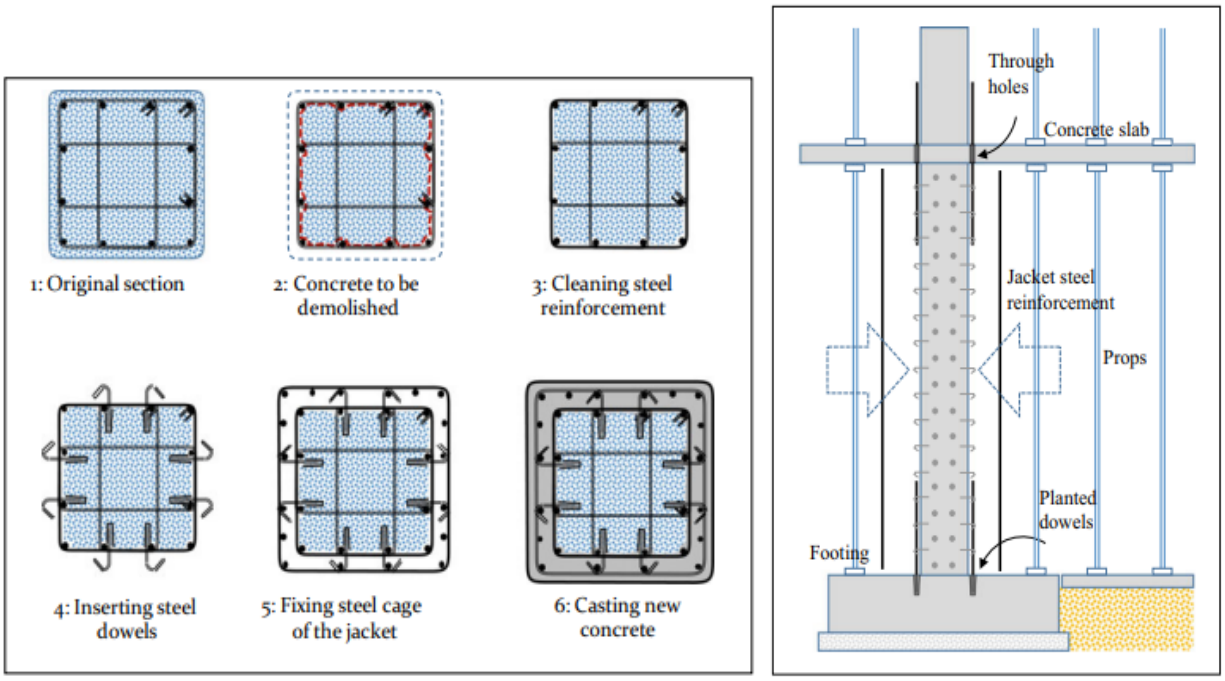

(a) (b)

Figure I.14: Column jacketing; (a) construction steps for the concrete jacket, (b) concrete jacket in progress (Abdelrahman 2023).

3. Installation of steel dowels: Steel dowels are inserted around the column edges to establish a firm mechanical connection between the existing and added concrete sections. The dowel depth and anchoring substance must be chosen to ensure development of at least the bar's yield capacity. The longitudinal bars of the jacket should be fixed into the foundation, requiring drilled holes through the slabs for vertical continuity. After placing the specified longitudinal and transverse steel, the inserted dowels should ideally be hooked to the vertical bars. This hooking arrangement minimizes early buckling in the longitudinal steel and improves the confinement performance of the column section.

4. Pouring the jacket: The jacket should be cast using a material compatible with the original concrete to ensure proper adhesion and structural integrity. Minimizing shrinkage in the jacket material is crucial to reducing stress on the steel dowels and preventing cracks in the newly added concrete. Specific recommendations for the appropriate jacket material are provided in the following section. If both steel dowels and adequate surface roughening of the existing column are implemented, the old and new concrete will act monolithically, preventing any separation at their interface (Abdelrahman 2023).

I.3.3.2. Material specifications for concrete jacketing

The concrete used for the jacket should be cast with a design mix that aligns with the physical properties of the original section's concrete, including compressive strength, elastic modulus, thermal expansion coefficient, and creep behavior. To maintain compatibility, the aggregate type should closely resemble that of the existing concrete unless testing confirms that similar physical characteristics are achieved. If the properties of the two materials differ significantly, vertical separation between the original section and the jacket may develop over time. Therefore, grout or mortar with long-term behavior that differs from concrete should be avoided in the jacket. To enhance the tensile properties of the jacket, fibers or shrinkage-compensating materials may be incorporated into the mix. A bonding agent can be applied to the old concrete before casting, following the manufacturer's instructions. The form-and-pump technique is preferred for concreting, as it prevents honeycombing and voids in the jacket. This method ensures that the top part of the jacket is fully filled with concrete and free from voids. It involves sealing the formwork and pumping concrete into the form under sufficient pressure. If this method is not feasible, holes with a minimum diameter of 100 mm can be created in the slab above to facilitate the placement of jacket concrete. Any voids that form in the newly cast concrete should be filled and repaired using cementitious or epoxy grout (Abdelrahman 2023).

Numerous research studies have focused on the strengthening and repair of columns using reinforced concrete jacketing. Below, we present a few examples to demonstrate that this so-called traditional technique remains widely used and has not been abandoned. Research on concrete-jacketed columns began in the 1980s. In 1988, Bett et *al.* investigated how concrete jacketing could recover the lateral load resistance of deteriorated columns. Their research included subjecting all test specimens to constant axial and lateral forces. The results showed that columns repaired with concrete jacketing exhibited greater stiffness and lateral load capacity compared to control columns, demonstrating the technique's effectiveness in repairing damaged concrete structures. A few years later, Ersoy et *al.* (1993) expanded on this research by investigating the behavior of jacketed columns under uniaxial load, as well as a combination of uniaxial and cyclic lateral loads. As anticipated, their findings confirmed that jacketed columns outperformed unjacketed ones in both test series. In 1994, Rodriguez and

Park performed experiments on four square concrete columns exposed to seismic forces. Two columns were initially damaged, retrofitted using jacketing, and then reloaded, while the remaining two were jacketed and compressed to failure. Their findings revealed that the repaired columns exhibited significantly higher ductility and strength. Later, Eduardo et *al.* (2005) tested seven full-scale column-footing specimens under monotonic loading after different surface treatments. The results indicated that for intact columns, efficient composite interaction was attainable even without enhancing the concrete surface texture before applying the jacket. More recently, Yuce et *al.* (2007) investigated how thin jacketing could be utilized to rehabilitate localized damage in concrete columns. In the initial test phase, four full-scale square columns were exposed to sustained axial force and repeated lateral shifts, using self-compacting concrete for the jacketing process. The second series focused on previously damaged and repaired columns. The study concluded that thin jacketing with self-compacting concrete enhanced both the lateral stiffness and strength of severely damaged columns. Tayeh et *al.* (2019) evaluated the effectiveness of various concrete cover types in rehabilitating damaged concrete columns. Their study examined 45 normal-strength concrete columns, including 9 reference columns, 3 unjacketed and 6 jacketed with 25–35 mm thick normal-strength concrete layers. The remaining 36 columns were strengthened using concrete jackets composed of either ultra-high-performance fiber-reinforced self-compacting concrete (UHPFRSCC) or normal-strength concrete (NSC). These jackets incorporated additional steel reinforcement (4 Ø 10 bars) and varied in thickness (25 or 35 mm). The bonding techniques employed included surface roughening through mechanical wire brushing, mechanical scarification, and the use of shear studs. The findings indicated that UHPFRSCC jackets demonstrated superior ultimate load capacity compared to NSC jackets, with thicker jackets further enhancing load-bearing performance. Among the bonding techniques, shear studs proved to be the most effective in increasing ultimate load capacity. The study concluded that the material properties of the cover jacket play a crucial role in structural performance, with UHPFRSCC outperforming other materials, including NSC. Mahmud et *al*. (2020) conducted an experimental study to evaluate the impact of interface preparation on the bond strength between a column and an added concrete jacket. They constructed twelve columns, each measuring 102 × 102 × 800 mm, using low-strength concrete (10–14 MPa). The strengthening process incorporated four longitudinal steel bars and a concrete jacket with a thickness ranging from 25 to 31.5 mm. Eleven of the columns underwent different bonding treatments, including untreated and unbonded surfaces, treated and bonded surfaces, and treated and bonded surfaces with welded ties. The findings revealed that the RC column jacket effectively increased the column's load capacity, with the degree of improvement depending on the bonding conditions. Among all configurations, the treated and bonded surface with welded ties achieved the highest load capacity.

The seismic strengthening of RC members using RC or high-performance cementitious mortar jackets has been validated through both laboratory research and practical applications

over the years. The key advantages and limitations of these strengthening techniques are outlined below:

a) Strengths

1. Significant increase in strength and ductility;
2. Adaptable to any shape of section;
3. Utilizes materials commonly recognized by both engineers and construction workers.

(b) Weaknesses

1. Costly, requires extensive labor, and consumes considerable time;
2. Causes major disturbance to building occupants;
3. Loss in floor area due to the increase of the cross section sizes;
4. Use of large quantities of materials (i.e. concrete and steel) with high environmental burden (higher embodied CO_2 emissions, more energy in manufacturing) (Gkournelos et *al.* 2021).

I.3.4. Steel Jacketing

Rather than employing RC or other cement-based materials, structural steel can be applied as external reinforcement through the steel jacketing technique to improve the performance of existing RC elements (Figure I.15). This method involves assembling steel angles and plates into a cage around the RC element, thereby enhancing its flexural and shear strength while also improving ductility and stiffness. Alternatively, sheeted steel elements can be wrapped around the RC component to provide additional confinement to the inner concrete, thereby increasing its ductility and shear capacity. In this approach, the gap between the added steel and the existing concrete can be filled with grout to ensure proper bonding and load transfer (Gkournelos et *al.* 2021).

Figure 1.15: Seismic strengthening using steel jacketing (Gkournelos et *al.* 2021).

On the other hand, concrete-filled steel tubular (CFST) elements have been extensively used in civil engineering applications, particularly in high-rise buildings and bridges. Their widespread adoption is attributed to several key advantages, including high strength, superior

ductility, excellent seismic performance, and enhanced fire resistance (Han and Li 2014). In CFST elements, the steel tube serves three primary functions: (1) providing structural support under various loading conditions, (2) offering lateral confinement to resist the crushing of the infilled concrete, and (3) acting as permanent formwork. Meanwhile, the concrete core plays a dual role by carrying loads and delaying the inward local buckling of the steel tube. However, to fully harness these benefits, the bond between the steel and concrete must be sufficiently strong to ensure composite action, particularly during the early elastic stage. Weak steel-concrete interaction can result from concrete shrinkage due to temperature variations or differences in the lateral dilation behavior of the steel tube and concrete core. (Alatshan et *al.* 2020).

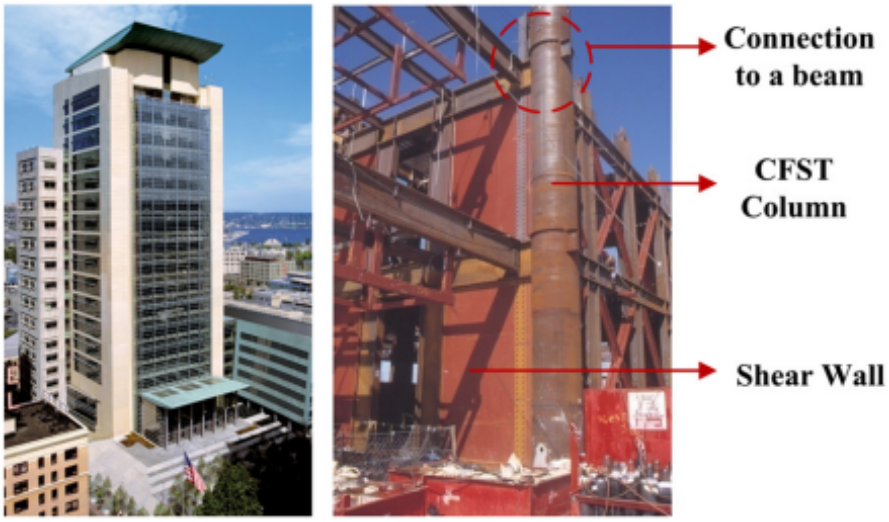

Figure 1.16: Example of application of CFST member to a building column (U.S. Federal Courthouse, Seattle, WA, USA (Moon et *al.* 2014).

Several researchers have investigated the behavior of strengthened RC columns using steel jacketing techniques. Research on steel-jacketed columns began in the 1990s. In 1997, Ghobarah et *al.* examined how corrugated steel jackets could improve the shear capacity and ductile behavior of columns subjected to lateral loading. Their findings demonstrated that this method significantly improved the seismic resistance of structures with initial deficiencies in seismic capacity. In a subsequent study, Ghobarah et *al.* evaluated the performance of steel jacketing on larger-scale concrete columns, further confirming its effectiveness. In 2003, Wu et *al*. applied steel plates as jackets on rectangular reinforced concrete (RC) columns and observed a significant increase in ductility. Sarno et *al.* (2006) later investigated the application of stainless-steel jacketing to upgrade framed concrete structures under seismic loading. The experimental specimens included both braced frames and moment-resisting frames. Findings showed that stainless steel jackets substantially improved plastic deformations and enhanced energy absorption capacity. Additionally, the strain-hardening properties of stainless steel helped prevent local buckling in steel members. Unlike concrete

jacketing, steel jacketing was particularly effective in increasing the shear strength of RC members. Despite its advantages, several limitations of steel jacketing have been reported. The effectiveness of this technique largely depends on the bonding between steel plates. In members with right-angled cross-sections (square or rectangular), steel jacketing was found to be less efficient in enhancing flexural stiffness. This limitation reduces its effectiveness in improving column deformability, restricting its applicability in certain structural configurations.

Recently, Fakharifar et *al*. (2016) introduced a quick restoration approach for heavily damaged circular RC columns using lightweight, pre-tensioned steel jackets. The technique includes encasing the RC member with a thin steel layer and preventing its buckling with multiple prestressed strands. Notably, the retrofitting process is highly efficient, as it can be executed by a two-worker team within 12 hours without altering the column's original shape. This approach restored the columns' strength and ductility to 115% and 140%, respectively. Although, while stiffness was not entirely recovered, it reached approximately 84% of the undamaged column's initial stiffness. More recently, Wang et *al*. (2017) proposed an innovative seismic strengthening approach for rectangular RC columns subjected to high axial loads (normalized axial loads of ~0.6). Their method involves applying pre-cambered steel plates to the column's opposite faces and post-compressing them using tightly secured anchor bolts. This pre-compression redistributes part of the axial load from the column to the steel plates, significantly reducing the stress on the original structure. Experimental results demonstrated that the strengthened columns maintained their shear capacity under high axial loads while exhibiting a substantial increase in ductility. Furthermore, the ductility enhancement could be fine-tuned by adjusting the thickness and initial pre-camber of the steel plates, making this technique highly adaptable to different structural needs.

Although steel jacketing is not widely used in engineering practice for upgrading RC elements, it remains an effective solution in certain scenarios. The key advantages and drawbacks of this method are outlined below.

b) Strengths

1. Notable enhancement in both strength and ductility;
2. Employs materials commonly known to engineers and construction crews.

(c) Weaknesses

3. Comparatively costly, demands high labor, and require extended execution time;
4. Causes disruption to building usage;
5. Corrosion protection is required;
6. Alters member stiffness and adds substantial extra mass. These limitations are less critical than in RC jacketing (Gkournelos et *al.* 2021).

I.3.5. FRP strengthening technique

I.3.5.1. Background on FRP composites

The evolution of fiber-reinforced polymer (FRP) materials started in the 1930s, marked by the first fiberglass patent from Owens Glass Company, which eventually merged with Corning during World War II. Significant progress in the FRP industry followed over the next two decades, primarily in military and aerospace applications. In the early 1960s, research efforts focused on exploring the use of FRP composites in structural engineering as a replacement for steel reinforcement to effectively address corrosion issues. However, due to practical limitations at the time, the development and implementation of FRP in construction remained slow. By the 1980s, FRP materials gradually found practical applications in engineering. Their use in concrete structures can be categorized into two main types: internal applications, which include FRP bars, rods, and tendons, and external applications, which involve FRP plates, fabrics, wraps, and near-surface mounted (NSM) FRP bars. Internal applications are primarily associated with new construction, such as FRP-reinforced and FRP-prestressed concrete structures. In contrast, external applications focus on strengthening, retrofitting, and repairing existing structures, typically those reinforced with steel. However, as FRP-reinforced concrete structures become more common, they too may require strengthening in the future (Ortiz et *al*. 2023). A tree diagram illustrating FRP composites, their components, and their applications is presented in Figure I.17.

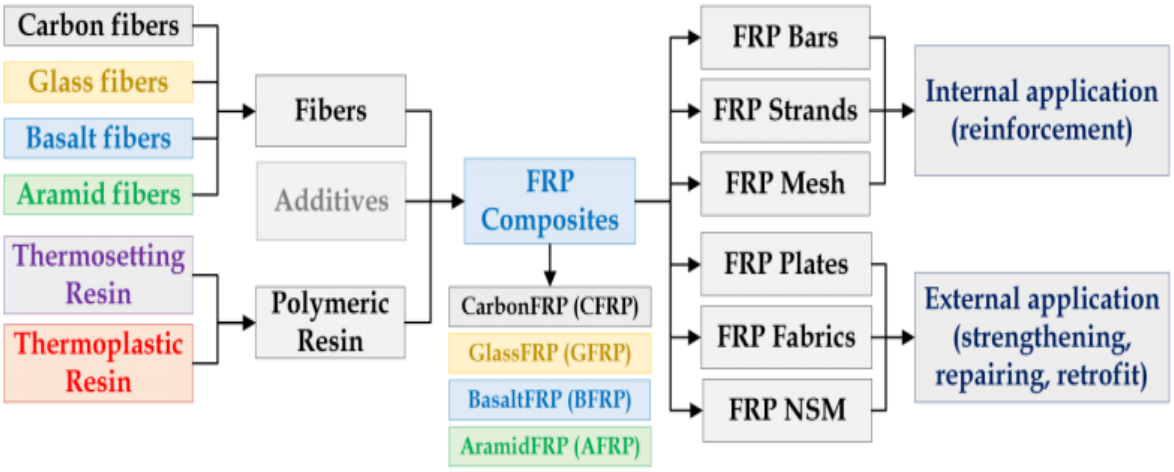

Figure I.17: Schematic representation of FRP applications in concrete structures (Ortiz et *al.* 2023).

The acronym "FRP" stands for fiber-reinforced polymers, also known as fiber-reinforced plastics. The term "composite material" broadly refers to a combination of two or more materials that, when combined, create a product with enhanced properties compared to its individual components. One component, known as the reinforcing or fiber phase, provides strength, while the other, called the matrix phase, serves as the binding medium. The matrix-

typically a cured resin such as epoxy, polyester, or vinyl ester-holds the fibers in place, ensuring the structural integrity of the composite by enabling shear transfer (Afifi 2013). Figure I.18 illustrates this concept.

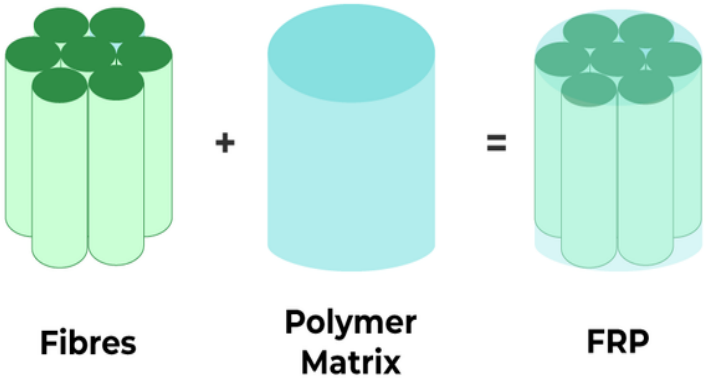

Figure I.18: Fundamental Components of an FRP Composite Material (Afifi 2013).

Four main types of FRP composites are frequently applied: carbon fiber-reinforced polymers (CFRP) include carbon fibers, glass fiber-reinforced polymers (GFRP) incorporate glass fibers, aramid fiber-reinforced polymers (AFRP) are strengthen with aramid fibers, and basalt fiber-reinforced polymers (BFRP) use basalt fibers (Afifi 2013).

I.3.5.2. Type of FRPs

- ***CFRP***

The Carbon fiber-reinforced polymer (CFRP) is one of the earliest fiber composite materials used for bridge reinforcement and remains widely utilized due to its high tensile strength and elastic modulus. CFRP is available in various structural forms, including sheets, bars (strips and rods), and grids (Figure I.19). However, its performance in the transverse direction is inferior to its longitudinal performance, leading to premature failure in tensile tests. Pultruded CFRP strips are composed of unidirectional carbon fibers embedded in a vinylester resin matrix. CFRP grids, a newer FRP configuration, have been employed to enhance the punching shear resistance of concrete slabs and reinforce steel deck plates, improving their stiffness. Compared to steel reinforcements, CFRP exhibits a higher elastic modulus, fatigue strength, and creep resistance, along with a lower expansion coefficient in the longitudinal direction. A comparison of mechanical properties and overall performance indicates that CFRP offers significant advantages over steel reinforcements. It combines high strength, a superior elastic modulus, and excellent corrosion resistance. However, its high cost remains a challenge due to the absence of key technologies for raw silk production. Additionally, CFRP-reinforced components are prone to brittle failure, especially under high temperatures, where the tensile strength of carbon fibers declines considerably. At 250°C, the elastic modulus and tensile strength of CFRP decrease by approximately 28% and 42%, respectively, compared to room temperature. Furthermore, CFRP exhibits electrical

conductivity, making it unsuitable for applications requiring electrical insulation (Hu et *al*. 2020).

(a) (b) (c)

Figure I.19: Structural form of CFRP; (a) CFRP sheets; (b) CFRP bars and (c) CFRP grids (www.frp-expert.com).

- ***GFRP***

The GFRP has been widely applied in civil engineering owing to its smooth surface, strong resistance to fluid penetration, and high durability against corrosive substances (including acids, alkalis, seawater, and fresh water), along with its cost-effective performance. This material is a composite system composed of glass fibers as reinforcement and a synthetic resin polymer matrix. Because of its affordability and corrosion resistance, GFRP is frequently used as a steel alternative in the rehabilitation of deteriorated concrete components (Figure I.20). Studies have confirmed that steel behaves as an isotropic material, prone to yielding and electrochemical corrosion, whereas GFRP, being anisotropic, offers superior tensile properties. Glass fiber is created by melting and drawing glass, making it a low-cost material. Furthermore, when GFRP is used for strengthening concrete bridges under cradle-to-grave assessment scenarios, it leads to reductions in global warming, photochemical oxidant formation, acid rain, and nutrient enrichment by 25%, 15%, 5%, and 50%, respectively. Nevertheless, GFRP has a relatively low elastic modulus, exhibits considerable creep behavior, and has limited long-term durability. It is also notably vulnerable to degradation in high-alkaline environments (Hu et *al.* 2020).

(a) (b) (c)

Figure I.20: Structural form of GFRP; (a) GFRP sheets; (b) GFRP bars and (c) GFRP grids (www.frp-expert.com).

- ***AFRP***

The Aramid fiber-reinforced polymer (AFRP) is a high-strength synthetic organic fiber composed of aromatic polyamides, known for its lightweight, exceptional tensile strength, and strong resistance to corrosion and heat. AFRP sheets are composed of aramid fibers aligned in one or two directions, offering advantages such as flexibility, durability, insulation, and resistance to corrosion (Figure I.21). Compared to glass fiber-reinforced polymer (GFRP), AFRP exhibits superior strength, a higher elastic modulus, enhanced heat resistance, and lower density. Its tensile strength is approximately five times that of steel and twice that of GFRP [81]. Additionally, in contrast to carbon fiber-reinforced polymer (CFRP), AFRP is more cost-effective, easier to manufacture, and demonstrates greater resistance to alkaline environments. However, despite these advantages, AFRP has limited application in civil engineering and construction due to its low compressive strength and high tensile strength, which restrict its use in structural load-bearing elements (Hu et *al*. 2020).

(a) (b) (c)

Figure I.21: Structural form of AFRP; (a) AFRP sheets; (b) AFRP bars and (c) AFRP grids (www.frp-expert.com).

- ***BFRP***

Basalt fiber is an inorganic material derived from volcanic basalt rock, processed through crushing, melting at high temperatures (1400°C), and stretching via a spinneret (Figure I.22). It has a dark brown appearance, resembling carbon fiber. Basalt fiber is known for its high strength, good modulus, thermal stability, chemical resistance, and ease of fabrication. Additionally, it is nontoxic, environmentally friendly, and cost-effective. Due to abundant raw materials and a straightforward production process, basalt fiber is six times more affordable than carbon fiber. BFRP maintains stable mechanical properties under elevated temperatures. Strength tests conducted at 100, 200, 400, 600, and 1200°C demonstrated that all three fibers; basalt, carbon, and glass showed strength reductions above 200°C. However, while carbon and glass fibers exhibited significant deterioration, basalt fiber retained over 90% of its strength at 600°C. Furthermore, when the temperature increased from 100 to 250°C, the tensile strength of basalt fiber improved by 30%, whereas glass fiber experienced a 23% reduction. In 70°C hot water, basalt fiber retained its strength for 1200 hours, whereas glass

fiber lost strength in less than 200 hours. Although its tensile strength and elastic modulus are lower than those of carbon fiber, basalt fiber offers superior ductility, cost-efficiency, corrosion resistance, and heat tolerance (Hu et *al.* 2020).

Basalt fiber serves as a reinforcement material for various basalt composite applications. Compared to other fiber materials, it offers distinct advantages and unique properties:

- ✓ Natural Composition: Derived from volcanic rock, basalt fiber is a pure inorganic material with outstanding mechanical properties, long-term durability, and adaptability to diverse environments.
- ✓ Cost Efficiency: With abundant raw materials, basalt fiber is a low-cost alternative. BFRP is expected to achieve properties comparable to GFRP in the future, potentially overcoming the cost barrier in FRP applications.
- ✓ Seismic Performance: Due to its high ultimate strain and excellent ductility, basalt fiber is well-suited for seismic-resistant structures.
- ✓ Basalt Enhanced Compatibility: It exhibits strong fatigue resistance, excellent adhesion to resin, and good compatibility with metals, plastics, and carbon fiber.

However, basalt fiber has certain limitations, including low shear strength, brittleness, and a relatively low elastic modulus (Hu et *al*. 2020).

(a) (b) (c)

Figure I.22: Structural form of BFRP; (a) BFRP sheets; (b) BFRP bars and (c) BFRP grids (www.frp-expert.com).

I.3.5.3. Mechanical properties of FRP composites

FRP composites are made of fibers and resin matrix. The finished characteristics of FRP composites depend on special preparation process. In the following subsections, the basic physical and mechanical properties of these FRP bars and sheets are listed in Tables I.1 and I.2, respectively.

Table I.1: Comparison of basic physical and mechanical properties between FRP and steel bars (Dong and Wu 2019).

FRP type	Elasticity modulus (GPa)	Yield Strength (MPa)	Tensile strength (MPa)	Density (g/cm^3)	Elongation (%)
CFRP bar (Gravina and smith 2008)	120-580	-	600-3690	1.50-1.60	0.5-1.7
GFRP bar (Gravina and smith 2008)	35-51	-	483-1600	1.25-2.10	1.2-3.1
AFRP bar (Gravina and smith 2008)	41-125	-	1720-2540	1.25-1.40	1.9-4.4
BFRP bar (Dong and Wu 2019)	50-65	-	600-1500	1.90-2.10	1.2-2.6
Steel bar (Gravina and smith 2008)	200	276-517	483-690	7.85	6.0-12.0

Table I.2: Mechanical properties of FRP sheets (Wu et *al*. 2020).

FRP type	Tensile strength (MPa)	Elasticity modulus (GPa)	Failure strain (%)
HS CFRP	3500	230	1.5
HM CFRP	1900	540	0.35
E GFRP	1500	73	2.1
AFRP	2060	118	1.7
BFRP	2800	89	3.15

I.3.6. Internal reinforcement for concrete

Internal reinforcement for concrete is another way to change the behavior of concrete columns from brittle to ductile behavior. The transverse reinforcement restricts the lateral expansion of the specimen under axial loading, thereby enhancing the ductility of the column. The most widely accepted and used method for reinforcement in structural concrete columns applications is the steel bar cages. Concrete and steel work very well together in a structural application. The design of columns is centered on having the concrete to resist the compressive forces because concrete is strong in compression. Furthermore, the steel is present in the column to resist any tensile forces, as steel is strong in tension, as well as in compression. The steel is designed as a cage to surround the concrete, while concrete is poured inside and outside this cage to the limits of the formwork. The inner concrete is intended to carry most of the applied compressive load, while the outside or "cover" concrete protects the steel from weather, fire, and corrosion (Ross 2007). The steel is placed in two directions, longitudinal and transverse. The longitudinal steel helps to carry the tension loads as well as the compressive load and to prevent collapse failure. The transverse steel encases the longitudinal reinforcement, aiding in concrete confinement, resisting shear forces, and reducing the buckling length of the longitudinal bars. Figure I.23 displays how the steel can mesh very well as a complete reinforcement system (Ortiz et *al.* 2023).

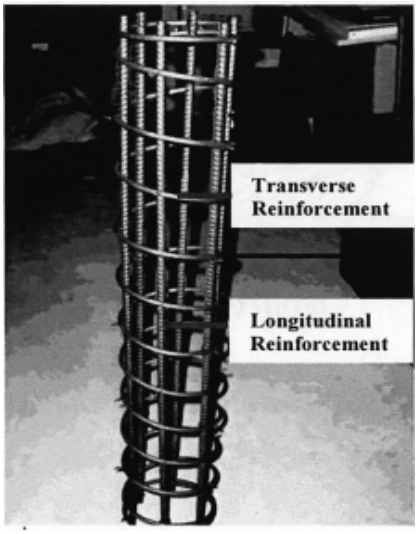

Figure I.23: Steel cage assembly (Afifi 2013).

In the design of traditional bar reinforced concrete construction, spiral reinforcement provides greater confinement than circular or rectangular hoop reinforcement. The Optimal confinement is achieved by reducing the spacing of transverse reinforcement and ensuring a well-distributed longitudinal reinforcement. Additionally, the volume of transverse reinforcement should be increased relative to the concrete core volume. (Mander et *al*. 1988). The concrete confinement is important because the cover concrete will begin to spall at a strain of 0.002. At this point, the core concrete will carry the load as long as it is effectively confined by the bar reinforcement'. The longitudinal bars will eventually begin to buckle in between the transverse reinforcement. As shown in Figure 1.24, failure will be reached once the longitudinal and transverse reinforcement fails, and can no longer confine the concrete core (Afifi 2013).

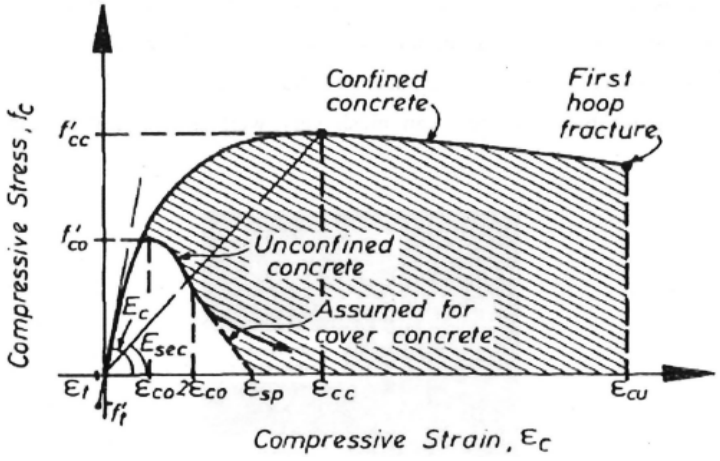

Figure I.24: Stress-strain model (Mander et *al.* 1988).

Steel reinforcement has a restricted service life and requires significant maintenance due to corrosion, particularly in aggressive or harsh marine environments, as commonly found in many regions of North America. This challenge has driven interest in noncorrosive

alternatives such as fiber-reinforced polymer (FRP) bars. Compared to traditional steel reinforcement, FRP bars provide several benefits, including a density that is only one-quarter to one-fifth of steel, superior tensile strength, and complete resistance to corrosion, even in highly aggressive chemical conditions (Mohamed and Benmokrane 2014).

FRP reinforcement is essential in providing confinement to columns after the concrete starts cracking (Figure I.25). Near failure, the concrete is cracked internally and the cracking is not uniform throughout. This also causes high stress concentrations in specific areas of the FRP reinforcement as opposed to areas where little cracking has occurred.

Figure I.25: CFRP cage assembly (Mohamed and Benmokrane 2014).

The FRP reinforcement is subjected to two different types of loading while the column undergoes axial deformation. There is a transverse loading from the concrete crushing and trying to push out radially. There is also some axial loading due to the epoxy resin connection between the concrete and the FRP reinforcement. This combination of loads produces strength limitations that are difficult to predict, and the failure strength of the FRP system is a portion of its ultimate strength.

Several Studies have been conducted on the behavior of FRP-reinforced concrete columns and shown that increasing the FRP strength and stiffness are directly related to the increase in concrete stress and strain limits. Moreover, the strength and stiffness of FRP depend on the selected material and its mechanical properties. These characteristics play a crucial role in restricting the dilation of concrete (Ross 2007). Controlling concrete dilation under increasing axial load enhances both stress and strain capacity. (Afifi 2013).

I.3.6.1. Study of De Luca et al.

De Luca et *al*. (2010) examined the compressive behavior of RC columns reinforced with GFRP hoops and their role in concrete core confinement. Tests on five square RC specimens (610×610×3000 mm) under axial load revealed no significant behavioral differences between columns reinforced with GFRP bars and those with steel bars when the longitudinal

reinforcement ratio was 1.0%. The results indicated that failure in steel RC specimens occurred due to longitudinal reinforcement buckling, whereas GFRP RC specimens failed through concrete core crushing at higher axial strains than those observed in the steel RC counterpart. The contribution of GFRP and steel bars to the column's load capacity was approximately 5% and 12%, respectively. Although reducing hoop spacing in GFRP-reinforced columns did not enhance peak load capacity, it effectively delayed longitudinal bar buckling, crack propagation, and concrete core crushing, thus controlling the failure mode. Figure I.26 illustrates the test column details from De Luca et *al.* (2010).

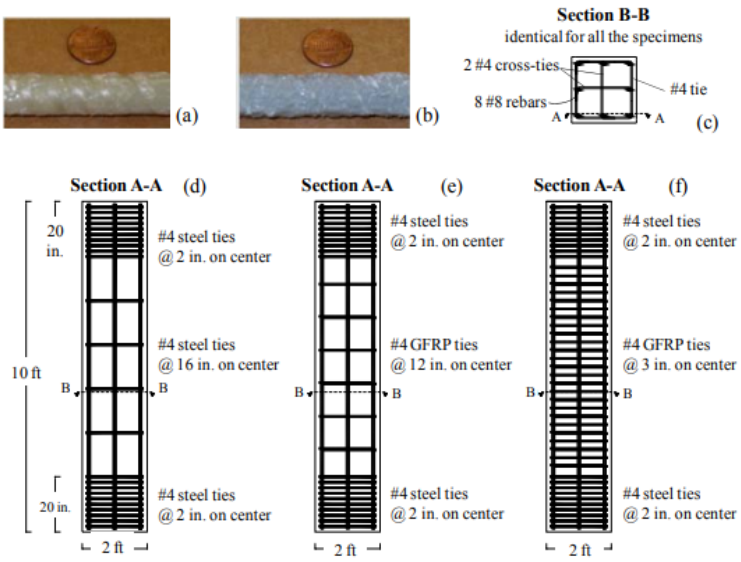

Figure I.26: Schematic representation of the reinforcement layout for specimen S-16 (a), A-12 and B-12 (b), and A-3 and B-3 (c); cross-sectional arrangement for all specimens (d); and detailed views of Bar A (e) and Bar B (f) as described by De Luca et *al*. (2010).

I.3.6.2. Study of Tobbi et al.

Tobbi et *al*. (2012) investigated the effect of stirrup spacing on square GFRP-RC columns under concentric loading. The tested columns were 350 x 350 mm and 1400 mm height. Based on test results it was noted that, decreasing stirrup spacing results an increasing in confinement efficiency and the hoop spacing controlled the buckling of the longitudinal bars. Also, the reduction in hoop spacing from 120 to 80 mm causes a gain in yield strength more than 20% and decreasing in strain of transverse reinforcement. Figure I.27 shows the dimensions and properties of Tobbi's tests.

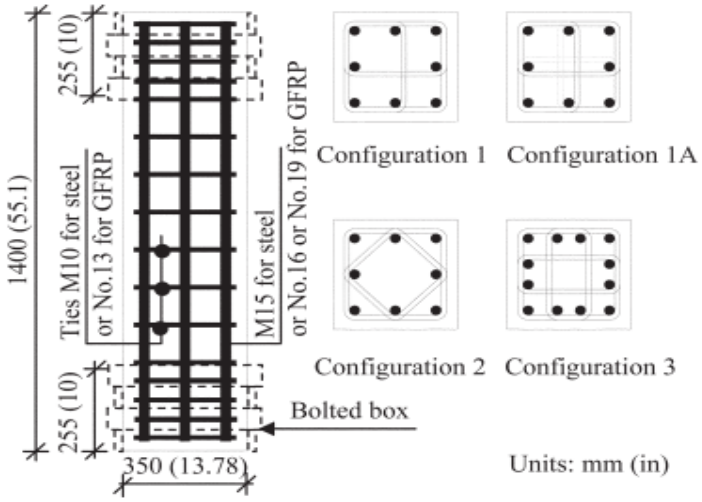

Figure I.27: Various transverse rebar configurations and dimensions of Tobbi et *al.* (2012) tests.

I.3.6.3. Study of Afifi et al.

In 2013, Afifi et *al.* conducted an experimental study on the axial behavior of circular concrete columns reinforced with GFRP and CFRP reinforcements. The study involved testing 27 concrete columns with a diameter of 300 mm, categorized into three groups. The first group included three specimens: one plain concrete column (unreinforced) and two with steel reinforcement. The second group consisted of 12 columns reinforced with GFRP in both longitudinal and transverse directions, while the third group mirrored the second but replaced GFRP with CFRP reinforcement. Various parameters were examined, including reinforcement type, longitudinal reinforcement ratio, volumetric spiral reinforcement ratio, bar diameter, spiral spacing, transverse reinforcement arrangement, and tie overlap length. The results demonstrated that GFRP-reinforced columns exhibited similar behavior to their steel-reinforced counterparts, though their axial load capacity was, on average, 7% lower than that of the steel-RC columns. Moreover, the experimental findings showed that the small GFRP spirals with closer spacing enhanced the ductility and effectively confined the concrete core in the post-peak stages. In conclusion the research work cited indicates the suitability of concrete columns longitudinally and transversely reinforced with GFRP bars. Figure I.28 shows the overall view of the samples tested and some of its properties.

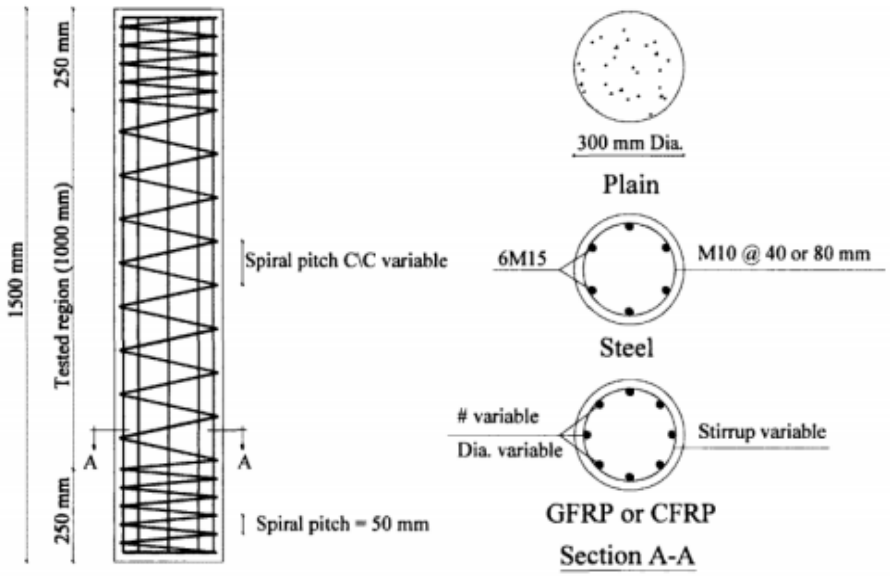

Figure I.28: Overall view of Afifi's (2013) samples (Afifi et *al.* 2013 tests).

I.3.6.4. Study of Prachasaree et al.

Prachasaree et *al*. (2015) investigated the structural behavior and performance of concrete columns reinforced internally with GFRP bars. The study involved testing 12 circular and square RC columns, each 500 mm in height, under compression loading. The parameter investigated included the longitudinal reinforcement, cross-section shape, concrete cover, and lateral reinforcement type. The columns incorporated GFRP rebars, with lateral reinforcement provided by ties, spirals, or hoops. The gross area-to-core area ratio was 1.44 for both section shapes, and the concrete cover was 15 mm thick. Longitudinal reinforcement comprised four GFRP rebars, with reinforcement ratios ranging from 1.42 to 2.05 for square sections and 1.91 to 2.63 for circular ones. Lateral reinforcement area was 0.011 times the core area, with spacing reduced at end zones to prevent premature failure. The authors concluded that GFRP reinforcement marginally influenced column strength, while lateral reinforcement significantly improved confining pressure and inelastic deformation. Increased GFRP reinforcement ratios enhanced confined compressive strength and deformability, with a confinement effectiveness coefficient of 3.0-7.0. Columns with spirals exhibited an average deformability factor of 4.2, while those with ties had 2.8, highlighting the greater influence of lateral reinforcement on deformability than strength. Figure I.29 presents the Geometry of the test columns by Prachasaree et *al.* (2015).

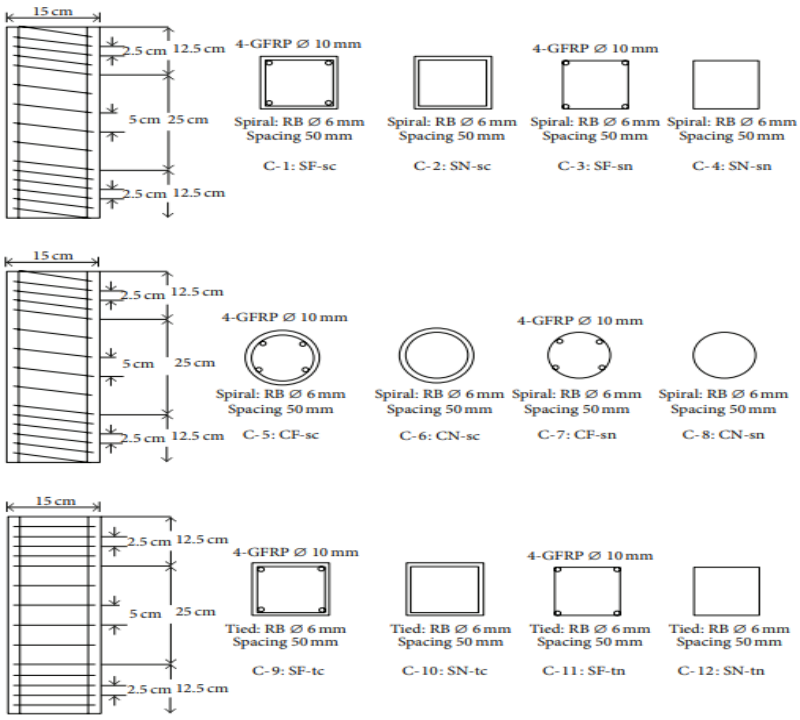

Figure I.29: Geometry of the test columns Prachasaree et *al*. (2015).

I.3.6.5. Study of Hales et al.

Hales et *al*. (2016) explored the behavior of slender high-strength concrete columns reinforced with internal GFRP spirals and longitudinal bars made of steel, GFRP, or a combination of both under both concentric and eccentric loading. The research involved nine circular concrete columns with a 305 mm diameter, comprising three short columns (760 mm in height) and six slender columns (3730 mm in height), following the slenderness criteria outlined in ACI 318-14. Three reinforcement configurations were used, as depicted in Figure I.30. Type DB columns incorporated a double-layer system: an inner layer consisting of six 13-mm steel bars confined by a 178-mm diameter 10-mm GFRP spiral and an outer layer of six 16-mm GFRP bars enclosed by a 216-mm diameter 10-mm GFRP spiral, both with a 76-mm pitch. Type SS columns contained a single layer of six 13-mm steel bars, encased by a 216-mm diameter 10-mm GFRP spiral, spaced at 76 mm. Type SG columns featured a single layer of six 16-mm GFRP bars, similarly confined by a 216-mm diameter 10-mm GFRP spiral with the same spacing. The experimental results demonstrated that the failure mode of slender columns with minor eccentricity (8.3% of the column size) was predominantly governed by material failure, whereas those with significant eccentricity (33% of the column size) exhibited buckling failure. The study concluded that GFRP spirals and longitudinal GFRP bars offer a practical reinforcement alternative for slender concrete columns subjected to eccentric axial loads.

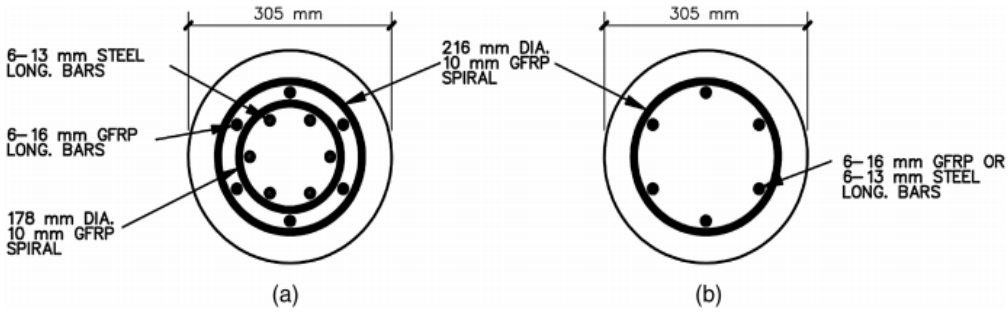

Figure I.30: Reinforcement configuration of concrete columns: (a) type DB-double layer; (b) type SS and SG-single layer (Hales et *al*. 2016).

I.3.6.6. Study of ElMessalami et al.

ElMessalami et *al*. (2021) carried out an experimental study on concrete columns reinforced with longitudinal BFRP bars and confined using either BFRP or steel ties under concentric and eccentric load conditions. The study involved twelve full-scale RC columns with a cross-section of 180 mm × 180 mm and a height of 1100 mm. Main test variables included the type and spacing of lateral reinforcement (BFRP and steel ties), along with the eccentricity-to-width ratio (e/h = 0, 22.2%, 44.4%). Findings revealed that reducing the spacing between BFRP ties improved ductility and confinement performance in BFRP-reinforced concrete (BFRP-RC) columns. However, this modification had little influence on both column load-bearing capacities and the longitudinal bars' contribution to final strength. The study concluded that BFRP-RC columns confined with BFRP ties demonstrated similar ultimate capacities, bar strength contributions, and confinement efficiencies to those confined with steel ties at identical spacing.

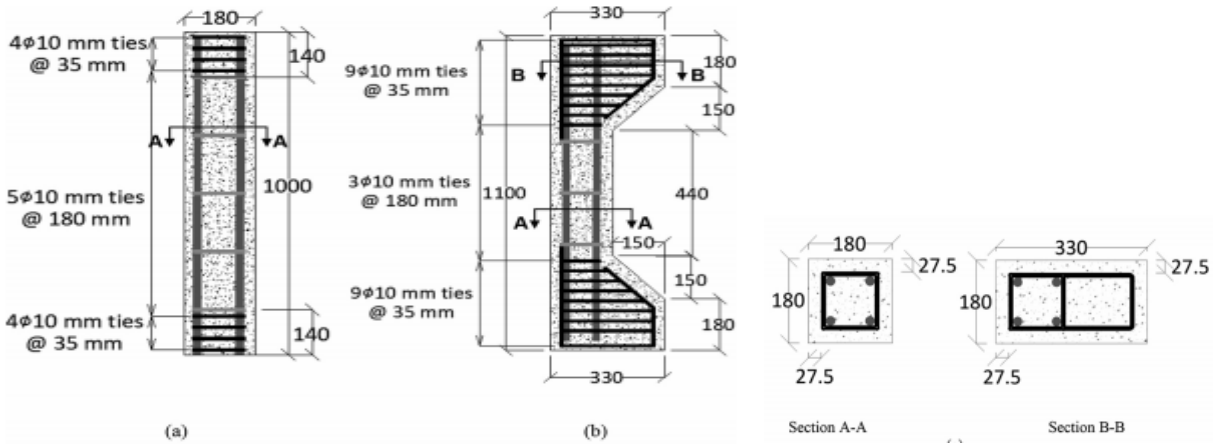

Figure I.31: The reinforcement details of the tested columns by ElMessalami et *al.* (2021), including (a) the concentric columns, (b) the eccentric columns, and (c) the cross-sectional layout of the specimens.

I.3.6.7. Study of Zeng et al.

Zeng et *al.* (2023) carried out an experimental study on the compressive behavior of FRP spiral-confined concrete within FRP-RC columns subjected to axial loading, both with and

without longitudinal FRP reinforcement. The research also assessed the role of longitudinal FRP bars in these columns. A total of 32 FRP-RC columns were examined, including 10 without longitudinal FRP reinforcement, 20 with longitudinal FRP bars, and 2 made of plain concrete. Each specimen had a height of 500 mm and a diameter of 192 mm. The primary test parameters were the spiral pitch (20, 40, 60, 80, and 100 mm) and the longitudinal FRP bar diameters (10 mm and 16 mm). Experimental results indicated that FRP spiral-confined concrete in FRP-RC columns exhibits a bilinear axial stress–strain behavior. The minimum confinement ratio required for effective confinement was identified as 0.12, exceeding previously reported values for FRP jacket-confined concrete. At the ultimate load stage, FRP bars with a 16 mm diameter (reinforcement ratio of 4.6%) contributed approximately 25%–35% of the total axial capacity, though this contribution declined significantly with smaller bar diameters. Additionally, when estimating the axial load contribution of longitudinal FRP bars in FRP-RC columns, the reduction in their tensile elastic modulus should be taken into account.

I.3.6.8. Study of Samra et al.

Samra et *al.* (1996) carried out study to investigate the required transverse reinforcement with spiral confinement for different eccentricity diameter ratio e/D to achieve adequate ductility for spirally confined columns. Based on the test results, it was got a modification equation for calculating the transverse reinforcement ratio ρ_s which is depended on the eccentricity value. And from the proposed equation, as the eccentricity to section diameter ration e/D. increases, more transverse reinforcement is required.

$$\rho_s = 0.45\left(\frac{A_g}{A_c} - 1\right)\frac{f_c'}{f_{yh}}\left(0.5 + 0.25\frac{e}{D}\right) \quad \text{(I.1)}$$

Where; ρ_s is ratio of volume to transverse confining steel to volume of confined concrete core, A_g is gross area of section, A_c is area of core of section within centerlines of perimeter spiral, f_c', is compressive strength of standard 28-day cylinder, f_{yh} is yield strength of transverse reinforcement, e is eccentricity at which axial load is applied, and D is overall diameter. Figure I.32 shows stress-strain diagram for circular cross section under eccentric load.

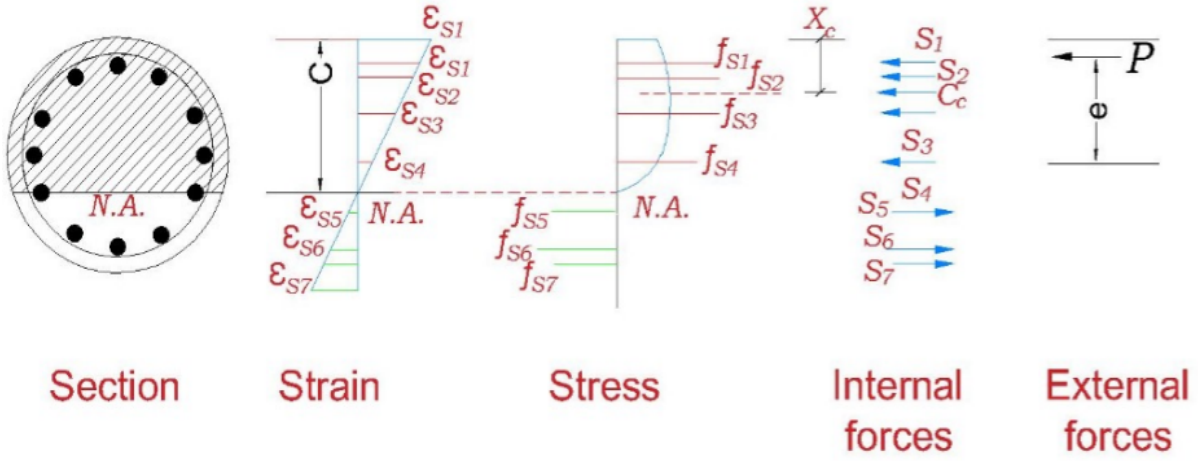

Figure I.32: Theoretical moment-curvature analysis: section with strain, stress, and force distribution (Samra et *al.* 1996).

I.3.6.9. Study of Sharbatdar

Sharbatdar (2003) conducted tests on five square concrete columns, each measuring 230 × 230 mm in cross-section and 1680 mm in height, which were reinforced with CFRP and subjected to eccentric loading. The findings revealed that the columns reinforced with CFRP achieved their flexural capacity, primarily limited by the compressive failure of the concrete. The CFRP used in the compression zones retained its structural integrity and continued to support loads even after the adjacent concrete had failed. Additionally, the longitudinal CFRP reinforcement demonstrated a high tensile strain capacity, ensuring equilibrium within the section as bending increased and the compression zone of the concrete progressively deteriorated.

I.3.6.10. Study of Tikka et al.

Tikka et *al*. (2010) investigated the structural behavior of slender concrete beam-columns subjected to eccentric loading. The study involved eight columns, each 1800 mm in length with a square cross-section of 150 × 150 mm, reinforced with GFRP longitudinal bars and confined laterally using a carbon fiber spiral wrap. The experimental findings indicated that the GFRP bars contributed minimally to the overall load-bearing capacity of the columns. However, the application of CFRP spirals proved effective in offering sufficient lateral confinement for the longitudinal reinforcement.

I.3.7. External application

Externally FRP confinement for reinforced concrete is a way to enhance the properties of concrete columns, most importantly reducing the effect of its brittle behavior, and allowing the column to attain maximum load carrying capacity. These higher strengths are achieved as a result of the lateral pressures, applied by the external reinforcement of the concrete column. Lateral high pressures results a higher strength concrete column which is able to carry higher loads than if it was unreinforced. Several techniques have been developed to strengthen or

rehabilitate existing reinforced concrete columns using FRP composites. However, the most commonly used methods are wet lay-up process, jacketing with prefabricated shells, and automated winding (Afifi 2013).

I.3.7.1. Wet lay-up process

This technique is widely employed in both buildings and bridges, where FRP sheets, impregnated with resin, are wrapped around concrete elements (Figure I.33). The installation process involves applying a saturating resin to the concrete surface, typically after a primer has been applied. There are two methods for applying FRP: either by uniformly spreading the resin on the concrete surface before wrapping it with the FRP jacket or by impregnating the FRP with resin using a saturator machine before wrapping the element (Cozmanciuc et *al.* 2009).

Figure I.33: RC columns Confinement using FRP Wet lay-up process (Chakra 2016).

The FRP wrapping can be fully or partially using one or multiple layers. For partial strengthening, FRP strips can be applied in the form of a continuous spiral or as discrete rings (Figure I.34).

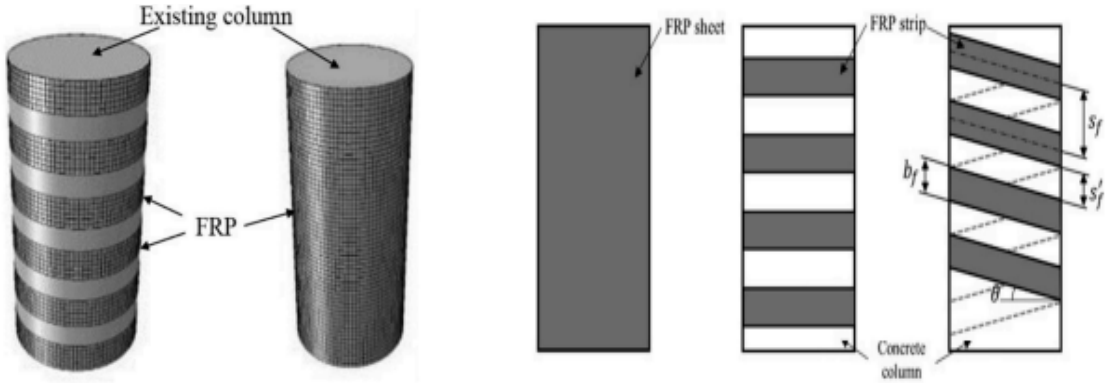

(a) (b)

Figure I.34: Configurations of confinement for RC columns. (a) Partial and full confinement techniques (b) external FRP wraps using hoop and spiral strips (Ghani et *al.* 2024).

This technique is straightforward and very fast. However, because it is completely carried out by hands, it is more difficult to control the quality of resin mix, attainment of good wet-out of the FRP jacket with uniform resin impregnation without excessive voids and wrinkling (Wu et *al*. 2020).

I.3.7.2. Jacketing with prefabricated shells

In this technique, the column is wrapped with prefabricate FRP shells (prepreg: FRP sheets pre-impregnated with a saturated resin at the manufacturer's facility (Figure I.35). The FRP shells can be either circular or rectangular, depending on the cross-sectional shape of the column. The technique is simple for site applications and can ensure a high level of material quality control due to the controlled factory-based fabrication of shells. However, the shells must be fabricated with strict tolerance with respect to column dimensions. The confining action of shells is less efficient in rectangular sections, so it is usually better to change the cross-sectional shape of the column. For multiple layers, the shells must be appropriately positioned to ensure the desired jacketing effect (Wu et *al*. 2020).

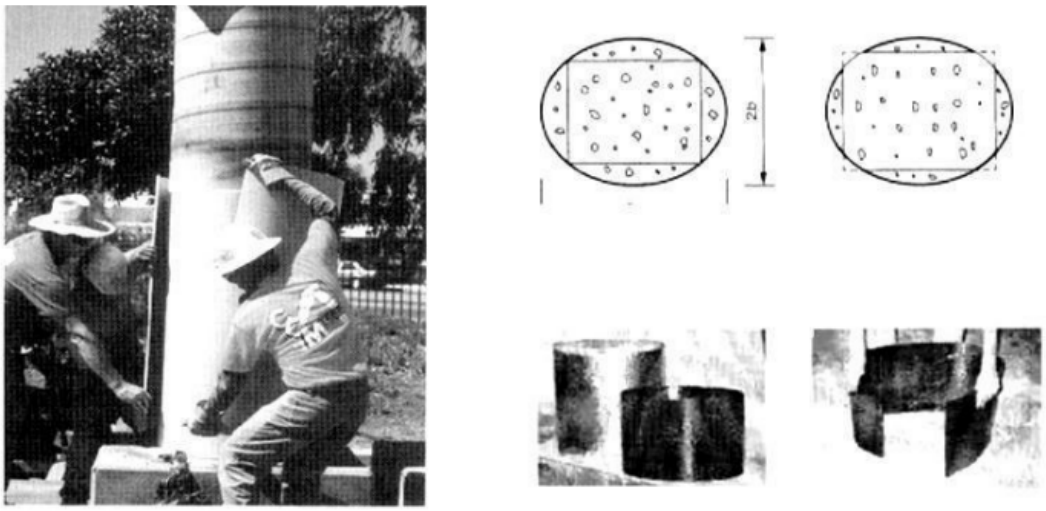

Figure I.35: RC columns strengthened using prefabricated FRP shells (Monti 2003).

I.3.7.3. Automated winding

The automated winding technique consists of using a wrapping machine to automatically wind the fibers around the column (Figure I.36). The machine, which was developed for the first time in Japan, was created to enhance bridge piers, but it can also be used to reinforce building columns. The fibers are wound on reels, and then inserted into the fiber winding head, impregnated with resin, and wound around the columns. After the winding the fibers while pre-tensioning them to obtain an active confining system. Computers monitor the winding angle, fiber volume fraction, and thickness (Wu et *al*. 2020). A key advantage of the technique, apart from good quality control, is the rapid installation. While the disadvantage is that preliminary calibration operations are required for non–leveled soils, which logical slow down its use (Wu et *al*. 2020).

Figure I.36: RC element strengthened using automated winding technique (Master Builders, Inc. and Structural Preservation Systems 1998, Balaguru et *al*. 2009).

As discussed in Section 1.3.4, circular hollow steel tubes are extensively used as columns in various structural systems. A common failure mode of these tubes under axial compression and bending is local buckling near the column ends. In standard circular tubular members, elephant's foot buckling occurs post-yielding, marking the depletion of load-carrying capacity and/or the conclusion of ductile behavior. This aspect is particularly critical in seismic design, where the column's ductility and energy absorption capacity determine its seismic resilience. Several techniques have been proposed for retrofitting hollow steel tube bridge piers to enhance ductility without significantly increasing strength; however, each approach presents certain limitations (Hu 2011).

Recently, the application of FRP for strengthening metallic structures has attracted growing interest (Hollaway and Cadei 2002; Zhao and Zhang 2007; Teng et *al*. 2009b). Xiao (2004) and Xiao et *al*. (2005) explored the confinement of critical zones in concrete-filled steel tubes using FRP jackets. Expanding on this idea, Teng and Hu (2004) applied the concept to circular hollow steel tubes, showing that even without suppressing inward local buckling, FRP jacketing remains a simple yet efficient solution for enhancing ductility and retrofitting such columns to resist seismic loads. Separately, Nishino and Furukawa (2004) investigated the same approach for hollow steel tubes (Hu 2011).

Within bridge engineering, FRP-confined CFST columns have emerged as a novel structural solution, gradually becoming a key method to boost both the strength and seismic performance of bridges. The adoption of this technique not only enhances structural safety but also extends bridge service life, contributing new advancements to modern bridge construction. In recent years, researchers worldwide have undertaken various experimental and theoretical studies on FRP-confined CFST systems, which have already been used in real-world applications. For instance, the northeastern segment of the Nanjing Ryuyue Expressway incorporated FRP-confined structures in its design. CFST columns have been employed as

pier structures (Zhai et *al.* 2012). The pier, located within the central divider of the Ninglian Expressway, is subject to strict dimensional constraints. Utilizing FRP confinement for CFST columns effectively reduced both section size and construction duration, while significantly enhancing the load-bearing and seismic capacity of the piers. In the practical application shown in Figure I.37, the FRP is tightly wrapped around the steel tube's exterior, creating an integrated assembly with the concrete core inside the steel tube. This configuration maximizes the combined benefits of both FRP and the steel tube under external loading, producing a synergistic effect that boosts the structure's safety and stability. Furthermore, in other bridge developments such as the pylons of major river or sea-crossing bridges and piers at critical transportation hubs FRP-restrained concrete-filled steel tubes have seen wide application. These projects have demonstrated the excellent performance of FRP-confined CFST columns in practice, laying a solid groundwork for their broader utilization across bridge engineering applications (Fang 2024).

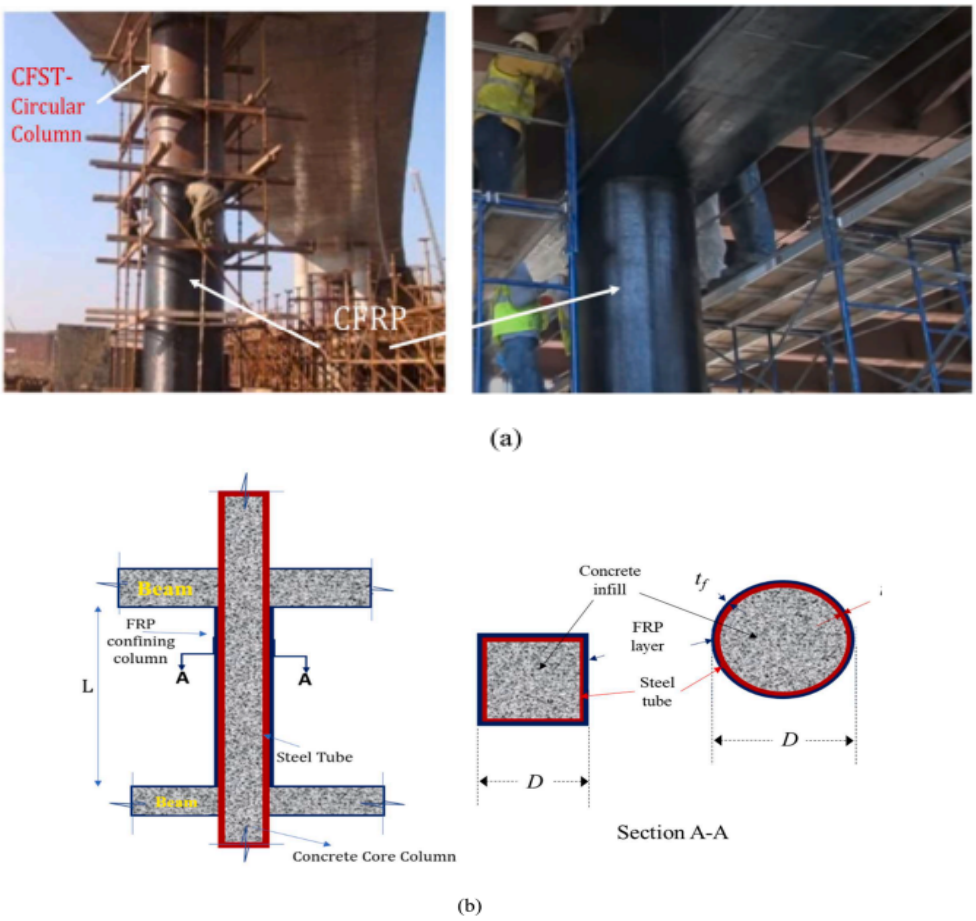

Figure I.37: CFRP-confined CFST columns including (a) photographic images of the circular columns in a bridge in Nanjing City, PR China (Wang et *al*. 20017) and (b) schematic views of both square and circular cross-sections (Hassanein et *al*. 2023).

Currently, numerous studies have been carried out to examine the axial behavior of fiber-reinforced polymer (FRP)-confined concrete-filled steel tube (CFST) columns under axial compression. Notable experimental investigations include:

I.3.7.8. Study of Xiao et al.

Xiao et *al*. (2005) conducted an experimental study to assess the seismic performance of confined concrete-filled steel tubular (CCFT) columns. Their research involved axial compression tests on 13 cylindrical specimens, incorporating carbon-fiber-reinforced plastic (CFRP) wraps for additional confinement and comparing CCFT columns with conventional concrete-filled steel tubular (CFT) columns and hollow steel tubes. Seismic loading tests were also performed on four large-scale CCFT and CFT columns under cyclic lateral loads to simulate earthquake conditions, with CFRP confinement applied to potential plastic hinge regions to delay local buckling and improve ductility. The columns were evaluated under sustained axial loads and repeated lateral forces to evaluate hysteretic response, energy dissipation, and failure mechanisms. The experimental findings show that CCFT columns exhibited significantly higher axial strength and ductility than conventional CFT columns, with CFRP confinement effectively preventing early failure by enhancing transverse confinement. A cushion gap between the CFRP and steel tube delayed confinement activation, increasing deformability and energy absorption. In terms of seismic performance, conventional CFT columns experienced early local buckling, reducing load capacity, whereas CCFT columns demonstrated stable hysteretic behavior and improved resistance to cyclic lateral loading, with well-confined plastic hinge regions preventing premature rupture. The authors concluded that applying FRP shielded the steel tubes from buckling while enhancing the columns' axial load-bearing capacity and deformation resistance.

I.3.7.9. Study of Tao et al.

Tao et *al.* (2007) investigated compression properties of concrete-filled steel tubular (CFST) stub columns strengthened with carbon fiber-reinforced with circular and rectangular cross-sections. A series of nine CFST specimens unconfined, one-ply CFRP-wrapped, and two-ply CFRP-wrapped along with two CFRP-confined concrete cylinders for benchmarking were investigated. The test results indicated that the CFRP jackets improved the load-carrying capacity of the circular columns effectively, whereas the enhancement was not so significant for rectangular columns. However, ductility was enhanced to some extent for those rectangular columns. The authors concluded that the CFRP layers had a more significant impact on the load-bearing capacity of circular columns and the ductility of rectangular columns.

I.3.7.10. Study of Liu et al.

Liu et *al*. (2010) examined the axial load-bearing capacity of FRP-confined concrete-filled steel tubular (FRP-CFST) columns under axial compression. Eleven short circular column specimens were tested to failure, with key parameters including FRP type (carbon fiber-

reinforced polymer (CFRP) and glass fiber-reinforced polymer (GFRP)), the number of FRP wrap layers (1, 2, and 3 layers), steel tube thickness (3.0 mm, 4.0 mm, and 5.0 mm), and concrete strength (C40, C50, and C60). The results demonstrated that FRP-CFST columns exhibited significantly higher axial load-bearing capacity compared to conventional CFST columns. FRP confinement effectively mitigated local buckling of the steel tube, enhancing structural performance. Increasing the number of FRP layers improved both strength and ductility, while thicker steel tubes led to higher yield and ultimate loads. Additionally, higher concrete strength increased the ultimate load but had a limited effect on ductility. The study concluded that the axial load-bearing capacity of short FRP-CFST columns was substantially greater than that of comparable CFST columns.

I.3.7.11. Study of Park et al.

Park et *al*. (2011) investigated the structural performance of CFRP confined concrete-filled steel tubular (FRP-CFST) columns. A series of ten specimens varying diameter-thickness ratios (D/t) and different numbers of CFRP layers (0, 1, 2, or 3) were tested under axial compression. The experimental findings revealed that CFRP reinforcement significantly increased axial load capacity by providing additional confinement, effectively reducing local buckling. Furthermore, an increase in the number of CFRP layers resulted in enhanced axial strength, though it also led to reduced ductility due to CFRP rupture, causing a sudden drop in load capacity.

I.3.7.12. Study of Sulimane et al.

Sulimane et *al*. (2013) investigated the structural behavior of circular concrete-filled steel tubes (CFSTs) and confined concrete-filled steel tubes (CCFSTs) wrapped with glass fiber-reinforced polymer (GFRP) sheets under quasi-static axial compression. A total of 35 specimens, including both CFST and CCFST configurations, were tested. The study considered key parameters such as concrete compressive strength (44 MPa and 60 MPa) and the diameter-to-thickness (D/t) ratio (54, 32, and 20). The results demonstrated that CCFST specimens exhibited significantly higher axial load capacity and enhanced ductility compared to CFST specimens, owing to the additional confinement provided by the GFRP wraps. However, CCFST specimens primarily failed due to the explosive rupture of the GFRP wraps at mid-height, whereas CFST specimens predominantly exhibited local buckling. Increasing the concrete compressive strength from 44 MPa to 60 MPa improved axial capacity but had a limited effect on stiffness. Additionally, reducing the D/t ratio enhanced both load-carrying capacity and stiffness by intensifying the confinement effect. The application of GFRP wrapping effectively delayed steel tube buckling, thereby extending the load-bearing phase of the columns.

I.3.7.13. Study of Wei et al.

Wei et *al.* (2014) conducted an experimental study to investigate the performance of concrete-filled fiber-reinforced polymer-steel composite tube (CFCT) columns. These

columns featured an inner concrete core encased by an exterior fiber-reinforced polymer-steel tube. A total of twenty-two specimens measuring 300 mm in diameter and 900 mm in height, including four conventional concrete-filled steel tube (CFT) columns for comparison and eighteen CFCT columns to assess the impact of fiber-reinforced polymer (FRP) confinement, were tested under axial compression. The primary parameters examined in the study included the steel tube thickness (3.0 mm, 4.5 mm, 6.0 mm, and 7.5 mm), the number of FRP layers (one or two), the type of FRP reinforcement (carbon-FRP or basalt-FRP), and the hybridization of FRP layers. The experimental results indicated that FRP confinement significantly enhanced the axial load capacity of the columns by reducing local buckling and providing additional confinement to the concrete core. An increase in the number of FRP layers improved compressive strength and ductility; however, excessive confinement sometimes led to sudden failure upon FRP rupture. Basalt-FRP (BFRP) exhibited better deformation capacity than carbon-FRP (CFRP), allowing for a more gradual failure process. Additionally, the hybridization of FRP layers effectively delayed strength degradation, resulting in a progressive failure mechanism rather than a sudden drop in load capacity. The steel tube thickness played a crucial role in axial strength and residual load capacity, with thicker steel tubes offering better confinement and reducing post-peak strength degradation.

1.3.7.14. Study of Ding et al.

Ding et *al*. (2018) examined the influence of different CFRP layer counts and concrete strengths on the mechanical behavior of CFRP-confined concrete-filled circular steel tube (CFT) stub columns. The researchers conducted an experimental study on sixteen specimens, including four conventional CFT stub columns and twelve CFRP-confined CFT stub columns, subjected to concentric loads. Each column specimen had nominal dimensions of 300 mm in diameter and 900 mm in height. The test findings demonstrated that CFRP confinement significantly enhanced the ultimate capacity of the CFT stub columns by reducing local buckling and providing additional confinement to the concrete core. Increasing the number of CFRP layers improved axial strength; however, an excessive number of layers resulted in reduced ductility. The CFRP confinement significantly impacted the failure mode by delaying local buckling of the steel tube and reducing concrete crushing. Furthermore, while the ultimate capacity of the columns increased linearly with the number of CFRP layers in lower-strength concrete specimens, this effect was less noticeable in high-strength concrete columns.

1.3.7.15. Study of Tang et al.

Tang et *al*. (2020) investigated the axial compressive behavior of FRP-confined concrete-filled stainless-steel tube (CFSST) stub columns. The researchers conducted an experimental study on twenty-four specimens, including six conventional CFSST stub columns and eighteen CFRP-confined CFSST stub columns, subjected to axial compression. Each specimen had a nominal outer diameter of 114 mm and a height of 400 mm, with stainless steel tube thicknesses of 3 mm, 5 mm, and 7 mm. The test results revealed that CFRP

confinement significantly enhanced the ultimate load capacity and energy absorption of CFSST stub columns by providing additional confinement to the concrete core and reducing outward buckling of the stainless-steel tube. Increasing the number of CFRP layers improved axial strength, with the maximum enhancement reaching 71.35%; however, specimens with thinner stainless-steel tubes exhibited greater benefits from CFRP wrapping. The failure mode of FRP-confined CFSST columns was dominated by the first rupture of the CFRP wrap at mid-height, followed by gradual strength degradation. Furthermore, while the ultimate capacity increased approximately linearly with the number of CFRP layers, its effectiveness was reduced for columns with thicker stainless steel tubes.

1.3.7.16. Study of Zhang et al.

Zhang et *al*. (2023) conducted an experimental and theoretical study on the axial compressive behavior of concrete-filled steel tube (CFST) columns strengthened with fiber-reinforced polymer (FRP) and welded steel strips. The researchers examined 14 CFST columns, which included two unconfined CFST specimens, eight columns reinforced with FRP layers, and four columns strengthened using welded steel strips, to assess their mechanical properties. Each column had an external diameter of 159 mm, a height of 636 mm, and a steel shell thickness of 4 mm. The investigation focused on the effects of varying parameters, such as the number of FRP layers (1, 2, 3, and 4 layers) and the welded steel strip thicknesses (3.0 mm and 6.0 mm). The results showed that FRP confinement significantly enhanced the ultimate capacity of CFST columns, with load improvements ranging from 28.72% to 64.16% as the number of FRP layers increased. Similarly, welded steel strip reinforcement improved the load capacity by 28.46% to 49.82%. The study found that increasing the number of FRP layers or steel strip thickness enhanced axial strength, but FRP confinement led to a more brittle failure due to CFRP rupture.

1.4. CONCLUSION

This chapter examined the main causes of deterioration in reinforced concrete columns, with particular emphasis on corrosion of steel reinforcement and seismic effects, both of which significantly reduce structural performance and safety. It also reviewed the principal strengthening and retrofitting techniques used in practice, including conventional methods such as reinforced concrete jacketing and steel jacketing, before highlighting the growing importance of fiber-reinforced polymer (FRP) composites in structural rehabilitation. Through the review of previous studies, the chapter established that both internal and external FRP confinement constitute promising solutions for improving the strength, ductility, and durability of concrete columns. In this way, the chapter laid the conceptual foundation of the thesis and clarified the relevance of FRP-based strengthening systems in modern structural engineering. The next chapter discusses the integration of regression analysis, machine learning, and deep learning methods as analytical tools for predicting the behavior of structural elements reinforced with internal or external FRP materials.

CHAPTER II:

Integration of Training Sciences as Analytical Methods for Predicting the Behavior of Structural Elements Reinforced with Internal or External FRP Materials

II.1. INTRODUCTION

The progressive integration of training sciences into civil engineering has opened new avenues for analyzing the structural behavior of elements reinforced with internal and/or external Fiber Reinforced Polymer (FRP). As conventional reinforcement strategies face increasing limitations particularly in seismic zones and corrosive environments, innovative materials like FRP offer promising alternatives due to their high strength-to-weight ratio, corrosion resistance, and ease of application. This chapter presents a comprehensive investigation into data-driven methodologies, beginning with regression analysis and extending into machine learning (ML) and deep learning (DL) approaches. By comparing classical statistical techniques with more advanced artificial intelligent (AI)-based models, the chapter highlights the advantages, limitations, and suitability of each method for predicting the performance of FRP-confined concrete columns. The aim is to bridge traditional engineering analysis with intelligent computational tools to enhance the accuracy, efficiency, and generalization of structural performance predictions.

II.2. REGRESSION ANALYSIS

The statistical technique referred to as regression is a foundational approach used to examine the relationship between a single dependent variable and one or more independent variables. In its most basic sense, regression analysis focuses on understanding how the dependent variable changes in response to variation in one of the independent variables, while keeping the others constant. This technique is widely applied across various disciplines such as economics, biology, engineering, and the social sciences because it allows for both prediction and inference. The most straightforward form of regression, called linear regression, assumes a linear association between the dependent variable and the independent variable(s). This relationship can be illustrated as a straight line in a two-dimensional space, where the slope of the line signifies the strength and direction of the relationship (Berhane et *al*. 2008). The general form of a simple linear regression model is:

$$Y = \beta_0 + \beta_1 X + \varepsilon \tag{II.1}$$

Where:

- Y is the dependent variable,
- X is the independent variable,
- β_0 is the intercept,
- β_1 is the slope coefficient, and

- Ɛ epsilon represents the error term, accounting for the variability in Y that cannot be explained by X.

When more than one independent variable is involved, the model extends to multiple linear regression, which can handle multiple predictors. The equation then becomes:

$$Y = \beta_0 + \beta_1 X_1 + \beta_2 X_2 + \cdots + \beta_n X_n \varepsilon \quad \text{(II.2)}$$

Where X_1, X_2, ..., X_n are the independent variables, and β_1, β_2,..., β_n are the corresponding coefficients.

The scope of regression analysis extends beyond the investigation of linear relationships. To capture more complex associations, nonlinear regression models such as polynomial regression or logistic regression may be employed. Polynomial regression, for instance, can represent curved patterns by including higher-degree terms of the independent variable(s), while logistic regression is used for binary outcomes, modeling the probability of a particular event occurring. Selecting the appropriate regression model is of critical importance, as it underpins the accuracy and reliability of the predictions and interpretations. A poor model choice can lead to biased estimates, unreliable forecasts, and incorrect conclusions, whereas a well-fitted model will reflect the actual underlying relationship between variables. Therefore, understanding the assumptions, advantages, and limitations of different regression approaches is essential for effective data analysis (Chambers & Hastie 1992).

II.2.1. Linear regression

This is the most basic form of regression in which the relationship between the output variable and the input variable(s) is represented by a straight line (linear function) (Figure II.1). The model's coefficients are calculated by minimizing a cost function such as Mean Squared Error (MSE) or Mean Absolute Error (MAE) which quantifies the difference between predicted and actual values. When only one input variable is involved, the model is referred to as simple linear regression Eq. (II.1). (Abdulazeez et *al*. 2020)

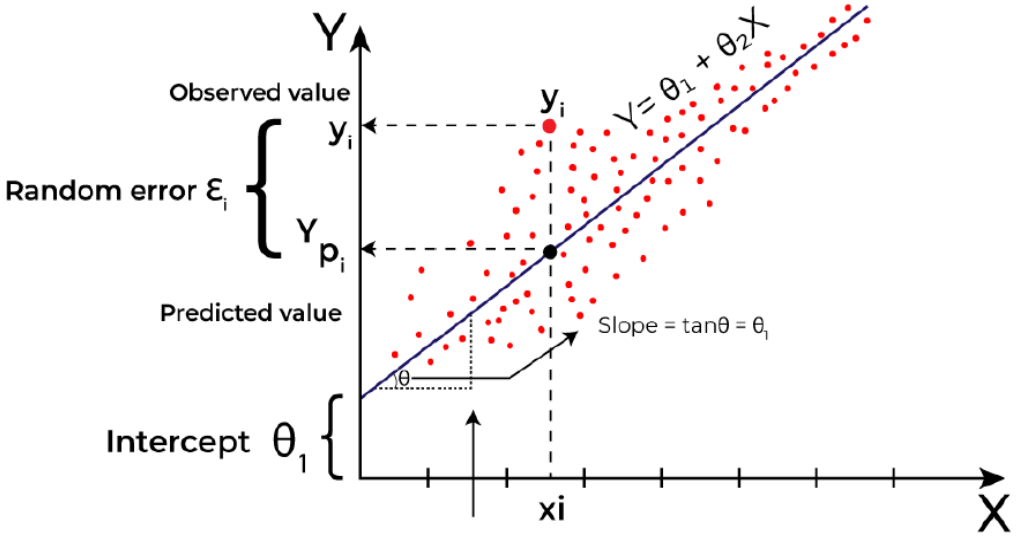

Figure II.1: Linear regression (Bengani 2024).

II.2.2. Multivariate linear regression

Multivariate linear regression (MLR) is an extension of multiple linear regression used when a problem involves more than one output variable. The term "multivariate" signifies the presence of multiple dependent (output) variables, while "multiple" refers to having more than one independent (input) variable. This approach is valuable for analyzing and understanding the relationships between sets of input and output variables (Zhang et *al*. 2019), providing insights into how changes in the inputs influence several outcomes simultaneously. The basic model for MLR is given by Eq. (II.2):

II.2.3. Polynomial regression

Polynomial regression **(**Roziqin et *al.* 2016**)** differs from the linear regression model in the form of the regression line. Instead of a straight line, this model fits a curved line defined by a polynomial function, where the input variables are raised to powers greater than one. While this approach can capture more complex relationships, it may lead to overfitting if a high-degree polynomial is used merely to minimize the error. For this reason, it is advisable to visualize the fitted model to ensure the results remain logical and interpretable. Model of polynomial (Mohammed & Abdulazeez 2017) is:

$$Y = \beta_0 + \beta_1 X + \beta_2 X^2 \ldots + \beta_h X^h + \varepsilon \quad \text{(II.3)}$$

II.3. REVIEW OF EXISTING WORK USING REGRESSION METHOD

II.3.1. Berradia and Kassoul work

Berradia and Kassoul (2018) proposed new empirical models using regression analysis method to predict the ultimate compressive strength and strain of circular concrete columns confined with CFRP wraps. The general form of these models is expressed as follows:

$$\frac{f_{cc}}{f_{co}} = 1 + k_1 \left(\frac{f_l}{f_{co}}\right)^{\alpha} \tag{II.4}$$

$$\varepsilon_{cc} = \varepsilon_{co} \left(a + k_2 \left(\frac{f_l}{f_{co}}\right)^{\beta} \left(\frac{\varepsilon_{h,rup}}{\varepsilon_{co}}\right)^{\gamma}\right) \tag{II.5}$$

By applying nonlinear regression analysis on a database of CFRP-confined concrete and incorporating key confinement parameters, these general expressions were calibrated into the following practical formulations:

$$\frac{f_{cc}}{f_{co}} = 1 + 2.3 \left(\frac{f_l}{f_{co}}\right)^{0.85} \tag{II.6}$$

$$\varepsilon_{cc} = \varepsilon_{co} \left(2.3 + 1.2 \left(\frac{f_l}{f_{co}}\right)^{0.75} \left(\frac{\varepsilon_{h,rup}}{\varepsilon_{co}}\right)^{1.25}\right) \tag{II.7}$$

II.3.2. Djafar-Henni and Kassoul work

Djafar-Henni and Kassoul (2018) proposed a new model to predict the ultimate conditions confined compressive strength (f_{cc}) and ultimate strain (ε_{cc}) for circular concrete columns confined with aramid fiber reinforced polymer (AFRP) wraps. The model was developed through a regression analysis approach aimed at minimizing prediction errors. Using Microsoft Excel, they calibrated the model by incorporating key parameters influencing the confinement behavior, resulting in a reliable and accurate predictive formulation. The proposed expressions of strength and strain models are given as follows:

$$f_{cc} = f_{co} \left(1 + 1.2 \left(\frac{f_l}{f_{co}}\right)^{1.25} \left(\frac{K_l}{f_{co}}\right)^{0.37}\right) \tag{II.8}$$

$$\varepsilon_{cc} = \varepsilon_{co}\left(2.3 + 1.2\left(\frac{f_l}{f_{co}}\right)^{0.75}\left(\frac{\varepsilon_{h,rup}}{\varepsilon_{co}}\right)^{1.25}\right) \quad \text{(II.9)}$$

II.3.3. Arabshahi et *al.* work

Arabshahi et *al*. (2019) developed new strength models for predicting the compressive strength of concrete columns confined with fiber-reinforced polymers (FRP) for both circular and rectangular sections based on nonlinear regression analysis. The regression approach focused on identifying the most influential parameters such as column diameter, FRP thickness, FRP tensile strength, and unconfined concrete strength and integrating them into dimensionless predictive equations.

For circular columns, the best-performing model was expressed as:

$$f'_{cc} = f'_{co}\sqrt{1 + 7.72\left(\frac{f_{frp}}{f'_{co}}\right)^{1.46}\left(\frac{t_{frp}}{d}\right)^{1.36}} \quad \text{(II.10)}$$

And for rectangular columns, the optimized model was:

$$f'_{cc} = f'_{co}\left(1 + \left(\left(\frac{A_e}{A_c}\right)^{1.75}\left(\frac{t_{frp}}{D}\right)^{0.49}\left(\frac{f_{frp}}{f_{co}}\right)^{0.49}\right)^{2.5}\right) \quad \text{(II.11)}$$

II.3.4. Diboune et *al.* work

Diboune et *al*. (2022) proposed a new analytical model using linear regression to predict the ultimate compressive strength and strain of square and rectangular concrete columns confined with CFRP wraps. The general form of these models is expressed as follows:

$$\frac{f_{cc}}{f_{co}} = 1 + \alpha k_1 K_{s1}\left(\frac{f_l}{f_{co}}\right)^{\beta} \quad \text{(II.12)}$$

$$\frac{\varepsilon_{cc}}{\varepsilon_{co}} = \gamma + \delta k_2 K_{s2}\left(\frac{f_l}{f_{co}}\right)^{\eta} \quad \text{(II.13)}$$

By applying linear regression techniques using Microsoft Excel and incorporating key confinement parameters**,** these general expressions were calibrated into the following practical formulations:

$$\frac{f_{cc}}{f_{co}} = 1 + 0.10(\frac{2r_c}{h})\left(\frac{f_l}{f_{co}}\right)^{1.5}\left(\frac{t_f}{D}\right)^{-60} \quad \text{(II.12)}$$

$$\frac{\varepsilon_{cc}}{\varepsilon_{co}} = 3.5 + 15(\frac{2r_c}{h})\left(\frac{f_l}{f_{co}}\right)^{1.5}\left(\frac{t_f}{D}\right)^{-0.12} \quad \text{(II.13)}$$

II.3.5. Berradia et *al*. work

Berradia et *al*. (2023) proposed a new empirical model using regression analysis to predict the ultimate axial compressive strength of circular concrete columns confined with both external CFRP wraps and internal transverse steel reinforcement (SCC columns). The model was developed using nonlinear regression techniques in MATLAB, incorporating key confinement parameters into a predictive expression. The general form of the regression-based model is expressed as follows:

$$f_{cu} = f_{co}\left[1 + 3.367\left(\frac{f_{lf}}{f_{co}}\right)^{0.961} + 0.594k_e\left(\frac{f_{ls}}{f_{co}}\right)^{0.745}\left(\frac{E_{frp}\,.\,t_{frp}\,.s\,.d_c}{E_s\,.\,A_s\,.D}\right)^{0.015}\right] \quad \text{(II.14)}$$

Regression analysis, including linear regression, multivariate linear regression, and polynomial regression, is a widely used approach for modeling the relationship between variables. Despite its usefulness, it has several limitations. These techniques often rely on relatively simple mathematical relationships and typically perform best when applied to structured datasets of limited size. When the available database is small or lacks diversity, the model's predictive accuracy can be significantly reduced. Additionally, regression methods are sensitive to outliers and multicollinearity, and they may not capture complex or nonlinear interactions effectively. In such cases, advanced methods like machine learning and deep learning provide more robust alternatives, capable of handling large, complex datasets and uncovering deeper patterns without relying on strict predefined equations.

II.4. MACHINE LEARNING AND DEEP LEARNING

The civil engineering community often misinterprets the concepts of AI, ML, and DL. In this context, Artificial Intelligence (AI) refers to a collection of algorithms and techniques designed to replicate natural intelligence, enabling tasks such as reasoning, decision-making, problem-solving, and interaction (Stefano & Bini 2018, Dimiduk et *al*. 2018). Machine Learning (ML), a subset of AI, encompasses various methods that allow machines to learn from data, primarily for prediction and classification purposes (Stefano & Bini 2018). Deep Learning (DL), in turn, is a specialized branch of ML that leverages advanced neural network

architectures to process large datasets and perform intricate classification and prediction tasks (Dimiduk et *al*. 2018). (Figure II.2) provides a clear distinction between AI, ML, and DL.

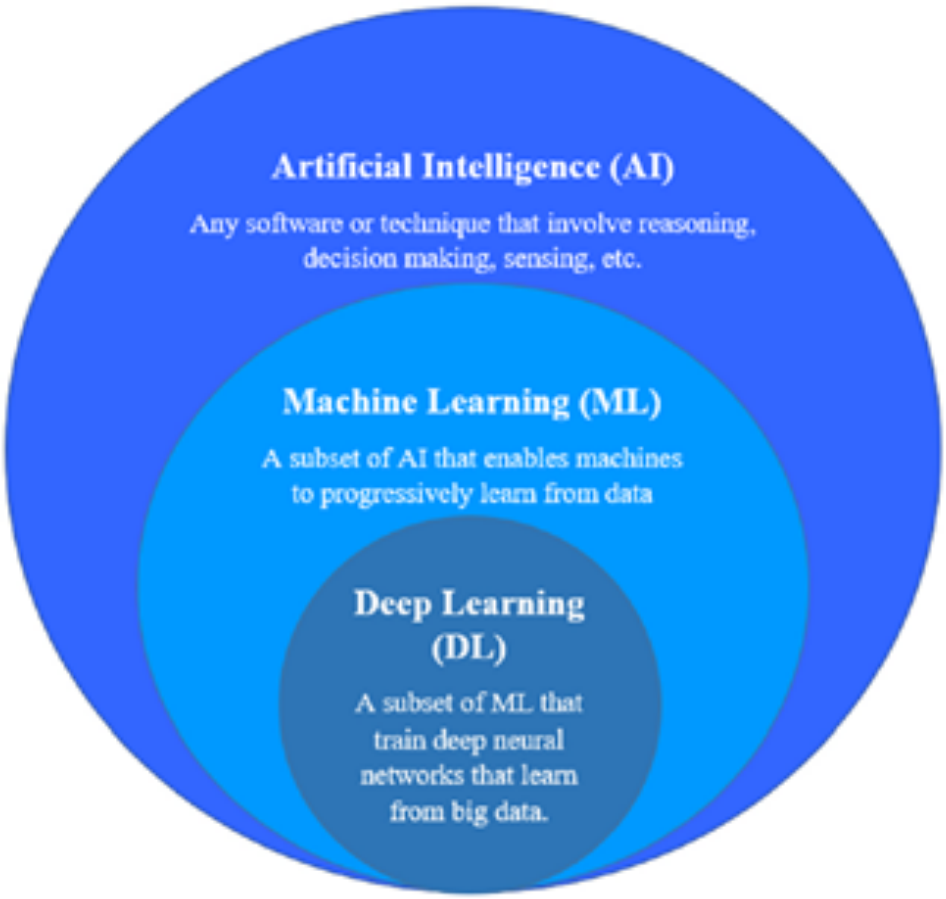

Figure II.2: Schematic representation of AI, ML, and DL (Nizar et *al*. 2024).

II.5. MACHINE LEARNING

Machine Learning (ML) is a branch of Artificial Intelligence (AI) focused on developing models capable of learning from data and making predictions or classifications without explicit programming. The primary objective of ML is to refine mathematical models, often perceived as black boxes, by training them on datasets, enabling them to generate predictions or decisions when presented with new or unseen data (Gianey & Choudhary 2017). This powerful capability allows ML models to be applied across various engineering domains.

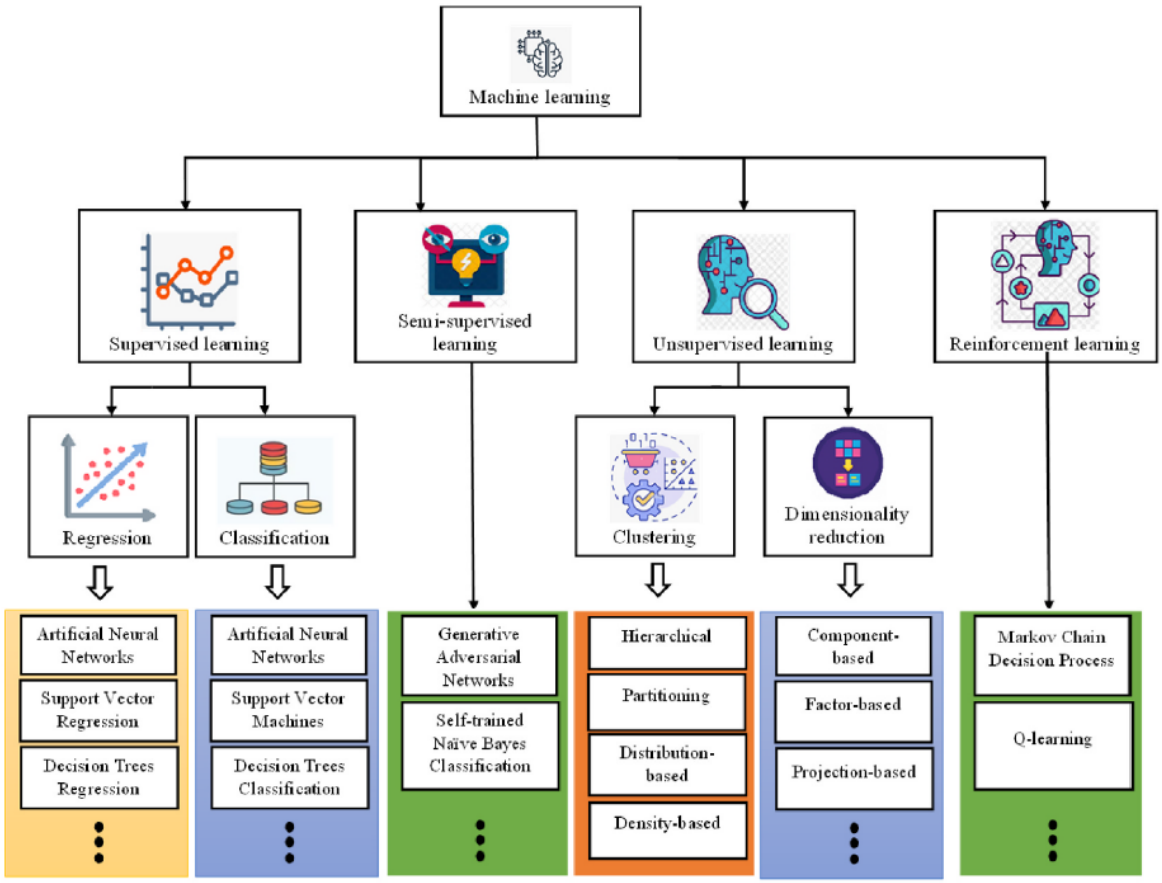

Figure II.3: Overview of Machine Learning Paradigms and Their Categories (Samrity & Manju 2024).

There are four main types of ML: supervised learning, unsupervised learning, semi-supervised learning, and reinforcement learning, as in (Figure II.3). Every kind of ML has its theory, training, testing procedure, applications, etc. The four types of ML can be listed as:

1. **Supervised Machine Learning (SML)** is a widely used ML approach that relies on labeled data obtained from numerical or experimental results related to specific applications or phenomena (Ahmad et *al*. 2022). Its primary objective is to establish relationships between independent and dependent variables within training datasets, enabling accurate predictions or classifications of the dependent variable. SML encompasses various techniques, including linear and polynomial regression, logistic regression, artificial neural networks, support vector machines, decision trees, random forest regression, and K-nearest neighbors, Nithurshan & Elakneswaran 2023).
   SML methods are extensively applied in computer science and engineering, particularly for classification and regression tasks. In civil engineering, SML regression models play a crucial role in capturing complex nonlinear relationships within numerical or experimental data, aiding in structural material analysis, structural health monitoring, and damage detection.

2. **Unsupervised Machine Learning (UML)** is a category of machine learning that operates without labeled data, making it particularly useful for tasks like clustering, anomaly detection, and dimensionality reduction. Unlike Supervised Machine Learning (SML), UML identifies underlying patterns in data autonomously, without external guidance (Suna et *al*. 2021).

   In clustering, UML groups similar data points based on shared characteristics, while anomaly detection isolates outliers that deviate significantly from normal patterns. Dimensionality reduction, on the other hand, helps eliminate redundant or irrelevant features, enhancing computational efficiency without compromising key input-output relationships (Stergiou et *al*. 2023).

   Despite being less commonly applied in engineering compared to SML, UML has proven useful in concrete science, particularly in nanoindentation and microindentation analyses, where it aids in classifying indentation curves using clustering techniques and Gaussian process classification (Mohammadi et *al.* 2020). Additionally, UML can assist in preprocessing large datasets by filtering out erroneous data caused by environmental factors, human errors, or inconsistencies in experimental setups. These capabilities make UML a valuable tool for improving data quality and extracting meaningful insights from complex datasets.

3. **Semi-supervised machine learning (S-SML)** utilizes labeled and unlabeled training instances different from SML and UML. S-SML aims to hoist the existing labeled instances to boost the performance of the ML tool to learn the pattern of unlabeled instances. S-SML links the SML and the UML tools to overcome their major challenges, where a preliminary model is trained based on a small labeled data portion and later gradually feeds the model with unlabeled instances to learn the unknown correlations. S-SML solves the limitation of UML in solving regression problems; it also uses a small portion of labeled data and a large part of unlabeled data, reducing the required time for data preprocessing (Cao et *al*. 2016, Rosa 2016).

4. **Reinforcement Machine Learning (RML)** is an ML approach where agents learn through trial-and-error using a reward-based system. Unlike Supervised ML, which maps input-output relationships, RML optimizes decisions by maximizing cumulative rewards. It also differs from Unsupervised ML, which focuses on pattern recognition. Key RML methods include Q-learning, ε-greedy, deep Q-learning, and Markov decision processes, widely used in AI. However, applying RML in complex environments is challenging due to high-dimensional spaces and nonlinear interactions. While rarely used in engineering, it has applications in nanoindentation and microindentation for analyzing cementitious materials (Hilloulin et *al.* 2022).

II.5.1. Machine Learning Methodology

The machine learning process begins with Input, where raw data is collected and introduced into the system. Next, Feature Extraction is performed to identify and select the most relevant characteristics from the data, ensuring better model performance. These extracted features are then processed in the Prediction using ML phase, where machine learning algorithms analyze patterns and relationships to generate predictions. Finally, the Output stage provides the model's decision or predicted value based on the learned patterns Figure II.4. This structured workflow is essential for achieving accurate and reliable results in various applications, including regression, classification and decision-making tasks.

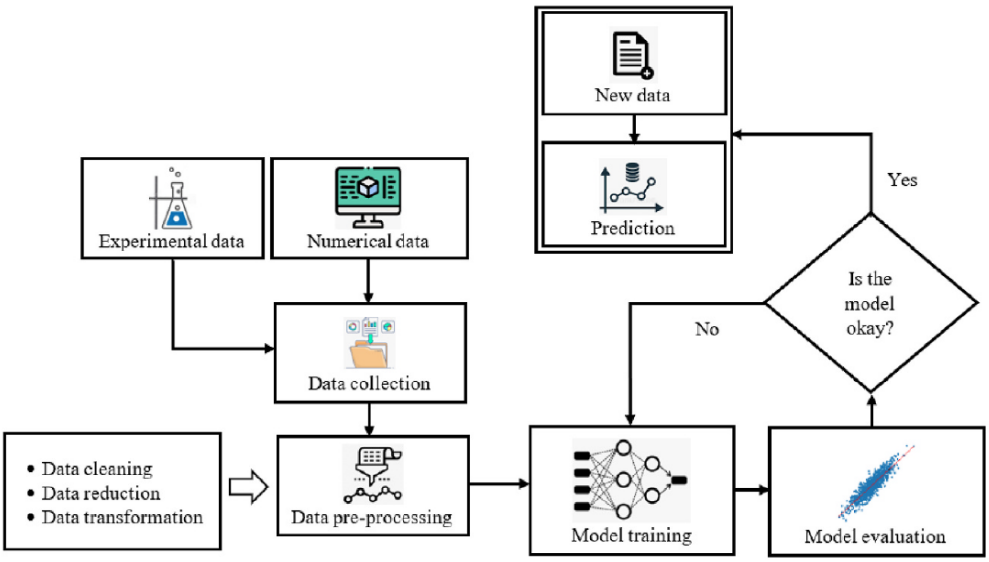

Figure II.4: Step-by-step process of machine learning workflow (Nizar et *al*. 2024).

1. Effective Data Collection and Partitioning

Effective data collection is essential for developing accurate ML models, as the dataset provides learning patterns for training. Data can be sourced from experimental or numerical methods, or a combination of both. While numerical data is cost-effective, its accuracy may be limited when simulating complex physical and chemical behaviors. In such cases, integrating experimental data enhances reliability, especially when numerical modeling is challenging. Additionally, data collection can be resource-intensive, requiring significant time and effort. Ensuring data diversity and comprehensive parameter coverage is crucial for creating robust models. However, available datasets often suffer from limitations such as small sample sizes, partial parameter representation, and inconsistencies in recorded variables. These challenges may necessitate data imputation techniques to fill gaps. Moreover, issues like skewness and imbalance can lead to underfitting or overfitting, affecting the model's generalization ability. To build a reliable ML model for real-world applications, datasets should be carefully curated, incorporating a broad range of relevant parameters and the largest

available data instances. Once collected, the dataset must be properly partitioned to ensure effective training, validation, and testing of the ML model. The Figure II.5 illustrates two common methods of dataset partitioning:

a) Two-Way Holdout Method: The dataset is split into two subsets-training and testing. The training set is used to train the model, while the testing set is reserved for evaluating its performance. However, this approach does not include a separate validation phase, which may lead to potential issues like overfitting.

b) Three-Way Holdout Method: The dataset is divided into three subsets-training, validation, and testing. The training set is used for model learning, the validation set helps tune hyperparameters and prevent overfitting, and the testing set assesses the final performance of the model on unseen data.

The three-way split is generally preferred in ML applications as it allows for better model generalization by optimizing hyperparameters without affecting the final test performance. Proper data partitioning ensures a well-trained and reliable model suited for real-world applications.

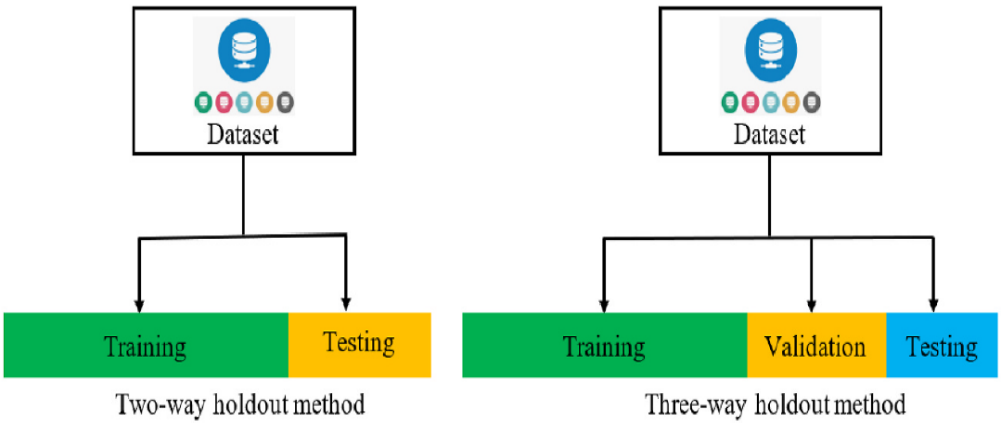

Figure II.5: The holdout validation method.

2. Data Preprocessing

Data preprocessing is a crucial step in data mining, aimed at enhancing data quality and ensuring its reliability for training ML models. It consists of three primary stages: data cleansing, transformation, and reduction. (See Figure II.6).

a) **Data Cleansing**: This step addresses missing and noisy data. Missing values can be handled by either removing incomplete entries when the dataset is large enough or imputing missing values using averages or the nearest possible estimates. Noisy data, which may result from measurement errors, inconsistencies, or biases, can be corrected using techniques such as binning, regression, and clustering;

b) **Data Transformation**: This process prepares data for ML training by performing various operations. Normalization ensures that values are rescaled within a defined range, such as [−1,1] [-1,1] or [0,1] [0,1], to standardize differences between input parameters. Feature selection is then applied to identify the most relevant attributes that significantly impact data correlations. Additionally, discretization converts continuous variables into categorized subsets, simplifying complex data. In some applications, concept hierarchy generation is used to organize attributes into hierarchical levels, though this may not be applicable in all domains;

c) **Data Reduction**: When working with large datasets, data reduction techniques help optimize model performance by limiting the number of data instances while preserving essential information. However, in cases where datasets are inherently small due to constraints such as high collection costs or lengthy preparation processes, data reduction may not always be necessary.

Effective data preprocessing ensures that the dataset is clean, well-structured, and optimized for ML models, ultimately improving their accuracy and efficiency.

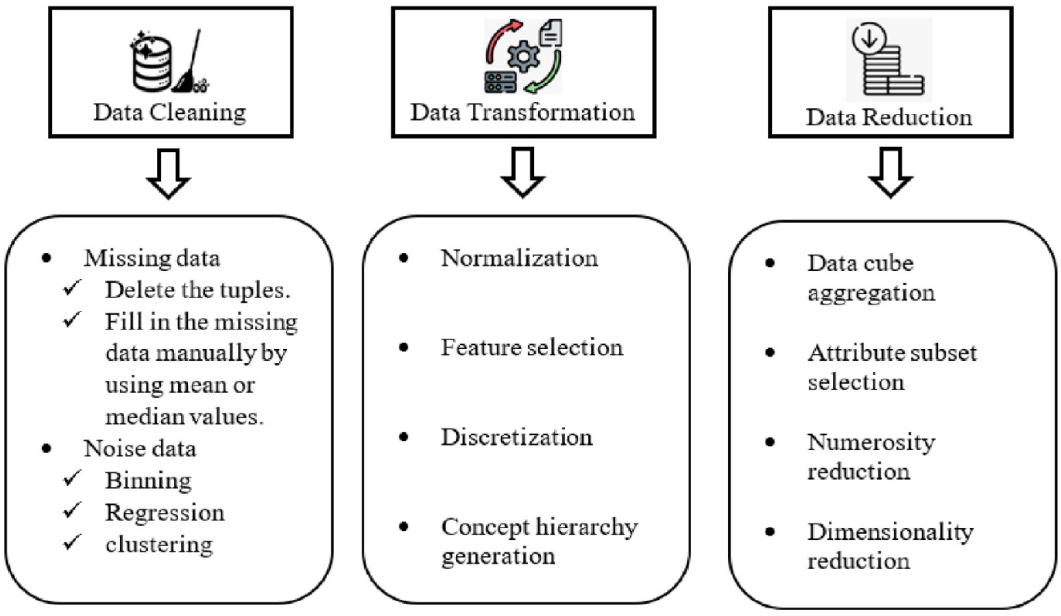

Figure II.6: Data preprocessing.

3. Model training

Model training is a crucial phase where patterns are learned from input data. The process involves feeding the preprocessed data into a selected model, which adjusts its parameters to minimize the error between predicted and actual values. During training, optimization techniques are employed to update model weights. Hyperparameters (e.g., learning rate, number of trees) are fine-tuned to enhance performance. Overfitting is a common challenge, requiring techniques like cross-validation and regularization. The training dataset should be

well-represented to ensure model generalization. The process continues iteratively until a satisfactory level of accuracy is achieved. Once trained, the model is validated using unseen data before deployment.

4. Model Evaluation and Testing:

Once training and validation are complete, the model's performance must be assessed using statistical metrics. Evaluating model accuracy through these metrics is a standard approach. If the results meet the required performance criteria, the training process concludes; otherwise, adjustments are necessary. Model refinement may involve expanding the dataset, optimizing hyperparameters, or modifying the model architecture to enhance accuracy. Several statistical performance metrics are commonly used to assess predictive capabilities, ensuring the model's reliability for practical applications.

a) The coefficient of determination (R^2) is a statistical measure that indicates how well the independent variables explain the variability of the dependent variable in a regression model. It ranges from 0 to 1, where a value closer to 1 means the model explains a large proportion of the variance, while a value near 0 indicates a poor fit.

$$R^2 = \left(\frac{n(\sum_{i=1}^{n} x_i y_i) - (\sum_{i=1}^{n} x_i)(\sum_{i=1}^{n} y_i)}{\sqrt{[n\sum_{i=1}^{n} {x_i}^2 - (\sum_{i=1}^{n} x_i)^2][n\sum_{i=1}^{n} {y_i}^2 - (\sum_{i=1}^{n} y_i)^2]}} \right)^2 \quad \text{(II.15)}$$

b) Mean Absolute Error (MAE) is a statistical measure used to evaluate the accuracy of a predictive model. It represents the average of the absolute differences between the predicted values and the actual observations, providing an indication of how close the predictions are to the real outcomes. Lower MAE values indicate better model performance.

$$MAE = \frac{\sum_{i=0}^{N-1} |x_i - y_i|}{N} \quad \text{(II.16)}$$

c) Mean Squared Error (MSE) is a common evaluation metric used to assess the performance of regression models. It calculates the average of the squared differences between the predicted values and the actual values. By squaring the errors, MSE gives more weight to larger differences, making it sensitive to outliers. Lower MSE values indicate more accurate predictions.

$$MSE = \frac{1}{n}\sum_{i=1}^{n} (x_i - y_i)^2 \quad \text{(II.17)}$$

d) The Root Mean Square Error (RMSE) is a widely used metric for evaluating prediction models, calculated as the square root of the Mean Squared Error (MSE). It is defined as follows:

$$RMSE = \sqrt{\frac{1}{n}\sum_{i=1}^{n}(x_i - y_i)^2} \quad \text{(II.18)}$$

e) Average Absolute Error (AAE) is a performance measure used to evaluate the accuracy of predictive models. It calculates the average of the absolute differences between predicted and actual values, similar to MAE. AAE provides a straightforward interpretation of the model's prediction error, with lower values indicating higher accuracy.

$$AAE = \frac{1}{n}\sum_{i=1}^{n}\left|\frac{x_i - y_i}{y_i}\right| \quad \text{(II.19)}$$

f) Standard Deviation (SD) is a statistical measure that indicates the amount of variation or dispersion in a set of values. It shows how much individual data points deviate from the mean of the dataset. A low SD suggests that the values are close to the mean, while a high SD indicates greater spread or variability in the data.

$$SD = \sqrt{\frac{\sum_{i=1}^{n}\left|\frac{x_i}{y_i} - \left(\frac{x}{y}\right)_{average}\right|^2}{n-1}} \quad \text{(II.20)}$$

II.5.2. Overview of machine learning algorithms

II.5.2.1. Artificial neural network (ANN)

Artificial Neural Networks (ANNs) are powerful machine learning algorithms inspired by biological neural networks. They are capable of learning complex nonlinear relationships between inputs and outputs (Rosa & Rosa 2016, Cao et *al*. 2016, Abunassar et *al*. 2023). ANNs consist of interconnected nodes (neurons) organized into layers, where the weighted connections are iteratively adjusted during training to optimize performance. The basic structure of an ANN includes an input layer, one or more hidden layers, and an output layer (Figure II.7). Inputs are propagated through the network, with each hidden neuron computing a weighted sum that is transformed by a nonlinear activation function, enabling the network to model intricate nonlinearities. Optimization algorithms, such as backpropagation (a gradient-based technique), are used to adjust the weights during training to minimize prediction errors.

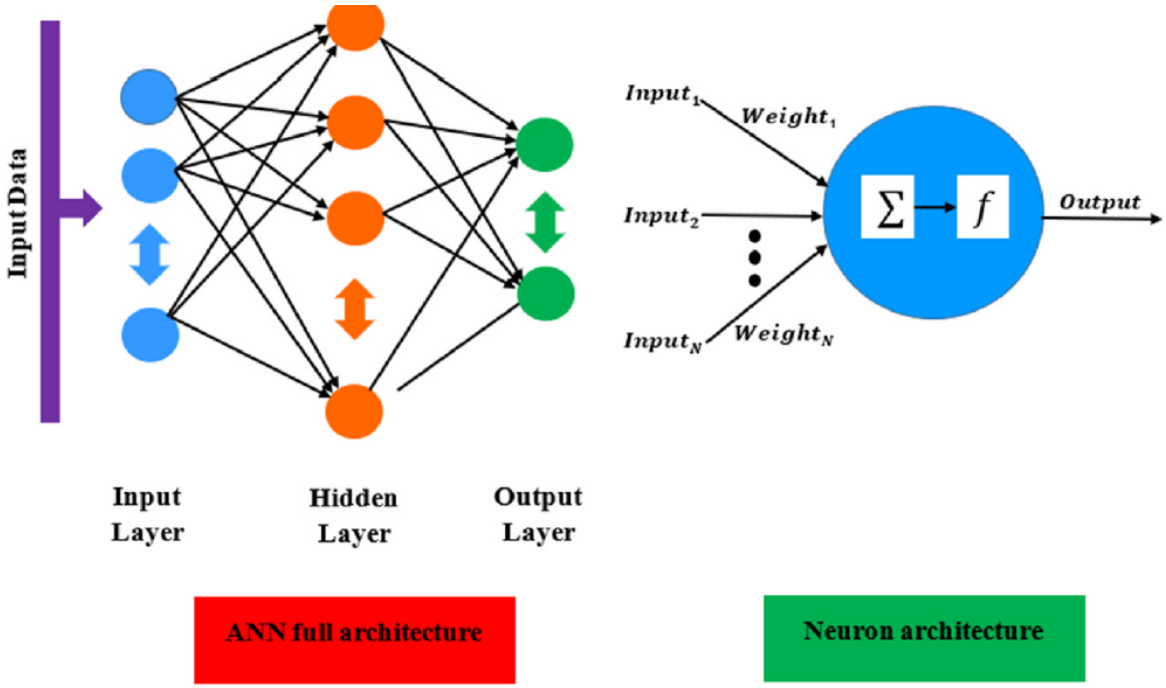

Figure II.7: The architecture of a simple ANN and its basic component, the neuron.

Artificial Neural Networks (ANNs) offer several advantages, including their ability to learn from data without relying on explicitly programmed rules, their effectiveness in modeling complex and nonlinear relationships, and their potential for parallel processing, which can enhance computational efficiency. However, they also present certain limitations, such as the risk of overfitting when the model becomes too complex and memorizes the training data, the requirement for large and representative training datasets, and challenges in interpretability, as ANNs are often regarded as "black-box" models.

II.5.2.2. Decision trees-based models

Decision Trees (DTs) are widely used, straightforward, yet powerful machine learning models that can be applied to both regression and classification problems (Cañete-Sifuentes et *al*. 2021, Mienyea et *al*. 2019). A DT model is structured as a hierarchical, tree-like graph composed of decision nodes and leaf nodes. The input data is initially passed to the root decision node, which splits the dataset into smaller subsets based on specific conditions. This recursive splitting process continues down the tree, with each decision node applying a rule to partition the data further (Rivera-Lopez et *al*. 2022). The fundamental architecture of a decision tree is illustrated in Figure II.8.

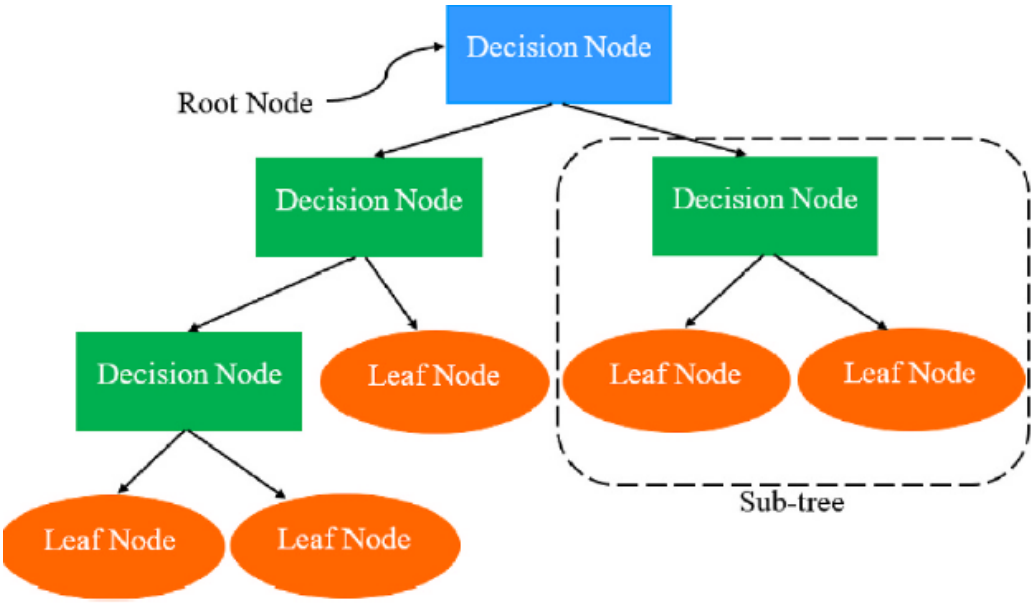

Figure II.8: The DTs structure.

Although Decision Trees (DTs) are commonly used for classification, their performance tends to decrease when applied to regression problems. As a result, various techniques have been developed to enhance the performance of DTs, including pruning and ensemble learning (Parmar et *al*. 2018). Pruning involves simplifying a DT by removing certain subtrees, which helps reduce overfitting and manage complexity as the tree deepens. This can be done either by stopping the tree at a certain level or by fully constructing the tree and eliminating subtrees that do not contribute significantly to its performance. On the other hand, ensemble learning is often preferred due to its ability to mitigate both underfitting and overfitting of a single model. Ensemble methods for DTs typically include three main approaches: bagging, boosting, and Random Forests (RFs).

A. Bagging Algorithm

Bagging (Bootstrap Aggregating) is an ensemble machine learning technique designed to improve the accuracy and stability of models by reducing variance and preventing overfitting. It works by generating multiple versions of a predictor using different random subsets of the training data (created through bootstrapping) Figure II.9, training a separate model on each subset, and then combining their outputs typically by averaging for regression tasks or majority voting for classification tasks.

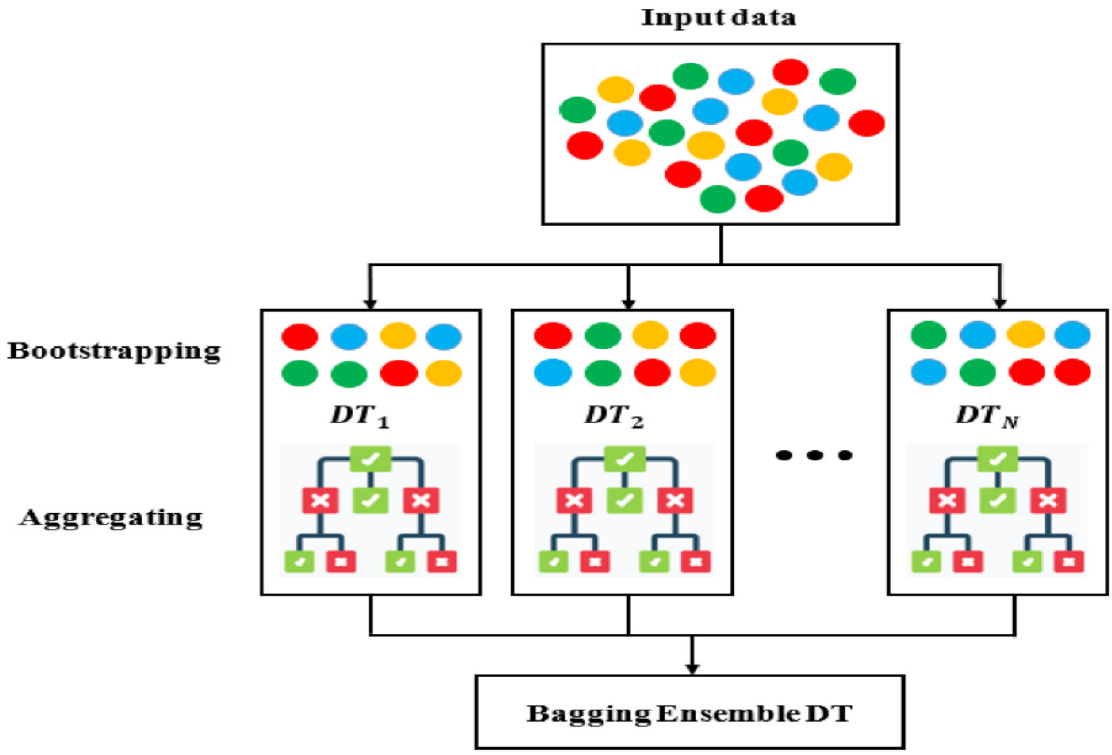

Figure II.9: The bagging DT ensemble. (Nizar et *al*. 2024)

B. Boosting Algorithm

Boosting algorithms (BA) are ensemble methods that enhance predictive performance by combining multiple individual models into a single, more powerful model (Schapire 1999). The concept of "boosting" involves converting weak learners such as decision trees into strong ones through a sequential learning process. This technique was initially introduced by Freund and Schapire (Freund & Schapire 1996, 1997) with the development of the Adaptive Boosting algorithm (AdaBoost). Since then, several boosting methods have been proposed to improve both efficiency and accuracy, including Gradient Boosting Machine (GBM) introduced by Friedman (Friedman 2001) also known as gradient tree boosting), Extreme Gradient Boosting (XGBoost) by Chen and Guestrin (Chen & Guestrin 2016), Light Gradient Boosting Machine (LightGBM) by Ke et al (Ke et *al*. 2017), and Categorical Gradient Boosting (CatBoost) by Prokhorenkova (Prokhorenkova et *al.* 2018). A recent comparative study by Bentéjac et *al*. (2021) concluded that CatBoost yields the highest accuracy, although it is slightly slower than its counterparts. XGBoost ranks second in both speed and accuracy, while LightGBM stands out as the fastest, though its accuracy is somewhat lower compared to the others.

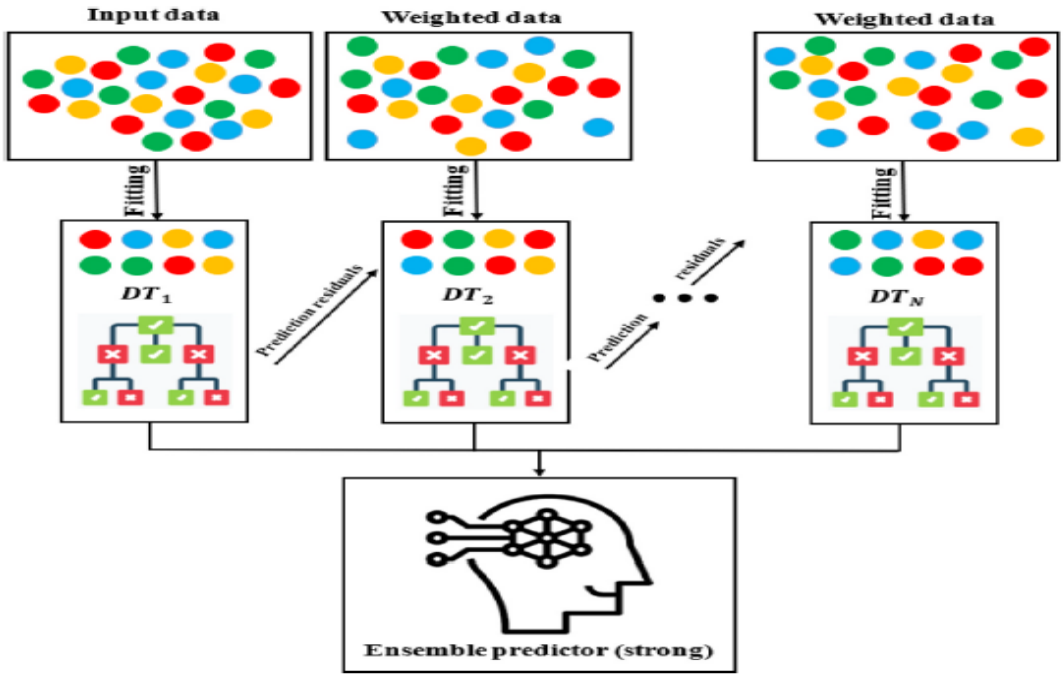

Figure II.10: The boosting DT ensemble. (Nizar et *al.* 2024)

✓ **AdaBoost (AdaB)** (Freund and Schapire 1996, 1997) iteratively trains weak learners (single-division decision trees) on weighted data, increasing the weights of poorly ranked instances. The final model combines low-weighted learners based on their performance (Figure II.11).

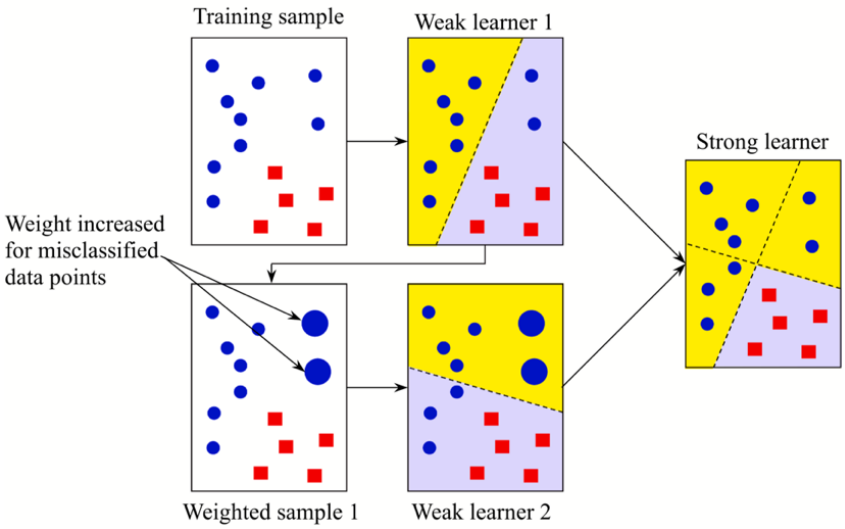

Figure II.11: AdaBoost algorithm: a visual representation with two weak learners (Thai 2022).

✓ **Gradient boosting machine (GBM)** (Friedman 2001): Uses gradient descent with weak decision tree learners. At each iteration, a new tree adjusts to the residual errors of the previous set (Figure II.12). Provides adjustment of trees, learning rate, etc.

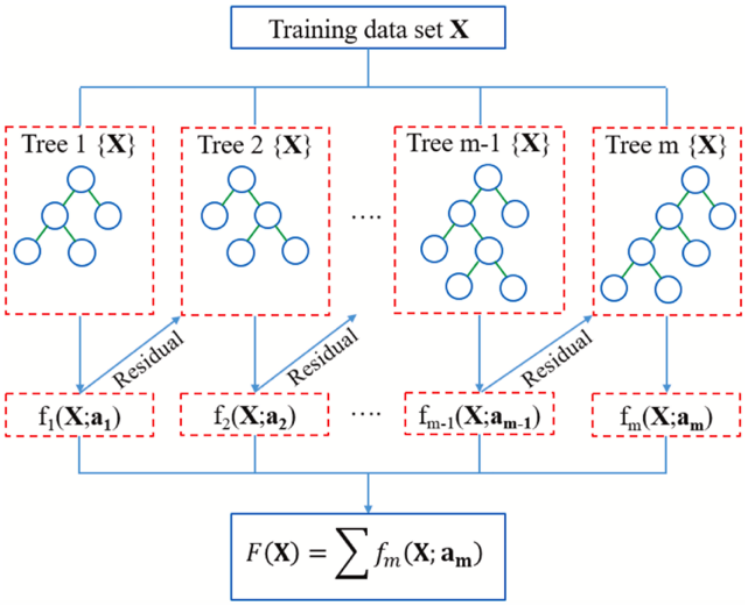

Figure II.12: A visual representation of the GBM model (Thai 2022).

✓ **LightGBM:** developed by Ke et *al.* (Ke et *al*. 2017), is a fast-boosting algorithm, up to 20 times faster than GBM (Friedman 2001). It uses a leaf-wise (best-first) strategy to minimize loss more effectively than traditional level-wise methods. Two key optimizations enhance its speed: Gradient-Based One-Side Sampling (GOSS), which reduces instances, and Exclusive Feature Bundling (EFB), which merges features. These techniques lower computational cost, making LightGBM efficient for large datasets, though it may overfit small ones (Figure II.13).

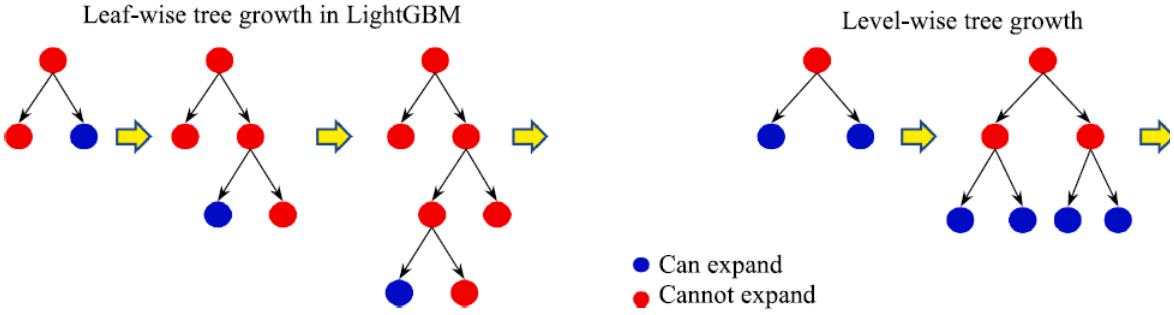

Figure II.13: A visual representation of the GBM model.

✓ **XGBoost**: Introduced by Chen & Guestrin in 2016, XGBoost was developed to enhance both the speed and efficiency of the Gradient Boosting Machine (GBM), which is known for its slow performance due to its inherently sequential training process. XGBoost incorporates several optimizations that significantly accelerate training while maintaining high predictive accuracy. For instance, it employs a randomization technique to reduce overfitting and speed up learning, and it utilizes a compressed column-based data structure to minimize the computational cost associated with sorting typically the most time-intensive step in decision tree

construction. Additionally, XGBoost supports parallel and distributed computing, allowing full utilization of CPU resources during model training and split calculation. These enhancements make XGBoost exceptionally well-suited for handling large-scale problems with vast datasets, earning it a reputation as one of the most powerful and widely used algorithms in modern data analysis.

- ✓ **Random Forest (RF)**, introduced by Breiman in 2001, is an ensemble learning method that utilizes decision trees (DTs) as base learners. It employs the bagging approach, where multiple trees are trained in parallel using different subsets of the training data. The core concept of RF is to create a "forest" of decision trees, each constructed from randomly selected features hence the term “Random Forest.” The final prediction is derived by aggregating the outputs of all individual trees, using majority voting for classification tasks or averaging for regression tasks, as illustrated in (Figure II.14). This technique helps to significantly reduce the overfitting tendency commonly associated with single decision trees, improving overall model stability and accuracy.

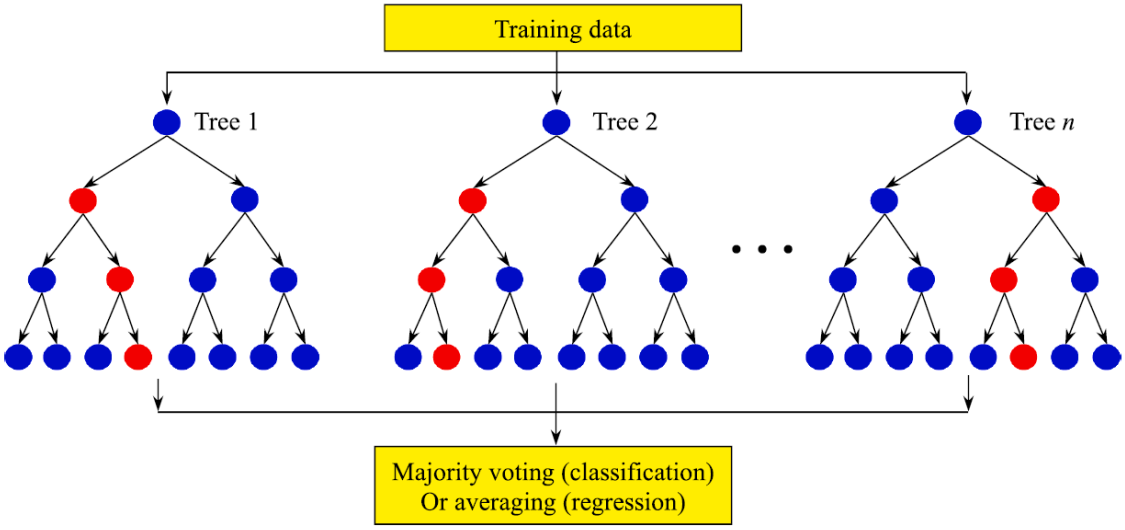

Figure II.14: Flowchart of RF (parallel training).

Random Forest (RF) retains the strengths of the decision tree (DT) approach while offering additional benefits. One key advantage is its ability to handle large datasets with thousands of input features effectively. Due to its ensemble nature, RF can train more quickly than a single DT when utilizing numerous trees; however, generating predictions from a trained RF model can be relatively slower. Despite this, RF is known for its ease of use, as its default settings often yield strong performance without extensive tuning. Nevertheless, the algorithm provides several hyperparameters that can be adjusted to enhance either the model’s accuracy or its computational efficiency.

II.6. DEEP LEARNING

Deep learning is a subset of artificial intelligence inspired by the structure and function of the human brain. It uses artificial neural networks composed of three or more layers Figure II.15 commonly referred to as deep neural networks to model and learn complex, non-linear patterns and relationships within data. These networks automatically extract features and build hierarchical representations without the need for manual input, allowing them to learn directly from raw data. By mimicking the way, the human brain processes information, deep learning systems can identify patterns, make decisions, and adapt to new inputs. This ability to learn and improve from experience enables deep learning models to analyze vast amounts of data with high accuracy, making them powerful tools in a wide range of applications.

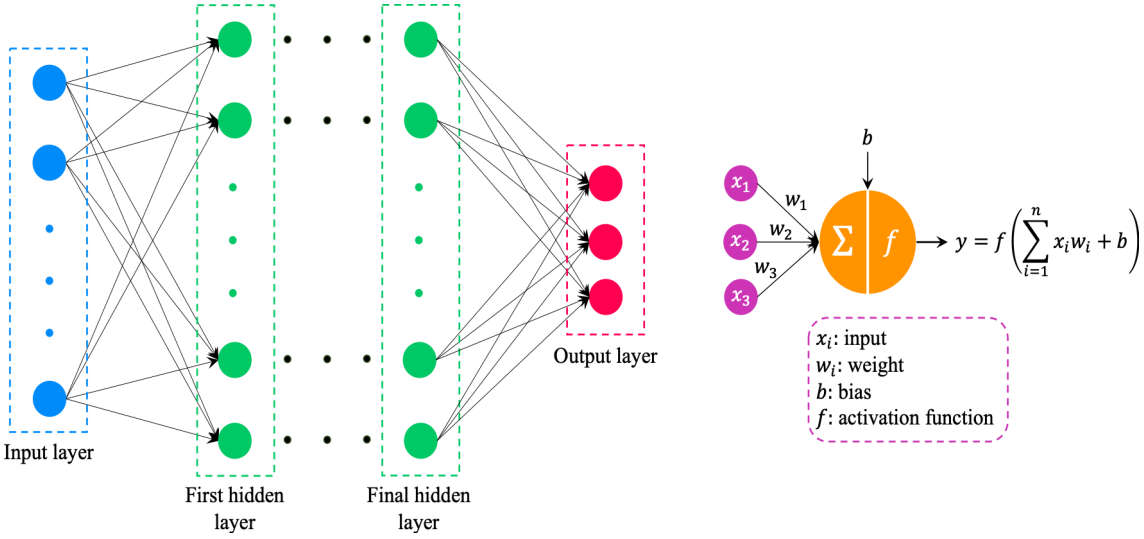

Figure II.15: The architecture ANN.

II.6.1. Features Deep Learning

- **Scalability**: Deep learning models are highly scalable and capable of handling large and complex datasets. They can be trained on massive amounts of data, making them ideal for solving sophisticated problems that require extensive information. For example, deep learning algorithms used in image recognition have been successfully trained on datasets like Google's ImageNet, which contains over 14 million images.
- **High Accuracy**: When provided with sufficient training data, deep learning models can achieve exceptional accuracy. This is due to their ability to learn intricate patterns and representations within the data that are often difficult to detect using more traditional approaches.

- **Object Detection and Translation**: Deep learning models excel in tasks such as object recognition in images and language translation, leveraging their layered structure to extract meaningful features automatically.
- **Robustness**: These models are generally resilient to noisy or imperfect data. Even when inputs are blurry or contain visual distortions, deep learning systems can still perform reliably. This robustness makes them suitable for real-world applications where data quality may vary.
- **Flexibility**: Deep learning models are versatile and can be applied to a wide range of problems. Their ability to learn and generalize allows them to adapt to different domains, including speech recognition, image classification, and natural language processing.
- **End-to-End Learning**: One of the key advantages of deep learning is its ability to perform end-to-end learning. This means the model can learn to map raw input data directly to the desired output, without the need for manually crafted features or intermediate processing stages. This holistic learning approach enables the network to optimize all layers simultaneously for better performance. (Alzubaidi et *al.* 2021)

II.6.2. Deep Learning Techniques

II.6.2.1. Convolutional Neural Network

Convolutional Neural Networks (CNNs) represent an advanced and specialized form of deep neural networks, primarily employed for analyzing and interpreting visual data (Zhou 2020). Their architectural design is highly effective in capturing spatial hierarchies within the input, allowing the network to detect and learn patterns in a more intuitive and structured manner compared to conventional, general-purpose neural networks. A notable variant, the one-dimensional Convolutional Neural Network (1D-CNN) (Figure II.16), extends these capabilities to sequential or time-series data by applying convolutional filters along a single spatial dimension. This makes 1D-CNNs particularly suitable for tasks involving structured signals such as sensor readings, speech signals, or numerical sequences in engineering and scientific applications.

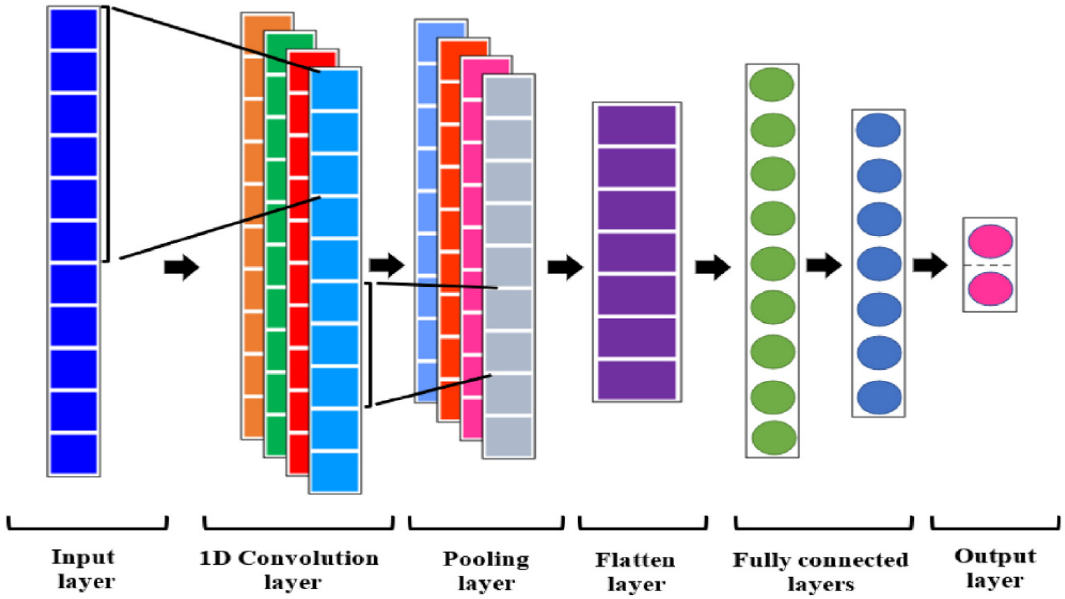

Figure II.16: 1D-CNN (Nizar et *al*. 2024).

✓ **Core Elements of CNNs**

- **Convolutional Layers**: These form the foundation of CNNs, utilizing a series of learnable filters that slide across the spatial dimensions of the input to detect specific features like edges, curves, and textures. Each filter generates a corresponding feature map that highlights the regions where the pattern is detected.
- **Activation Functions**: Non-linear activation functions, such as the Rectified Linear Unit (ReLU), are applied after convolution operations. These functions introduce non-linearity into the network, enabling it to learn and represent more complex patterns within the data.
- **Pooling Layers**: These layers are responsible for downsampling the feature maps, effectively reducing the spatial dimensions and computational load while preserving critical information. Common pooling strategies include max pooling and average pooling.
- **Fully Connected Layers**: Positioned near the end of the CNN, these layers compile and interpret the features extracted by the convolutional and pooling layers. They play a key role in mapping the features to the final classification tasks.
- **Output Layer**: The final layer in a CNN typically employs a SoftMax activation function to generate a probability distribution over the target classes, enabling the model to assign input data to specific categories (Alzubaidi et *al.* 2021).

II.6.2.2. Recurrent Neural network

Recurrent Neural Networks (RNNs) Figure II.17 are a specialized type of neural network developed to manage sequential or time-dependent data (Hewamalage et *al*. 2020). They are

particularly effective for tasks involving time-series information or data where the order of elements is crucial, such as in natural language processing, financial forecasting, or sensor readings. What sets RNNs apart is their capacity to retain information over time by feeding their previous outputs back into the network as inputs for subsequent steps. This feedback mechanism allows RNNs to establish temporal dependencies and patterns across sequences (Jiang et *al*. 2020, John et *al*. 2020).

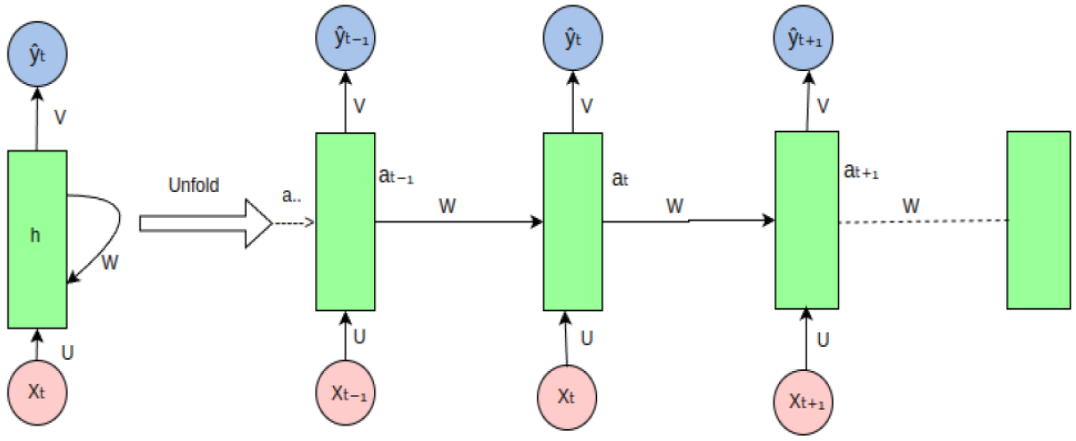

Figure II.17: Recurrent Neural network (Bengani 2024).

✓ **Core Mechanism:**

The basic architecture of an RNN includes a layer of neurons that have recurrent connections looping back on themselves. This looping mechanism allows the network to take not only the current input but also the previously received inputs into account, because the output from a layer of neurons at one time step becomes part of the input to those same neurons at the next time step. This sequential memory allows RNNs to make predictions based on the entire history of inputs it has seen so far (Pascanu et *al*. 2014).

✓ **Training RNNs:**

The training of Recurrent Neural Networks (RNNs) is commonly carried out using a technique known as backpropagation through time (BPTT). This approach involves unfolding the RNN across its time steps and applying the backpropagation algorithm to adjust the network's weights in a manner that reduces prediction errors. Despite its effectiveness, this process can be difficult due to challenges such as vanishing and exploding gradients. In these cases, the gradients used for updating the model's parameters may either diminish to near zero or grow excessively large, making it difficult for the network to learn from long sequences (Das et *al.* 2023).

✓ **Common Variants :**

To overcome challenges like the vanishing gradient issue, several enhanced versions of RNNs have been introduced (Das et *al*. 2023), including:

- **Long Short-Term Memory (LSTM):**

  LSTM networks incorporate special components known as gates that control the flow of information through the network. These gates determine which data should be retained, updated, or discarded, enabling the model to preserve relevant information and sustain gradient flow across long sequences.

- **Gated Recurrent Units (GRUs):**

  GRUs offer a more streamlined alternative to LSTMs by combining certain gating functions. Specifically, they merge the forget and input gates into a single "update gate" and unify the cell state and hidden state. This simplified structure reduces the number of parameters, making GRUs more computationally efficient while still effectively handling sequence-based tasks.

II.6.2.3. Long Short-Term Memory Networks (LSTMs)

Long Short-Term Memory networks (LSTMs) Figure II.18 are a sophisticated form of Recurrent Neural Networks (RNNs) specifically developed to capture and retain long-range dependencies in sequential data. Their architecture enables them to perform exceptionally well in tasks that demand contextual understanding across extended sequences, including time-series forecasting, language modeling, and speech interpretation (Sak et *al*. 2014).

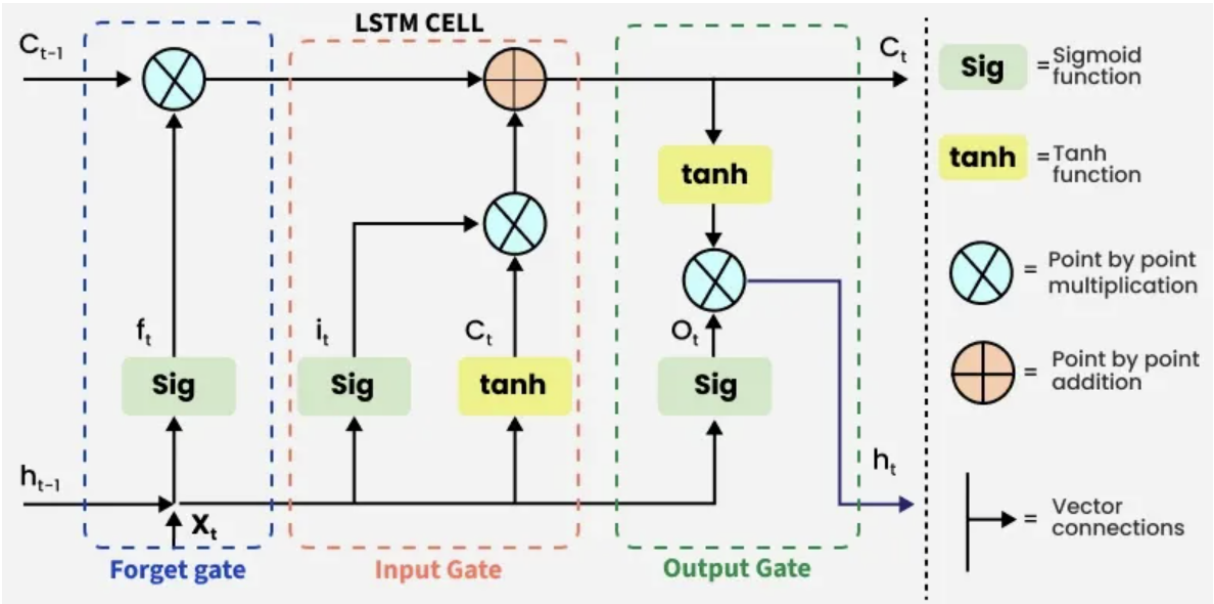

Figure II.18: LSTM Model (geeksforgeeks).

✓ **Fundamental Mechanics :**

LSTMs are specifically designed to address the vanishing gradient issue that affects traditional RNNs. In standard RNNs, as the loss gradients are propagated backward through time, they can diminish exponentially, limiting the model's ability to learn from earlier time steps in long sequences. LSTMs overcome this challenge through a

carefully structured system of gates that regulate the flow of information within the network:

1) **Forget Gate**: This gate critically evaluates information from the past, deciding what to retain or discard from the cell state.
2) **Input Gate**: It manages the incorporation of new information into the cell state, effectively updating the memory.
3) **Output Gate**: This gate influences the output of the LSTM unit by filtering the information that should be passed along from the cell state.

These gates function using sigmoid activation functions, producing values between zero and one to control the extent to which information is allowed to pass through, enabling the network to maintain long-term memory effectively (Das et *al*. 2023).

✓ **Primary Benefits**

- **Improved Memory Management**: LSTMs are highly effective at retaining crucial information over extended durations, making them invaluable for modeling intricate sequences;
- **Adaptability**: The architecture of LSTMs enables their use in a wide array of sequential data applications, ranging from forecasting financial trends to aiding in medical diagnoses (Das et *al*. 2023).

II.7. HYBRID LEARNING APPROACHES

Hybrid learning systems in machine learning combine traditional machine learning (ML) and deep learning (DL) techniques to enhance model performance, efficiency, and adaptability, addressing the limitations of each when used alone. By leveraging the strengths of both methodologies, these systems are particularly valuable in applications that require both high accuracy and interpretability. The following provides an in-depth exploration of the rationale for employing hybrid models, presenting an original approach suitable for academic purposes (Bengani 2024).

II.7.1. Components of Hybrid Learning Systems

II.7.1.1. Ensemble Methods

Ensemble methods play a crucial role in hybrid learning by combining multiple learning models to enhance predictive accuracy beyond what any single model can achieve. Key techniques include:

✓ **Bagging (Bootstrap Aggregating)**: This method boosts stability and accuracy by training multiple models on different subsets of the dataset and averaging their predictions to make a final decision;

✓ **Boosting**: Boosting trains models sequentially, with each new model focusing on the errors made by the previous one, gradually improving accuracy;

- ✓ **Stacking**: In stacking, the predictions from various models are used as inputs for a final model, which enhances overall prediction accuracy.

II.7.1.2. Transfer Learning

Transfer learning (Figure II.19) involves applying knowledge gained from solving one problem to a different, yet related, problem. This approach is especially useful in situations where data is limited:

- ✓ **Pre-trained Models**: Leveraging models that have been trained on large datasets to improve performance on tasks with smaller amounts of data;
- ✓ **Cross-domain Adaptation**: Adapting models from one domain to another by utilizing the similarities between tasks to enhance performance.

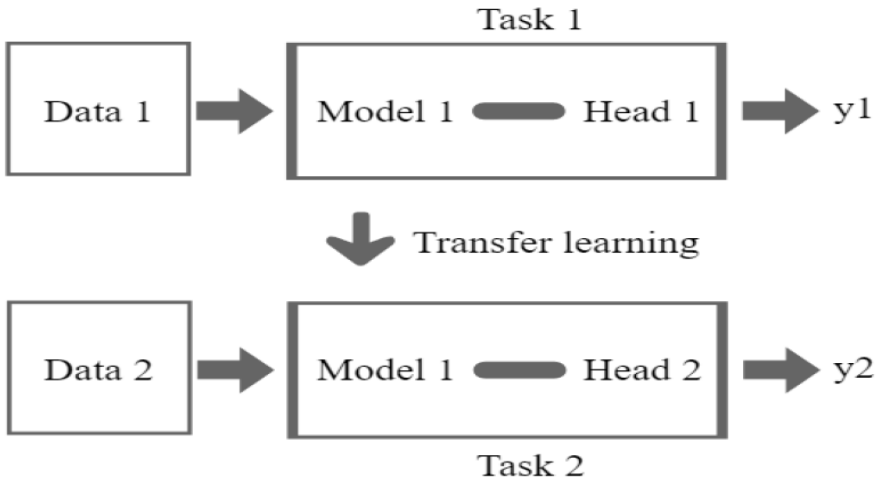

Figure II.19: Transfer Learning (Bengani 2024).

II.7.1.3. Model Fusion Techniques

Model fusion (Figure II.20) involves integrating multiple models to form a more robust and effective system by combining their most advantageous features and capabilities:

- ✓ **Soft Alignment**: This technique aligns features across different models, regardless of variations in architecture or training data, to unify their learned representations;
- ✓ **Parameter Averaging**: Methods such as optimal transport theory are employed to average model parameters, reducing inconsistencies and improving overall model performance.

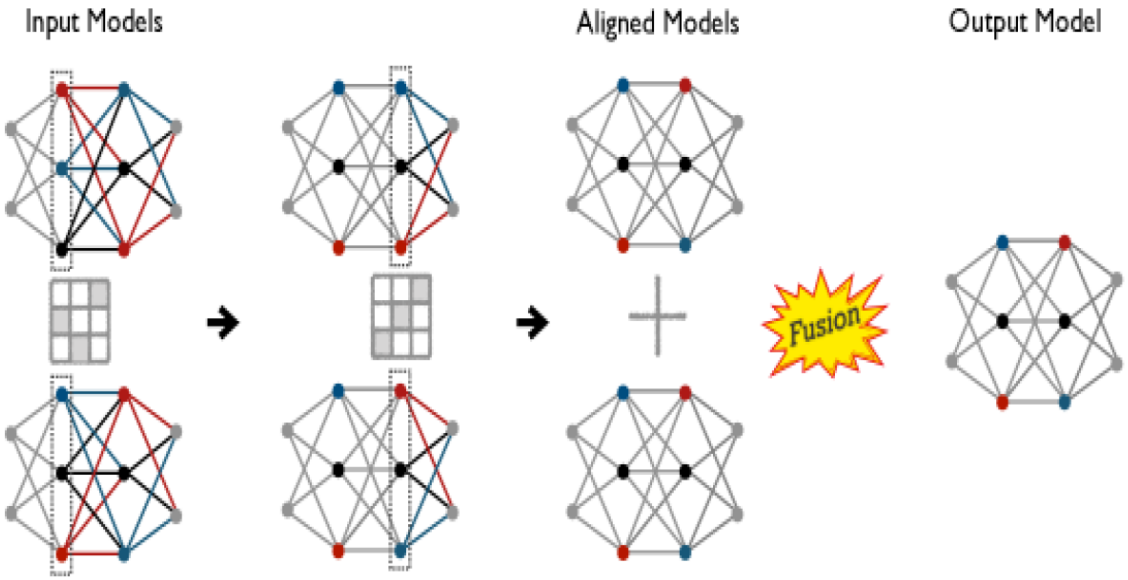

Figure II.20: Model Fusion Techniques (Bengani 2024).

The advancement of hybrid learning systems marks a major step forward in building more adaptable, precise, and efficient machine learning models. By integrating the strengths of diverse models and techniques, these systems are equipped to address a broad spectrum of challenges ranging from enhancing predictive accuracy to facilitating knowledge transfer between tasks and optimizing computational efficiency. The ongoing progress in ensemble methods, transfer learning, and model fusion underscores the dynamic and innovative spirit of machine learning research, striving to leverage the combined capabilities of multiple approaches for improved performance across a wide array of applications (Bengani 2024).

II.7.2. Advantages of hybrid learning systems

1. **Increased Accuracy**: Hybrid systems integrate multiple learning techniques to enhance predictive accuracy, particularly in complex problems involving extensive or heterogeneous datasets;
2. **Better Generalization**: The diverse learning strategies within hybrid models enable them to generalize more effectively across various tasks and domains.
3. **Optimized Resource Utilization**: These systems make efficient use of computational resources by dynamically adjusting learning strategies according to the task's specific demands and resource availability.

II.8. PYTHON PROGRAM

Among the programming languages used in machine learning (ML) and deep learning (DL), Python has established itself as the most widely adopted due to its simplicity, readability, and extensive ecosystem. Its flexibility and the availability of numerous open-source libraries such as TensorFlow, Keras, PyTorch, Scikit-learn, and Pandas make it an

ideal choice for developing and deploying data-driven models. In addition to these libraries, Python is supported by a vast community, comprehensive documentation, and seamless integration with cloud platforms, enabling researchers and developers to efficiently implement and experiment with complex ML and DL algorithms. Consequently, this paper highlights key Python libraries and platforms that facilitate the implementation of such models. Table II.1 provides a summary of the most commonly used Python libraries in ML and DL applications (geeksforgeeks).

Table II.1: Commonly utilized Python libraries in ML applications (geeksforgeeks).

Name	Features
TensorFlow	Can run on a variety of computational platforms, and suit for very large numerical computations
Keras	Have a bunch of features to work on image and text, and ease of use with neural networks
PyTorch	Have a robust framework to build computational graphs, and ease of using and learning
Scikit-learn	Handle wide ranges of ML algorithms for statistical analysis, data mining, and data analysis
Pandas	Support for different types of data, and suit for data analysis with highly optimised performance
Spark MLlib	Make practical ML easy and scalable with the merits of speed and ease of use
Theano	Perform data-intensive computations with mathematical expressions and matrix calculations
NumPy	Process large multi-dimensional arrays and matrices, and easily integrate with most databases
SciPy	Suit for computational tasks for scientific and analytical computing
Matplotlib	Suit for data visualization with quality image plots and figures in a variety of formats

- ✓ **TensorFlow**: Developed by Google and first released in 2015, TensorFlow is an open-source machine learning library that incorporates a broad spectrum of state-of-the-art ML algorithms. It is widely recognized as one of the leading platforms for developing machine learning models, particularly those involving deep neural networks. As a high-level framework, TensorFlow offers numerous pre-built models and ready-to-use packages, making it suitable for both research and practical applications.
- ✓ **Keras**: is an open-source library designed for building and evaluating deep neural networks. Developed by François Chollet in 2015, it serves as a user-friendly interface for the TensorFlow library, emphasizing ease of use and rapid prototyping. Keras is compatible with both TensorFlow and Theano backends, and it provides a variety of features for constructing neural network architectures. Additionally, it includes a rich set of tools for processing image and text data, making it well-suited for a wide range of deep learning tasks.
- ✓ **PyTorch:** Introduced by Facebook in 2016, PyTorch has quickly gained prominence as one of the most widely used deep learning libraries, following Keras and TensorFlow. Its intuitive design and user-friendly interface have contributed to its rapid adoption within the research and development community. PyTorch features a dynamic computational graph framework, enabling flexible model building and debugging. It also offers a comprehensive suite of tools and libraries that support various machine learning and deep learning tasks.
- ✓ **Scikit-learn**: This library was built in 2007 based on two Python numerical and scientific libraries of NumPy and SciPy. Scikit-learn provides a wide range of functions for classification, regression, clustering, and dimensionality reduction algorithms. It has become one of the most popular ML libraries especially for data mining and data analysis.
- ✓ **Pandas**: This is the most popular Python ML library for data analysis. Pandas was first released in 2008. It offers high-level data structures and options to manipulate different types of data including matrix data, tabular data, and time series data. It also provides a lot of great features for efficiently handling large datasets.
- ✓ **Spark MLlib**: is a machine learning library specifically developed to address the challenges of processing large-scale data. Built on top of Apache Spark—a high-performance engine for distributed data processing it aims to make scalable and practical machine learning more accessible. Spark MLlib offers a range of tools for developing machine learning algorithms and applications, with a focus on simplicity, efficiency, and ease of use.
- ✓ **Theano**: developed by the University of Montreal, is a symbolic mathematical computation library designed to facilitate efficient numerical operations, particularly in scientific computing. It was created to handle large-scale, computationally intensive

tasks with high performance. Often regarded as the "grandfather" of deep learning libraries, Theano laid the foundation for many modern frameworks, such as Keras, which were originally built on top of it.

- ✓ **NumPy**: short for “Numerical Python,” is a general-purpose library designed for efficient array processing. Built on top of the earlier “Numeric” library, NumPy has become a fundamental tool in the machine learning ecosystem. It offers a wide range of mathematical functions to manipulate large, multi-dimensional arrays and matrices. Its capabilities are especially valuable for performing basic linear algebra operations, random number simulations, and Fourier transforms, making it an essential component in many scientific and ML workflows.
- ✓ **SciPy**: short for “Scientific Python,” is a library developed to support scientific and technical computing. Built on top of NumPy, it extends its functionality by offering a wide array of advanced mathematical functions for tasks such as optimization, linear algebra, signal processing, and fast Fourier transforms. Known for its efficiency and ease of use, SciPy is widely adopted in scientific research and engineering applications requiring high-performance computation.
- ✓ **Matplotlib:** is a comprehensive plotting library in Python, built on top of NumPy, designed for creating static, animated, and interactive visualizations. It provides a wide variety of plotting functions such as line graphs, scatter plots, bar charts, and histograms that assist in exploring data patterns and distributions. Renowned for its simplicity and ease of use, Matplotlib is a foundational tool for data visualization in scientific and analytical applications (geeksforgeeks).

II.9. CONCLUSION

This chapter underscores the evolving role of data-driven methods in structural analysis, particularly in evaluating the behavior of concrete elements reinforced with internal and/or external FRP. Regression techniques, including linear, multivariate, and polynomial forms, have long provided a foundation for predicting mechanical properties based on empirical data. However, the growing complexity and volume of structural data necessitate more robust approaches hence the shift toward machine learning and deep learning. These advanced techniques, especially when combined in hybrid learning systems, offer improved accuracy, adaptability, and scalability. Moreover, Python-based implementations provide a flexible and efficient platform for deploying these models in practical applications. Ultimately, this integrated approach enhances predictive capabilities and supports the development of more resilient, optimized structural systems in modern engineering. The next chapter focuses on the prediction of the load-carrying capacity of concrete columns internally confined with FRP bars through empirical formulations and machine learning models.

CHAPTER III:

Predicting The Load-Carrying Capacity Of Concrete Columns Internally Confined With Fiber Reinforced Polymer Bars

III.1. INTRODUCTION

The load-bearing capacity is a fundamental aspect in the structural design of reinforced concrete (RC) columns, particularly under the influence of axial compressive forces. Various design standards and published research have introduced predictive formulations to estimate the axial capacity of fiber-reinforced polymer-reinforced concrete (FRP-RC) columns. Nonetheless, notable inconsistencies persist between theoretical estimations and outcomes derived from experimental investigations. This chapter introduces a refined approach for estimating the peak axial strength of RC compression members reinforced with FRP bars under varying eccentricity conditions (e/h = 0 and e/h ranging from 0.08 to 1). The study begins with a comprehensive overview of current design approaches for FRP-RC columns. A dataset consisting of 308 experimental results sourced from existing literature was compiled for analysis. The predictive performance of existing models was evaluated using five statistical metrics: coefficient of determination (R^2), root mean square error (RMSE), mean absolute error (MAE), average absolute error (AAE), and standard deviation (SD). Additionally, three load-carrying capacity (LCC) prediction models were developed; one using a general regression technique and two employing machine learning algorithms: eXtreme Gradient Boosting (XGBoost) and Random Forest (RF) regression methods. Finally, the proposed models were benchmarked against existing design standards and previously suggested empirical equations to assess their accuracy and reliability.

III.2. REVIEW OF DESIGN FORMULATIONS OF FRP-RC COLUMNS

So far, several investigations suggested design models for calculating the ultimate axial load-caring capacity (P_u) of FRP-RC compressive members. In this section, fifteen existing models will briefly summarize, including four models from current codes of ACI 440.1R-15, CSA S806-02, CSA S806-12 and AS-3600 and eleven empirical formulations developed by Tobbi et *al*. (2012), Tobbi et *al*. (2014), Afifi et *al*. (2014a,b), Maranan et *al.* (2016), Xue et *al*. (2018), Mohammed et *al*. (2014a,b), Samani and Attard (2012), Khan et *al*. (2016) and Hadhood et *al*. (2017). The explanation details of all existing models with their expressions are reported in Table III.1. The illustration of FRP-RC compressive members is shown in Figure III.1.

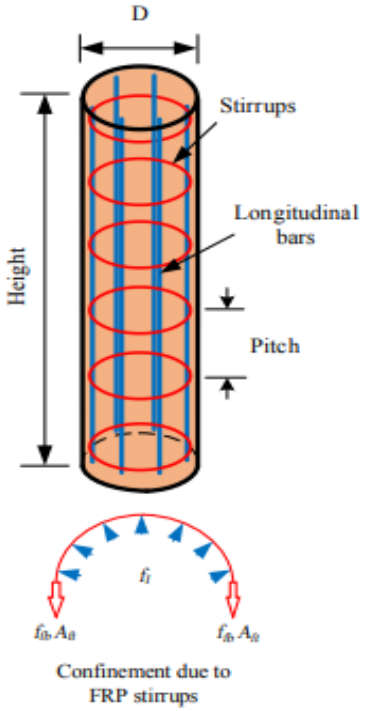

Figure III.1: Illustration of lateral confinement of FRP-RC columns.

Table III.1: Existing design formulations of FRP-RC compressive members.

Reference	Section form	FRP type	Design formulas, P_u	
ACI 440.1R-15	-	FRP	$P_n = 0.85\, f'_c\,(A_g - A_{frp})$	(III.1)
CSA S806-02	-	FRP	$P_n = 0.85\, f'_c\,(A_g - A_{frp})$	(III.2)
CSA S806-12	-	FRP	$P_n = \alpha_1 f'_c\,(A_g - A_{frp})$ $\alpha_1 = 0.85 - 0.0015 f'_c \geq 0.67$	(III.3)
AS-3600	-	FRP	$P_n = 0.85\, f'_c\,(A_g - A_{frp}) + 0.0025 E_{frp} A_{frp}$	(III.4)
Tobbi et *al.* (2012)	Square	GFRP	$P_n = \alpha_1\, f'_c\,(A_g - A_{frp}) + \alpha_{frp} f_{frp} A_{frp}$ $\alpha_1 = 0.85\,;\ \alpha_{frp} = 0.35$	(III.5)
Tobbi et *al.* (2014)	Square	GFRP	$P_n = 0.85\, f'_c\,(A_g - A_{frp}) + \varepsilon_\infty E_{frp} A_{frp}$ $\varepsilon_\infty = 0.003$	(III.6)
Afifi et *al.* (2014a)	Circular	CFRP	$P_n = \alpha_1\, f'_c\,(A_g - A_{frp}) + \alpha_{frp} f_{frp} A_{frp}$ $\alpha_1 = 0.85\,;\ \alpha_{frp} = 0.25$	(III.7)
Afifi et *al.* (2014b)	Circular	GFRP	$P_n = 0.85\, f'_c\,(A_g - A_{frp}) + \alpha_g f_{frp} A_{frp}$ $\alpha_g = 0.35$	(III.8)

Table III.1: *Continued*

Maranan et *al*. (2016)	Circular	GFRP	$P_n = \alpha_1 f'_c (A_g - A_{frp}) + 0.002 E_{frp} A_{frp}$ $\alpha_1 = 0.9$	(III.9)
Xue et *al*. (2018)	Square	GFRP	$P_n = \alpha_1 f'_c (A_g - A_{frp}) + 0.002 E_{frp} A_{frp}$ $\alpha_1 = 0.85$	(III.10)
Mohammed et *al*. (2014a)	Circular	GFRP CFRP	$P_n = 0.85 f'_c (A_g - A_{frp}) + \varepsilon_p E_{frp} A_{frp}$ $\varepsilon_p = 0.002$	(III.11)
Mohammed et *al*. (2014b)	Circular	GFRP CFRP	$P_n = 0.9 f'_c (A_g - A_{frp}) + \varepsilon_{fg} E_{frp} A_{frp}$ $\varepsilon_{fg} = 0.002$	(III.12)
Samani and Attard (2012)	-	-	$P_n = 0.85 f'_c (A_g - A_{frp}) + 0.0025 E_{frp} A_{frp}$	(III.13)
Khan et *al.* (2016)	Circular	GFRP	$P_n = 0.85 f'_c (A_g - A_{frp}) + \alpha E_{frp} A_{frp}$ $\alpha = 0.61$	(III.14)
Hadhood et *al*. (2017)	Circular	CFRP	$P_n = \alpha_1 f'_c (A_g - A_{frp}) + 0.0035 E_{frp} A_{frp}$ $\alpha_1 = 0.85 - 0.0015 f'_c$	(III.15)

III.3. COLLECTED TEST DATASET

Numerous researchers conducted experimental investigations to study the axial behavior of concrete compressive members internally confined with FRP bars in the literature. In this section, a large dataset of 377 of FRP-RC compressive member samples as listed in Table III.2 was compiled from 42 experimental studies of De Luca et *al*. (2010), Tobbi et *al*. (2012), Afifi et *al*. (2014a,b), Tobbi et *al*. (2014), Mohamed et *al.* (2014), Prachasaree et *al*. (2015), Maranan et *al*. (2016), Xiaochun et *al*. (2016), Hales et *al*. (2016), Hadi and Youssef (2016), Ali et *al*. (2016), Khan et *al.* (2016), Hadi et *al*. (2017), Elchalakani et *al*. (2017), Hadhood et *al*. (2017), Hadhood et *al.* (2017), Hadhood et *al*. (2017), Hadhood et *al.* (2017), Khorramian et *al*. (2017), Sun et *al*. (2017), Elchalakani et *al*. (2017), Hadhood et *al.* (2018), Hadhood et *al*. (2018), Zhang et *al*. (2018), Tabatabaei et *al*. (2018), Tu et *al*. (2019), Xue et *al*. (2018), Salah-Eldin et *al.* (2019), Salah-Eldin et *al*. (2019), Elchalakani et *al*. (2019), Othman et *al*. (2019), Dong et *al*. (2019), El-Gamal et *al.* (2020), Elchalakani et *al.* (2020), Abdelazim et *al*. (2020), Khorramian et *al*. (2020), Barua et *al*. (2020), El Messalami et *al*. (2021), Bakouregui et *al*. (2021), Afaq et *al*. (2023) published between the year 2010 and 2023. This dataset encompasses both circular and square cross-sections of FRP-RC compressive members, transversally reinforced with FRP hoops, spirals, and ties, as well as longitudinally reinforced with FRP bars under both concentric and eccentric axial loads. It includes 235 samples with circular cross-sections and 142 samples with square cross-sections. Among these, 213 samples were transversally confined with FRP spirals, 35 with FRP hoops, and 129 with FRP

ties. The dataset covers three types of FRP reinforcements: carbon fiber-reinforced polymer (CFRP), glass fiber-reinforced polymer (GFRP), and basalt fiber-reinforced polymer (BFRP).

In this study, we systematically considered all parameters that influence the axial structural behavior of FRP-RC columns. The dataset provides comprehensive information on the geometric and material properties of unconfined concrete and FRP reinforcement, encompassing essential factors like cross-sectional dimensions, reinforcement types, and load eccentricity levels. These factors were incorporated to capture the interactions between concrete and FRP bars that affect axial load capacity. Each parameter was selected based on its documented impact in the literature and relevance to the structural response of FRP-RC compressive members. For instance, the elastic modulus and tensile strength of the FRP bars influence axial stiffness and load-bearing capacity, while geometric properties and cross-section type affect confinement and load distribution. By compiling a detailed dataset, we aimed to develop robust predictive models applicable across diverse design scenarios.

The parameters included in this dataset were chosen specifically for their effect on the axial capacity (P_u) of FRP-RC compressive members, accounting for both geometric and material properties of unconfined concrete and FRP reinforcement. For the geometric, the properties include the cross-section type of concrete (S_{type}), height of the sample (H), gross cross-sectional area (A_g). For the unconfined concrete properties presented include the compressive strength (f'c). For the FRP, the important properties include, the cross-sectional area of the FRP reinforcing bar (A_{frp}), Percentage of FRP reinforcement (ρ_{frp}), number of FRP bars (n), form of tie bar ($Form$), type of longitudinal FRP reinforcement (l_{type}), type of transverse FRP reinforcement (t_{type}), the diameter of stirrups (d_s), the diameter of the main FRP bar (d_m), the elastic modulus of FRP bar (E_{frp}), the tensile strength of FRP bar (f_{frp}), and spacing of stirrups (S_v), α_1 and α_{frp} are the coefficients whilst the axial load condition (P_{cond}) (concentric or eccentric) was also given in Table III.1.

A summary of the ranges of data and test results of the selected dataset is presented in Table III.3. The values of height (H), gross cross-sectional area (A_g), the compressive strength of unconfined concrete (f'_c), Percentage of FRP reinforcement (ρ_{frp}), the cross-sectional area of FRP reinforcing bar (A_{frp}), number of FRP bars (n), the diameter of the main FRP bar (d_m), elastic modulus of FRP bar (E_{frp}), the tensile strength of FRP bar (f_{frp}), diameter of stirrups (d_s), spacing of stirrups (S_v), and axial capacity of FRP-RC compressive members (P_u) of the samples are in the range of 500 mm - 3730 mm, 12272 mm² - 372100 mm², 21 MPa - 90 MPa, 1 % - 5 %, 200 mm² - 3721 mm², 3 - 16, 8 mm - 25 mm, 39 GPa - 151 GPa, 574 MPa - 2000 MPa, 4 mm - 13 mm, 30 mm - 305 mm, 90 kN - 15234 kN, respectively.

Table III.2: Summary of the collected test dataset of FRP-RC compressive members.

Ref.	No.	l_{type}	P_{cond} / e/h	S_{type}	H (mm)	A_g (mm²)	f'_c (MPa)	ρ_{FRP} (%)	A_{FRP} (mm²)	n	d_m (mm)	E_{frp} (GPa)	f_{frp} (MPa)	t_{type}	d_s (mm)	Form	s_v (mm)	P_{ue} (kN)
De Luca et *al*. (2010)	4	GFRP	0	S	3 000	372100	32.8-43.7	1.0	3721	8	25.4	44.2	608-712	GFRP	12.7	ties	76-305	10750.8-15234.4
Tobbi et *al*. (2012)	5	GFRP	0	S	1 400	122500	32.6	1.9	2327.5	8-12	15.9-19.0	47.6-48.2	728-751	GFRP	12.7	ties	80-120	3928.5-4067.0
Afifi et *al*. (2014)a	9	GFRP	0	C	1 500	70685.8	42.9	1.1-3.2	777.5-2261.9	4-12	15.9	55.4	934	GFRP	6.4-12.7	spirals	35-145	2804.0-3019.0
Afifi et *al* (2014)b	9	CFRP	0	C	1 500	70685.8	42.9	1.0-2.4	706.8-1696.4	6-14	12.7	140.0	1899	CFRP	6.4-12.7	spirals	35-145	2905.0-3148.0
Tobbi et *al*. (2014)	4	GFRP CFRP	0	S	1 400	122500	35.0	0.8-1.9	980.0-2327.5	8-16	12.7-19.0	46.3-137.0	728-1902	CFRP GFRP	9.5-12.7	ties	67-120	3900.0-5159.0
Mohamed et *al*. (2014)	9	GFRP CFRP	0	C	1 500	70685.8	42.9	1.7-2.2	1201.6-1555.1	8-10	12.7-15.9	55.4-140.0	934-1899	GFRP CFRP	6.4-12.7	spirals hoops	80	2840.0-3019.0
Prachasaree et *al*. (2015)	13	GFRP	0	S-C	500	12271.8-22500.0	20.8	1.4-2.6	319.5-337.5	4	10.0	50.0	735	GFRP	6.0	spirals ties	50	310.0-390.0
Maranan et *al*. (2016)	7	GFRP	0	C	1000-2000	49087.4	38.0	2.4	1192.8	6	15.9	62.6	1184	GFRP CFRP	9.5	hoops-spirals	50-200	1208.0-2063.0
Xiaochun et *al*. (2016)	2	BFRP	0.17-0.67	S	900	14400.0	34.9	1.4	201.6	4	8.0	50.0	1000	BFRP	6.0	ties	100	90.0-270.0
Hales et *al*. (2016)	6	GFRP	0-0.08	C	760-3730	73061.7	90.0	1.6-2.7	1205.5-1979.9	6	16.0	43.0	715	GFRP	10.0	spirals	76	667.0 - 7126.0
Hadi and Youssef (2016)	3	GFRP	0-0.24	S	800	44 100.0	33.2	1.1	507.1	4	12.7	67.9	1641	GFRP	9.5	ties	50	615.0-1285.0
Hadi and Youssef (2016)	6	GFRP	0-0.24	C	800	33006.4	37.0	2.3	759.1	6	12.7	50.0	1200	GFRP	9.5	spirals	30-60	479.0-1309.0
Ali et *al*. (2016)	7	GFRP	0	S	1 650	122500.0	38.4-41.0	1.2-2.5	1580.2-3172.7	8-16	15.9	62.0	1184	GFRP	9.5	ties	75-150	133.0-201.0
Khan et *al*. (2016)	3	GFRP	0-0.24	C	812	33312.3	37.0	3.5	1189.2	6	15.9	56.0	1395	GFRP	9.5	hoops	60	910.0-2812.0
Hadi et *al*. (2017)	6	GFRP	0-0.24	C	800	34636.1	85.0	2.2	761.9	6	12.7	52.0	1190	GFRP	9.5	spirals	30-60	958.0-2721.0
Elchalakani et *al*. (2017)	7	GFRP	0-0.17	S	1200	41600.0	32.7	1.8	761.2	6	12.7	46.3	708	GFRP	6.3	ties	75-250	584.2-1449.0
Hadhood et *al*. (2017)	10	GFRP	0-0.33	C	1500	73061.7	70.2	2.1-3.2	1592.7-2389.1	8-12	15.9	54.9	1289	GFRP	9.5	spirals	80	497.0-4716.0
Hadhood et *al*. (2017)	5	CFRP	0-0.33	C	1500	73061.7	35.0	2.1	1592.7	8	15.9	141.0	1680	CFRP	9.5	spirals	80	529.0-3090.0

Table III.2: *Continued*

Hadhood et *al*. (2017)	5	CFRP	0-0.33	C	1500	73061.7	70.2	2.2	1607.3	8	15.9	141.0	1680	CFRP	9.5	spirals	80	611.0-5120.0
Hadhood et *al*. (2017)	8	GFRP	0-0.33	C	1500	73061.7	35.0-42.9	2.2	1607.3	8	15.9	54.9	1289	GFRP	9.5	hoops	80	366.0-2 935.0
Khorramian et *al*. (2017)	4	GFRP	0-0.3	S	500	22500.0	37.0	1.6	366.7	6	16.0	41.2	783	GFRP	6.0	ties	90	354.1-774.9
Sun et *al*. (2017)	9	GFRP	0.42-0.97	S	1000	45000.0	33.5	1.0	468.0	6	10.0	60.2	689	GFRP	4.0	ties	50	174.0-677.0
Elchalakani et *al.* (2017)	7	GFRP	0-0.17	S	1 200	41600.0	32.7	1.8	761.2	6	12.7	46.3	708	GFRP	6.3	ties	75-250	584.2-1449.0
Hadhood et *al.* (2018)	25	GFRP CFRP	0-0.33	C	1500	73061.7	35.1	2.2-3.3	1607.3-2411.0	8-12	15.9-16.0	54.9-141.0	1289-1680	GFRP CFRP	9.5-12.7	spirals hoops	80	354.0-3090.0
Hadhood et *al*. (2018)	40	GFRP CFRP	0-0.33	C	1500	73061.7	70.2	2.2	1607.3	8-12	15.9	54.9	1289	GFRP CFRP	9.5	spirals hoops	80	354.0-5120.0
Zhang et *al*. (2018)	8	GFRP	0	S	1200	122500.0	50.0	1.3-2.6	1702.7-3234.0	8-12	16.0-18.0	45.0	840	GFRP	8.0-12.0	ties	38-130	4500.0-5670.0
Tabatabaei et *al*. (2018)	5	GFRP	0	C	1 600	70685.8	49.3	1.6	1130.9	6	15.9	51.2	1374	GFRP	9.5	spirals	80	2871.0-3290.0
Tu et *al*. (2019)	8	GFRP	0	S	600	40000.0	32.1	1.1	440.0	4	10.0-14.0	43.7-46.0	574-735	GFRP	8.0	spirals hoops	30-80	927.7-981.7
Xue et *al*. (2018)	15	GFRP	0-1	S	1800-3 600	90000.0	29.1-55.2	0.9-2.5	810.0-2295.0	4-8	15.9-2.5	39.0-44.0	654-729	BFRP	8.0	ties	150	300.0-3091.0
Salah-Eldin et *al*. (2019)	4	GFRP	0.2-0.6	S	2000	160000.0	71.2	1.0	1600.0	6	19.0	62.7	1236	GFRP	10.0	ties	150	1367.0-5100.0
Salah-Eldin et *al*. (2019)	4	BFRP	0.2-0.6	S	2000	160000.0	71.2	1.0	1600.0	6	20.0	63.7	1646	BFRP	13.0	ties	150	1309.0-4965.0
Elchalakani et *al*. (2019)	9	GFRP	0-0.29	S	1200	41600.0	26.8	2.2	923.5	6	14.0	59.0	930	GFRP	8.0	ties	75-250	234.0-1357.0
Othman et *al*. (2019)	15	CFRP	0-1	S	1500	22500.0	44.7	1.4-3.6	315.0-810.0	4	10.0-16.0	145.0-151.0	2000	CFRP	6.0	ties	40.0-140.0	113.0-960.0
Dong et *al*. (2019)	12	GFRP	0-0.35	C	1150	36305.0	40.0	0.5-1.1	199.6-399.3	3-6	10.0	59.0	930	GFRP	8.0	spirals	40.0-120.0	296.0-1459.0
El-Gamal et *al*. (2020)	6	GFRP	0	C	1500	41547.6	25.6	1.6-3.8	677.2-1607.8	6-8	12.0-16.0	61.2 - 62.3	1102-1250	GFRP	10.0	spirals	50.0-100.**0**	1055.0-1227.0
Elchalakani et *al.* (2020)	11	GFRP	0-0.35	C	1150	36305.0	34.0	0.5-0.9	199.6-334.0	3-5	10.0	59.0	930	GFRP	8.0	spirals	40.0-120.0	342.0-1286.0
Abdelazim et *al.* (2020)	16	GFRP CFRP	0-0.66	C	1000-2500	73061.7	46.6	2.1	1600.0	8	15.9	61.8	1449	GFRP	9.5	spirals	80.0	371.0-3535.0
Khorramian et *al*. (2020)	9	GFRP	0.21-0.23	S	1020-3660	62730.0	48.4	2.8-4.8	1800.3-3011.0	6-10	19.0	43.4	963	GFRP	11.0	ties	300.0	844.0-1550.0

Table III.2: *Continued*

Barua et *al.* (2020)	5	GFRP	0-0.34	C	1750	98979.8	37.3-40.7	1.2	1187.7	6	15.9	64.0	1558	GFRP	9.5	spirals	85.0	1 278.0-4224.0
El Messalami et *al*. (2021)	9	BFRP	0-0.44	S	1100	32400.0	28.4	3.8	1257.1	4	20.0	45.9	913	BFRP	10.0	ties	60.0-180.0	315.0-879.0
Bakouregui et *al*. (2021)	24	GFRP BFRP CFRP	0-0.66	C	1500	73061.7	52.0	1.0 - 3.3	759.8-2411.0	6 - 12	12.7-15.9	54.9-144.0	1289-1765	GFRP BFRP CFRP	9.5	spirals hoops	60.0-120.0	440.0-3705.0
Afaq et *al*. (2023)	4	GFRP	0	C	1000	49087.4	31.8	2.4-2.7	1183.0-1364.6	6	15.9	60.0	1237	GFRP	9.5	spirals	50.0	1582.4-5 958.0

Table III.3: Summary of the ranges of data and test results the collected dataset.

Parameters	H (mm)	A_g (mm²)	f'_c (MPa)	ρ_{frp}	A_{frp} (mm²)	n	d_m (mm)	E_{frp} (GPa)	f_{frp} (MPa)	d_s (mm)	S_v (mm)	P_{ue} (kN)
Minimum	500	12272	21	1	200	3	8	39	574	4	30	90
Maximum	3730	372100	90	5	3721	16	25	151	2000	13	305	15234
Average	1456	67539	45	2	1300	7	15	65	1176	9	92	1834
St. deviation	588.65	42889.79	15.82	0.81	687.76	2.29	2.82	30.5	372.49	1.8	49,5	1766.02
Coef. of variance	0.41	0.64	0.35	0.41	0.53	0.33	0.2	0.47	0.32	0.21	0,54	0.97

III.4. ASSESSMENT OF THE PERFORMANCE OF EXISTING MODELS

III.4.1. Performance criteria

The evaluation of axial load-carrying capacity prediction models is carried out through a statistical analysis, using a dataset comprising 308 experimental records, as presented in Table III.2. To determine the predictive accuracy of these models in estimating the axial load-carrying capacity of FRP-RC concrete columns, multiple assessment metrics are utilized. In this study, fiver key statistical parameters are adopted to measure model reliability, goodness-of-fit, and overall precision. These include the coefficient of determination (R^2), root mean square error (RMSE), mean absolute error (MAE), average absolute error (AAE), and standard deviation (SD). The mathematical explanations Eqs (III.16)-(III.19) are given are follows:

$$R^2 = \left(\frac{n(\sum_{i=1}^{n} x_i y_i) - (\sum_{i=1}^{n} x_i)(\sum_{i=1}^{n} y_i)}{\sqrt{[n\sum_{i=1}^{n} {x_i}^2 - (\sum_{i=1}^{n} x_i)^2][n\sum_{i=1}^{n} {y_i}^2 - (\sum_{i=1}^{n} y_i)^2]}} \right)^2 \quad \text{(III.16)}$$

$$RMSE = \sqrt{\frac{1}{n}\sum_{i=1}^{n}(x_i - y_i)^2} \quad \text{(III.17)}$$

$$MAE = \frac{\sum_{i=0}^{N-1}|x_i - y_i|}{N} \quad \text{(III.18)}$$

$$AAE = \frac{1}{n}\sum_{i=1}^{n}\left|\frac{x_i - y_i}{y_i}\right| \quad \text{(III.19)}$$

$$SD = \sqrt{\frac{\sum_{i=1}^{n}\left|\frac{x_i}{y_i} - \left(\frac{x}{y}\right)_{average}\right|^2}{n-1}} \quad \text{(III.20)}$$

In which x_i, y_i refer to the experimental measurement values and the prediction values, respectively. n denotes the total number of datasets.

III.4.1.1. Coefficient of determination (R^2)

In statistical analysis, the coefficient of determination (R^2) serves as a key metric to evaluate the effectiveness of a simple linear regression. It quantifies how well the regression model corresponds to the observed dataset, indicating the extent to which the regression equation accurately captures the pattern of data distribution (Sadeghian and Fam, 2015). This coefficient ranges between 0 and 1, representing a scale from low to high predictive capability. As illustrated in Figure (III.2), an R^2 value of zero indicates that the regression line accounts for none of the variation in the data points—meaning the model fails entirely to describe the distribution. On the other hand, an R^2 value of one signifies that the regression equation perfectly explains 100% of the data variability. In essence, the closer R^2 is to zero, the more dispersed the data points are around the regression line. Conversely, the nearer R^2 approaches one, the more tightly the points cluster along the regression line. When all data points lie exactly on the regression line, the coefficient reaches its maximum value of $R^2 = 1$.

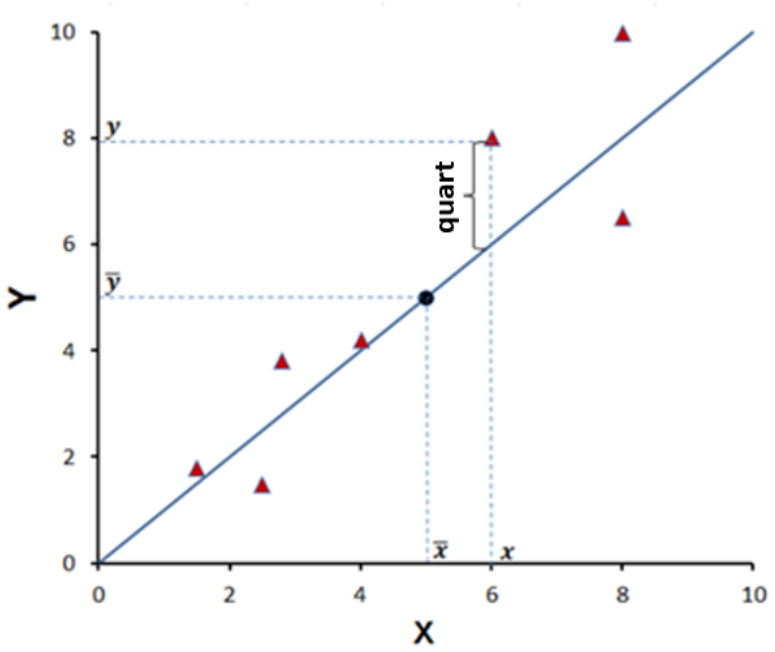

Figure III.2: Dispersion of data points around the regression line.

III.4.1.2. Error (RMSE, MAE, AAE)

The Root Mean Square Error (RMSE) (see Figure III.3) is a commonly adopted statistical metric used to assess the predictive capability of models. The primary objective is to minimize the RMSE value, as a lower RMSE corresponds to a smaller standard deviation, which is indicative of superior model accuracy. Additionally, when using the least squares method, the sum of residuals equals zero, confirming that the residuals represent deviations

from the mean, which is also zero. This makes RMSE a valuable fitting criterion for enhancing prediction precision.

The Mean Absolute Error (MAE) and Average Absolute Error (AAE) (refer to Figure III.3) are widely used metrics in model evaluation. They quantify the average deviation between predicted results and experimental values. Lower MAE, AAE, and RMSE values indicate higher predictive accuracy, with values approaching zero signifying near-perfect predictions, where all data points align along a 45-degree diagonal line. While MAE and AAE measure the average magnitude of prediction errors, RMSE also captures the distribution and variability of these errors.

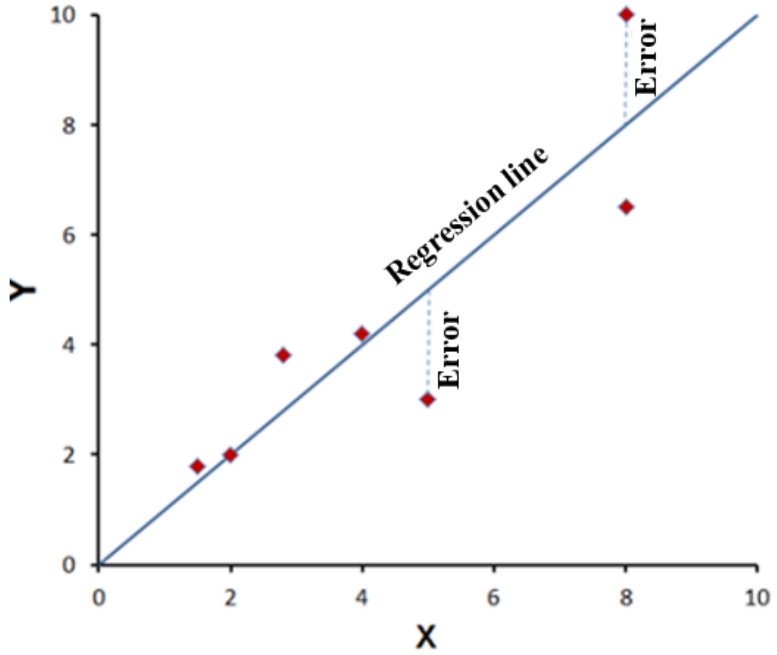

Figure III.3: Graphical representation of errors (RMSE, MAE, AAE).

III.4.1.3. Standard deviation (SD)

The Standard Deviation (SD) (see Figure III.4) is a statistical indicator of both dispersion and precision, offering insights into the true average of a population. It helps determine how widely the predicted values deviate from their mean. A low SD suggests that most values are concentrated near the average, indicating consistency in model performance. Conversely, a high SD implies that the data points are more scattered and potentially random, signaling reduced model reliability.

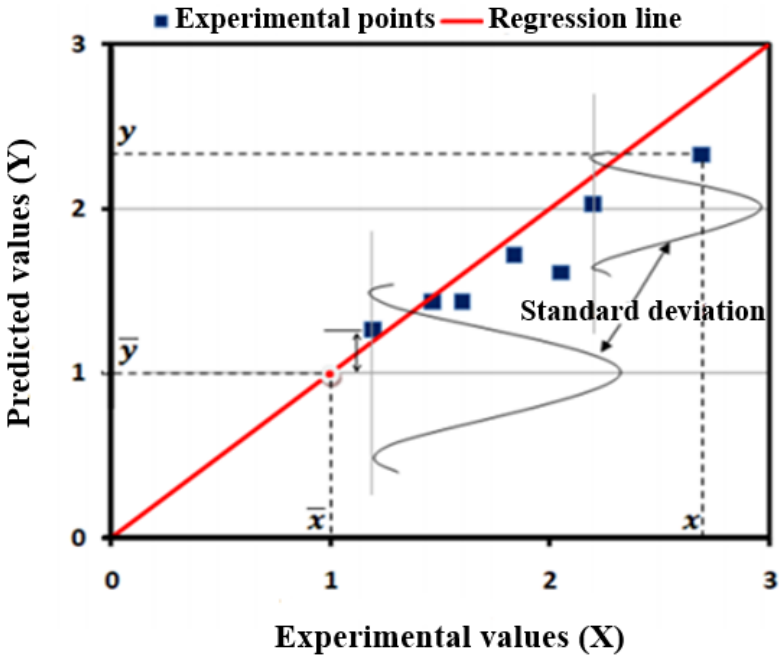

Figure III.4: SD between predicted and experimental values.

III.4.2. ACI 440.1R-15 model

Using the experimental dataset comprising 308 collected data points, the performance of the ACI 440.1R-15 model was evaluated. Figure III.5a presents the statistical indicator values, with R^2 = 0.70, RMSE = 909.12 kN, MAE = 662.12 kN, AAE = 0.80, and SD = 1.44. These statistical indicators indicate poor performance between the experimental and predicted values. This observation is clearly illustrated by the majority of data points lying above the 45° diagonal line, indicating high dispersion of the data points.

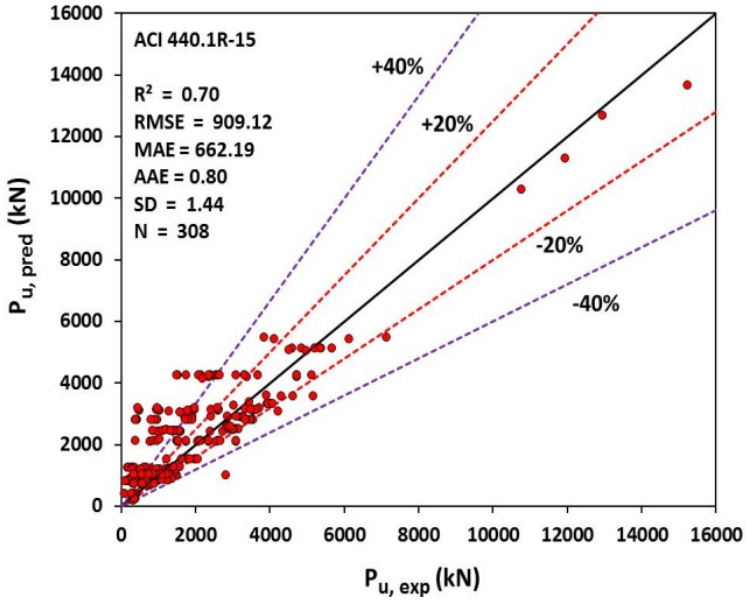

Figure III.5: Assessment results of ACI 440.1R-15 model of FRP-RC compressive members.

III.4.3. AS-3600 model

The assessment of the ALCC model from the AS-3600 code is depicted in Figure III.6. This figure illustrates that the majority of data points lie above the 45° diagonal line and the upper limit line of 40%, indicating that this model overestimates the ALCC values. Furthermore, the value of $R^2 = 0.70$ indicates a weak correlation between the predicted and experimental values. Additionally, the other indicators RMSE = 909.18 kN, MAE = 662.19 kN, AAE = 0.80, and SD = 1.44 confirm the poor performance of this model.

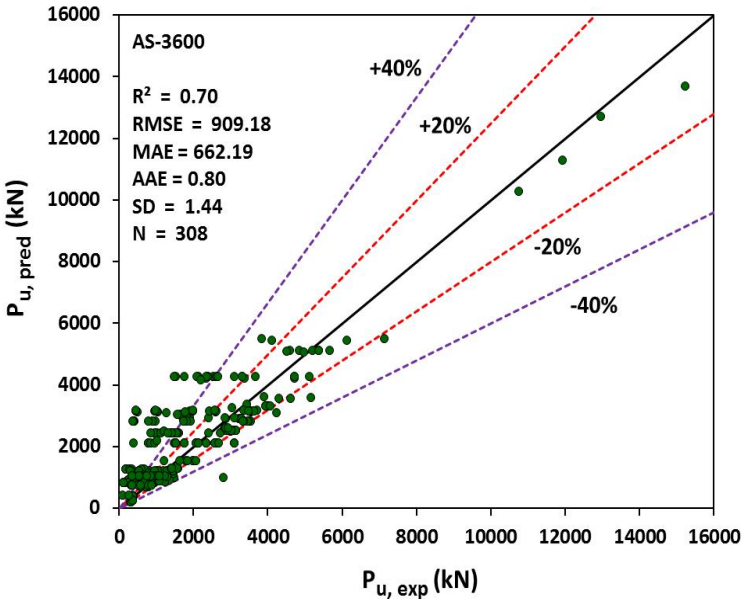

Figure III.6: Assessment results of AS-3600 model of FRP-RC compressive members.

III.4.4. CSA S806-02 model

Figure III.7 illustrates the statistical evaluation of the ALCC model from the CSA S806-02 code, using the experimental dataset developed in the previous section. The evaluation of this figure suggests that the statistical indices of this model are comparable to those obtained for the ACI 440.1R-15 model and AS-3600 model. These indices confirm that the performance of this model remains consistent with that of the previously discussed models.

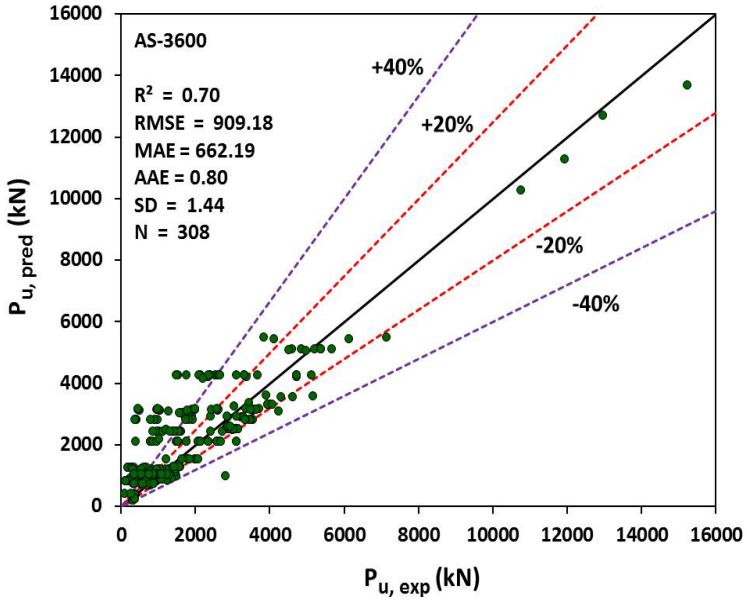

Figure III.7: Assessment results of CSA S806-02 model of FRP-RC compressive members.

III.4.5. CSA S806-12 model

The ALCC model of CSA S806-12, designed for FRP-RC compressive members, underwent evaluation against 308 experimental data points. Figure III.8 displays a coefficient of correlation $R^2 = 0.71$, indicating a weak correlation between the experimental and predicted values. However, this model achieves minimum values for four other statistical indicators: RMSE = 846.58 kN, MAE = 651.92 kN, AAE = 0.74, and SD = 1.33. These indicators confirm the satisfactory performance of this model compared to the ACI 440.1R-15, AS-3600, and CSA S806-02 models.

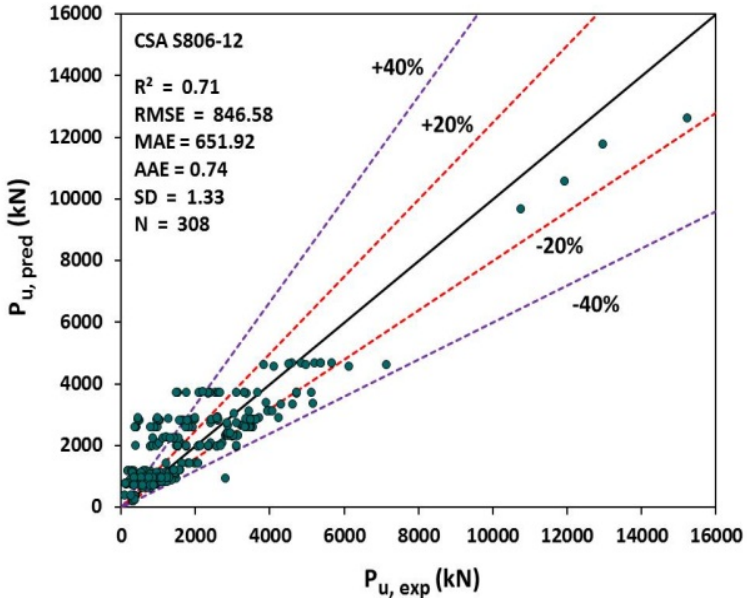

Figure III.8: Assessment results of CSA S806-12 model of FRP-RC compressive members.

III.4.6. Tobbi et *al.* model

The ALCC model developed by Tobbi et *al.* (2012) was assessed using 308 experimental data points and five statistical indices. As shown in Figure III.9, the indicators RMSE = 1245.82 kN, MAE = 861.72 kN, AAE = 1.10, and SD = 1.86 reach maximum values, indicating significant errors divergence and very high dispersion. Moreover, R^2 = 0.61 suggests a weak correlation between the experimental and predicted values, with all data points lying above the 45° diagonal line. Consequently, the performance of this model remains poor compared to the four previously evaluated models.

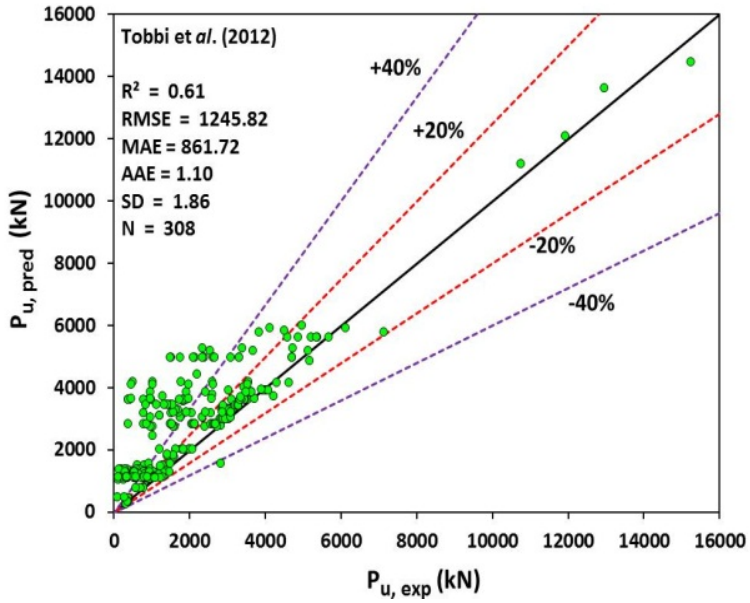

Figure III.9: Assessment results of Tobbi et *al*. (2012) model of FRP-RC compressive members.

III.4.7. Samani and Attard. model

Figure III.10 compares the measured and experimentally determined axial capacity values for both the existing experimental studies and the Samani and Attard (2012) model sets. From this figure, it can be observed that the quality line (black line) is surrounded by the majority of the data points. The Samani and Attard (2012) model has an R^2 value of 0.70, indicating a weak correlation between the predicted and experimental values. Other evaluation indices for the prediction results of the Samani and Attard (2012) model are presented in the same figure. The values of RMSE and MAE are 909.18 kN and 662.19 kN, respectively, indicating poor accuracy of the prediction values. However, the values of AAE and SD are 0.80 and 1.44, respectively, illustrating high dispersion in the estimated values. Consequently, the Samani and Attard (2012) offers a performance similar to the other previously evaluated models, except for the Tobbi et *al.* (2012) model.

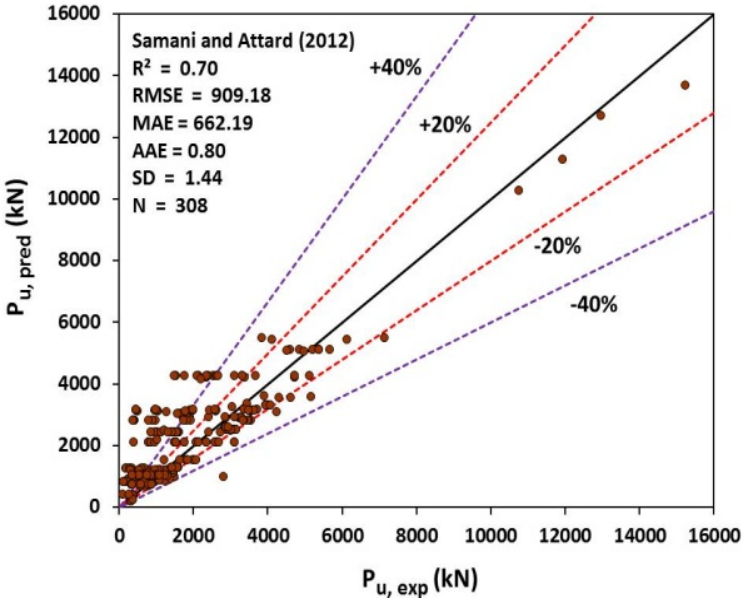

Figure III.10: Assessment results of Samani and Attard (2012) model of FRP-RC compressive members.

III.4.8. Afifi et *al.* model

The assessment of the predicted axial capacity values of the Afifi et *al.* (2014a) model, based on the verification data from the developed test dataset, is shown in Figure III.11. This figure illustrates that the correlation (R^2) between the calculated results and the test results is 0.63, with an RMSE of 1128.73 kN, MAE of 754.62 kN, AAE of 1.00, and SD of 1.74. The empirical prediction points can be evenly arranged in the upper part of the ideal line. These statistical indicators indicate that the Afifi et *al.* (2014a) model has a lower R^2 value, suggesting that it cannot adequately account for data variance, The RMSE and MAE values indicate poor prediction accuracy, while the AAE and SD values suggest satisfactory dispersion. In summary, the model proposed by Afifi et *al.* (2014a) exhibits poor performance compared to all other models previously studied.

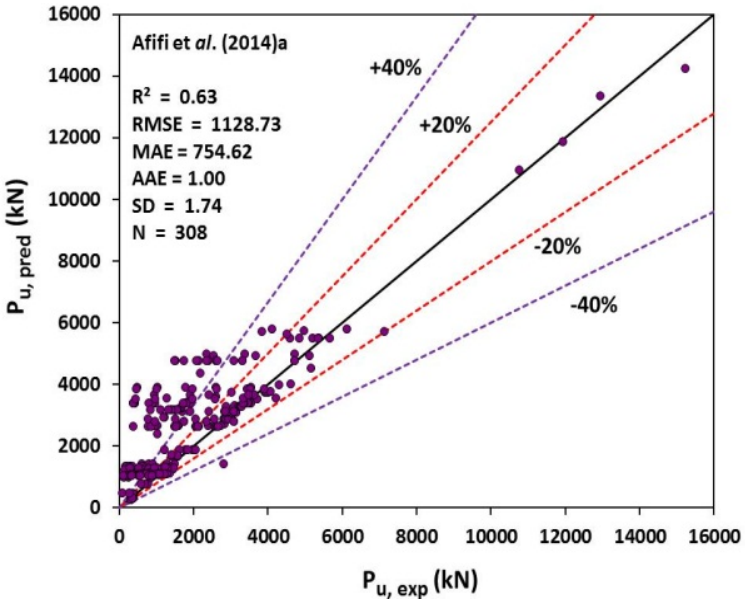

Figure III.11: Assessment results of Afifi et *al*. (2014a) model of FRP-RC compressive members.

III.4.9. Afifi et *al*. model

Figure III.12 illustrates the evaluation results of the axial capacity model developed by Afifi et *al.* (2014b) against the 308 test results collected from the literature and reported in Appendix A. According to this figure, it can be observed that this model provides relatively similar statistical index values as the Afifi et *al.* (2014a) model. Consequently, the performance of the Afifi et *al.* (2014b) model is also poor compared to all other models.

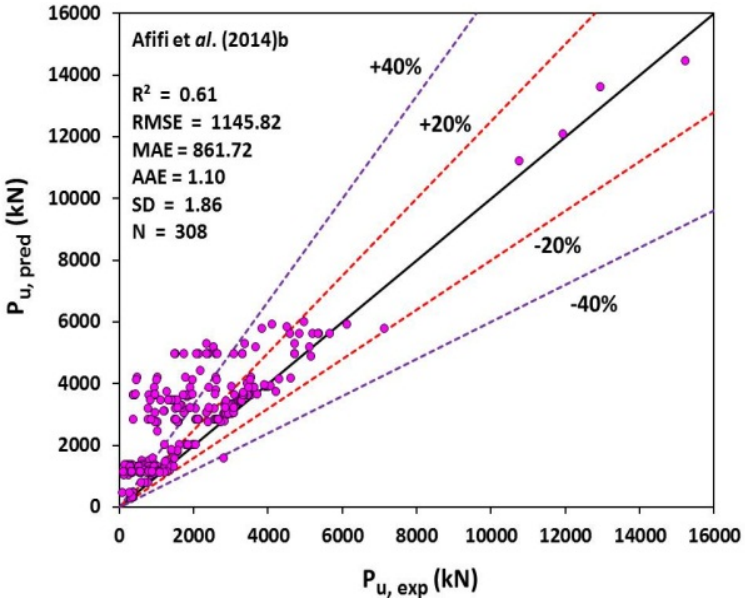

Figure III.12: Assessment results of Afifi et *al*. (2014b) model of FRP-RC compressive members.

III.4.10. Tobbi et *al*. model

To assess the performance of the proposed axial capacity model by Tobbi et *al*. (2014) and to verify the accuracy of this model in predicting test results, the statistical index values are shown in Figure III.13. In this figure, the more the predicted points by this model are located above the diagonal 45° line, and $R^2 = 0.70$, which demonstrates a poor correlation between the predicted and test results. On the other hand, there is a high percentage of data points in the low range of error (0-40%) with RMSE = 909.19 kN and MAE = 662.19 kN, confirming low accuracy. In the same figure, the values of AAE and SD are 0.80 and 1.44, respectively, demonstrating that prediction values have high dispersion. These observations indicate better performance of this model compared to the other models previously evaluated, except for the models of ACI 440.1R-15, AS-3600, CSA S806-02, CSA S806-12, and Samani and Attard. (2012). These models show relatively similar predictions compared to the Tobbi et *al*. (2014) model.

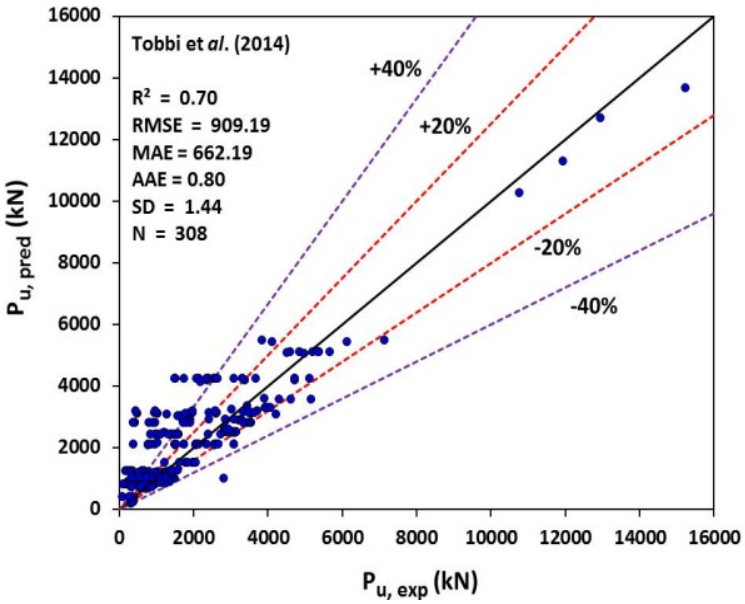

Figure III.13: Assessment results of Tobbi et *al*. (2014) model of FRP-RC compressive members.

III.4.11. Maranan et *al*. model

The estimated and experimentally determined axial capacity values are compared in Figure III.14. In this figure, the statistical indicators R^2, RMSE, MAE, AAE, and SD are presented. The deviation values of the predicted values from the proposed model by Maranan et *al*. (2016) from the ideal line are also shown in the same figure. According to Diboune et *al*. (2022), if the linear correlation coefficient is greater than 0.8 and the RMSE, MAE, AAE, and SD are within a desirable range (considering the dispersion of the data points), it can be concluded that the experimental and predicted values are highly dependent. Regarding Figure III.14, it can be observed that the developed model has a correlation coefficient $R^2 = 0.70$.

Additionally, based on the same figure, it can be seen that the error values obtained from the proposed model by Maranan et *al*. (2016) are RMSE = 974.97 kN, MAE = 677.80 kN, AAE = 0.86, and SD = 1.53. These statistical indicators demonstrate that this model has low accuracy and high dispersion of the estimation values. In summary, this model provides similar observations as the Tobbi et *al*. (2014) model.

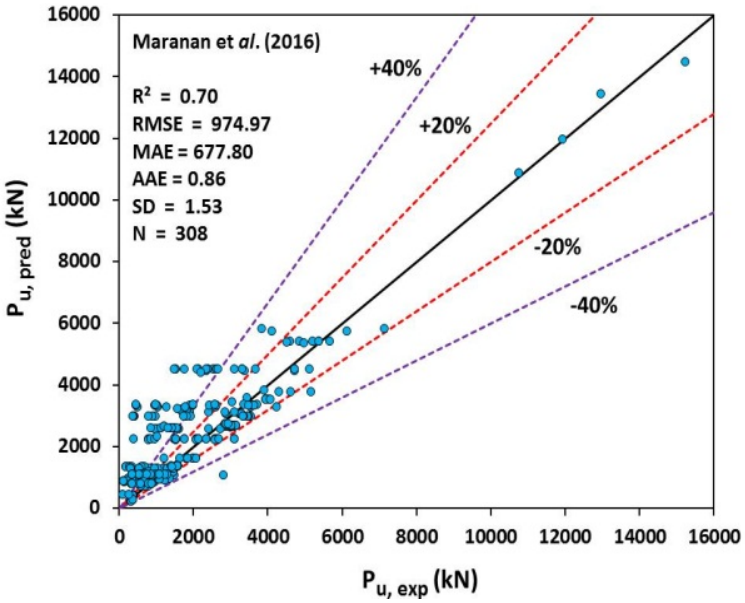

Figure III.14: Assessment results of Maranan et *al*. (2016) model of FRP-RC compressive members.

III.4.12. Khan et *al*. model

Figure III.15 compares the predicted axial capacity values using the expression by Khan et *al*. (2016) with the developed 308 test results reported in Appendix A, where $P_{(u,pred)}$ represents the predicted values and $P_{(u,exp)}$ represents the experimental values. As evident from the model evaluation results, the R^2 of the model developed by Khan et *al*. (2016) is 0.70, which is far from 1 and smaller than 0.8. This indicates a poor correlation between the predicted and experimental values. The RMSE and MAE values of Khan et *al*. (2016) model are 925.94 kN and 662.47 kN, respectively, with the majority of data points located in the error range of 0-40%. This suggests low accuracy. Additionally, the AAE and SD of this model are 0.83 and 1.48, respectively. These indicators show a high dispersion of the data points. Consequently, the observations from the assessment of this model are similar to the observations of the previous models studied in this section, except for the Tobbi et *al*. (2012) model, Afifi et *al*. (2014a) and (2014b) models.

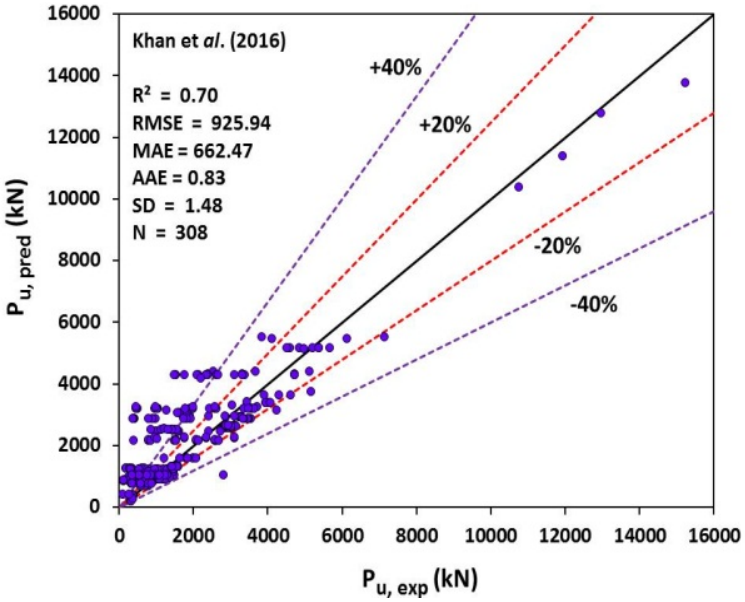

Figure III.15: Assessment results of Khan et *al*. (2016) model of FRP-RC compressive members.

III.4.13. Hadhood et *al*. model

The statistical evaluation of the Hadhood et *al*. (2017) model is conducted using the collected dataset. The results obtained are depicted in Figure III.16. According to this figure, the value of $R^2 = 0.34$, indicates a poor correlation between the estimated and test values. This observation is clearly illustrated by the distribution of the majority of the data points below the diagonal 45° line. Additionally, the RMSE and MAE provide high values of 1380.89 kN and 960.00 kN, respectively, confirming the low accuracy of this model in predicting the experimental values. Moreover, this model exhibits a random scatter of points below the 45° diagonal and outside the upper limit line of 40%. This observation can be explained by the high values of AAE = 1.00 and SD = 1.70. The statistical indices indicate the weak performance of this model, which remains significantly lower compared to all other models.

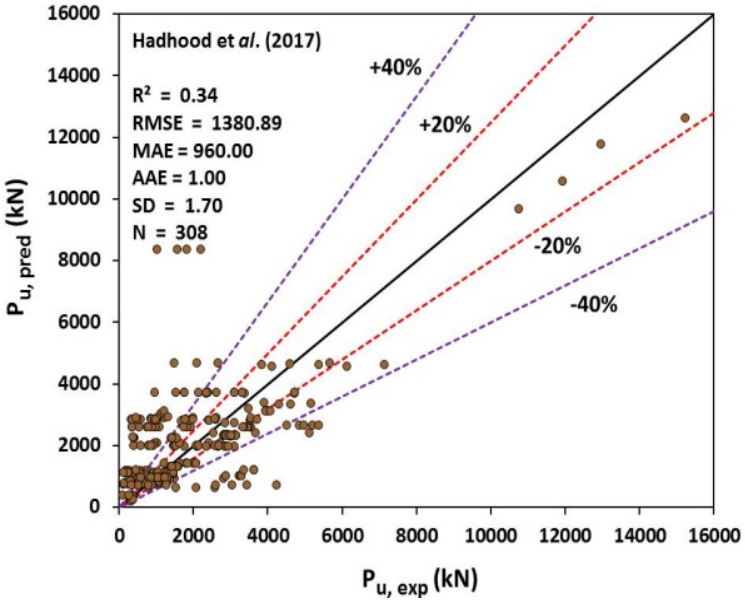

Figure III.16: Assessment results of Hadhood et *al*. (2017) model of FRP-RC compressive members.

III.4.14. Mohammed et *al*. model

Mohammed et *al*. (2014a) model is evaluated using the developed database. The outcomes are depicted in Figure III.17. According to this figure, the ALCC model's performance yields an R^2 value of 0.70, indicating a weak correlation between predicted and experimental values. This finding is evident from the dispersion of most points over the 45° diagonal. Similarly, the other statistical indices of RMSE = 909.17 kN and MAE = 662.19 kN present very high values; this indicates a poor and random distribution of the model, as indicated by AAE = 0.80 and SD = 1.44. Therefore, the performance of this model remains better than the Tobbi et *al*. (2012), Afifi et *al*. (2014a) and (2014b), Hadhood et *al*. (2017) models, and similar to the others previously mentioned.

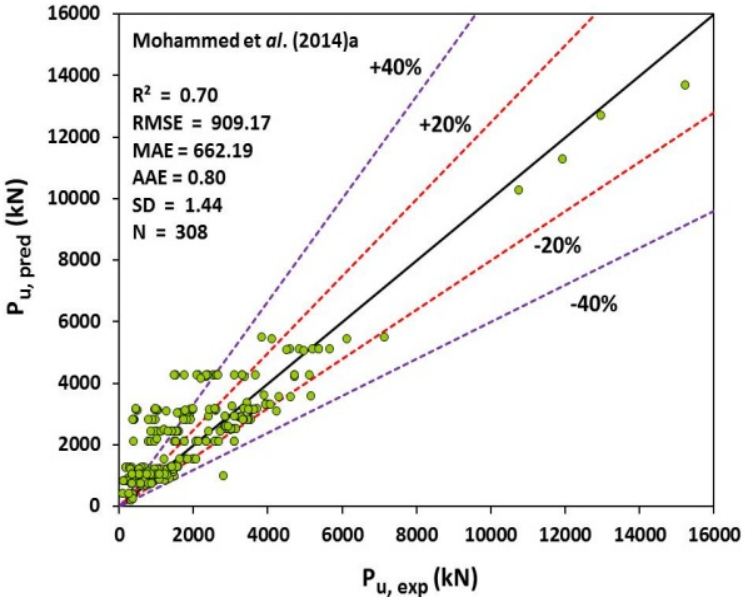

Figure III.17: Assessment results of Mohammed et *al*. (2014a) of FRP-RC compressive members.

III.4.15. Mohammed et *al*. model

Figure III.18 presents the assessment of the axial capacity model developed by Mohammed et *al*. (2014b) using the 308 test results compiled from the literature. From this figure, it can be observed that this model provides relatively similar statistical index values as the Mohammed et *al*. (2014b) model (see Figure III.17). Consequently, we can deduce that the performance of the Afifi et *al*. (2014b) model is also better than the Tobbi et *al*. (2012), Afifi et *al*. (2014a), Afifi et *al*. (2014b) and Hadhood et *al.* (2017) models, and similar to the others previously mentioned.

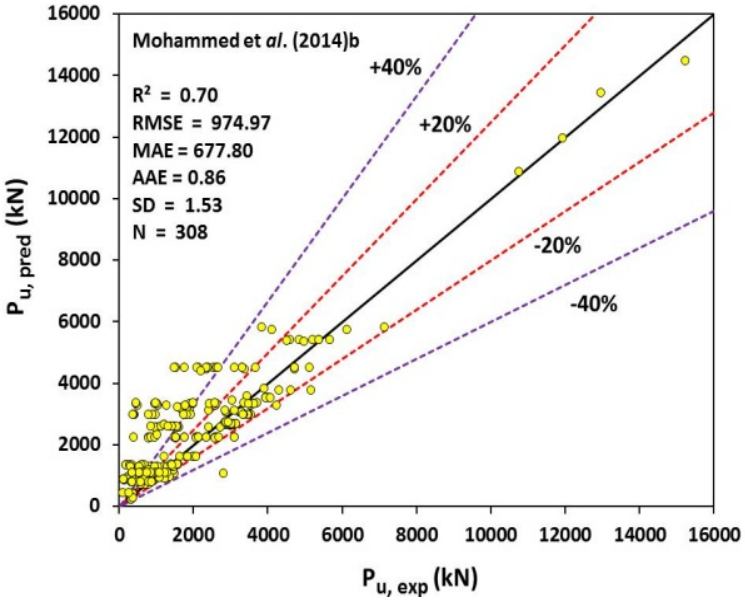

Figure III.18: Assessment results of Mohammed et *al.* (2014b) of FRP-RC compressive members.

III.4.16. Xue et *al.* model

In 2018, Xue et *al*. introduced a novel expression to compute the ALCC of FRP-RC compressive members. This section evaluates the performance of this model using 308 experimental data, as depicted in Figure III.19. The figure indicates an R^2 value of 0.70 alongside higher values of indicators such as RMSE = 909.17 kN, MAE = 652.19 kN, AAE = 0.80, and SD = 1.44. Additionally, the empirical prediction points may display an uneven distribution on both sides of the ideal line. These indices collectively signify the weak performance of this model, which aligns closely with the performance observed in all ALCC models assessed previously, except for the Tobbi et *al*. (2012), Afifi et *al*. (2014) a and b and Hadhood et *al*. (2017) models.

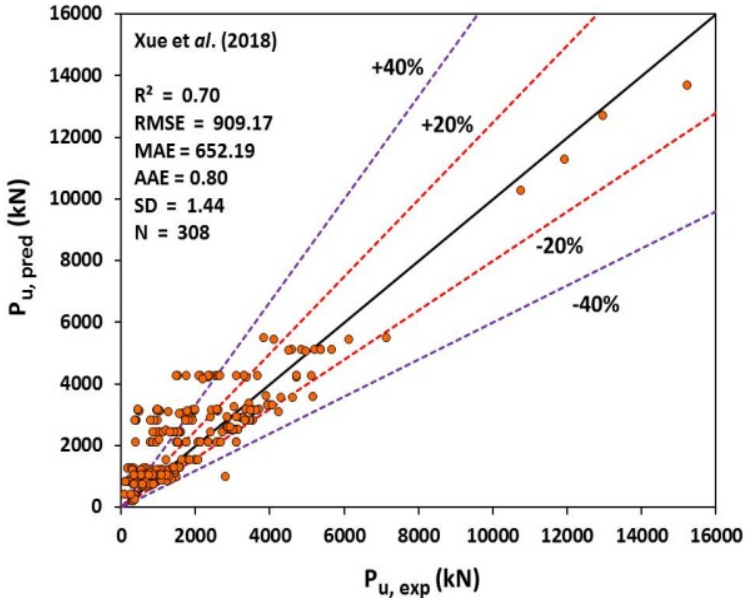

Figure III.19: Assessment results of Xue et *al*. (2018) model of FRP-RC compressive members.

From this section, it can be concluded that all 15 existing models predict the ALCC of FRP-RC compressive members significantly higher compared to that of tests. In other words, the previous models predict the ALCC of FRP- RC compressive members more conservatively. Moreover, the results obtained from these models have a large Scattering with small values of R^2 ranging from 0.34 to 0.70 and low accuracy with high values of errors. This discrepancy is likely due to the effects of eccentricity was not considered in the published formulas.

III.5. DEVELOPING THE NEW PREDICTIVE AXIAL LOAD-CARRYING CAPACITY MODELS

III.5.1. Confinement mechanism of FRP-RC columns

The transverse confinement stress (f_l) which is uniform throughout the external surface of the samples due to continuous confinement, delivered by the lateral ties or spirals is enhanced proportionately with the hoop rupture strain till damage of ties or spirals. Figure III.20 shows the confinement stress derived by considering the mechanism of the lateral confinement of FRPs. Thus, the confinement stress (f_l) can be expressed by Eq. (III.21).

$$f_l = \frac{2A_{sp}f_{sp}}{sd_c} \tag{III.21}$$

Where A_{sp} is the cross-sectional area of GFRP spirals, f_{sp} is the ultimate strength of FRP spirals, d_c is the diameter of concrete core confined with FRP spirals, and 's' is the center to center spacing of FRP spirals.

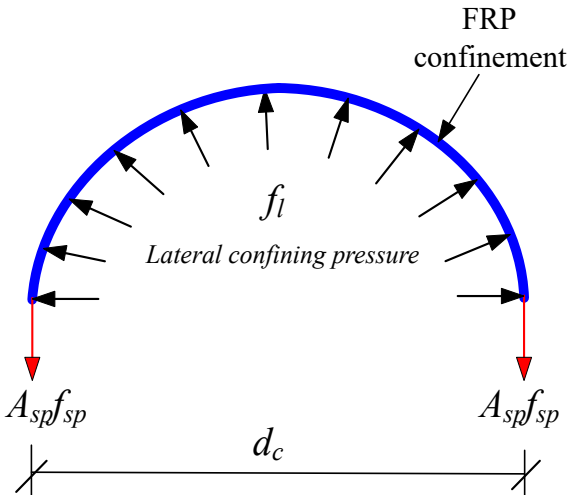

Figure III.20: Lateral stress due to FRP-transverse reinforcement.

The FRP spirals or ties provide non-uniform lateral confinement along with the height of the columns like FRP spiral strip-confinement or FRP ring-confinement for the concrete columns acting as an arching effect along the longitudinal axis of the members. Figure III.21 shows the arching action along with the height of the columns. The parameter f_l due to lateral confinement of FRP ties or spirals can be specified for the effective region of the core only dividing the whole core material into two different areas; first is the effectively confined area and the second is ineffective confined area. The slope of the curve for the arching effect of the effectively confined area of the core is usually taken as 45° from the horizontal axis as shown in Figure III.21 (Mander et *al.* 1988, Sheikh and Uzumeri 1980). The lateral arching mechanism lies between the successive turns of the FRP spirals or ties defining a new

coefficient known as the effective coefficient (k_v) that can be described as the ratio of effective confinement area (A_c) to the ineffective confinement area between the FRP spirals or ties (A_{cc}). The relationships for the coefficient k_v and areas A_c and A_{cc} are represented by Eqs. (III.22-III.24), respectively.

$$k_v = \frac{A_e}{A_{cc}} = \begin{cases} \left(1 - \frac{s'}{2d_c}\right)^2 \Big/ (1 - \rho_{cc}) & ; \text{ for tied column} \\ \left(1 - \frac{s'}{2d_c}\right) \Big/ (1 - \rho_{cc}) & ; \text{ for spiral column} \end{cases} \quad \text{(III.22)}$$

$$A_c = \begin{cases} \frac{\pi}{4}\left(d_c - \frac{s'}{2}\right)^2 = \frac{\pi}{4} d_c^2 \left(1 - \frac{s'}{2d_c}\right)^2 & ; \text{ for tied column} \\ \frac{\pi}{4}\left(d_c - \frac{s'}{2}\right)^2 = \frac{\pi}{4} d_c^2 \left\{1 - \frac{s'}{2d_c} + \left(\frac{s'}{4d_c}\right)^2\right\} \approx \frac{\pi}{4} d_c^2 \left(1 - \frac{s'}{2d_c}\right) & ; \text{ for spiral column} \end{cases} \quad \text{(III.23)}$$

$$A_{cc} = \frac{\pi}{4} d_c^2 (1 - \rho_{cc}) \quad \text{(III.24)}$$

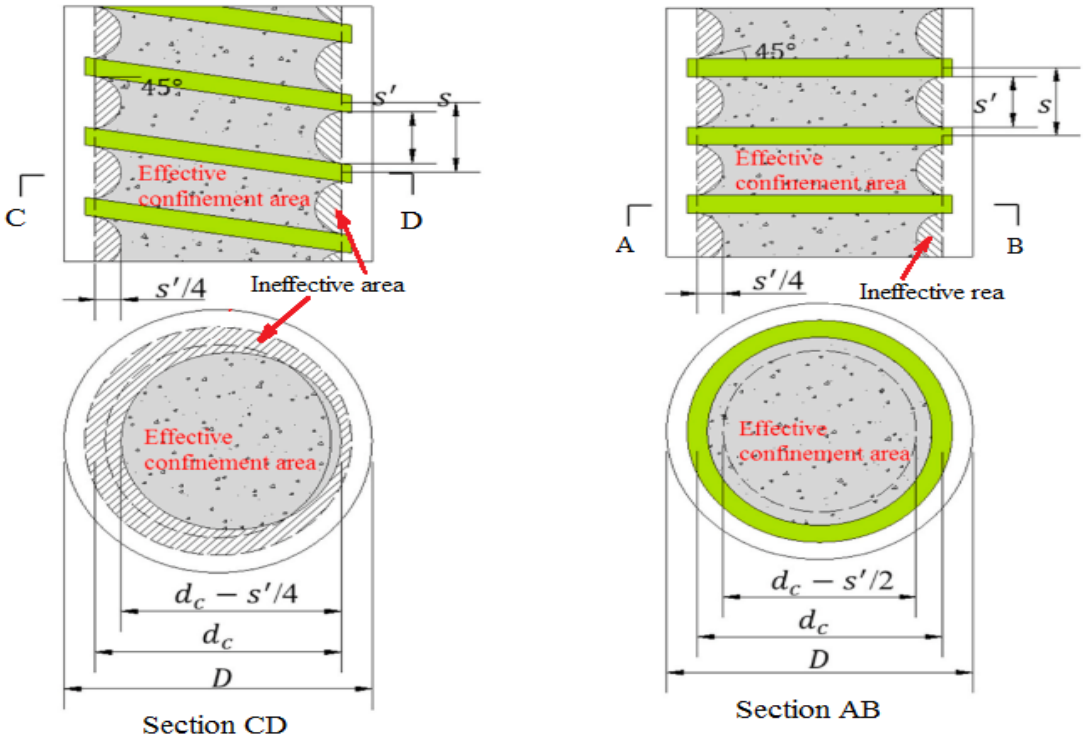

(a) (b)

Figure III.21: Arching effect of lateral FRP-reinforcement (a) spiral column (b) tied column (Berradia et *al.* 2023).

III.5.2. Developing the predictive model using general regression analysis

This research primarily concentrates on formulating an empirical model to predict the ultimate axial capacity of FRP-RC compressive members under concentric and eccentric compression loads. Prior research has introduced several models for predicting the peak axial load-carrying capacity (ALCC) of FRP-RC compressive members. It's noteworthy that the concrete contribution to the empirically determined ALCC of FRP-RC compressive members remains consistent across all the proposed formulas. In essence, the variations in the empirically determined values of P_u for FRP-RC compressive members primarily stem from the differing concepts used in the various formulations to evaluate the contribution of FRP main bars. Among these models, fifteen formulations were taken from the literature and reported in Table III.1. For example, ACI 440.1R-15 provided no recommendations for the contribution of longitudinal FRP bars. The CSA S806-12 allows for the longitudinal reinforcement of concrete compressive members with FRP bars. However, it recommends ignoring the influence of the FRP bars when capturing the peak ALCC of FRP-RC compressive members. Nevertheless, numerous research studies have found that neglecting the contribution of FRP main bars in compression could lead to a significant disparity between the empirically calculated ALCC and the experimentally obtained one for FRP-RC compressive members (Tobbi et *al*. 2012, Afifi et *al*. 2014 and Hadi et *al*. 2016). Thus, several researchers suggested including the contribution of FRP main bars in the peak axial capacity of FRP-RC compressive members through different methods. One method is to obtain the stress in the FRP bars by assuming a linear stress-strain relationship (that is $\sigma_{frp} = E_{frp} \times \varepsilon_{frp}$). Maranan et *al*. (2016) Eq. (III.9), Xue et *al*. (2018) Eq. (III.10), and Mohammed et *al*. (2014) (a and b) Eq. (III.11 and III.12), Samani and Attard (2012) Eq. (III.13), and Hadhood et *al.* (2017) Eq. (III.15) have been estimated the axial load supported by FRP main bars based on the axial strain (ε_{frp}) in the FRP bars as well as their stiffness (E_{frp}), given by $\varepsilon_{frp}\ E_{frp}\ A_{frp}$. However, Maranan et *al*. (2016), Xue et *al*. (2018), Mohammed et *al*. (2014) (a and b) suggested taking $\varepsilon_{frp} = 0.002$, Samani and Attard (2012) recommended taking $\varepsilon_{frp} = 0.0025$, and Hadhood et *al*. (2017) suggested taking $\varepsilon_{frp} = 0.0035$. Whereas, other researchers such as Tobbi et *al*. (2012) Eq. (III.5), Afifi et *al*. (2014a), and Afifi et *al*. (2014b) Eq. (III.7 and III.8) have considered the contribution of FRP main bars by adding the axial load supported by FRP main bars, given by $\alpha_{frp}\ f_{frp}\ A_{frp}$, where f_{frp} is the tensile strength of the FRP bars, and α_{frp} is the reduction factor that shows the ratio between the strength of the FRP bar under compression and the tension strength of the FRP bars. Tobbi et *al*. (2012) and Afifi et *al*. (2014b) suggested taking $\alpha_{frp} = 0.35$, and Afifi et *al*. (2014a) recommended taking $\alpha_{frp} = 0.25$. It should be noted that several research studies have proposed different models for the ALCC, all based on a limited set of test data. Consequently, there is no consensus among previous research studies regarding a unified model to predict the ultimate ALCC of FRP-RC compressive members. This diversity can also be attributed to variations observed in the response of FRP bars when subjected to axial

compression. On the other hand, no model exists in the literature to capture the axial capacity of FRP-RC compressive members under both concentric and eccentric compression loads. In this section, a new and simple model was developed to estimate the peak ALCC of FRP-RC compressive members based on regression analysis. Considering that the confinement effect of internal FRP bars on core concrete varies under different core concrete strengths, section forms, restraint levels, and concentric and eccentric compression loads (Ma et *al*. 2022). This method was employed to simulate the relationship between the input parameters (independent variables) and the output parameter (ALCC of FRP-RC compressive members), which is the dependent variable. It should be noted that linear regression is one of the most commonly used equations in statistical procedures. In this context, the general form of linear regression that can be used to fit the independent and dependent variables is expressed as follows:

$$\boldsymbol{Y = a_o + a_1 X_1 + a_2 X_2 + a_3 X_3 + \cdots + a_n X_n} \quad \text{(III.25)}$$

Or,

$$\boldsymbol{Y = a_o + aX} \quad \text{(III.26)}$$

Where Y is the output parameter (i,e., the dependent variable), X_1, X_2, X_3, ... X_n are the input parameters (i,e., independent variables), a_o and a are the regression coefficients (Berradia et *al*. 2021, Berradia et *al*. 2022 and Berradia et *al*. 2023).

Where $a = [a_1\ a_2\ a_3\ \ldots . a_n]$

Microsoft Office Excel (Version 10) was used to propose the new expression. To assess the optimal model, five performance indices, which include goodness of fit (R^2), root mean square error (RMSE), mean absolute error (MAE), Average absolute error (AAE), and standard deviation (SD), were used to measure the accuracy of the predictive model, as was done to evaluate the fifteen existing models. The expressions of these indicators are given by Eqs. (III.16-III.20).

The general form of the developed ALCC model was expressed by the following expression:

$$\boldsymbol{P_u = \alpha f'_c (A_g - A_{frp}) + \varepsilon_{reg} E_{frp} A_{frp}} \quad \text{(III.27)}$$

Where α is the reduction factor indicating the ratio between the strength of the FRP bar under compression and the tension strength of the FRP bas, ε_{reg} represents the axial strain in the FRP bar, A_g is the area of cross-section, A_{frp} is the cross-sectional area of the FRP reinforcing bar.

A regression analysis has been conducted based on the available experimental data with eccentricity equal to 0, reported in Table III.2 to obtain the reduction factor α and the optimal strain value ε_{reg} for the use in Eq. (III.27)

The regression analysis yielded α and β values of 0.85 and 0.0037, respectively. These values were used in Eq. (III.27) to calculate the carrying capacity of FRP-reinforced concrete compressive members under concentric compression loads. The final formula is expressed as follows:

$$\boldsymbol{P_u = 0.85 f'_c (A_g - A_{frp}) + 0.0037 E_{frp} A_{frp}} \quad \text{(III.28)}$$

In this second part, the peak axial capacity was calculated for FRP-reinforced concrete compressive members at different eccentricity levels based on regression analysis. The calculation was applied on 294 FRP-RC compressive member samples reported in Table III.2 (14 FRP-RC compressive member samples were ignored). For this calculation, the Eq. (III.28) developed for the concentric compressive member was adopted.

According to Mahmoudabad et *al*. (2024) work, the increment in the eccentricity value reasonably decreased the axial capacity of the samples. For this reason, the proposed unified expression (model II) for calculating the peak axial capacity of FRP-RC compressive members at different eccentricity levels is formulated as follows:

$$\boldsymbol{P_u = 0.85 f'_c (A_g - A_{frp}) + 0.0037 E_{frp} A_{frp} - \gamma (e/h) \times \delta \times n} \quad \text{(III.29)}$$

Where $(e\ /\ h)$ is the eccentricity-sample dimension ratio and n is the number of FRP bars.

Through regression analysis of the experimental data with eccentricity-sample dimension ratio (e/h) ranges from 0 to 1, reported in Table III.2, the coefficient γ and δ values were obtained.

The final expression for calculating the peak axial capacity of FRP-reinforced concrete compressive members at different eccentricity levels is expressed as follows:

$$\boldsymbol{P_u = 0.85 f'_c (A_g - A_{frp}) + 0.0037 E_{frp} A_{frp} - 5,022 (e/h) \times 100 \times n} \quad \text{(III.30)}$$

Figure III.22 compares the predicted values of the peak axial capacity of FRP-RC samples with $(e/h\ =\ 0)$ and FRP-RC samples with (e/h) ranges from 0 to 1 obtained by Eq. (III.28) and Eq. (III.30), respectively, and the experimental values. From this figure, it can be seen that the equality line (black line) is surrounded by most of the data points. The model I has R^2 = 0.97, RMSE = 387.27 kN, MAE = 214.20 kN, AAE = 0.10, and SD = 0.15 and the model II has R^2 = 0.88, RMSE = 635.75 kN, MAE = 405.08 kN, AAE = 0.31, and SD = 0.52. These indicator values show that the predicted value of the carrying capacity of the compressive

members is in good agreement with the experimental value, which indicates that the models of carrying capacity proposed in this work have good predictability.

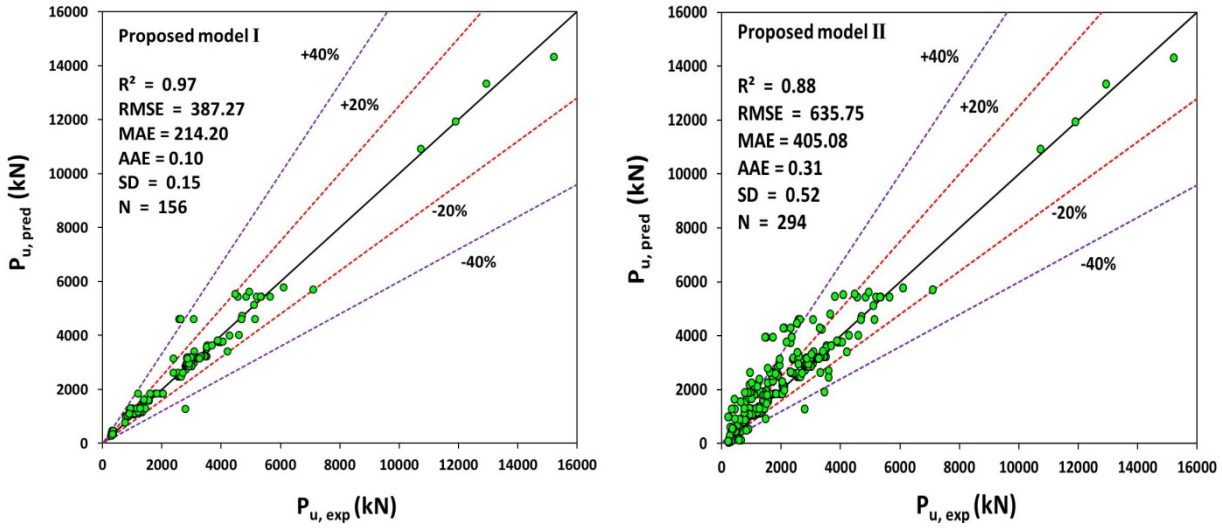

a- Sample with $(e/h = 0)$ Sample with (e/h) ranges from 0 to 1

Figure III.22: Comparison between the predicted value and the experimental value of the carrying capacity of samples.

III.5.3. Developing the predictive model using eXtreme Gradient Boosting approach

III.5.3.1. Description of the eXtreme Gradient Boosting approach

XGBoost, short for eXtreme Gradient Boosting, is an ensemble machine-learning algorithm rooted in decision trees, essentially a composite predictor formed from numerous smaller predictors (Chen and Guestrin 2016). XGBoost consists of a collection of classification and regression trees, representing one of the most advanced and effective machine learning techniques developed in recent years. XGBoost constructs a sequential sequence of weak learners, with each learner trying to complement the others and correct any errors in the predictions made by preceding learners. XGBoost can manage missing data and utilizes regularization techniques to mitigate overfitting in individual predictors. It boasts a speedy implementation and achieves cutting-edge accuracy in both regression and classification tasks. Ultimately, XGBoost proves to be a potent approach for modeling nonlinear relationships (Bakouregui et *al*. 2021). The mathematical development model of XGBoost is shown as follows.

XGBoost represents an advanced enhancement of Friedman's original gradient-boosted trees model Friedman (2001). It employs an additive approach, wherein, for a dataset with *n* samples and *m* features denoted as $\boldsymbol{D} = \{(\boldsymbol{X_i},\ \boldsymbol{Y_i})\}$, the prediction is expressed as follows:

$$\widehat{\boldsymbol{y}}_{\boldsymbol{i}} = \sum_{\boldsymbol{k=1}}^{\boldsymbol{k}} \boldsymbol{f_k}\,(\boldsymbol{X_i}), \boldsymbol{f_k} \in \boldsymbol{F} \qquad \text{(III.31)}$$

Where *F* is the space of the regression tree, given by the following expression:

$$\boldsymbol{F = \{f(X) = w_q(x)\}} \tag{III.32}$$

and $\boldsymbol{k}$ is the number of trees, Each $\boldsymbol{f_k}$ corresponds to an independent tree structure $\boldsymbol{q}$ and leaf weights $\boldsymbol{w}$.

The aim formulation is

$$\boldsymbol{L = \sum_i l(\hat{y}_i, y_i) + \sum_k \Omega(f_k)} \tag{III.33}$$

The prediction of the $\boldsymbol{i-th}$ instance at the $\boldsymbol{t-th}$ iteration is

$$\boldsymbol{\hat{y}_i^{(t)} = \hat{y}_{i-1}^{(t-1)} + f_l(X_i)} \tag{III.34}$$

Therefore, the aim formulation can be expressed as follows:

$$\boldsymbol{L^{(t)} = \sum_{i=1}^{n} l\left(y_i, \hat{y}_i^{(t-1)} + f_t(X_i)\right) + \Omega(f_k)} \tag{III.35}$$

Where

$$\boldsymbol{\Omega(f_k) = \gamma T + \frac{1}{2}\lambda \sum_{j=1}^{T} w_j^2} \tag{III.36}$$

XGBoost utilyzes second-order Taylor approximation to optimize the aim formulation:

$$\boldsymbol{L^{(t)} \simeq \sum_{i=1}^{n}\left[l\left(y_i, \hat{y}_i^{(t-1)} + g_i f_t(X_i) + \frac{1}{2}h_i f_t^2(X_i)\right)\right] + \Omega(f_k)} \tag{III.37}$$

Where

$$\boldsymbol{g_i = \frac{\partial l\left(y_i, \hat{y}_i^{(t-1)}\right)}{\partial \hat{y}_i^{(t-1)}}} \tag{III.38}$$

And

$$\boldsymbol{h_i = \frac{\partial^2 l\left(y_i, \hat{y}_i^{(t-1)}\right)}{\partial \hat{y}_i^{(t-1)}}} \tag{III.39}$$

The final aim formulation is given as follows:

$$\boldsymbol{\tilde{L}^{(t)} = \sum_{i=1}^{n}\left[\left(g_i f_t(X_i) + \frac{1}{2}h_i f_t^2(X_i)\right)\right] + \gamma T + \frac{1}{2}\lambda \sum_{j=1}^{T} w_j^2} \tag{III.40}$$

$$\tilde{L}^{(t)} = \sum_{j=1}^{T}\left[\left(\sum_{i\in I_j} g_i\right)w_j + \frac{1}{2}\left(\sum_{i\in I_j} h_i + \lambda\right)w_j^2\right] + \gamma T \quad \text{(III.41)}$$

The optimal weight w_j^* and the corresponding optimal value $\tilde{L}^{(t)}(q)$ leaf *j* are, respectively,

$$w_j^* = -\frac{\sum_{i\in I_j} g_i}{\sum_{i\in I_j} h_i + \lambda} \quad \text{(III.42)}$$

$$\tilde{L}^{(t)}(q) = -\frac{1}{2}\sum_{j=1}^{T}\frac{\left(\sum_{i\in I_j} g_i\right)^2}{\sum_{i\in I_j} h_i + \lambda} + \gamma T \quad \text{(III.43)}$$

It's important to acknowledge that there are numerous programs available for data science and machine learning, with Python emerging as one of the most widely used programming languages. In this study, we employed the Python XGBoost library (Chen and Guestrin 2016) for tasks ranging from data preprocessing to model training and testing. Additionally, all data were initially arranged in Excel format (.xlsx) and subsequently imported and analyzed in Python utilizing the pandas package (Bakouregui et *al*. 2021).

III.5.3.2. Detail of modeling

eXtreme Gradient Boosting (XGBoost) technique was utilized to obtain a meanihful relationship between the axial capacity of FRP-reinforced concrete compressive members and numerical and categorical variables presented in Table III.2. It should be noted that the XGBoost algorithm is suitable for processing numerical values. For this work, categorical independent parameters such as cross-section type of concrete (S_{type}), form of tie bar ($Form$), type of longitudinal FRP reinforcement (l_{type}) and type of transverse FRP reinforcement (t_{type}) were changed into new numerical independent parameters with the one hot encoding process before the start of the training and testing processes.

The XGBoost algorithm's basic model was chosen to be decision trees. The experimental dataset was divided into two groups at random to improve the model's capacity for generalization and reduce frequent problems such as overfitting. The testing group (20% or 61 FRP-RC samples) was set aside to evaluate the performance of the final XGBoost model on unobserved data, whereas the training group (80% or 247 FRP-RC samples) was used for modeling. The XGBoost methodology is shown in Figure III.23.

A statistical evaluation was conducted to assess the performance and agreement of XGBoost model predictions using different statistical indicators such as coefficient of determination (R^2), root mean square error (RMSE), mean absolute error (MAE), average absolute error (AAE), and standard deviation (SD) given by Eqs. (III.16-III.20). Then after,

the best XGBoost model was derived by measuring statistically the goodness of fit and error values.

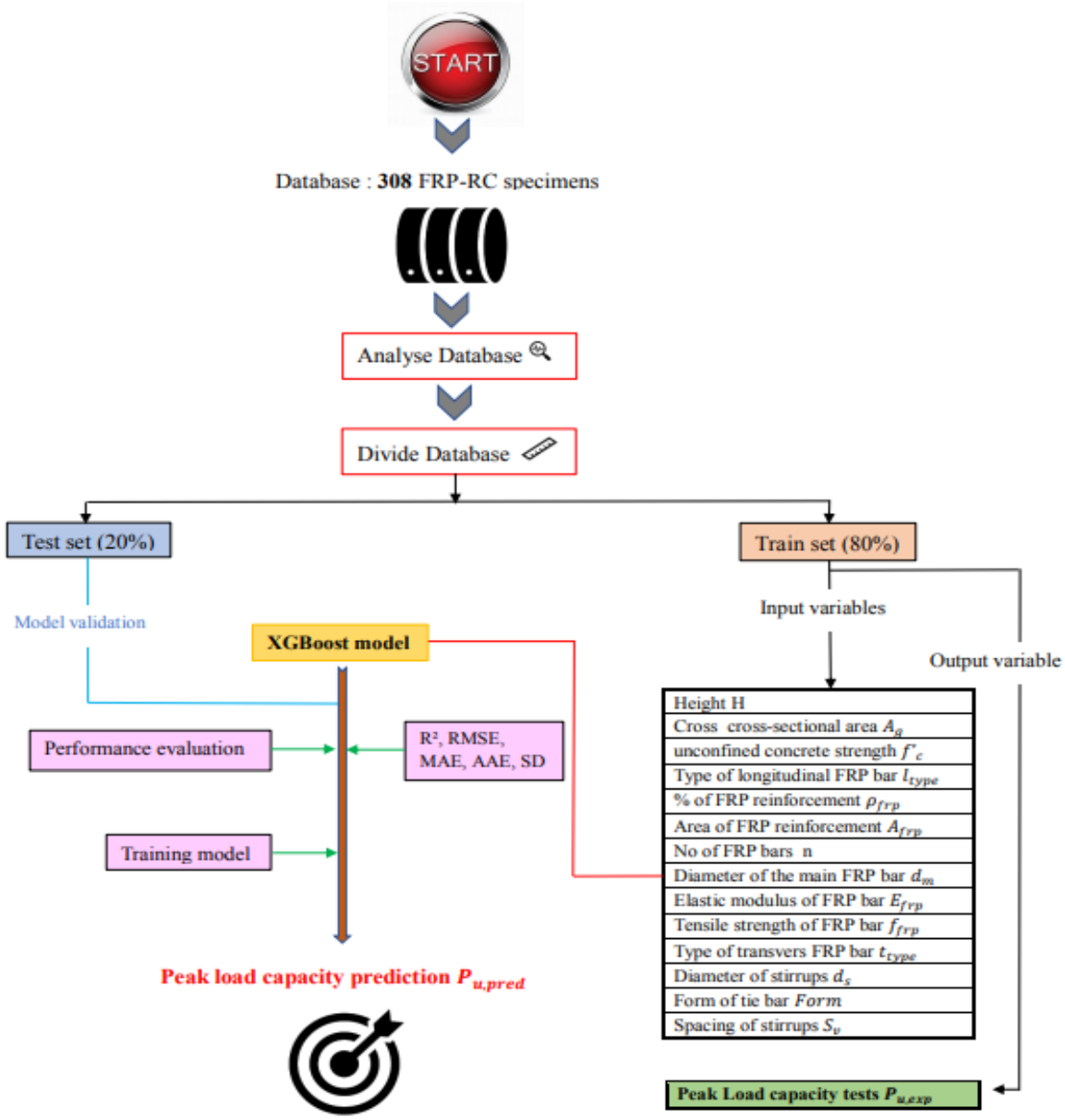

Figure III.23: Flow chart of XGBoost methodology.

III.5.3.3. Discussion of research findings

The regression results for the XGBoost model are illustrated in Figure III.24 and Table III.4. It can be seen from this figure that there is a strong correlation coefficient (R^2) (0.98 for training, 0.96 for testing, and 0.98 for whole) between the calculated and experimental values. In addition, the developed model is accurate enough to predict the axial capacity of FRP-reinforced concrete compressive members at different eccentricity levels. The developed XGBoost model presented the statistical indicators of RMSE = 222.52 kN, MAE =

123.97 kN, AAE = 0.10, SD = 0.13 for the training process, RMSE = 370.01 kN, MAE = 225.26 kN, AAE = 0.14, SD = 0.18 for the testing process, and RMSE = 259.05 kN, MAE = 144.36 kN, AAE = 0.11, SD = 0.14 for the whole datasets, as reported in Table III.4.

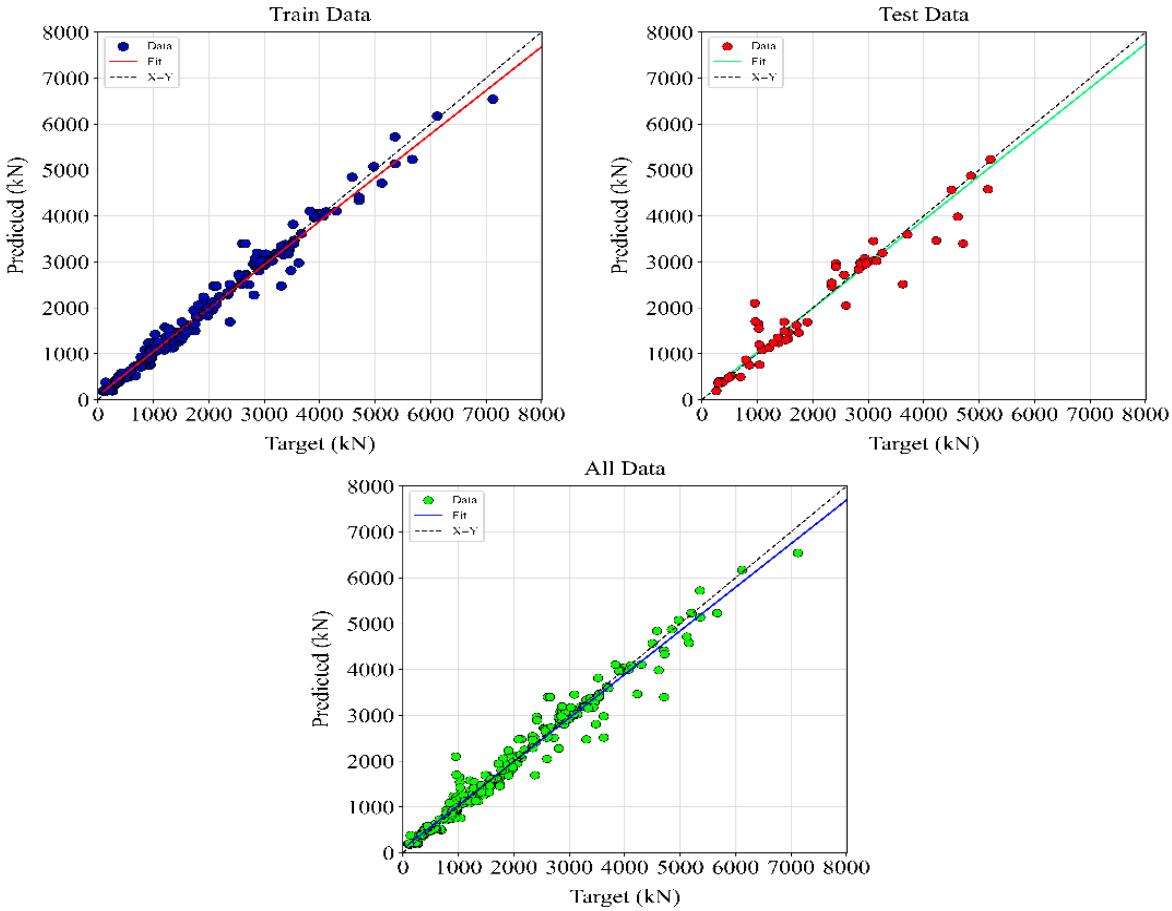

Figure III.24: Grid regression diagram after training.

Table III.4: A summary of performance indicators of the XGBoost algorithm.

Training set		Testing set		All set	
R^2	0.98	R^2	0.96	R^2	0.98
RMSE (kN)	222.52	RMSE (kN)	370.01	RMSE (kN)	259.05
MAE (kN)	123.97	MAE (kN)	225.26	MAE (kN)	144.36
AAE	0.10	AAE	0.14	AAE	0.11
SD	0.13	SD	0.18	SD	0.14

Figures III.25 (a)-(c) compare the predicted values (P_{pred}) of the peak axial capacity of the FRP-RC compressive members obtained by the optimized XGBoost model and experimental values (P_{exp}). As it is presented in these figures, the relative difference between the predicted values (both from training, testing and whole sets) and the experimental values are very small, indicating a perfect agreement. Consequently, the prediction performance of the XGBoost model is excellent.

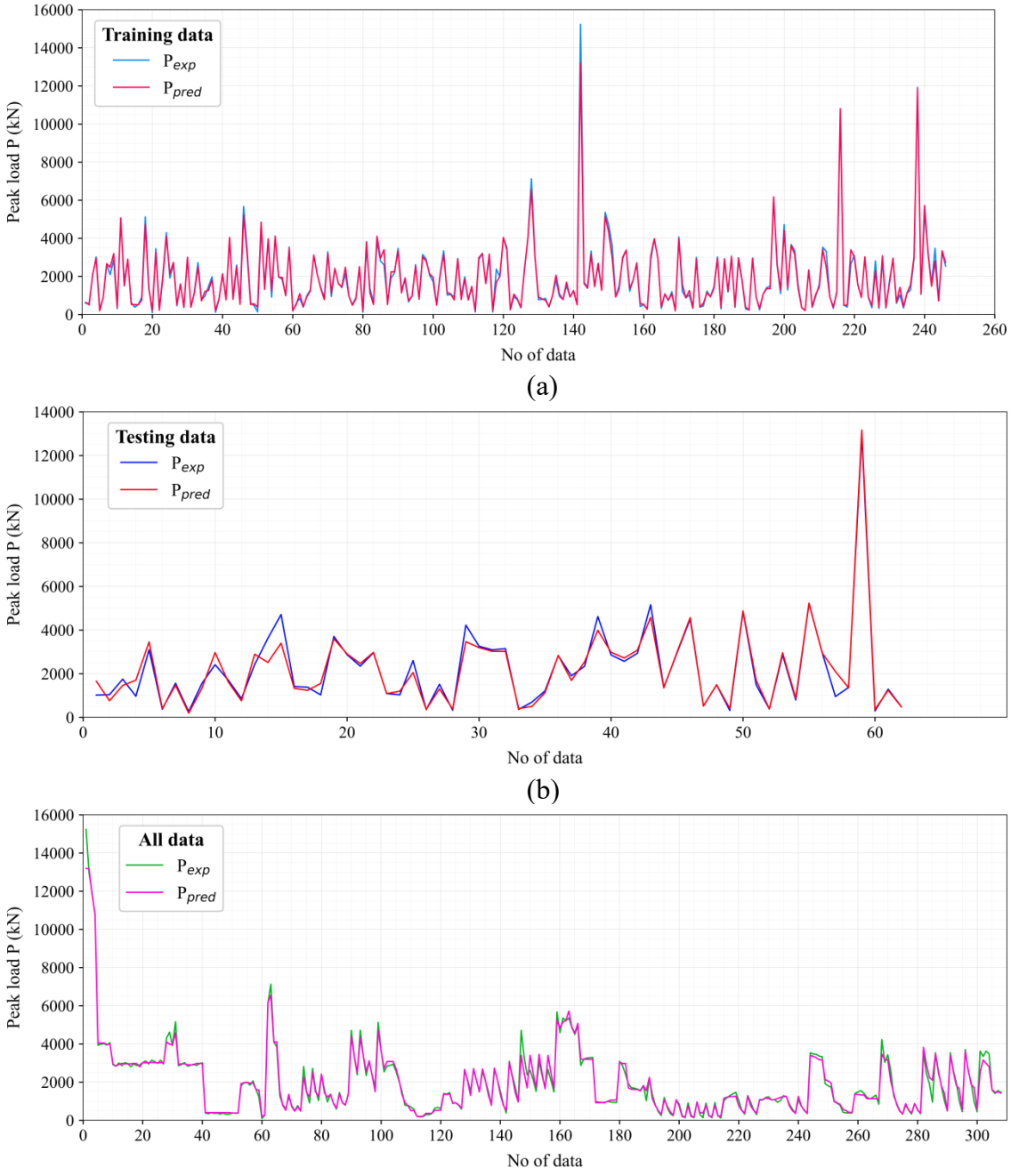

Figure III.25: Comparison between XGBoost predicted value $\boldsymbol{P_{pred}}$ and experimental value $\boldsymbol{P_{exp}}$: (a) training data set, (b) testing data set, and (c) whole data set.

From Figure III.26, the prediction capability of the developed model in terms of the normalized value ($P_{u,pred}/P_{u,exp}$) vs. the experimental axial capacity (($P_{u,\exp}$)) values can be illustrated. A ±20% error band is given in the graphic to show how the model's predictions and the experimental data differ from one another. As a reference point, the normalized value of 1.0 denotes an ideal estimation. The data primarily forms a tight cluster around this ideal line,

indicating a close match between the experimental results and the predictions of the XGBoost model.

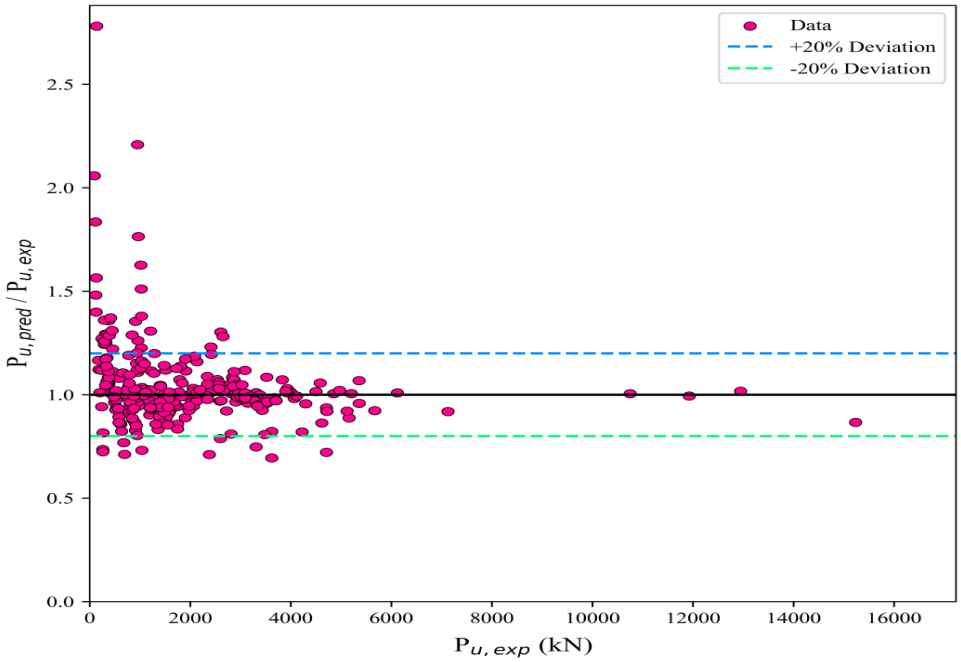

Figure III.26: Prediction capability of the XGBoost model in terms of the normalized value vs. the experimental axial capacity value.

III.5.3.4. Comparison of XGBoost and empirical models with existing models

In Table III.5 and Figures III.27(a)-(e), the performance indicators R^2, RMSE, MAE, AAE, and SD of the models developed in this study and the previous research works (Table III.1) in predicting the peak axial capacity of FRP-reinforced concrete compressive members were compared. Table III.5 and Figure 27a visualizes that the proposed models have a better correlation between the predicted and experimental values (high R^2 values and very close to 1). On contrary, the other models give a low coefficient of determination R^2 values, ranging from 0.34 to 0.71. These findings show that the proposed models offer the best correlation compared to all of the other existing models. Table III.5 and Figure 27(b)-(e) illustrate the comparison between the error values between the proposed models and the fifteen existing models. Form these figures, it can be noted the RMSE values of ACI 440.1R-15, CSA S806-02, CSA S806-12, AS-3600, Tobbi et *al.*(2012), Tobbi et *al.*(2014), Afifi et *al.* (2014a), Afifi et *al.* (2014b), Maranan et *al.* (2016), Xue et *al.* (2018), Mohammed et *al.* (2014a), Mohammed et *al.* (2014b), Samani and Attard (2012), Khan et *al.* (2016), Hadhood et *al.* (2017) models are 909.12 kN, 909.12 kN, 846.58 kN, 909.18 kN, 909.19 kN, 1128.73 kN, 1145.82 kN, 974.97 kN, 909.17 kN, 909.17 kN, 974.97 kN, 909.18 kN, 925.94 kN, 1380.89 kN, respectively, whereas that of whole set of XGBoost and empirical models are only 259.05 kN and 635.75 kN, respectively. Similar to the RMSE results, the proposed models have much lower MAE, AAE and SD values compared to the findings obtained from the other expressions. According to these indicators, it can be noted that the calculated

results of the proposed models have a close agreement with the experimental results, which indicate the better accuracy of the proposed models in the prediction of the axial capacity of FRP bars reinforced concrete compressive members when compared to the existing expressions. Particularly, the XGBoost model exhibited outstanding performance with a high R^2value of 0.98 and minimal RMSE, MAE, AAE, and SD values of 259.05 kN, 144.36 kN, 0.11, and 0.14 respectively, indicating excellent efficiency and accuracy compared to both the empirical model proposed and other existing models. This outcome highlights the ability of machine learning models to estimate the axial capacity of FRP-RC compressive members. Consequently, the XGBoost model offers a viable alternative method to empirical models for design applications.

Table III.5: Performance indicators of existing design formulations.

Model	R^2	RMSE (kN)	MAE (kN)	AAE	SD
XGBoost model proposed	**0.98**	**259.05**	**144.36**	**0.11**	**0.14**
Empirical model proposed	**0.88**	**635.75**	**405.08**	**0.31**	**0.52**
ACI 440.1R-15	0.70	909.12	662.19	0.80	1.44
CSA S806-02	0.70	909.12	662.19	0.80	1.44
CSA S806-12	0.71	846.58	651.92	0.74	1.33
AS-3600	0.70	909.18	662.19	0.80	1.44
Tobbi et *al.* (2012)	0.61	1245.82	861.72	1.10	1.86
Tobbi et *al*. (2014)	0.70	909.19	662.19	0.80	1.44
Afifi et *al*. (2014a)	0.63	1128.73	754.62	1.00	1.74
Afifi et *al.* (2014b)	0.61	1145.82	861.72	1.10	1.86
Maranan et *al*. (2016)	0.70	974.97	677.80	0.86	1.53
Xue et *al*. (2018)	0.70	909.17	652.19	0.80	1.44
Mohammed et *al*. (2014a)	0.70	909.17	662.19	0.80	1.44
Mohammed et *al*. (2014b)	0.70	974.97	677.80	0.86	1.53
Samani and Attard (2012)	0.70	909.18	662.19	0.80	1.44
Khan et *al.* (2016)	0.70	925.94	662.47	0.83	1.48
Hadhood et *al*. (2017)	0.34	1380.89	960.00	1.00	1.70

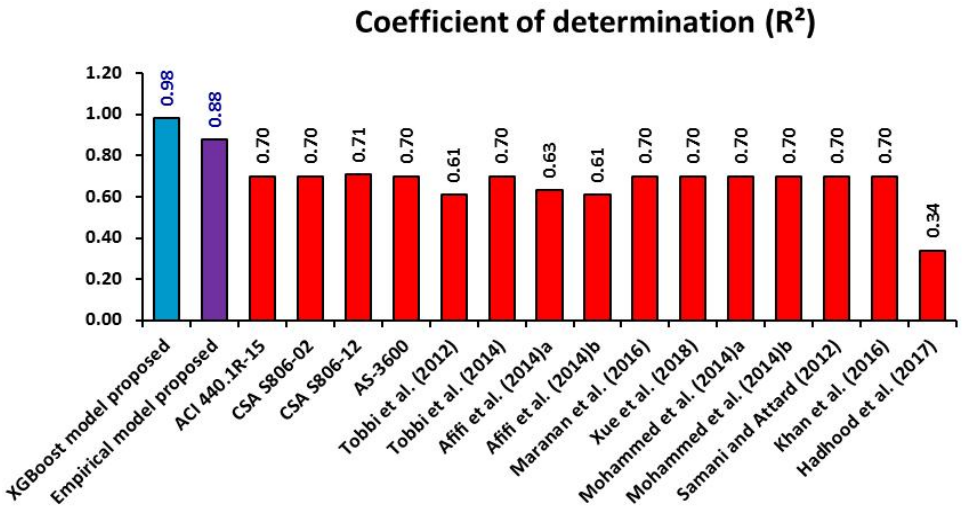

(a)

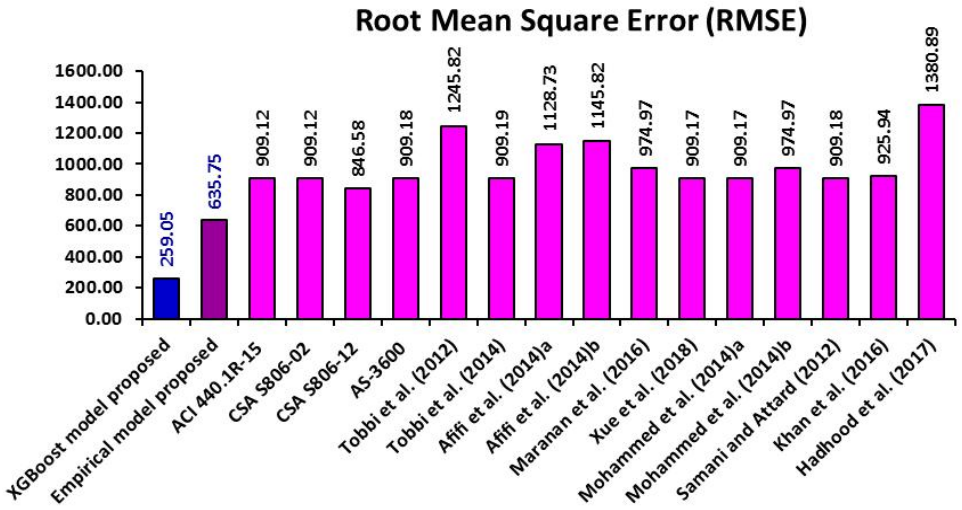

(b)

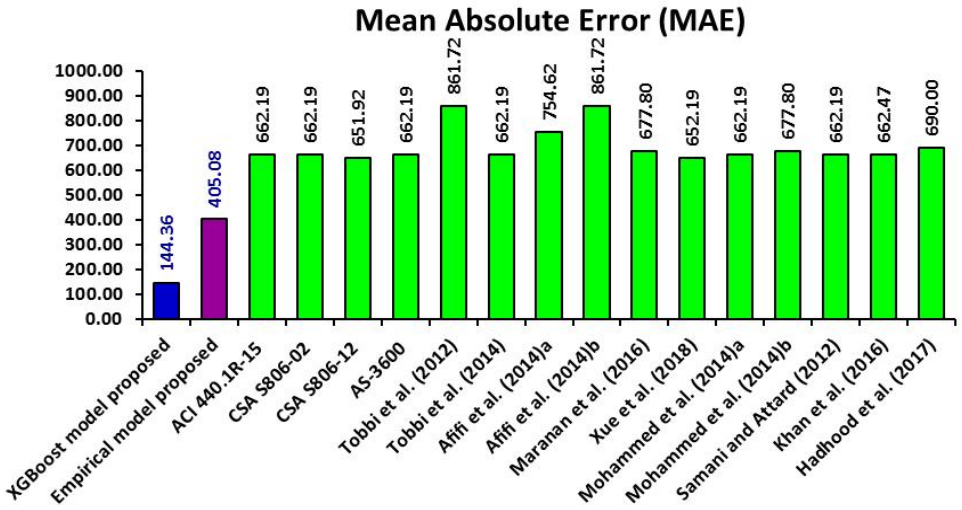

(c)

Figure III.27: *Continued.*

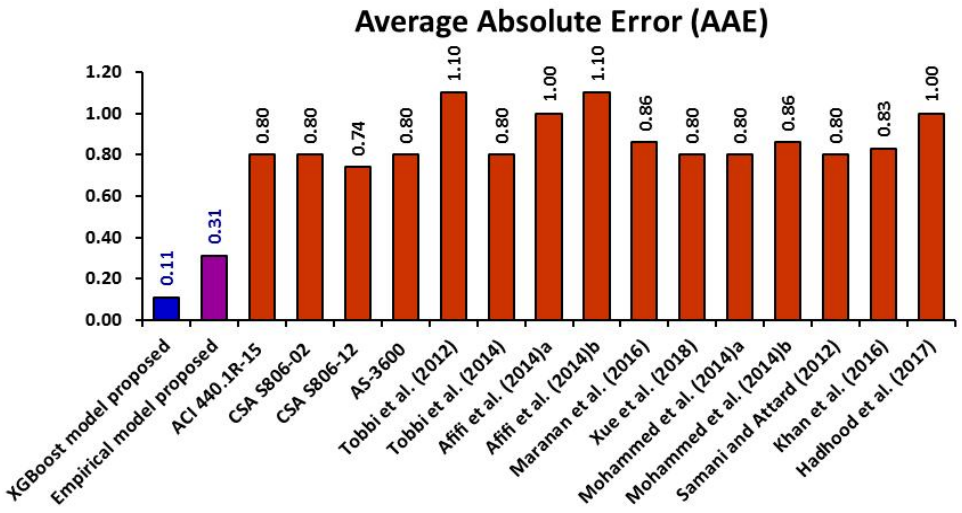

(d)

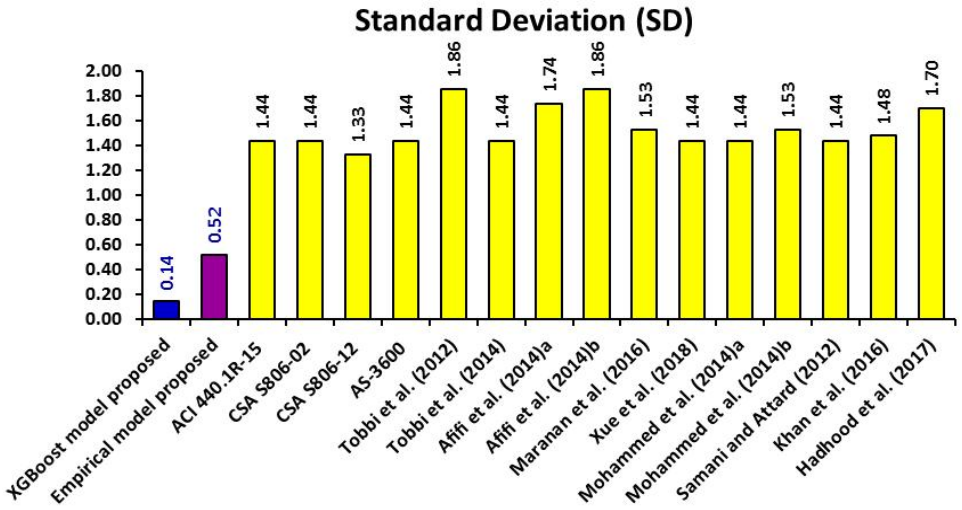

Figure III.27: Comparison of performance indicators of developed and existing models in predicting the ultimate axial capacity of FRP-reinforced concrete compressive members.

III.5.4. Developing the predictive model using random forest (RF) regression

In this section, a machine learning model was employed to predict the axial load-carrying capacity of FRP-reinforced concrete columns, categorized into tree-based models. The tree-based category included the Random Forest (RF) regression (Abda et *al*. 2022, Huang and Hsieh 2020). To identify the accuracy of proposed model for predicting the load-carrying capacity of FRP-reinforced concrete columns, the results from RF model was compared with fifteen empirical models, as shown in Table III.1.

III.5.4.1. Description of the random forests regressor

Random Forests are a machine learning method primarily used for classification and regression. They are based on building a collection of decision trees, each trained on a random subset of the data. The RF has three working principles:

1- **Bootstrap Sampling:**

Bootstrap sampling in Random Forest regression involves creating multiple random samples of the training dataset through sampling with replacement. Each sample is used to train an individual decision tree, allowing for diversity in the training data and helping to mitigate overfitting. In this stage, for each decision tree, a random sample of data is drawn with replacement (bootstrap method). Let D be the original dataset. For each tree i, a subset D_i s created

$$D_i = \{x_1, x_2, x_3, \ldots\ldots, x_n\} \text{ ou` } x_j \sim \text{D} \tag{III.44}$$

2- Tree Construction:

- Each decision tree is constructed using a random subset of features at each split, which introduces diversity among the trees and helps prevent overfitting.
- The splitting criteria for regression trees often use mean squared error (MSE) to minimize prediction error.

3- Prediction:

- The aggregation of predictions in Random Forest regression refers to combining the output of all individual trees to produce a final prediction. This is done by averaging the predictions from each tree, which helps to smooth out errors and provides a more accurate and stable estimate of the target variable. For a given input x, each tree in the forest produces a prediction $f(x)$. The final prediction is the average of all individual tree predictions:

$$Prediction = \frac{1}{T} \tag{III.45}$$

Where T is the total number of trees.

The RF methodology is shown in Figure III.28.

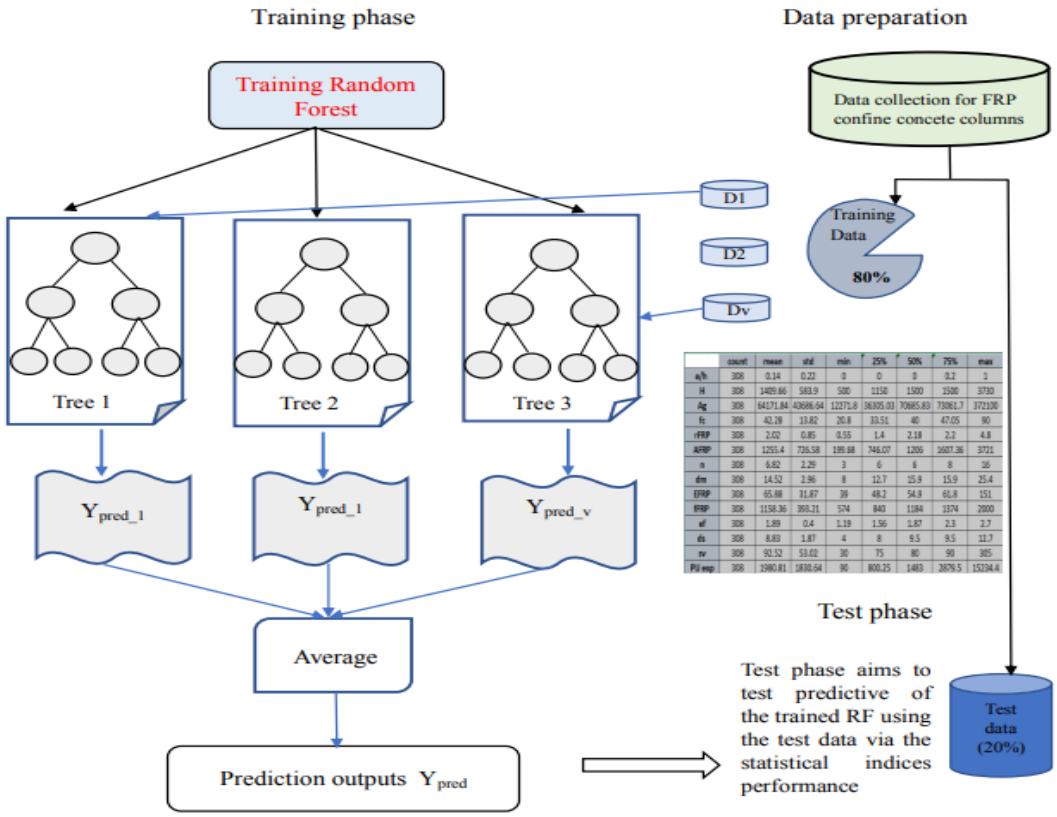

Figure III.28: Random Forests: Training and test processes.

III.5.4.2. Discussion of research findings

Figure III.29 illustrates the relationship between the measured and predicted values of the axial load-carrying capacity (ALCC) of FRP-RC columns laterally strengthened with FRP ties or spirals. The visualization reveals a strong alignment between the measured data and the outputs predicted by the RF model, indicating a high degree of agreement. This confirms that the RF model is effective in accurately predicting the ALCC of FRP-RC columns reinforced with FRP ties or spirals.

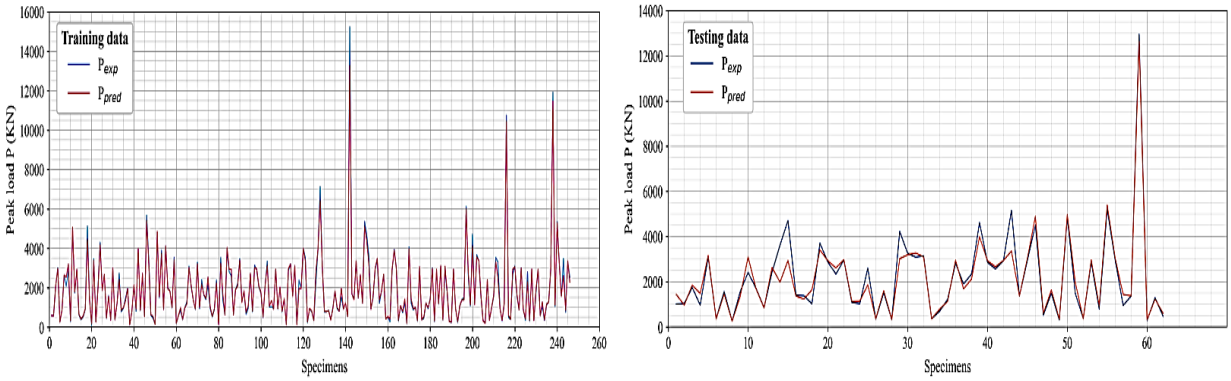

Figure III.29: Performance of RF model.

The results in Table III.6 reveal significant differences in the predictive accuracy of the various models for estimating the axial load-carrying capacity (ALCC) of FRP-reinforced concrete columns. The developed Random Forest (RF) model stands out with an

exceptionally high R^2 value of 0.98, indicating a strong correlation between predicted and actual values and demonstrating that it accounts for nearly all the variability in the data. In contrast, the empirical formulas exhibit R^2 values ranging from 0.34 to 0.71, with the highest value reflecting only a moderate correlation, suggesting that these formulas fail to capture the underlying data trends consistently (Table III.6). Furthermore, the Root Mean Square Error (RMSE) for the RF model is 282.11 kN, indicating relatively accurate predictions, whereas the empirical formulas show significantly higher RMSE values, with the worst performer (Hadhood et *al*. 2017) reaching 1380.89 kN (Table III.6). This discrepancy highlights the unreliability of the empirical models. Similarly, the Mean Absolute Error (MAE) for the RF model is 131.32 kN, suggesting that the absolute differences between predicted and actual values are minimal. In contrast, the MAE for the empirical formulas varies widely, with values as low as 652.19 kN and as high as 961.00 kN, further emphasizing the RF model's superior performance (Table III.6). The superior performance of the RF model is clearly shown by the concentration of data points closer to the 45° diagonal (Figure III.30). Overall, these results underscore the effectiveness of machine learning approaches, particularly the RF model, in providing more accurate and reliable predictions compared to traditional empirical methods.

Table III.6: Predictive accuracy of machine learning model, design codes and exiting empirical formulas.

Models	Statistical metrics				
	R^2	RMSE	MAE	AAE	SD
Developed RF model	**0.98**	**282.11**	**131.32**	**0.12**	**0.07**
ACI 440.1R-15	0.70	909.12	662.19	0.80	1.44
AS-3600	0.70	909.18	662.19	0.80	1.44
CSA S806-02	0.70	909.12	652.19	0.80	1.44
CSA S806-12	0.71	846.58	651.92	0.74	1.33
Tobbi et *al*. (2012)	0.61	1245.82	861.72	1.10	1.86
Tobbi et *al*. (2014)	0.70	909.19	662.19	0.80	1.44
Afifi et *al*. (2014a)	0.63	1128.73	754.62	1.00	1.74
Afifi et *al*. (2014b)	0.61	1145.82	861.72	1.10	1.86
Maranan et *al*. (2016)	0.70	974.97	677.80	0.86	1.53
Xue et *al*. (2018)	0.70	909.17	652.19	0.80	1.44
Mohammed et *al*. (2014a)	0.70	909.17	662.19	0.80	1.44
Mohammed et *al*. (2014b)	0.70	974.97	677.80	0.86	1.53
Samani and Attard. (2012)	0.70	909.18	662.19	0.80	1.44
Khan et *al*. (2016)	0.70	925.94	662.47	0.83	1.48
Hadhood et *al*. (2017)	0.34	1380.89	960.00	1.00	1.70

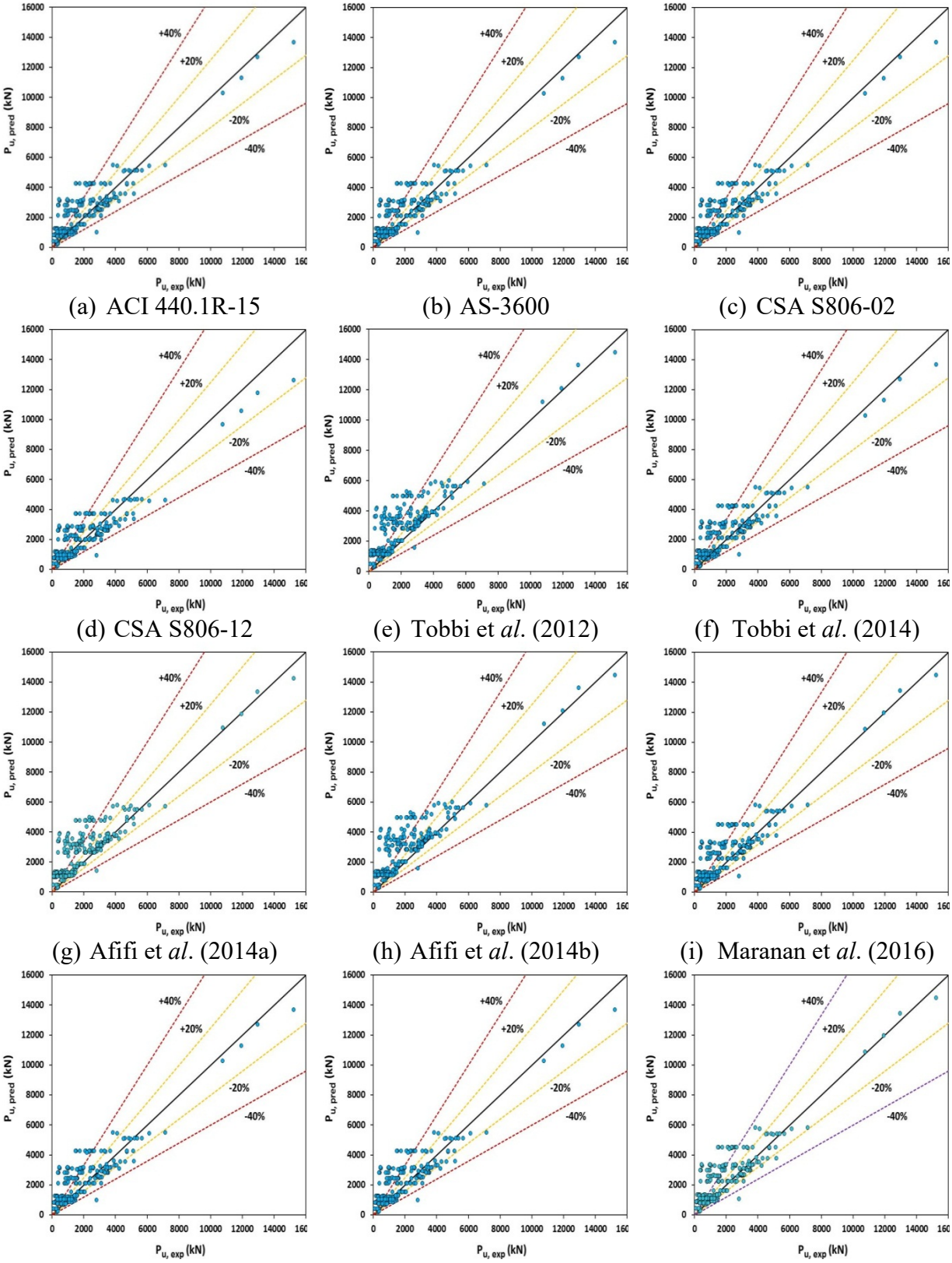

(a) ACI 440.1R-15 (b) AS-3600 (c) CSA S806-02

(d) CSA S806-12 (e) Tobbi et *al*. (2012) (f) Tobbi et *al*. (2014)

(g) Afifi et *al*. (2014a) (h) Afifi et *al*. (2014b) (i) Maranan et *al*. (2016)

(j) Xue et *al*. (2018) (k) Mohammed et *al*. (2014a) (l) Mohammed et *al*. (2014b)

Figure III.30 : *Continued*

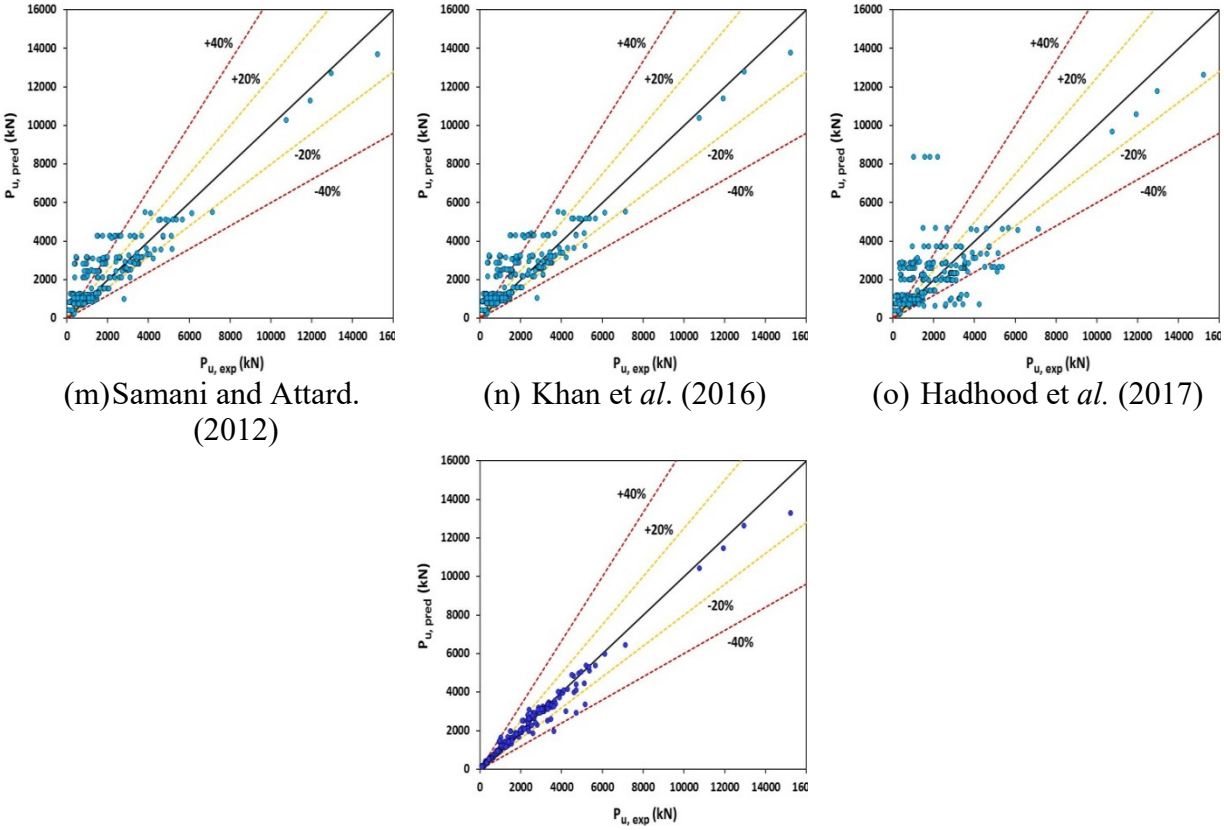

(m)Samani and Attard. (2012) (n) Khan et *al*. (2016) (o) Hadhood et *al.* (2017)

(p) Developed RF model

Figure III.30 : Evaluation of all considered predictive models.

Figure III.31 (a-d) presents a comparison of the accuracy metrics RMSE, MAE, AAE, and SD, defined in Eqs. (8-11), respectively, for both the proposed RF model and 15 existing formulas used to predict the axial capacity of FRP-RC columns laterally strengthened with FRP ties or spirals. The histogram in Figure III.31a shows the RMSE values for the RF model compared to the 15 empirical formulas previously discussed. From this, it can be observed that the RF model yields the lowest RMSE value of 282.11 kN, indicating that it provides the best fit.

FigureIII.31b compares the MAE values of the proposed RF model with those of the 15 existing formulas for predicting the ultimate capacity. The histogram shows that the RF model achieves an MAE of 131.32 kN, whereas the MAE values for the existing formulas range from 652.19 kN to 960.00 kN, confirming the high accuracy of the RF model.

Similarly, Figure III.31c highlights the AAE values of the RF model in comparison with the 15 existing formulas. The RF model achieves a minimum AAE of 0.12, while the AAE values of the existing formulas range from 0.74 to 1.10. This further supports the accuracy of the RF model in estimating the peak load of FRP-RC columns strengthened with FRP ties or spirals.

Additionally, Figure III.31d compares the standard deviation (SD) values between the RF model and the 15 empirical formulas. The RF model has the lowest SD of 0.07, while the SD

values of the existing formulas range from 1.33 to 1.86. This demonstrates that the RF model provides a better dispersion between the actual and predicted data.

In conclusion, the RF regression model shows superior performance in predicting the ultimate capacity of FRP-RC columns laterally confined with FRP ties or spirals. It excels in correlation, precision, fit, and error dispersion compared to the 15 existing empirical formulas.

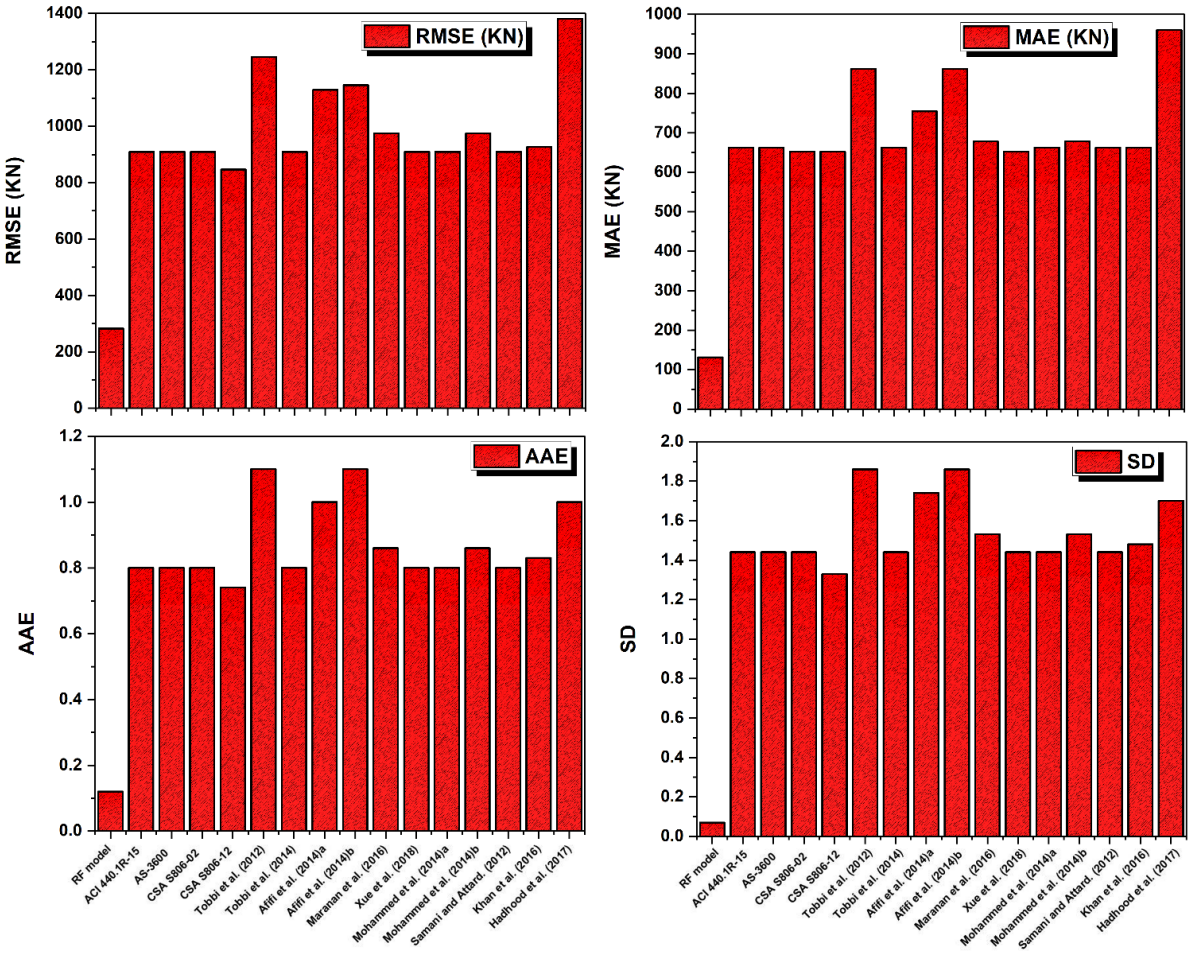

Figure III.31: Comparison of obtained statistical indicators of all considered models.

The Taylor diagram presented in the Figure III.32 provides a comprehensive comparison of the predictive performance of the developed Random Forest (RF) model and various empirical formulas for estimating the axial load-carrying capacity (ALCC) of FRP-reinforced concrete columns. The RF model, depicted as a black square, stands out as the best-performing approach, exhibiting the highest correlation coefficient and the standard deviation closest to the actual data represented by the black star. This demonstrates the superior ability of the RF model to accurately capture the underlying relationships in the data, outperforming the empirical formulas shown. Among the empirical models, the ACI 440.1R-15, AS-3600, CSA S806-02, and CSA S806-12 formulas show relatively better performance, with higher

correlation coefficients and standard deviations closer to the actual data compared to the other empirical approaches. However, these formulas still fall short of the RF model's exceptional predictive accuracy.

In contrast, the empirical formulas proposed by Tobbi et *al*. Afifi et *al*. and Hadhood et *al*. exhibit lower correlation and higher standard deviation compared to the top-performing models, indicating their limited ability to reliably estimate the ALCC of FRP-reinforced concrete columns. The clear visual representation provided by the Taylor diagram highlights the significant advantage of the developed RF model over the traditional empirical methods, underscoring the potential of machine learning techniques in enhancing predictive modeling in structural engineering applications.

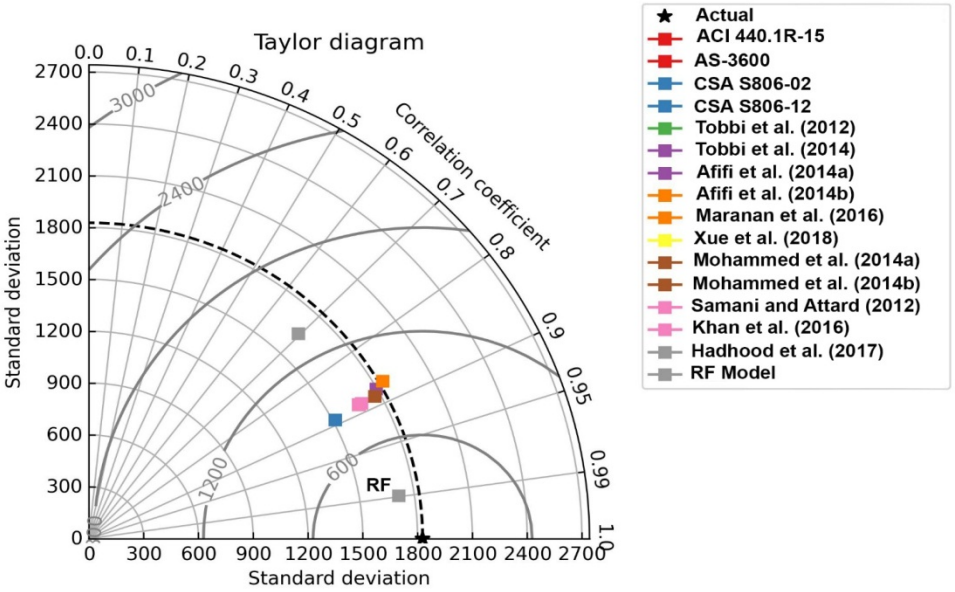

Figure III.32: Comparing predictive performance of machine learning and empirical models for FRP-reinforced concrete column axial load capacity.

III.6. CONCLUSION

The present study aimed to assess the load-carrying capacity of reinforced concrete (RC) compressive members reinforced with FRP bars at varying eccentricity levels, using both empirical modelling and the eXtreme Gradient Boosting (XGBoost) algorithm. A comprehensive dataset comprising 308 test results on FRP-RC compressive members subjected to concentric and eccentric compression loads was analyzed. Utilizing this dataset, new empirical models and an XGBoost algorithm were developed to predict the load-carrying capacity of FRP-RC compressive members. These models are applicable to cases with eccentricity ratios (e/h) ranging from 0 to 1.

The key conclusions drawn from this investigation are as follows:

1. A statistical evaluation of 15 existing models for predicting axial load-carrying capacity (ALCC) in FRP-reinforced concrete compressive members revealed that these models tend to overestimate capacity compared to test results, showing conservative estimates. Additionally, the predictions from these models displayed significant variability, with low R^2 values ranging from 0.34 to 0.70 and high error rates. This discrepancy is likely due to the lack of consideration for eccentricity effects in the existing formulas.
2. A regression analysis was conducted to derive new, simplified equations for calculating ALCC in FRP-RC compressive members. First, an expression specific to members under concentric compression was developed, incorporating the impact of FRP bars' axial strain (ε_{frp}) and stiffness (E_{frp}). Then, a unified expression for both concentric and eccentric compression loads (e/h from 0 to 1) was created, accounting for eccentricity effects.
3. The proposed empirical models demonstrated robust predictive performance over the test dataset. The first model, designed for concentric loading, achieved $R^2 = 0.97$, RMSE = 387.27 kN, MAE = 214.20 kN, AAE = 0.10, and SD = 0.15, indicating high precision and consistency. The second model, suitable for both concentric and eccentric loading, showed $R^2 = 0.88$, RMSE = 635.75 kN, MAE = 405.08 kN, AAE = 0.31, and SD = 0.52, highlighting its effective predictability across a wider range of load conditions.
4. The proposed XGBoost model exhibited exceptional predictive capability for the load-carrying capacity of FRP-RC compressive members, achieving an R^2 value of 0.98 and low error values (RMSE = 259.05 kN, MAE = 144.36 kN, AAE = 0.11, SD = 0.14). This indicates the model's superior precision and reliability in comparison to empirical models.
5. When compared to existing formulas, the XGBoost model consistently outperformed empirical models in accuracy. This suggests that both the empirical and XGBoost models developed here offer reliable predictions for the load-carrying capacity of FRP-reinforced concrete compressive members under both concentric and eccentric loads, making them valuable tools for structural analysis and design applications.

Our study contributes to a more nuanced understanding of the behavior of FRP-reinforced concrete (FRP-RC) compressive members by demonstrating the effectiveness of machine learning techniques, specifically the XGBoost model, in predicting peak axial capacity. This predictive

accuracy advances our understanding of FRP-RC behavior under varying eccentricity levels by providing reliable and data-driven estimates for complex structural scenarios that traditional empirical models may struggle to capture. The findings underscore the potential for machine learning to handle nonlinear relationships and variability in FRP-RC performance, offering insights that could lead to improved design codes and standards for FRP-reinforced members.

The same study set out to answer whether machine learning, specifically Random Forest (RF) regression, could accurately predict the axial load-carrying capacity (ALCC) of FRP-reinforced concrete (FRP-RC) columns reinforced laterally with FRP ties or spirals, outperforming traditional empirical models. Through analyzing a dataset of 308 records, the RF model used eleven key input variables to predict the ultimate capacity of these columns with high precision.

The results affirmatively answer the research question: the RF model not only closely aligned with actual test data but also outperformed fifteen existing empirical formulas, achieving a robust R^2 of 0.98 and lower errors across multiple metrics (e.g., RMSE of 282.11 kN). These findings confirm that RF regression provides a reliable, more accurate approach to ALCC prediction, offering a practical tool for structural engineers and advocating for the broader integration of machine learning in civil engineering applications.

The next chapter discusses the prediction of the axial load-carrying capacity of externally FRP-confined concrete-filled steel tube columns using hybrid deep learning models.

CHAPTER IV:

High-Fidelity Simulation of Externally FRP-Confined CFST Columns: The Synergy of Hybrid Deep Learning

IV.1. INTRODUCTION

The aim of the present chapter is to investigate the behavior of hybrid FRP-confined concrete filled-steel tube (CFST) columns with circular cross-sections. The study was carried out by gathering information through literature, which resulted eight existing design models and 250 experimental data. Moreover, advanced hybrid deep learning predictive models were developed to accurately predict the axial load-carrying capacity (ALCC) of FRP-confined CFST columns under compression loads. BiLSTM and CNN-BiLSTM were utilized for the developed ALCC models. The suggested models were validated against developed experimental database and previously suggested empirical equations to assess their accuracy and reliability.

IV.2. REVIEW OF EXISTING MODELS OF FRP-CONFINED CFST COLUMNS

In the last few decades, the behavior of FRP confined circular concrete filled steel tube columns was extensively investigated and various empirical models were developed to predict the axial load carrying capacities (N_u) of columns. In this section, eight existing design models suggested by Tao et *al*. (2007), Park et *al*. (2011), Che et *al*. (2012), , Lu et *al*. (2014), Dong et *al*. (2017), Ding et *al*. (2018), Tang et *al*. (2020), Ma et *al*. (2022), and are presented. It should be noted that all of these existing models function with two unified parameters, namely the confinement index of the steel tube (ξ_s) and the confinement index of the PRF wraps (ξ_f), which makes the comparison of these models convenient. The tow confinement indexes are calculated as follows:

$$\boldsymbol{\xi_s = \frac{A_s f_y}{A_c f_{co}}} \tag{IV.1}$$

$$\boldsymbol{\xi_f = \frac{A_f f_f}{A_c f_{co}}} \tag{IV.2}$$

Where $\boldsymbol{A_s}$= the steel tube section area, $\boldsymbol{f_y}$= the yield strength of the steel tube, $\boldsymbol{A_c}$= the area of the core concrete, $\boldsymbol{f_{co}}$= the compressive strength of unconfined concrete, $\boldsymbol{A_f}$= the FRP section area, $\boldsymbol{f_f}$ = the tensile strength of FRP.

Concerning the collected existing design expressions, more comprehensive clarifications are presented below.

IV.2.1. Tao et *al.* model

To calculate the load-bearing capacity of CFRP confined CFST stub columns, Tao et *al*. (2007) developed a new model based on the expression suggested by Han et *al*. (2004) for circular CFST stub column and the expression proposed by Yu (2002) for CFRP-confined concrete. The new model developed is given by the following expression:

$$N_u = (1 + 1.02\xi_s) f_{co} A_{sc} + 1.15\xi_f f_{co} A_c \tag{IV.3}$$

Where

$$A_{sc} = A_s + A_c \tag{IV.4}$$

IV.2.2. Park et *al.* model

Park et *al*. (2011) compared two axial design formulas. For The first formula, by using the ACI 440R-96 codes, the expression for (N_u) of CFST confined by FRP is determined by the following expression:

$$N_u = A_s f_s + A_c 0.85 f'_{cc} \tag{IV.5}$$

Where $\boldsymbol{f'_{cc}}$ = the compressive strength of confined concrete, it can be calculated by the equation suggested by Mander et *al.* (1988), which was originally developed for confinement provided by steel jacket. This equation is given as follows:

$$\boldsymbol{f'_{cc} = f_{co}\left[2.25\sqrt{1 + 7.9\frac{f_l}{f_{co}}} - 2\frac{f_l}{f_{co}} - 1.25\right]} \tag{IV.6}$$

f_l = the lateral confining pressure provided by FRP and steel tube, given by:

$$f_l = \frac{2t_f f_f}{d} + \frac{2t_s f_s}{d} \tag{IV.7}$$

Where, d = the diameter of infilled concrete.

For the second formula, the authors utilized a modify formula suggested by ACI 440R-96 codes with ignored the coefficient 0.85. The modify formula can be expressed as follow:

$$N_u = A_s f_s + A_c f'_{cc} \tag{8}$$

For calculating the $\boldsymbol{f'_{cc}}$, they used a simplified confined concrete model in accordance with previous researches of Richard et *al.* (1928) and Lam and Teng (2002). The $\boldsymbol{f'_{cc}}$ was given as:

$$\frac{f'_{cc}}{f_{co}} = 1 + k\frac{f_l}{f_{co}} \tag{IV.9}$$

Where, k = the confinement effectiveness coefficient, which calibrated based on 11 tests data on the compressive strength of FRP strengthened circular CFT columns from researches of Xiao et *al.* (2005) and Park et *al*. (2009). The simplified formula was expressed as follows:

$$\frac{f'_{cc}}{f_{co}} = 1 + 2.86\frac{f_l}{f_{co}} \tag{IV.10}$$

IV.2.3. Che et *al.* model

Che et *al*. (2012) developed a constitutive expression to predict the load bearing capacity of concrete filled circular CFRP-steel tube columns using regression analysis, with considering the strength improvement factors related to the steel confinement index, ξ_s and FRP confinement index, ξ_f. The new expression was given as follows:

$$N_u = A_{sc}f_{cu} \tag{IV.11}$$

$$f_{cu} = \left[1 + 1.02\left(\xi_s + 3\xi_f\right)\right]f_{co} \tag{IV.12}$$

Where A_{sc} = the cross-sectional area of the specimens.

IV.2.4. Lu et *al.* model

Lu et *al*. (2014) thought that the combined effect of the steel tube and FRP wrap was unnecessary to be considered for calculating the strength of FRP-confined (CFST) columns. In this context, the researchers were decomposed the ultimate load capacity (N_u) of FRP-confined (CFST) columns into the ultimate load of steel tube (N_s), the ultimate load of unconfined concrete (N_{co}), the ultimate load of concrete under the circumferential constrain of steel tube (N_{cs}), and the ultimate load of concrete under the circumferential constrain of FRP (N_{cf}):

$$N_u = N_s + N_{co} + N_{cs} + N_{cf} \tag{IV.13}$$

To consider the effect of the steel tube on the ultimate load of FRP-confined (CFST) columns, the researchers based on the theoretical design model proposed by Han et *al*. (2004) for the ultimate load of concrete-filled steel tube columns; while, for considering the influence of FRP on the ultimate load of FRP-confined (CFST) columns, the researchers based on the design model proposed for the ultimate load of FRP confined concrete columns by Yu (2002). The ultimate axial load capacity for FRP-confined concrete-filled steel tube columns can be developed as follow:

$$N_u = (1 + 1.8\xi_s + 1.15\xi_f) f_{co} A_c \tag{IV.14}$$

IV.2.5. Dong et *al*. model

Dong et *al*. (2017) suggested a new formulation for predicting the load bearing capacity of FRP-confined concrete filled steel tube columns. The proposed formulation was calibrated using a regression analysis on large database of FRP-confined concrete filled steel tube columns under axial compression loading collected from the literature. The proposed formulation can be expressed as follows:

$$N_u = [0.95 + f_l + min(f_2, f_3)] A_c f_{co} + A_s f_s \tag{IV.15}$$

$$f_l = 0.49(A_s f_s / A_c f_{co})^{0.51} \tag{IV.16}$$

$$f_2 = 0.00085(k)^{0.80} (f_{co})^{-0.29} \tag{IV.17}$$

$$f_3 = 0.60\left(k\varepsilon_{rup}\right)^{0.86} (f_{co})^{-0.59} \tag{IV.18}$$

$$k = \frac{2E_f t_f}{D} \tag{IV.19}$$

Where $\boldsymbol{k}$ = the confinement stiffness of the FRP, $\boldsymbol{E_f}$ = the elastic modulus of the FRP.

IV.2.6. Ding et *al*. model

Based on the limit equilibrium and elastoplastic methods, Ding et *al*. (2018) determined a simplified formulation for the ultimate load ($\boldsymbol{N_u}$) of CFRP-confined CFT stub columns, which considered its relation to the longitudinal bearing capacity of the steel tube and the bearing capacity of the concrete confined by both external CFRP wraps and the steel tube. This relationship is given as follows:

$$N_u = f_{cc} A_c + \sigma_{L,s} A_s \tag{IV.20}$$

Where $\boldsymbol{A_c}$ and $\boldsymbol{A_s}$ = the cross-sectional area of concrete and the cross-sectional area of steel tube, respectively. $\boldsymbol{f_{cc}}$ = the axial strength of CFRP-confined CFT stub columns, expressed as follows:

$$f_{cc} = f_c + 3.4\sigma_{r,c} \tag{IV.21}$$

$\boldsymbol{\sigma_{r,c}}$ = the circumferential banding force of concrete, calculated by the following expression:

$$\sigma_{r,c} = \frac{\rho}{2(1-\rho)}\sigma_{\theta,s} + \frac{\rho_1}{2(1-\rho)}f_{cf} \tag{IV.22}$$

$\boldsymbol{\sigma_{\theta,s}}$ = the perimeter stress provided by the steel tube, $\boldsymbol{f_{cf}}$ = the tensile strength of CFRP, $\boldsymbol{\rho}$ = the steel ratio is defined as the ratio of the cross-sectional area of the steel tube to the sum of the cross-sectional areas of both the steel tube and the concrete core, $\boldsymbol{\rho_1}$ = The CFRP ratio is described as the proportion of the combined cross-sectional area of CFRP and the concrete core to the total cross-sectional areas of both the steel tube and the concrete core, $\boldsymbol{\sigma_{L,s}}$ = the axial stress of steel tube, given as follows:

$$\sigma_{L,s} = \left[\sqrt{1 - \frac{3}{\xi_s^2}\left(\frac{\sigma_{r,c}}{f_{co}} - \frac{\xi_f}{2}\right)^2} - \frac{1}{\xi_s}\left(\frac{\sigma_{r,c}}{f_{co}} - \frac{\xi_f}{2}\right)\right]\xi_s \tag{IV.23}$$

To predict the ultimate load-bearing capacity of CFRP-confined CFT stub columns, Ding et *al.* (2018) incorporated Eqs. (IV.22) and (IV.23) into Eq. (IV.20). Subsequently, they took the derivative of the resulting formulation. In this context, the maximum ultimate load-bearing capacity of the CFRP-confined CFT stub column can be calculated using the following expression:

$$N_u = f_{co}A_c\left(1 + 1.7\xi_s + 1.7\xi_f\right) \tag{IV.24}$$

$$f_{co} = 0.4f_{cu}^{7/6} \tag{IV.25}$$

Where $\boldsymbol{f_{cu}}$ = compressive strength of cube concrete.

IV.2.7. Tang et *al.* model

Tang et *al.* (2020) developed an increase index of capacity (η_{cap}) to assess the contribution of the FRP wrap on the enhancement of the bearing capacity of the FRP confined filled stainless steel tube columns. This index (η_{cap}) can be determined by the following expression:

$$\eta_{cap} = \frac{N_u - N}{N} \times 100 \quad \text{(IV.26)}$$

Where N_u= the ultimate loads of the FRP confined concrete filled stainless steel tube columns, N = the unconfined concrete filled stainless steel tube columns.

For predicting the ultimate load caring capacity (N_u) of FRP-confined CFSST columns under axial compression, Tang et *al*. (2020) proposed a simplified theoretical model based on regression analysis. The expression of the proposed model was given as follow:

$$N_u = (1 + \eta_{cap})(1.27FA_s + 0.85f_{co}A_c) \quad \text{(IV.27)}$$

$$F = min(f_y + 0.7f_u) \quad \text{(IV.28)}$$

$$\eta_{cap} = 0.42\frac{\xi_{frp}}{\xi_s} \quad \text{(IV.29)}$$

Where f_u = the ultimate tensile strength of the steel tube, η_{cap} = the simplified rise index;

IV.2.8. Ma et *al.* model

Ma et *al.* (2022) suggested new nonlinear formulations to calculate the ultimate bearing capacity of CFRP-confined CFST short columns with square and circular cross-sections, by considering the confinement effect coefficient of CFRP and based on more experimental data collected from the existing literature combined with their own experimental data, as given by the following relation:

$$N_{CFST} = f_{co}A_c\left(1 + a\xi_s + b\sqrt{\xi_s}\right) \quad \text{(IV.30)}$$

$$N_{FCFST} = \Omega\left(\xi_f\right)N_{CFST} \quad \text{(IV.31)}$$

$$\Omega\left(\xi_f\right) = 1 + c\xi_f\frac{f_{co}}{f_{C30}} \quad \text{(IV.32)}$$

With $\boldsymbol{c = 0.220}$ for circular cross-section.

The coefficient values a et b of circular cross-section are obtained through regression analysis of the experimental data. The final expression developed by Ma et *al.* (2022) for calculating the load bearing capacity of CFRP-confined CFST short columns is given as follows:

$$N_{FCFST} = \left(1 + 0.220\xi_f\frac{f_{co}}{f_{C30}}\right)\left(1 + 1.311\xi_s + 0.556\sqrt{\xi_s}\right)f_{co}A_c \quad \text{(IV.33)}$$

The formulas developed by the various researchers have been systematically are summarized in Table IV.1.

Table IV.1. Summary of existing axial load-bearing capacity models for FRP - CFST columns.

Model	**Formulas of axial load-bearing capacity N_u (kN)**
Tao et al. (2007)	$\boldsymbol{N_u = (1 + 1.02\xi_s) f_{co} A_{sc} + 1.15\xi_f f_{co} A_c}$ $\boldsymbol{A_{sc} = A_s + A_c}$
Park et al. (2011) Eq (5)	$N_u = A_s f_s + A_c 0.85 f'_{cc}$ $\boldsymbol{f'_{cc} = f_{co}\left[2.25\sqrt{1 + 7.9\frac{f_l}{f_{co}}} - 2\frac{f_l}{f_{co}} - 1.25\right]}$ $f_l = \frac{2t_f f_f}{d} + \frac{2t_s f_s}{d}$
Park et al. (2011) Eq (8)	$\boldsymbol{N_u = A_s f_s + A_c f'_{cc}}$ $\boldsymbol{\frac{f'_{cc}}{f_{co}} = 1 + 2.86\frac{f_l}{f_{co}}}$
Che et al. (2012)	$\boldsymbol{f_{cu} = \left[1 + 1.02\left(\xi_s + 3\xi_f\right)\right] f_{co}}$
Lu et al. (2014)	$\boldsymbol{N_u = (1 + 1.8\xi_s + 1.15\xi_f) f_{co} A_c}$
Dong et al. (2017)	$N_u = [0.95 + f_l + min(f_2, f_3)] A_c f_{co} + A_s f_s$ $f_l = 0.49(A_s f_s / A_c f_{co})^{0.51}$ $f_2 = 0.00085(k)^{0.80}(f_{co})^{-0.29}$ $f_3 = 0.60\left(k\varepsilon_{rup}\right)^{0.86}(f_{co})^{-0.59}$ $k = \frac{2E_f t_f}{D}$
Ding et al. (2018)	$N_u = f_{co} A_c\left(1 + 1.7\xi_s + 1.7\xi_f\right)$ $f_{co} = 0.4 f_{cu}^{7/6}$
Tang et al. (2020)	$N_u = (1 + \eta_{cap})(1.27 F A_s + 0.85 f_{co} A_c)$ $F = min(f_y + 0.7 f_u)$

	$\eta_{cap} = 0.42 \frac{\xi_{frp}}{\xi_s}$
Ma et al. (2022)	$N_{FCFST} = \left(1 + 0.220\xi_f \frac{f_{co}}{f_{C30}}\right)\left(1 + 1.311\xi_s + 0.556\sqrt{\xi_s}\right) f_{co} A_c$

IV.3. COLLECTED TEST DATASET

The performance of FRP confined circular CFST columns was experimentally investigated in several research studies. In this present study, totally 250 data of FRP-confined concrete filled steel tubes (CFST) columns under axial compression loads are assembled from 20 different existing experimental studies published between the year 2004 and 2022 and are listed in Table IV.2. Ten parameters of the assembled specimens, ie., compressive strength of unconfined concrete f_{co}, Diameter of the specimen cross section D, High of columns H, thickness of steel tube t_s, yield strength of steel tube f_y, FRP elastic modulus E_f, ultimate tensile strength of FRP f_f, thickness of FRP t_f and ultimate tensile strain of FRP ε_f are served as the input parameters. The ultimate load N_u of FRP-confined circular concrete columns-filled steel tube is served as the output parameter. The adequacy of the tested results was evaluated by using a set of carefully established selection criteria to ensure the reliability and the consistency of the database. These selection criteria are given as follows:

1) There is no database for relevant research on concrete beams; this work is only focused on analyzing FRP wraps and steel tube-strengthened circular columns;
2) The chosen concrete columns were not steel bar reinforced; instead, the emphasis was on how FRP affected the axial load-bearing capacity of unreinforced concrete;
3) Concrete columns that are completely confined using steel tubes and fiber-reinforced polymer (FRP) wraps are among the chosen specimens; those that are just partially confined, such as using FRP strips, are not included;
4) The chosen specimens consist of concrete columns wrapped with composite material made with carbon, glass or basalt fibers reinforced polymers (CFRP / GFRP / BFRP);
5) All the specimens opted for the dataset were tested experimentally under monotonic axial loading;
6) Only samples with the height-to-diameter H/D ratios ranges from 2 to 4 were included in this database.

It should be noted that the database of FRP-confined concrete filled steel tube columns having the compressive strength of unconfined concrete f_{co} ranging from 14.15 MPa to 140.3 MPa with the average (AVG) of 43 MPa, the diameter of the specimen cross section D ranges from 114 mm to 305 mm with an AVG of 156.37 mm, the High of columns H varies from 250 mm to 900 mm with an AVG of 466.52 mm, the H/D range from 2 to 4 with an AVG of 3.05, the thickness of steel tube t_s varies from 1 mm to 7.5 mm with an AVG of 4.28 mm, the D/t_s ranges from 16.28 to 202 with an AVG of 49.06, the yield strength of steel tube f_y ranges from 226 MPa to 369 MPa with an AVG of 306.99 MPa, the FRP elastic modulus E_f ranges from 35 MPa to 275 MPa with an AVG of 189.84 MPa, the ultimate tensile strength of FRP f_f varies from 897 MPa to 4500 MPa with an AVG of 3100.87 MPa, the thickness of

FRP t_f ranges from 0.111 mm to 5.6 mm with an AVG of 0.43 mm, the ultimate tensile strain of FRP ε_f ranges from 0.0032 to 0.026 with an AVG of 0.018, and The test result of ultimate load N_u varies from 654.11 kN to 6407 kN with an AVG of 2420.06 kN.

Table IV.2: Dataset and results of tests on FRP-confined CFST columns.

Reference	No.	f_{co} (MPa)	D (mm)	H (mm)	H/D	t_s (mm)	D/t_s	f_y (MPa)	FRP $Type$	E_{frp} (GPa)	f_{frp} (MPa)	t_{frp} (mm)	ε_{frp}	N_{ue} (kN)
Wei *et al*. (2014)	16	31.2;34.7	133	400	3.0	3.0;4.5;6.0;7.5	17.7;22.2;29.6;44.3	365.0	CFRP BFRP	91.4;240	2370;4067	0.111;0.222	0.017;0.026	1179.0-2363.0
Liu et *al*. (2010)	10	30.1;36.3;40.2	126;128;130	400	3.1;3.2	3.0;4.0;5.0	26.0;32.0;42.0	248.0	CFRP-GFRP	109.0;250.0	2930;3550	0.111;0.222;0.507	0.013;0.026	1300.0-1845.0
Park et *al*. (2011)	7	37.5	140	620	4.4	3.2;4.5;6.6	21.2;31.1;43.8	301.0;334.0;365.0	CFRP	35.0;52.5;105.0	3500	0.111-0.333	0.0210	1409.2-2274.6
Hu et *al*. (2011)	9	35.9;42.2	202;203;204	400	2.0	1.0;1.5;2.0	102.0;135.3;202.0	226.0;231.0;242.0	GFRP	80.1	1826	0.170-0.680	0.023	1878.0-2561.0
Gu et *al*. (2004)	8	40.15	127-133	400	3.1	1.5-4.5	29.6-84.7	310.0; 350.0	CFRP	230.0	1260	0.167	0.0210	1086.0-1798.8
Xiao et *al*. (2005)	4	46.6	152	304	2.0	2.95	51.5	356.0	CFRP	64.9	897	2.800; 5.600	0.007	2233.0-3439.0
Tao et *al*. (2007)	4	32	156;250	470;750	3.0	3.0	52.0;83.3	230.0	CFRP	255.0	4212	0.170; 0.340	0.017	1890.0-4790.0
Liu et *al*. (2018)	16	38.3;44.8	200;260	600;760	2.9; 3.0	2.0	100.0; 130.0	264.3	CFRP	235.0	3400	0.334; 0.668	0.0160	2607.0-5374.0
Lu et *al*. (2014)	10	30.1;36.3;40.2	128;130	400	3.1	4.0	26.0;32.0;42.0	242.0;243.0;248.0	CFRP; GFRP	109.0;250.0	2930;3550	0.111;0.169;0.222;0.333	-	1300.0-1845.0
Che et *al*. (2012)	10	36.2	127;129;131;133;13	381;387;393;408	3.0	1.5; 2.5; 3.5;4.5	22.7;29.6;37.4;51.6;84.7	330.0	CFRP	228.0	4500	0.167; 0.334	0.02	1018.0-2105.0

Table IV.2 *Continued*

Wei et *al*. (2021)	36	64.0	133	400	3.01	4.5;6.0;7.0	19.0;22.2;29.6;30.2	306.4;311.9;328.5	BFRP; CFRP	74.8;240.0	1642.8; 3331.7	0.334;0.501;0.668	0.014; 0.022	1934.0-3322.0
Ding et *al*. (2018)	12	33.4; 48.79	300	900	3.0	3.70-3.87	77.5-81.7	311.0	CFRP	245.0	3481.0	0.167;0.334;0.501	0.017	4498.0-7407.0
Zhang et *al*. (2020)	36	43.8	133	400	3.0	4.5;6.0; 7.0	19.0;22.2;29.6	306.4;311.9;328.5	BFRP; CFRP	74.8;240	1642,8; 3331.7	0.334;0.501;0.668	0.022	1768.0-2982.0
Suliman et *al*. (2013)	6	44.0;60.0	114; 167	250;350	2.1; 2.2	3.1;3.6;5.6	20.4;31.7; 53.9	350.0	GFRP	72.0	3400.0	0.352		1268.0; 2048.0
Cao et *al*. (2020)	4	140.3	133	400	3.0	4.0	33.3	340.0	CFRP; GFRP	-	1582.0; 2471.0	0.334;0.668;0.338;0.676	0.017; 0.02	2628.0-3662.0
Tang et *al*. (2020)	18	24.8	114	400	3.5	3.0;5.0;7.0	16.3; 22.8; 38.0	279.0;340.0;355.0	CFRP	243.0	3814.0	0.017;0.334;0.501	0.017	871.5-1659.0
Ma et *al*. (2022)	12	14.15; 42.44	114	400	3.5	2.0	57.0	236.9	CFRP	232.0	3425.0	0.166; 0.332	0.016	654.1-1429.2
Chen et *al*. (2022)	15	31.8	152	600	3.9	5.0	30.4	369.0	CFRP	240.0	3667.5	0.167;0.334;0.501	0.015	2203.0-2985.0
Zhao et *al*. (2020)	12	46.2;47.9;30.1	255	510	2.0	1.37;2.25;2.54	100.4;113.3;186.1	272.7;284.0;302.5	CFRP	275.0	4050.0	0.150; 0.300	-	3002.0; 4453.0
Na et *al*. (2018)	5	38.0	128	588-2688	3.5-16	6.0	28.0	243.0	CFRP	250.0	3550.0	0.222		1513.04-2358.31

IV.4. HYBRID DEEP LEARNING BASED-MODELS

IV.4.1. Convolutional Neural Networks-Bidirectional Long Short-Term Memory

The Convolutional Neural Networks-Bidirectional Long Short-Term Memory (CNN-BiLSTM) model is an advanced hybrid deep learning architecture that combines the capabilities of Convolutional Neural Networks (CNNs) and Bidirectional Long Short-Term Memory (BiLSTM) networks (Gandhi et *al*. 2021, Lu et *al*. 2021, Méndez et *al*. 2023). The BiLSTM's dual processing paths enable the model to capture complex dependencies in the data that a standard LSTM might miss (Siami-Namini et *al*. 2019). This is particularly useful in tasks where the context from both past and future data points is crucial for making accurate predictions. In the CNN-BiLSTM model, the CNN layers first perform feature extraction by identifying key patterns in the input data. These extracted features are then passed to the BiLSTM layers, which process the sequence bidirectionally to understand the temporal dynamics and dependencies (Sun et *al*. 2024). The pooling layers in the CNN further reduce the dimensionality of the data, ensuring that the most significant features are retained while reducing computational complexity (Guo et *al*. 2024). This combination of CNN and BiLSTM allows the model to leverage the strengths of both architectures: the CNN's ability to capture intricate spatial features and the BiLSTM's capacity to understand complex temporal relationships (Sun et *al*. 2024). The mathematical description of the model architecture were described as follow:

1. Input Layer

- Let the input data be represented as $\boldsymbol{X} = [\boldsymbol{x_1}, \boldsymbol{x_2}, \dots, \boldsymbol{x_T}]$, where $\boldsymbol{T}$ is the sequence length and $\boldsymbol{x_t}$ is the input feature vector at time step $\boldsymbol{t}$. For a single feature vector, $\boldsymbol{x_t} \boldsymbol{\epsilon} \mathbb{R}^{\boldsymbol{F}}$ where $\boldsymbol{F}$ is the number of features.

2. Convolutional Layer (Conv1D)

- The 1D convolutional layer applies a convolution operation over the input sequence to extract local features.
- The convolution operation is defined as:

$$\boldsymbol{h_t^{(c)}} = \mathbf{ReLU}\left(\sum_{\boldsymbol{f=1}}^{\boldsymbol{F}} \boldsymbol{w_f} \ . \boldsymbol{x_{t+f-1}} + \mathbf{b}\right) \quad \text{(IV.45)}$$

Where: $\boldsymbol{w_f}$ are the convolutional filters (weights), b is the bias term, $\boldsymbol{h_t^{(c)}}$ is the output of the convolutional layer at position t, and $\mathbf{ReLU}$ is the activation function: $\mathbf{ReLU(z)} = \mathbf{max(0, z)}$

3. Max Pooling Layer (MaxPooling1D)

- The max-pooling layer reduces the dimensionality of the convolutional output by taking the maximum value over a specified window.
- The max-pooling operation is defined as

$$\boldsymbol{h_t^{(p)} = \max\left(h_t^{(c)}, h_{t+1}^{(c)}, \ldots., h_{t+k-1}^{(c)}\right.} \quad \text{(IV.46)}$$

Where: k is the pooling size, $\boldsymbol{h_t^{(p)}} =$ is the pooled feature at position t.

4. Bidirectional LSTM (BiLSTM) Layer

- The BiLSTM layer processes the pooled features in both forward and backward directions to capture long-term dependencies in the sequence.

For the forward pass:

$$\boldsymbol{\overrightarrow{h_t^l} = \mathbf{LSTM}\left(\overrightarrow{h_{t-1}^{(l)}}, h_t^{(p)}\right)} \quad \text{(IV.47)}$$

The forward LSTM processes the input sequence from the beginning to the end, maintaining a hidden state $\boldsymbol{\overrightarrow{h_t^l}}$

For the backward pass:

$$\boldsymbol{\overleftarrow{h_t^{(l)}} = \mathbf{LSTM}\left(\left(\overleftarrow{h_{t+1}^{(l)}}\right), h_t^{(p)}\right.} \quad \text{(IV.48)}$$

The backward LSTM processes the input sequence from the end to the beginning, maintaining a hidden state $\boldsymbol{\overleftarrow{h_t^l}}$

The BiLSTM output at time step t is the concatenation of the forward and backward LSTM outputs:

$$\boldsymbol{h_t^{(BiLSTM)} = \left[\overrightarrow{h_t^l}, \overleftarrow{h_t^l}\right]} \quad \text{(IV.49)}$$

5. Fully Connected (Dense) Layer

- The BiLSTM output is passed through a fully connected layer to produce the final output.
- The dense layer output is computed as

$$\boldsymbol{y_t = \sigma\left(W_d . h_t^{(BiLSTM)} + b_d\right)} \quad \text{(IV.50)}$$

Where: $\boldsymbol{W_d}$. Is the weight matrix for the dense layer, $\boldsymbol{b_d}$ is the bias term, and $\boldsymbol{\sigma}$ is the activation function, often a linear function for regression tasks. The model is trained by minimizing the loss function, typically Mean Squared Error (MSE) for regression tasks:

6. Optimization

- The model parameters (weights and biases) are updated during training using an optimization algorithm such as Adam, defined by:

$$\boldsymbol{\theta_{t+1} = \theta_{t-\eta} J(\theta)} \quad \text{(IV.51)}$$

Where, $\boldsymbol{\theta}$ represents the model parameters, $\boldsymbol{\eta}$ is the learning rate, $\boldsymbol{J(\theta)}$is the loss function, and $\boldsymbol{\nabla_\theta}$ is the gradient of the loss function with respect to $\boldsymbol{\theta}$

This mathematical framework describes the operations of a hybrid CNN-BiLSTM model, capturing the local features with CNN, reducing dimensionality with max pooling, and learning temporal dependencies with the BiLSTM layer, ultimately leading to the final output through the dense layer.

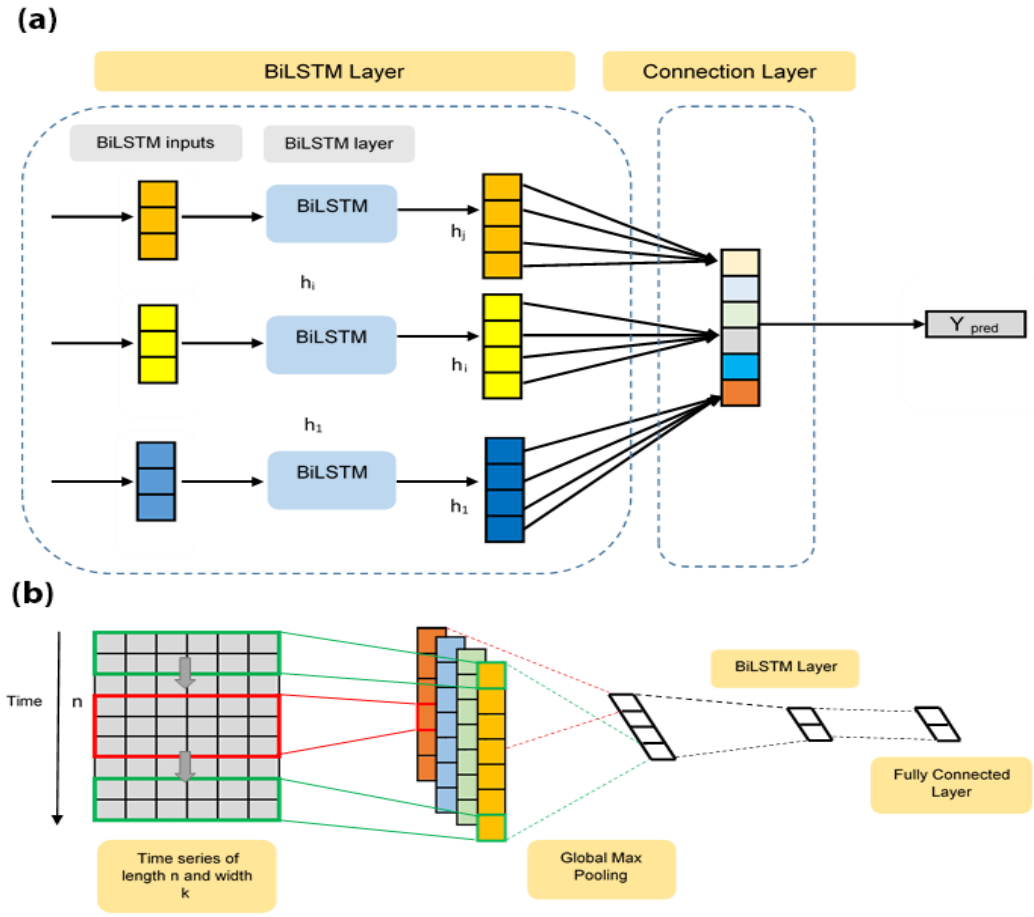

Figure IV.1: Representation of (a) BiLSTM and (b) hybrid CNN-BiLSTM model architecture.

IV.4.2. CNN-BiLSTM Model architecture and hyperparameters

The model architecture outlined in Table IV.3 is a carefully designed sequence of layers optimized for predicting the target variable, $\boldsymbol{N_u}$ $(\boldsymbol{kN})$. The model begins with an Input Layer that takes in the features of the dataset, with each feature represented in a 1-dimensional space. The Conv1D layer, which is the first processing layer, applies 64 filters with a kernel size of 1, utilizing the ReLU activation function. This layer is crucial for capturing local patterns and dependencies in the data. The small kernel size indicates that the model is focused on learning fine-grained details from each feature.

Following the convolutional layer, the MaxPooling1D layer is employed to down sample the output from the Conv1D layer. This reduces the dimensionality, helping the model generalize better by focusing on the most prominent features. The pooling size of 1 suggests that this operation is minimal, potentially retaining most of the convolutional output for subsequent layers.

The architecture then incorporates a BiLSTM (Bidirectional Long Short-Term Memory) layer with 50 units, again using the ReLU activation function. This layer is pivotal in capturing sequential patterns and temporal dependencies in the data, which is particularly useful in cases where the order or sequence of features plays a role in the prediction. The bidirectional nature of this LSTM allows the model to learn from both past and future information within the sequence, offering a comprehensive understanding of the input data.

Finally, the model concludes with a Dense layer that serves as the output layer, with a single unit to predict the target variable. The simplicity of this layer ensures that the model's predictions are directly related to the learned features from the preceding layers.

Table IV.4 details the hyperparameters that guide the training process of this model. The Adam optimizer is selected, known for its efficiency and adaptability in adjusting learning rates during training, which contributes to faster convergence. The choice of Mean Squared Error (MSE) as the loss function aligns with the goal of minimizing the difference between predicted and actual values, making it suitable for regression tasks like predicting $\boldsymbol{N_u}$ $(\boldsymbol{kN})$.

The model is trained for 100 epochs, allowing sufficient exposure to the data for the model to learn patterns without overfitting. The batch size of 32 strikes a balance between computational efficiency and the ability to generalize, as smaller batches help smooth out noise during the training process.

Regarding the data distribution, the model is trained on 70% of the data and tested on the remaining 30%, a standard split that ensures the model is well-evaluated on unseen data while being trained on a substantial portion of the dataset. This split also helps in assessing the model's generalizability and robustness.

In conclusion, the architecture and hyperparameters are thoughtfully chosen to maximize the model's ability to learn from the dataset and accurately predict the target variable, $\boldsymbol{N_u}$ $(\boldsymbol{kN})$. The combination of convolutional and LSTM layers, along with the Adam

optimizer and MSE loss function, provides a strong foundation for achieving high predictive performance in this research.

Table IV.3: Define CNN-BiLSTM model architecture.

Layer Name	Type	Parameters
Input Layer	-	Input Shape: (number of features, 1)
Conv1D	Convolutional 1D	Filters: 64, Kernel Size: 1, Activation: ReLU
MaxPooling1D	Max Pooling 1D	Pool Size: 1
BiLSTM	Bidirectional LSTM	Units: 50, Activation: ReLU
Dense	Fully Connected	Units: 1 (Output Layer)

Table IV.4: Define model hyperparameters.

Hyperparameter	Optimizer	Loss Function	Number of Epochs	Batch Size	Input Features	Training Set Size	Testing Set Size
Value	Adam	(MSE)	100	32	10	70%	30%

Several performance metrics were utilized to assess model effectiveness, including Mean Absolute Error (MAE), Root Mean Square Error (RMSE), Nash-Sutcliffe Efficiency (NSE), the Correlation Coefficient (R), and the Kling-Gupta Efficiency (KGE). Below are concise explanations of each performance measure.

$$MAE == \frac{1}{N}\sum_{i=1}^{N}[\left(N_{u_{o,i}}\right) - \left(N_{u_{s,i}}\right)] \tag{IV.52}$$

$$RMSE = \sqrt{\frac{1}{N}\sum_{i=1}^{N}\left[\left(N_{u_{o,i}}\right) - \left(N_{u_{s,i}}\right)\right]^2} \tag{IV.52}$$

$$NSE = 1 - \frac{\sum_{i=1}^{N}\left[\left(N_{u_{o,i}}\right) - \left(N_{u_{s,i}}\right)\right]^2}{\sum_{i=1}^{N}\left[QN_{u_{o,i}} - \overline{N_{u_o}}\right]^2} \tag{IV.53}$$

$$R = \frac{\sum_{i=1}^{N}\left(N_{u_{o,i}} - \overline{N_{u_o}}\right)\left(N_{u_{s,i}} - \overline{N_{u_s}}\right)}{\sqrt{\sum_{i=1}^{N}(N_{u_{obs,i}} - \overline{N_{u_{obs}}})^2 \sum_{i=1}^{N}(N_{u_{s,i}} - \overline{N_{u_s}})^2}} \quad \text{(IV.54)}$$

$$KGE = 1 - \sqrt{(r-1)^2 + (\beta-1)^2 + (\gamma-1)^2} \quad \text{(IV.55)}$$

Where:

$$\beta = \frac{\overline{N_{u_s}}}{\overline{N_{u_o}}} \quad \text{(IV.56)}$$

$$\gamma = \frac{STD_{N_{u}s} \Big/ \overline{N_{u_s}}}{STD_{N_{u}o} \Big/ \overline{N_{u_o}}} \quad \text{(IV.57)}$$

In these equations, $N_{u^{o,i}}$ *and* $N_{u^{s,i}}$ represent the observed and simulated observations, respectively. N is the sample size of the time series. $\overline{N_{u_o}}$, $\overline{N_{u_s}}$, $STD_{N_u o}$, and $STD_{N_u s}$ represent the mean values and standard deviation of the observed and simulated observations, respectively

IV.5. RESULTS OF DEEP LEARNING MODELS FOR $N_u(kN)$ PREDICTION

In this section using 12 scenarios with progressively more features to predict $\boldsymbol{N_u}$ $(\boldsymbol{kN})$ (Target) based on BiLSTM and CNN-BiLSTM. Before developing the predictive models, the database is divided into training and testing sets. Of those 168 samples (70%) are selected randomly of the training process, and 73 remaining samples (30%) are used for testing the performance of predictive models. Each model incorporates a different combination of features to see how they impact the prediction. The Table IV.5 below a summary of the models (M1 to M12) and their feature sets:

Table IV.5. Summary of the proposed inputs combinations suggested for $\boldsymbol{N_u}$ $(\boldsymbol{kN})$ prediction.

Model	Features	Scenarios	Impact on N_u (kN)
M1	Feature1	f_{co} (MPa)	Higher compressive strength typically results in higher structural capacity, which would influence the predictive model for N_u (kN). It's likely to be one of the most significant predictors in your model.
M2	Feature2	f_{co} (MPa), D (mm)	The diameter affects the load-bearing capacity and stiffness of the element. Larger diameters generally correlate with higher load capacities, making

			this an important feature for predicting structural performance.
M3	Feature3	$f_{co}\ (MPa), D\ (mm), H\ (mm)$	The height influences the buckling behavior and overall stability of the structure. In slender columns, the height-to-diameter ratio (slenderness ratio) is a key factor in determining the load capacity, and thus $N_u\ (kN)$.
M4	Feature4	$f_{co}(MPa), D\ (mm), H\ (mm), H/D$	Higher H/D ratios typically indicate greater susceptibility to buckling, especially in slender columns. This ratio is essential in stability analysis and directly influences the prediction of load-bearing capacity $N_u\ (kN)$.
M5	Feature5	$f_{co}\ (MPa), D\ (mm), H\ (mm), H/D, t_s\ (mm)$	Thicker FRP layers generally provide greater confinement and strength to the concrete element, which could significantly enhance the load capacity and influence the prediction of $N_u\ (kN)$.
M6	Feature6	$f_{co}\ (MPa), D\ (mm), H\ (mm), H/D\ , t_s\ (mm), D/t_s$	Lower D/ts ratios usually indicate better confinement, as a thicker FRP layer relative to the element's diameter improves the structural performance, leading to higher $N_u\ (kN)$ values.
M7	Feature7	$f_{co}\ \ (MPa), D\ (mm), H\ (mm), H/D,\ t_s\ (mm), D/t_s,\ f_y\ (MPa)$	Higher yield strength steel can significantly enhance the load-bearing capacity and ductility of the structural element, making it a key feature in predicting $N_u\ (kN)$
M8	Feature8	$f_{co}\ \ (MPa), D\ (mm), H\ (mm), H/D, t_s\ (mm), D/t_s, f_y\ (MPa), FRP\ type$	The type of FRP influences the effectiveness of the strengthening, with certain types (e.g., Carbon FRP) providing superior strength and stiffness compared to others (e.g., Glass FRP). This feature is important for capturing the variability in the

			performance of different FRP systems.
M9	Feature9	$f_{co}\ (MPa), D\ (mm),$ $H\ (mm), \frac{H}{D}, t_s\ (mm), D/t_s,$ $f_y\ (MPa), FRP\ type, E_{frp}\ (MPa)$	A higher modulus of elasticity means that the FRP is stiffer, providing greater resistance to deformation and improving the load-bearing capacity of the element. This feature will likely have a strong influence on the prediction of$N_u\ (kN)$.
M10	Feature10	$f_{co}\ (MPa), D\ (mm),$ $H\ (mm), H/D\ , t_s\ (mm), D/t_s\ ,$ $f_y\ (MPa), FRP\ type,\ E_{frp}\ (MPa)$ $f_{frp}\ (MPa)$	FRP with higher ultimate strength will contribute to greater overall capacity, affecting the prediction of $N_u\ (kN)$ by providing additional strength and ductility.
M11	Feature11	$f_{co}\ (MPa), D\ (mm),$ $H\ (mm), H/D\ , t_s\ (mm), D/t_s\ ,$ $f_y\ (MPa), FRP\ type, E_{frp}\ (MPa)$ $f_{frp}\ (MPa), t_{frp}\ (mm)$	The thickness of each laminate layer can influence the bonding and overall effectiveness of the FRP system, thereby impacting the load-bearing capacity and the predicted $N_u\ (kN)$.
M12	Feature12	$f_{co}\ (MPa), D\ (mm),$ $H\ (mm), H/D\ , t_s\ (mm), D/t_s\ ,$ $f_y\ (MPa), FRP\ type, E_{frp}\ (MPa)$ $f_{frp}\ (MPa), t_{frp}\ (mm),\ \varepsilon_{frp}$	The strain in the FRP provides insight into how much the FRP is deforming under load, which is crucial for understanding the load transfer mechanisms between the FRP and the concrete. It's an important feature for predicting $N_u\ (kN)$, particularly in scenarios involving high levels of deformation.

Each feature in this dataset plays a crucial role in predicting the ultimate load capacity $\boldsymbol{N_u\ (kN)}$ of the structural element. The features related to material properties (e.g., compressive strength, yield strength, modulus of elasticity) and geometric dimensions (e.g., diameter, height, thickness) are particularly important as they directly influence the structural behavior under load.

- Material Properties ($\boldsymbol{f_{co}, f_y, E_{frp}, f_{frp}, \varepsilon_{frp}}$): These properties define the strength and stiffness of the materials involved (concrete, steel, FRP), which are critical for accurate load capacity predictions.

- Geometric Dimensions ($\boldsymbol{D, H, t_s, t_{frp}}$): These dimensions determine the size, shape, and slenderness of the structural element, which affect stability and buckling behavior.
- Derived Ratios ($\boldsymbol{H/D}$, $\boldsymbol{D/t_s}$): These ratios provide insight into the stability and effectiveness of the structural design, influencing the element's capacity to bear loads.

By carefully analyzing and understanding these features, you can improve the accuracy and reliability of your predictive models for $\boldsymbol{N_u}$ ($\boldsymbol{kN}$).

In the comprehensive analysis of features for predicting the ultimate axial capacity of concrete columns reinforced with fiber-reinforced polymer (FRP), represented as $\boldsymbol{N_u}$ ($\boldsymbol{kN}$), several insights were gained regarding the relationships between input variables. Feature 2 (compressive strength of concrete, ($\boldsymbol{f_{co}}$) and Feature 3 (column diameter, *D*) emerged as the most influential predictors, demonsrating strong positive correlations with the target variable, $\boldsymbol{N_u}$ ($\boldsymbol{kN}$) (Figure IV.2). This suggests that the compressive strength of the concrete and the diameter of the column are critical factors in determining the axial load-carrying capacity. However, these features also exhibit high inter-correlations with each other and with Feature 6 (H/D ratio and the thickness of the concrete cover), indicating potential multicollinearity. Such high inter-correlations suggest that these features may carry overlapping information, which could lead to redundancy in the predictive model. To address this, dimensionality reduction techniques or careful feature selection may be necessary to enhance model performance and prevent overfitting (Figure IV.2).

Feature 1 ($\boldsymbol{f_{co}}$, the concrete compressive strength in MPa) also shows a positive correlation with $\boldsymbol{N_u}$ ($\boldsymbol{kN}$), though to a lesser extent than Feature 2 and Feature 3. Interestingly, Feature 1 has low correlations with other features, indicating that it may provide unique information to the model that is not captured by other predictors. This uniqueness could be valuable in improving the model's ability to generalize to new data.

Conversely, Feature 4 (the height-to-diameter ratio, $\boldsymbol{H/D}$) and Feature 12 (the FRP elastic modulus, $\boldsymbol{E_{frp}}$) show weak negative correlations with the target variable, implying that they have minimal inverse impacts on $\boldsymbol{N_u}$ ($\boldsymbol{kN}$). This could suggest that while these features are part of the structural characteristics of the column, their direct influence on the axial capacity might be less significant compared to other variables (Figure IV.2). Feature 5 (the thickness of the concrete cover, $\boldsymbol{t_s}$), despite a moderate negative correlation with Feature 6, appears to have a relatively low direct influence on the target variable. This might indicate that the concrete cover thickness, while important for durability and protection of reinforcement, may not be a primary factor in determining the axial load capacity.

Feature 11 (the type of FRP reinforcement, FRP type), although weakly correlated with the target, may still offer unique insights. Its generally low correlations with other features suggest that it could introduce additional variability into the model that is not accounted for by more strongly correlated features (Figure IV.2). This indicates the potential value of

including such features in the model, as they might capture aspects of the problem that are not immediately apparent from the more dominant predictors.

Overall, this analysis underscores the importance of balancing strong predictors with the potential for redundancy, ensuring that the model leverages the most informative variables while avoiding over-reliance on highly correlated features. Additionally, it highlights the need to consider the unique contributions of less correlated features, as they may capture important aspects of the relationship between the structural characteristics of the column and its axial capacity that are not evident from the more prominent predictors. By carefully selecting and possibly reducing features, the predictive model for $\boldsymbol{N_u}$ $(\boldsymbol{kN})$ can be optimized for both accuracy and robustness, ensuring reliable performance across a range of conditions.

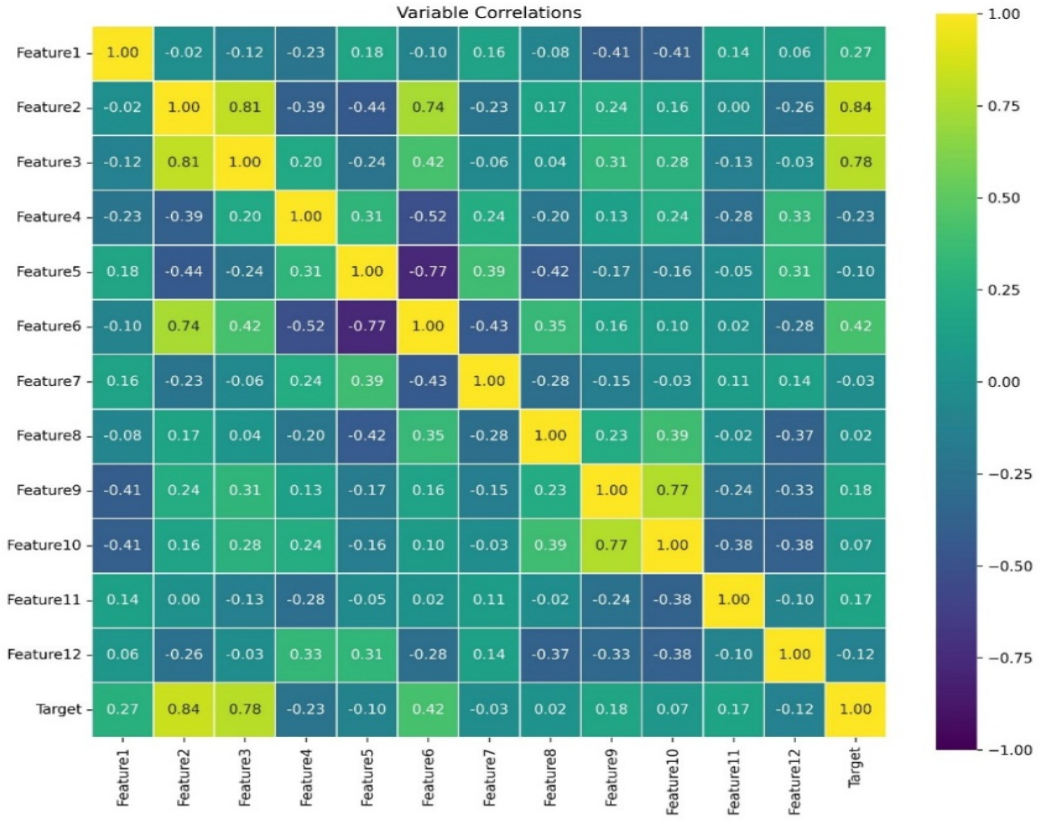

Figure IV.2: Pearson correlation heat map between suggested inputs combination and target.

The Root Mean Square Error (RMSE) results for the BiLSTM models reveal a clear trend in model performance improvement with the inclusion of more features (Table IV.6). Initially, Model M1, using only $\boldsymbol{f_{co}}$ $(\boldsymbol{MPa})$, shows high RMSE values of 1421.92 for training and 1452.667 for testing, indicating poor predictive accuracy. As additional features are introduced, starting with $\boldsymbol{D}$ $(\boldsymbol{mm})$ in Model M2 (training RMSE: 852.955, testing RMSE: 840.129) and continuing through $\boldsymbol{H}$ $(\boldsymbol{mm})$ in Model M3 (training RMSE: 650.116, testing RMSE: 600.584), $\boldsymbol{H/D}$ in Model M4 (training RMSE: 788.934, testing RMSE: 736.923), $\boldsymbol{t_s}$

(mm) in Model M5 (training RMSE: 804.694, testing RMSE: 786.178), $\boldsymbol{D/t_s}$ in Model M6 (training RMSE: 609.933, testing RMSE: 537.899), $\boldsymbol{f_y}$ $(\boldsymbol{MPa})$ in Model M7 (training RMSE: 609.428, testing RMSE: 547.444), $\boldsymbol{FRP\ type}$ in Model M8 (training RMSE: 569.28, testing RMSE: 505.02), $\boldsymbol{E_{frp}}$ $(\boldsymbol{MPa})$ in Model M9 (training RMSE: 525.481, testing RMSE: 473.508), $\boldsymbol{f_{frp}}$ $(\boldsymbol{MPa})$ in Model M10 (training RMSE: 539.219, testing RMSE: 486.46), $\boldsymbol{t_{frp}}$ $(\boldsymbol{mm})$ in Model M11 (training RMSE: 418.206, testing RMSE: 401.494), and $\boldsymbol{\varepsilon_{frp}}$ in Model M12 (training RMSE: 402.212, testing RMSE: 387.94), there is a noticeable decrease in RMSE for both training and testing datasets. This trend suggests that each additional feature contributes valuable information, helping the model capture the underlying patterns more effectively.

By Model M12, which incorporates all 12 features, the RMSE values reach their lowest point, demonstrating the highest accuracy in predictions. This model's close training and testing RMSE values indicate that it generalizes well and is not overfitting. The improvements across models reflect the importance of including diverse and comprehensive features to enhance predictive performance. The final model, M12, effectively utilizes the complete set of features to make the most accurate predictions for $\boldsymbol{N_u}$ $(\boldsymbol{kN})$, highlighting the significance of each feature in achieving optimal results.

The RMSE results for the CNN-BiLSTM models demonstrate a clear trend of improving performance as more features are incorporated. Model M1, which uses only $\boldsymbol{f_{co}}$ $(\boldsymbol{MPa})$, shows high RMSE values of 1145.455 for training and 1141.844 for testing, indicating limited predictive accuracy with minimal features. As additional features are added, such as $\boldsymbol{D}$ $(\boldsymbol{mm})$ in Model M2, RMSE values drop significantly to 431.687 for training and 475.457 for testing. Further inclusion of $\boldsymbol{H}$ $(\boldsymbol{mm})$ in Model M3 improves performance even more, with training and testing RMSEs of 323.604 and 380.175, respectively (Table .6). The trend continues with models M4 through M10, which progressively enhance predictive accuracy, with notable improvements in Models M9 and M10, where training RMSE reaches 277.751 and 275.48, and testing RMSEs are 381.925 and 331.812, respectively. The best performance is achieved with Model M11, which includes $\boldsymbol{t_{frp}}$ $(\boldsymbol{mm})$, showing the lowest RMSE values of 129.469 for training and 204.555 for testing, indicating the highest accuracy. Model M12, which adds $\boldsymbol{\varepsilon_{frp}}$, shows slightly higher RMSE values of 138.174 for training and 220.497 for testing but still maintains strong performance (Table 6). Overall, these results illustrate that incorporating a comprehensive set of features significantly enhances the CNN-BiLSTM model's ability to accurately predict $\boldsymbol{N_u}(\boldsymbol{kN})$, with Model M11 proving to be the most effective in capturing complex patterns and minimizing errors.

Table IV.6: Analysis of RMSE Results for BiLSTM and hydride CNN-BiLSTM models.

	BiLSTM		CNN-BiLSTM	
Model	**Training**	**Testing**	**Training**	**Testing**
M1	1421.92	1452.667	1145.455	1141.844
M2	852.955	840.129	431.687	475.457
M3	650.116	600.584	323.604	380.175
M4	788.934	736.923	327.327	411.927
M5	804.694	786.178	300.169	391.748
M6	609.933	537.899	301.683	432.32
M7	609.428	547.444	299.815	408.281
M8	569.28	505.02	317.284	436.525
M9	525.481	473.508	277.751	381.925
M10	539.219	486.46	275.48	331.812
M11	418.206	401.494	129.469	204.555
M12	402.212	387.94	138.174	220.497

The analysis of the RMSE improvement percentages for CNN-BiLSTM models compared to BiLSTM models reveals significant gains in predictive accuracy. The data demonstrates that the integration of convolutional layers with BiLSTM architecture substantially enhances performance, with improvements ranging from 13.56% to 69.04% in training RMSE and from 19.34% to 50.17% in testing RMSE (Figure IV.3). This substantial reduction in RMSE underscores the effectiveness of combining convolutional and bi-directional LSTM layers, which allows the model to better capture both complex spatial patterns and temporal dependencies within the data.

Specifically, models that include a more extensive set of features, such as Models M5, M10, M11, and M12, exhibit the most significant improvements. Model M11 stands out with the highest reductions, achieving a 69.04% decrease in training RMSE and a 49.05% reduction in testing RMSE. This model's performance highlights how integrating a full range of features with the CNN-BiLSTM architecture maximizes the model's ability to accurately predict $\boldsymbol{N_u}$ $(\boldsymbol{kN})$. Similarly, Model M12, while slightly less effective than M11, still shows considerable improvements with a 65.65% reduction in training RMSE and a 43.16% reduction in testing RMSE (Figure IV.3).

Models with fewer features also show notable improvements, indicating that even modest additions of convolutional layers can enhance predictive accuracy. For instance, Model M5 achieves a 62.70% reduction in training RMSE and a 50.17% reduction in testing RMSE, reflecting the value of adding CNN layers to the BiLSTM framework. The consistent trend of

improvement across various models highlights the hybrid CNN-BiLSTM approach's capability to leverage both spatial and temporal information more effectively than BiLSTM alone.

Overall, the results clearly demonstrate that the CNN-BiLSTM models significantly outperform their BiLSTM counterparts in terms of RMSE reduction. This hybrid model excels in providing more accurate predictions by integrating convolutional layers, which capture intricate feature interactions, with bi-directional LSTMs that handle temporal dependencies. The most substantial gains are observed with models that incorporate a comprehensive set of features, confirming the advantage of using a robust CNN-BiLSTM architecture for superior predictive performance.

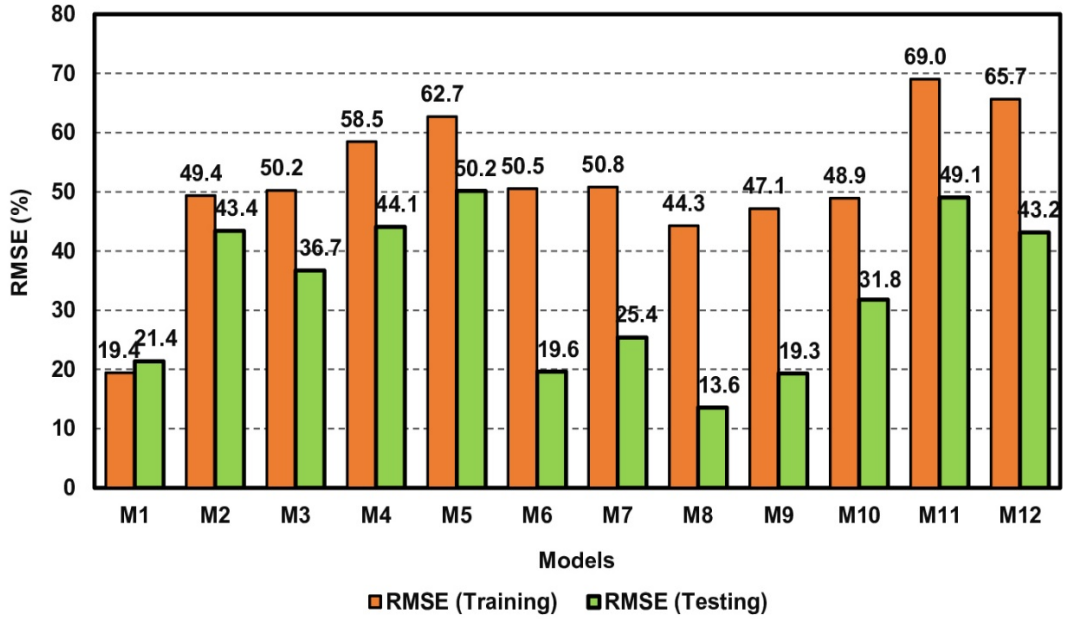

Figure IV.3: The analysis of RMSE improvement percentages for the CNN-BiLSTM models compared to BiLSTM.

Performance criteria are critical for evaluating and comparing the effectiveness of different deep learning models (Table 7). Key metrics include Root Mean Square Error (RMSE) and Mean Absolute Error (MAE), which measure the accuracy of predictions by quantifying the average magnitude of errors. The Nash-Sutcliffe Efficiency (NSE) assesses the predictive power of the model relative to the variance of the observed data, where values closer to 1 suggest higher predictive accuracy. The Pearson correlation coefficient (R) reflects the strength and direction of the linear relationship between predicted and observed values, with values near 1 indicating strong correlation. The Kling-Gupta Efficiency (KGE) is a composite metric that balances bias, variance, and correlation, providing a holistic view of model performance. The comparative analysis of performance metrics reveals that the CNN-

BiLSTM Model M11 significantly outperforms the BiLSTM Model M12 across all evaluated criteria. For training, CNN-BiLSTM Model M11 achieves a remarkable RMSE of 129.469 and an MAE of 96.588, with an NSE of 0.988, an RRR value of 0.995, and a KGE of 0.975, indicating exceptional predictive accuracy and reliability. In contrast, BiLSTM Model M12 has higher RMSE and MAE values of 402.212 and 255.728, respectively, with lower NSE, RRR, and KGE scores of 0.888, 0.95, and 0.798. The testing performance of the CNN-BiLSTM Model M11 is also superior, with an RMSE of 204.555 and an MAE of 150.589, maintaining high NSE (0.972), R (0.99), and KGE (0.924) values. Although these metrics are slightly lower than the training results, they still demonstrate strong generalization capabilities. Overall, the CNN-BiLSTM model provides a more accurate and reliable predictive performance compared to the BiLSTM model, highlighting the benefits of integrating convolutional layers with bi-directional LSTMs for improved model efficacy.

Table IV.7: Comparative analysis of the performance metrics for the BiLSTM and CNN-BiLSTM models.

		Model	RMSE	MAE	NSE	R	KGE
BiLSTM	Training	M12	402.212	255.728	0.888	0.95	0.798
	Testing	M12	387.94	238.561	0.899	0.952	0.853
CNN-BiLSTM	Training	M11	129.469	96.588	0.988	0.995	0.975
	Testing	M11	204.555	150.589	0.972	0.99	0.924

The analysis of RMSE percentage improvement reveals that the CNN-BiLSTM Model M11 substantially outperforms the BiLSTM Model M12. In training, Model M11 achieves a remarkable 67.81% reduction in RMSE compared to Model M12, reflecting a significant enhancement in predictive accuracy. For testing, the CNN-BiLSTM Model M11 shows a 47.27% improvement in RMSE over the BiLSTM Model M12. These improvements underscore the effectiveness of the CNN-BiLSTM approach in reducing error rates and enhancing model performance across both training and testing phases. The substantial reductions in RMSE highlight the CNN-BiLSTM model's superior capability to accurately predict N_u (kN), leveraging its advanced architecture to achieve more reliable and precise results.

To assess the performance of the BiLSTM and CNN-BiLSTM models, a detailed statistical comparison was conducted against the actual dataset. This comparison included the evaluation of maximum and minimum values, mean, variance, standard deviation, coefficient of variation, skewness, and kurtosis (Table IV.8).

The maximum value predicted by the CNN-BiLSTM model (7634.391) was slightly higher than the actual maximum (7309), suggesting that this model tends to predict extreme values more aggressively. Conversely, the BiLSTM model predicted a maximum value of 5151.561,

which is significantly lower than the actual maximum, indicating a more conservative approach in extreme value prediction. The minimum values predicted by both models were close to the actual minimum (849.8), with BiLSTM predicting a slightly lower minimum (799.9428) and CNN-BiLSTM a slightly higher one (807.7654) (Table IV.8). This suggests that both models maintain a reasonable approximation of the lower bounds but differ in their approach to the upper bounds. Mean: The mean values predicted by both models were close to the actual mean of 2451.244. The CNN-BiLSTM model provided a mean of 2481.973, which is marginally higher and closer to the actual data than the BiLSTM model's mean of 2384.736. This indicates that the CNN-BiLSTM model captures the central tendency of the data more accurately, whereas the BiLSTM model slightly underestimates it (Table IV.8).

Variance and standard deviation (STD) are critical metrics for understanding the spread and variability of the predictions. The actual data exhibited a variance of 1,485,179 and a standard deviation of 1,218.679. The CNN-BiLSTM model, with a variance of 1,734,362 and a standard deviation of 1,316.952, demonstrated greater variability than the actual data, suggesting that this model's predictions are more dispersed around the mean. In contrast, the BiLSTM model showed lower variance (1,150,528) and standard deviation (1,072.627), indicating more consistent and tightly clustered predictions. This difference in variability may reflect the CNN-BiLSTM model's ability to capture a broader range of the data distribution, albeit with more fluctuation. This is well represented by the violin plot of the actual data values and predicted values based on BiLSTM and CNN-BiLSTM (Figure IV.4)

The coefficient of variation (CV), which normalizes the standard deviation relative to the mean, provides insight into the relative variability of the predictions. The CV of the actual data was 0.497168. The CNN-BiLSTM model had a slightly higher CV of 0.530607, indicating a greater relative spread in its predictions compared to the actual data. The BiLSTM model, with a CV of 0.449788, exhibited lower relative variability, suggesting more consistent predictions relative to its mean.

Skewness measures the asymmetry of the distribution. The actual data exhibited a skewness of 1.555615, indicating a positive skew with a tail towards higher values. The CNN-BiLSTM model had a skewness of 1.646201, which closely mirrors the actual data's skewness, implying that this model captures the asymmetry in the distribution effectively. The BiLSTM model showed a lower skewness of 0.952724, indicating that its predictions are more symmetrically distributed around the mean, potentially underrepresenting extreme values. Kurtosis provides information about the "tailedness" of the distribution. The actual data had a kurtosis of 2.869253, suggesting a moderate level of peakedness. The CNN-BiLSTM model, with a kurtosis of 2.800561, closely approximated this characteristic, indicating that its predictions capture the distribution's peakedness and the likelihood of extreme values quite well. In contrast, the BiLSTM model had a significantly lower kurtosis of 0.402579, indicating a flatter distribution with fewer extreme outliers. The Figure IV.2 well

explain the correlation between the actual and predicted N_u output using BiLSTM, and CNN-BiLSTM for the best models, which clearly indicates that the CNN-BiLSTM well estimated the extreme values compared to BiLSTM model.

The comparison reveals that while both models provide reasonable approximations of the actual data, they differ in their statistical characteristics. The CNN-BiLSTM model tends to produce predictions that are more variable and closely aligned with the actual data in terms of skewness and kurtosis, making it better suited for capturing the distribution's shape and spread. On the other hand, the BiLSTM model offers more conservative and consistent predictions with lower variability and a more symmetric distribution. This suggests that the choice between these models should be informed by the specific requirements of the application, such as the need for capturing extreme values or maintaining consistent predictions.

Table IV.8: Comparison of statistical metrics between actual data, BiLSTM, and CNN-BiLSTM Models.

	Max	Min	Mean	Variance	STD	CV	Skewness	Kurtosis
Actual	7309	849.8	2451.244	1485179	1218.679	0.497168	1.555615	2.869253
BiLSTM	5151.561	799.9428	2384.736	1150528	1072.627	0.449788	0.952724	0.402579
CNN-BiLSTM	7634.391	807.7654	2481.973	1734362	1316.952	0.530607	1.646201	2.800561

To further evaluate the predictive performance of the BiLSTM and CNN-BiLSTM models, we employed a Taylor diagram analysis, which provides a comprehensive visual summary by considering standard deviation, correlation coefficient, and centered Root Mean Square Error (RMSE) (Figure IV.4). According to the table, the actual data exhibits a standard deviation of 1218.679. The BiLSTM model has a lower standard deviation of 1072.627, indicating less variability in its predictions compared to the actual values. On the other hand, the CNN-BiLSTM model shows a higher standard deviation of 1316.952, which is closer to the actual data but slightly overestimates the variability.

In terms of correlation coefficient, which is represented by the angle on the Taylor diagram, the BiLSTM model achieves a strong correlation of 0.9068 with the actual values, demonstrating that its predictions are generally accurate but slightly less aligned with the observed data. In contrast, the CNN-BiLSTM model achieves a near-perfect correlation of 0.9806, indicating that its predictions closely match the actual data, outperforming the BiLSTM model in this regard.

On a Taylor diagram, these observations would place the CNN-BiLSTM model closer to the actual data reference point, with a slightly larger radius (due to the higher standard deviation) but a smaller angular difference, reflecting its superior correlation. Meanwhile, the BiLSTM model, with its lower standard deviation, would appear further from the reference point in terms of correlation. This analysis confirms that the CNN-BiLSTM model offers better overall performance in terms of both capturing the variability of the data and providing more accurate predictions.

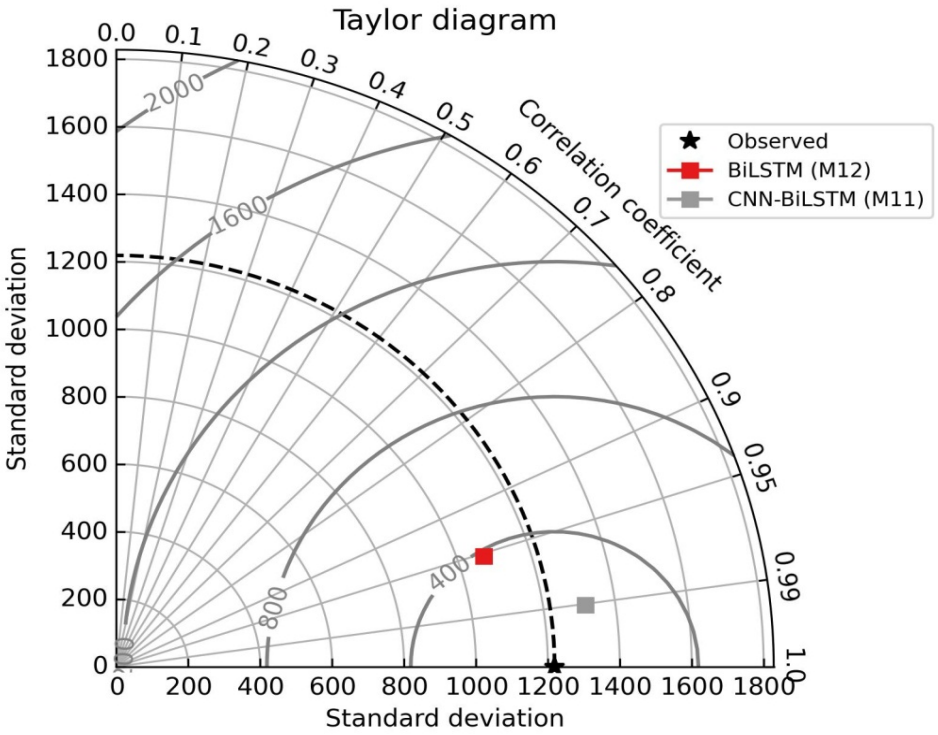

Figure IV.4: Violin plot of the actual data values and predicted values based on BiLSTM and CNN-BiLSTM.

Furthermore, the slope of the CNN-BiLSTM regression line being closer to 1 indicates that its predictions are more aligned with the actual values, with only a slight overestimation (Figure IV.5). The higher R^2 value further highlights the superior accuracy of the CNN-BiLSTM model, as it explains 98.06% of the variance in the actual values compared to the 90.68% explained by the BiLSTM model. These results highlight the enhanced predictive capability of the CNN-BiLSTM model, making it a more reliable tool for capturing the underlying patterns in the data and providing more accurate predictions.

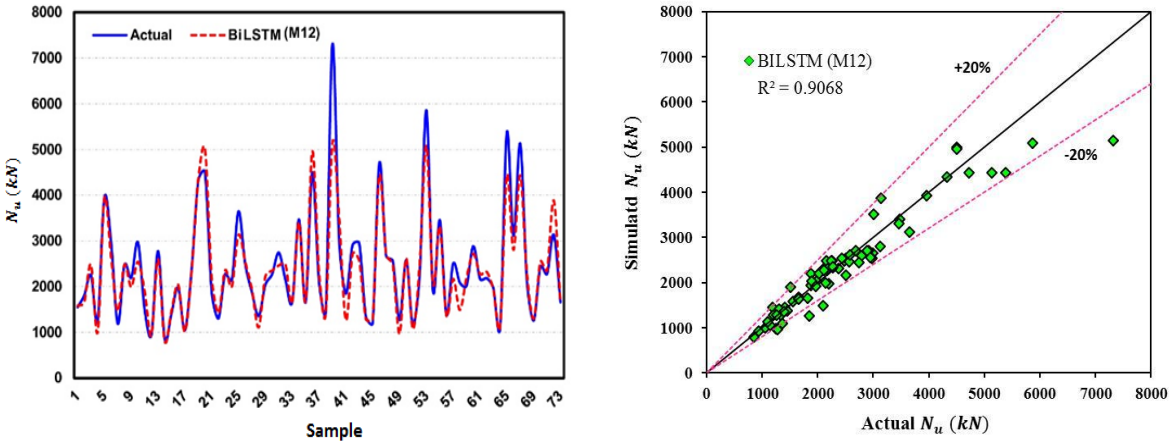

(a)

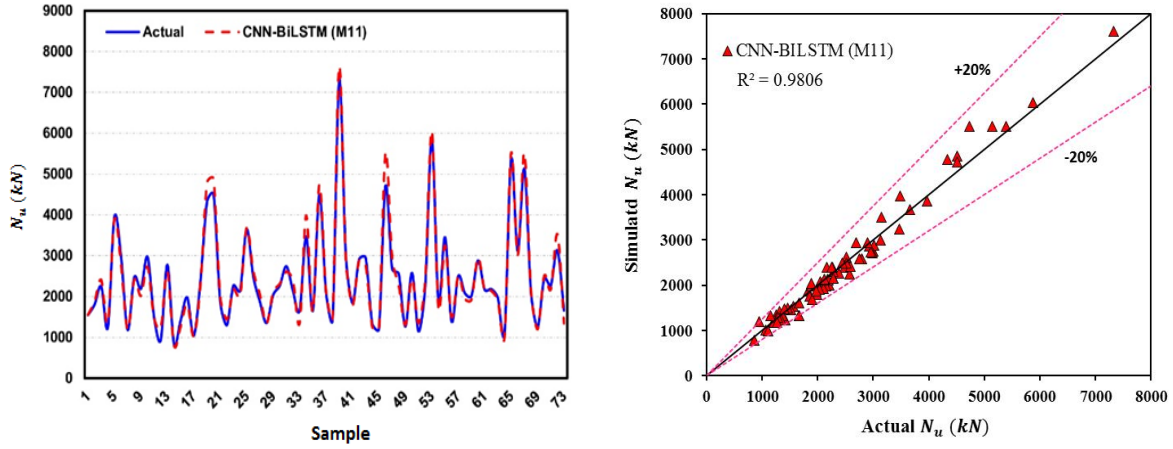

(b)

Figure IV.5: Correlation between the actual and predicted N_u output using (a) BiLSTM, and (b) CNN-BiLSTM for the best models during test phase.

IV.6. VALIDATION OF BILSTM AND CNN-BILSTM MODELS

The comparative evaluation of prediction models for FRP confined CFST columns highlights the remarkable performance of deep learning models, particularly the CNN-BiLSTM, when compared to traditional empirical models. The CNN-BiLSTM model demonstrates superior predictive accuracy, with a significantly lower RMSE of 204.555 and MAE of 150.589. Its performance is further validated by an impressive NSE of 0.972, a Pearson correlation coefficient (R) of 0.99, and a KGE of 0.924, indicating its robustness in modeling the complex behavior of FRP confined CFST columns (Table IV.8).

In contrast, the empirical models show a wide range of predictive accuracy. The model by Tao et *al*. (2007) has the highest RMSE of 949.523 and MAE of 874.451, indicating a significant deviation from observed data and lower predictive accuracy. The models proposed by Park et *al*. (2011), particularly Eq. (IV.8), show better performance among the empirical models, with RMSE values of 244.609 and 356.856, respectively, and relatively high NSE and KGE values. However, they still fall short when compared to the CNN-BiLSTM model. Similarly, the models by Che et *al*. (2012) and Lu et *al*. (2014) demonstrate moderate

performance, with RMSE values of 454.864 and 668.714, respectively, indicating that while they may be reasonably accurate, they do not match the precision of the ML-based models (Table IV.9).

The empirical model by Dong et *al*. (2017), with an RMSE of 1136.045 and MAE of 1033.141, exhibits poor predictive capability, underscored by a low NSE of 0.131 and KGE of 0.164. Ding et *al*. (2018) similarly show limited accuracy, with an RMSE of 640.256 and a modest NSE of 0.724. Among the empirical models, the worst performance is observed in the model by Tang et *al.* (2020), which not only has an extremely high RMSE of 7474.803 but also a negative NSE of -36.620, reflecting a model that fails to capture the underlying patterns in the data effectively. Ma et *al*. (2022) also presents suboptimal performance, with an RMSE of 1023.082 and a low NSE of 0.295, further emphasizing the limitations of empirical approaches (Table IV.9).

This comprehensive comparison underscores the effectiveness of deep learning models, particularly the CNN-BiLSTM, in predicting the behavior of FRP confined CFST columns with high accuracy. The substantial improvement in performance metrics across all indices, compared to empirical models, validates the CNN-BiLSTM model as a more reliable and precise tool for structural analysis and design in civil engineering. The empirical models, while valuable, are shown to be less capable of handling the complexities inherent in such predictions, thus supporting the transition towards advanced ML techniques in this domain.

Table IV.9: Performance of prediction models for FRP confined CFST columns.

	Models	Performance indices				
		RMSE	MAE	NSE	R	KGE
Machine learning-based models	BiLSTM (M12)	387.94	238.561	0.899	0.952	0.853
	CNN-BiLSTM (M11)	204.555	150.589	0.972	0.99	0.924
Empirical models	Tao et *al*. (2007)	949.522	874.451	0.393	0.976	0.366
	Park et *al*. (2011) Eq. (IV.5)	356.856	286.170	0.914	0.976	0.852
	Park et *al*. (2011) Eq. (IV.8)	244.608	189.112	0.960	0.982	0.910
	Che et *al*. (2012)	454.863	399.161	0.860	0.961	0.856
	Lu et *al*. (2014)	668.713	600.272	0.699	0.983	0.614
	Dong et *al*. (2017)	1136.044	1033.141	0.131	0.953	0.164
	Ding et *al*. (2018)	640.255	575.203	0.723	0.982	0.645
	Tang et *al*. (2020)	7474.803	3672.756	-36.620	-0.033	-0.420
	Ma et *al*. (2022)	1023.082	906.900	0.295	0.943	0.316

The comparison of statistical metrics between the actual data and various empirical models reveals significant variations in how these models capture the characteristics of FRP confined CFST columns (Table IV.10). The actual data exhibits considerable variability with a mean of 2451.3, a variance of 1,485,176, and a standard deviation of 1218.7, indicating a distribution with moderate relative variability (CV = 0.497), positive skewness (1.556), and kurtosis (2.869). Among the empirical models, the Park et *al*. (2011) Eq (IV.5) model closely mirrors the actual data with a high mean (2420.8), although it shows greater variability, as evidenced by its higher variance (2,034,875.4) and standard deviation (1426.5). On the other hand, models such as Tang et *al*. (2020) significantly deviate from the actual data, with extremely high maximum values and a variance (46,641,023.6) that far exceeds all other models, indicating a distribution with excessive relative variability (CV = 1.331) and extreme skewness (3.801) and kurtosis (16.912). Che et *al*. (2012) and Park et *al*. (2011) Eq (IV.8) also exhibit a closer alignment with the actual data in terms of mean values, but still show variations in terms of variance, skewness, and kurtosis, suggesting some discrepancies in capturing the distribution's tail behavior. In contrast, models like Dong et *al*. (2017) and Ding et *al*. (2018) present lower maximum values and reduced variability, which might limit their accuracy in predicting the actual data's broader range. This analysis highlights the strengths and limitations of various empirical models in modeling the behavior of FRP confined CFST columns, with certain models demonstrating better performance in capturing the central tendency while others struggle with representing the distribution's spread and extreme values (Table IV.10).

The empirical models exhibit varied performance in comparison to the actual data, with some aligning more closely with the distribution characteristics and others diverging significantly. Notably, when compared to the BiLSTM and CNN-BiLSTM models, the empirical models generally fall short in capturing the distribution's accuracy and variability (Table IV.10). For instance, the BiLSTM model has a mean (2384.7) and standard deviation (1072.6) that are closer to the actual data than most empirical models, with lower skewness and kurtosis, indicating a more accurate representation of the data's central tendency and distribution shape (Table IV.10). The CNN-BiLSTM model further improves upon this, with a mean (2482.0) and standard deviation (1317.0) that not only match the actual data more closely but also exhibit skewness (1.646) and kurtosis (2.801) values that better capture the data's distribution tail behavior (Table IV.9). In contrast, empirical models like Tang et *al*. (2020) and Dong et *al*. (2017) show significant deviations in these metrics, with Tang et *al*. (2020) displaying extreme values and high variability, which starkly contrasts the more stable and accurate predictions provided by the BiLSTM and CNN-BiLSTM models. This comparison underscores the superior predictive capabilities of the deep learning models in representing the complex behavior of FRP confined CFST columns (Table IV.10 and Figure IV.6).

Table IV.10: Comparison of statistical metrics between actual data, BiLSTM, CNN-BiLSTM, and empirical models.

	Max	Min	Mean	Variance	STD	CV	Skewness	Kurtosis
Actual	7309	849.8	2451.3	1485176.0	1218.7	0.497	1.556	2.869
BiLSTM	5151.6	799.9	2384.7	1150528.0	1072.6	0.450	0.953	0.403
CNN-BiLSTM	7634.4	807.8	2482.0	1734362.4	1317.0	0.531	1.646	2.801
Tao et *al*. (2007)	4957.2	418.2	1576.8	870476.3	933.0	0.592	1.596	2.217
Park et *al*. (2011) Eq. (IV.5)	7769.4	664.7	2420.8	2034875.4	1426.5	0.589	1.659	2.551
Park et *al*. (2011) Eq. (IV.8)	6634.4	696.0	2412.2	1257311.3	1121.3	0.465	1.369	2.257
Che et *al*. (2012)	6590.8	623.2	2159.5	1585979.1	1259.4	0.583	1.480	1.928
Lu et *al*. (2014)	5567.6	509.0	1851.0	1015304.9	1007.6	0.544	1.556	2.309
Dong et *al*. (2017)	4580.6	355.7	1418.1	750843.1	866.5	0.611	1.784	3.130
Ding et *al*. (2018)	5678.0	520.9	1876.0	1072372.4	1035.6	0.552	1.550	2.228
Tang et *al*. (2020)	43853.0	363.7	5132.6	46641023.6	6829.4	1.331	3.801	16.912
Ma et *al*. (2022)	4824.9	388.1	1544.4	820730.2	905.9	0.587	1.791	3.313

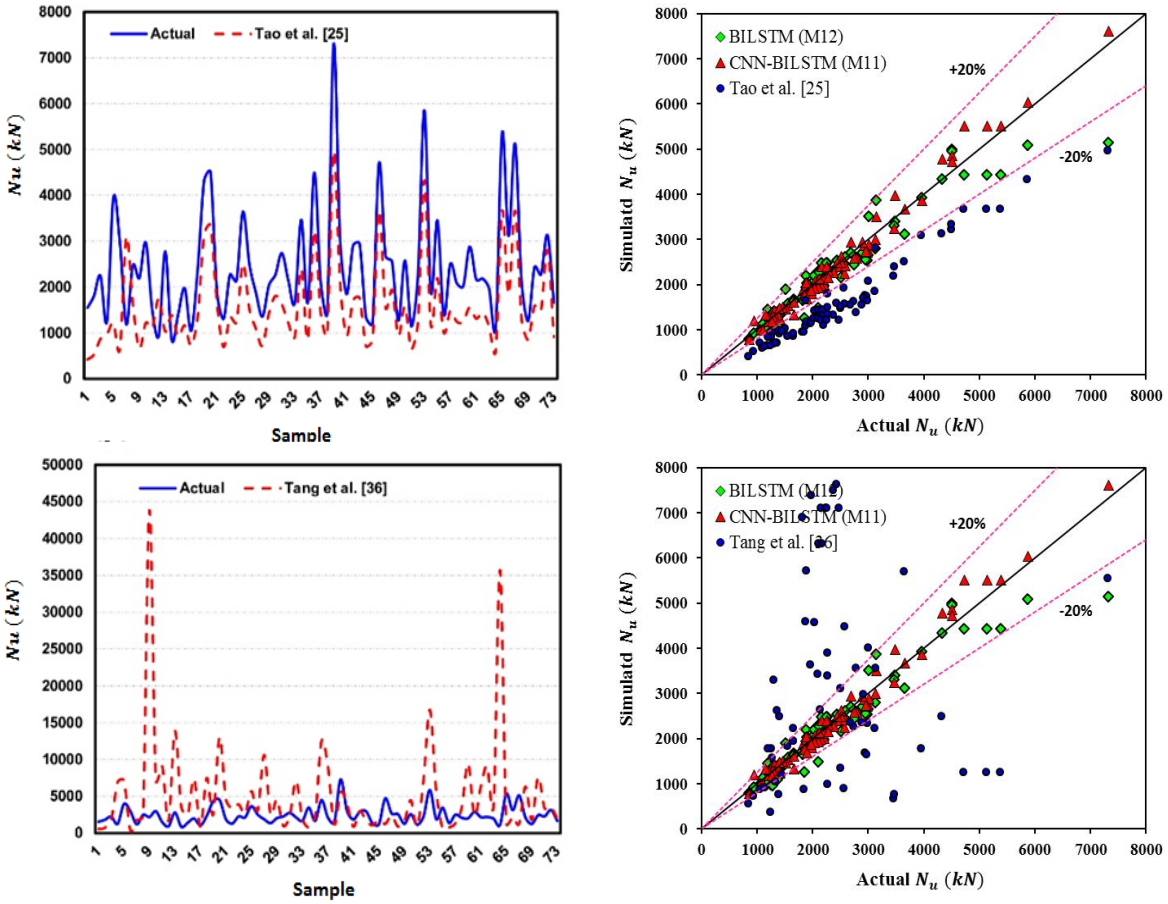

Figure IV.6: Comparison of BiLSTM and CNN-BiLSTM models with existing empirical models.

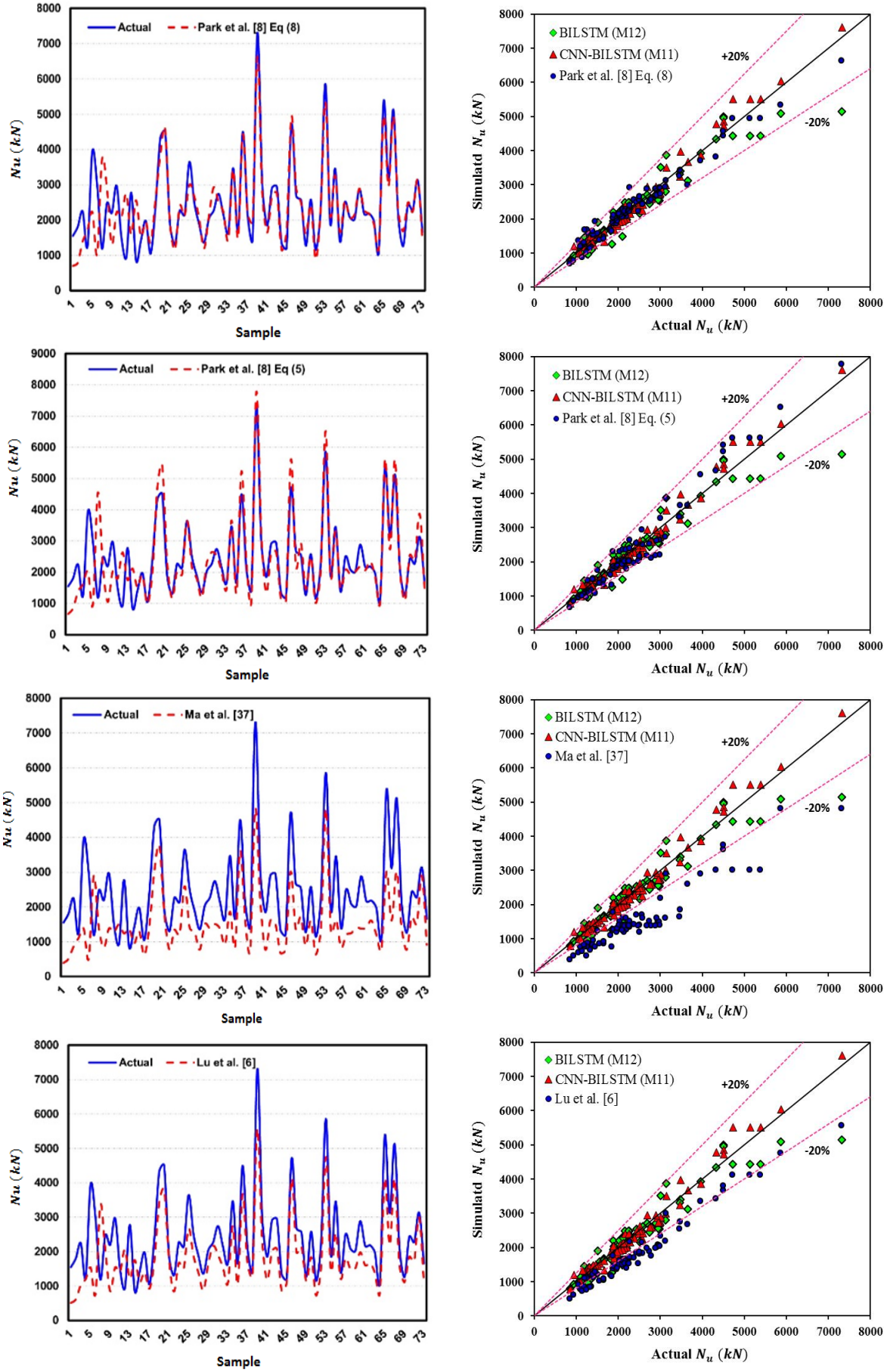

Figure IV.6: *Continued*

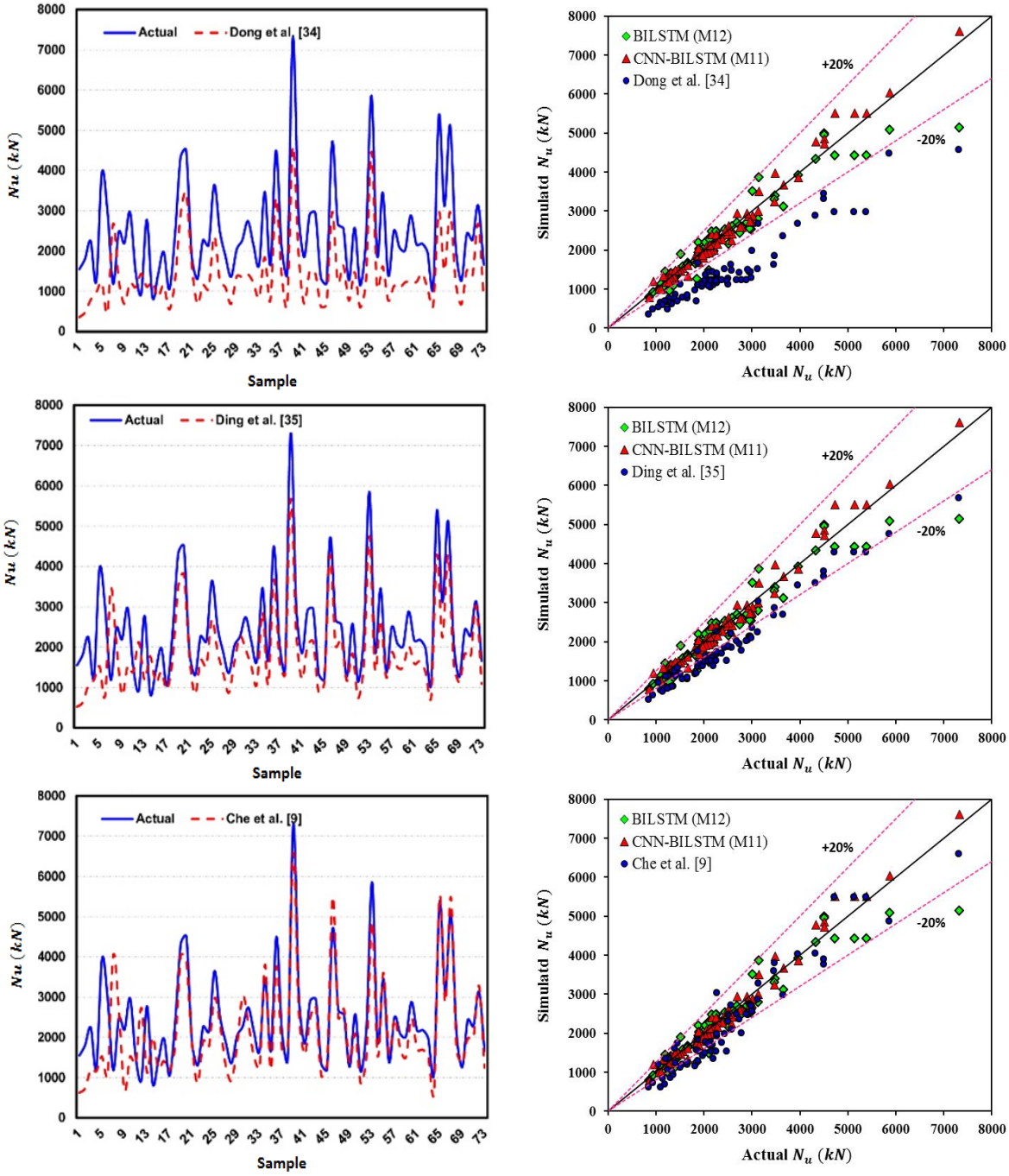

Figure IV.6: *Continued*

In the comparative analysis of various prediction models for FRP confined CFST columns, a comprehensive evaluation was performed using key statistical metrics, including the R, STD, and RMSE. The Taylor diagram, an effective graphical representation, was utilized to visualize the performance of these models, providing insights into their predictive accuracy and reliability (Figure IV.7). The deep learning-based models, particularly the BiLSTM (M12) and CNN-BiLSTM (M11), demonstrated superior performance compared to empirical models. The CNN-BiLSTM model (M11) achieved the highest correlation coefficient (R = 0.99), indicating an excellent agreement with the actual data, along with a moderate normalized standard deviation (1.08), suggesting a slight overestimation of variability. Its

RMSE of 204.555 further emphasizes its predictive accuracy, making it the most robust model in this study. In contrast, the empirical models displayed varied performance. For instance, the model by Tao et *al*. (2007) showed a relatively high correlation (R = 0.976) but was associated with a lower normalized standard deviation (0.77), indicating an underestimation of data variability, alongside a significantly higher RMSE (949.522). Similarly, the model by Park et *al*. (2011), using Equation (5), had a strong correlation (R = 0.976) but exhibited the highest normalized standard deviation (1.17) among the empirical models, reflecting an overestimation of variability, although its RMSE (356.856) was notably lower than that of Tao et *al*. (2007) (Figure IV.7).

Other empirical models, such as those by Che et *al*. (2012) and Lu et *al*. (2014), presented balanced performance, with Che et *al*. (2012) achieving a correlation of 0.961 and a normalized standard deviation close to unity (1.03), coupled with a moderate RMSE (454.864). Meanwhile, the model by Tang et *al*. (2020) markedly underperformed, with a negative correlation (R = -0.033) and an excessively high normalized standard deviation (5.61), reflecting significant predictive inaccuracy (Figure IV.7). This analysis underscores the efficacy of advanced deep learning models, particularly the CNN-BiLSTM, in capturing the complex behavior of FRP confined CFST columns. These models consistently outperformed traditional empirical approaches, offering more reliable and precise predictions. The results suggest that the integration of deep learning techniques, especially those incorporating bidirectional LSTMs and convolutional layers, can significantly enhance the prediction of structural performance, thereby advancing the field of civil engineering modeling.

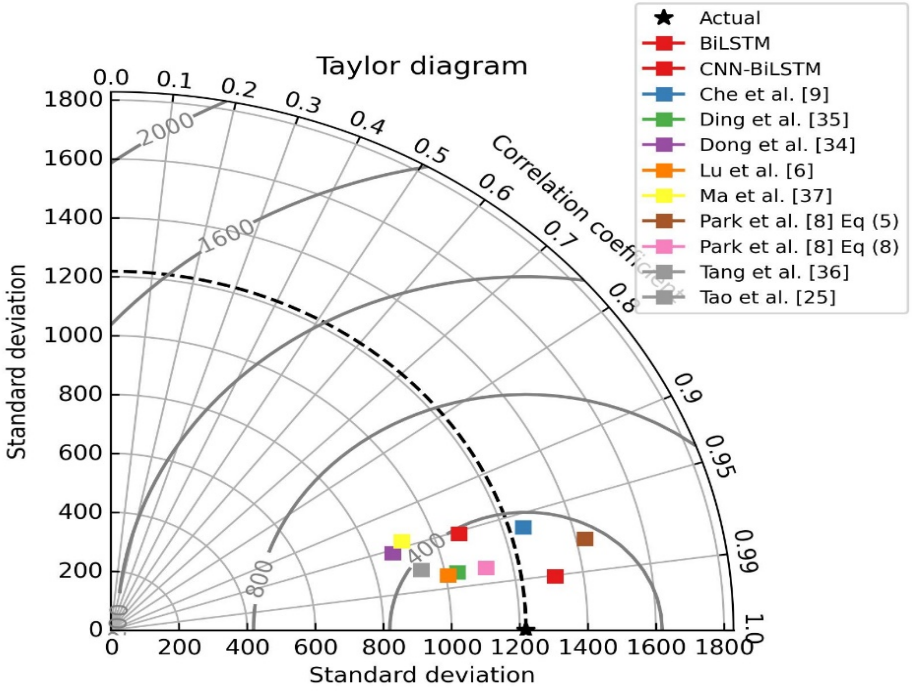

Figure IV.7: Violin plot for comparison of BiLSTM and CNN-BiLSTM models with existing empirical models.

IV.7. CONCLUSION

The research work presented in this chapter offers a comprehensive investigation into the prediction of the axial load-carrying capacity (ALCC) of Fiber Reinforced Polymer (FRP)-confined Concrete-Filled Steel Tubes (CFST) under axial compression using hybrid deep learning (HDL) approaches. A large dataset comprising 255 experimental results of FRP-confined CFST samples subjected to axial compression loads was compiled from previous literature. Based on this database, deep learning models, specifically a hybrid CNN-BiLSTM model and a traditional BiLSTM model were developed to predict the ALCC of strengthened columns with a hybrid confinement system (FRP wraps–steel tube).

The deep learning models, particularly the CNN-BiLSTM, outperformed the traditional BiLSTM model, demonstrating significant improvements in prediction accuracy. The CNN-BiLSTM model achieved the lowest root mean square error (RMSE) of 204.555 and a mean absolute error (MAE) of 150.589, indicating its superior predictive capability compared to empirical models. For example, CNN-BiLSTM outperformed empirical models such as that proposed by Tao et *al.* (2007), which reported an RMSE of 949.523 and an MAE of 874.451, highlighting the advantage of advanced deep learning models in addressing complex prediction tasks.

Empirical models, while valuable, exhibited greater deviations compared to deep learning models. For example, the model proposed by Park et *al*. (2011) (Eq. (8)) provided more accurate predictions than other empirical approaches but still fell short when compared to the CNN-BiLSTM results.

The next chapter focuses on the finite element analysis of axially loaded FRP-confined concrete-filled steel tube columns in order to numerically simulate their structural response and examine the influence of key governing parameters.

CHAPTER V:

Finite Element Analysis of Axially Loaded FRP-Confined Concrete Filled Steel Tube Columns

V.1. INTRODUCTION

Previous studies have primarily focused on predicting the axial strength and axial strain of FRP-confined concrete columns under concentric loading. However, limited research has been conducted on predicting the axial load-carrying capacity and ductility of hybrid FRP–steel tube confined concrete columns. The present chapter aims to investigate the structural behavior of fiber-reinforced polymer (FRP) wrapped concrete-filled steel tube (CFST) columns under axial concentric loading by employing a finite element analysis (FEA) model capable of accurately predicting axial load-carrying capacity and ductility. To achieve this, a total of 40 experimental tests on FRP-confined CFST columns, collected from previous studies, were simulated using the ABAQUS software package. The FEA results were then compared with experimental data from the 40 FRP-confined CFST specimens. Additionally, a detailed parametric study was conducted using the FEA model to investigate the effects of two parameters such as diameter-to-thickness ratio (D/t_s) and height-to-diameter ratio (H/D) ratio on the load-carrying capacity and ductility of the columns.

In this chapter, the work was carried out in collaboration with Dr. Asma Yasseen Hamed from the Construction and Building Department, Higher Institute of Engineering and Technology, Luxor, Egypt. We express our sincere gratitude to her for the valuable guidance and support provided throughout the finite element analysis phase using ABAQUS software. Dr. Hamed generously offered detailed explanations and practical insights that greatly enhanced the quality of the modelling process. She assisted me, in understanding how to accurately simulate all the experimental specimens and extract reliable FE results. In addition, she provided several instructional videos to further illustrate the modelling steps and clarify essential procedures. Her contributions were instrumental in advancing the numerical analysis presented in this chapter, and her expertise significantly strengthened the methodological robustness of the study.

V.2. EXPERIMENTAL TEST DATASET

The experimental database used in this study is derived from the comprehensive dataset that was developed in Chapter IV, ensuring consistency in data structure and parameter selection. The final dataset includes 40 experimental results on FRP-wrapped CFST columns subjected to concentric axial loading, collected from five key references (Gu et *al.* 2004; Che et *al*. 2012; Wei et *al*. 2014; Ding et *al*. 2018; Na et *al*. 2018), as summarized in Table V.1. None of the specimens contained internal steel reinforcement. Each column is defined by its designation, FRP type (CFRP or BFRP), geometric properties (height H, diameter D, steel

tube thickness (t_s), FRP thickness (t_{frp}), and number of layers (n_f), and material characteristics including steel yield strength (f_y), FRP tensile strength (f_{frp}), FRP elastic modulus (f_{frp}), and concrete compressive strength (f_c'). As presented in Table V.1, the concrete compressive strength varied between 31.2 and 57.4 MPa, while the steel tubes exhibited yield strengths of 310–365 MPa. The CFRP and BFRP materials used across the studies demonstrated tensile strengths ranging from 1260 to 4500 MPa, with single-layer FRP thicknesses between 0.111 and 0.167 mm. The diameter-to-thickness ratio (D/t_s) of the steel tubes ranged from 17.7 to 84.7, and the height-to-diameter ratio (H/D) varied from 3.00 to 16.00 across the entire dataset.

Table V.1: Details of modeled FRP-confined CFST specimens.

Specimen designation	FRP type	Geometric Properties							Material Properties			
		H	D	t_s	D/t_s	H/D	t_f	n_f	Steel	FRP		Concrete
		mm	mm	mm			mm		f_y MPa	f_f MPa	E_f GPa	f_c' MPa
Gu et *al.* (2004)												
1-1.5	CFRP	400	127	1.5	84.7	3.15	0.167	1	350	1260	230	40.15
1-2.5	CFRP	400	129	2.5	51.6	3.10	0.167	1	350	1260	230	40.15
1-3.5	CFRP	400	131	3.5	37.4	3.05	0.167	1	310	1260	230	40.15
1-4.5	CFRP	400	133	4.5	29.6	3.00	0.167	1	310	1260	230	40.15
2-1.5	CFRP	400	127	1.5	84.7	3.15	0.167	2	350	1260	230	40.15
2-2.5	CFRP	400	129	2.5	51.6	3.10	0.167	2	350	1260	230	40.15
2-3.5	CFRP	400	131	3.5	37.4	3.05	0.167	2	310	1260	230	40.15
2-4.5	CFRP	400	133	4.5	29.6	3.00	0.167	2	310	1260	230	40.15
Che et *al.* (2012)												
CSC A-2	CFRP	381	127	1.5	84.7	3.00	0.167	2	330	4500	228	36.2
CSC B-1	CFRP	387	129	2.5	51.6	3.00	0.167	1	330	4500	228	36.2
CSC B-2	CFRP	387	129	2.5	51.6	3.00	0.167	2	330	4500	228	36.2
CSC C-2	CFRP	393	131	3.5	37.4	3.00	0.167	2	330	4500	228	36.2
Wei et al. (2014)												
C-B1-3.0	BFRP	400	133	3.0	44.3	3.01	0.111	1	365	4067	239	31.2
C-B2-3.0	BFRP	400	133	3.0	44.3	3.01	0.111	2	365	4067	239	31.2
C-C1-3.0	CFRP	400	133	3.0	44.3	3.01	0.111	1	365	4067	239	31.2
C-C2-3.0	CFRP	400	133	3.0	44.3	3.01	0.111	2	365	4067	239	31.2
C-B1-4.5	BFRP	400	133	4.5	29.6	3.01	0.111	1	365	4067	239	34.7
C-B2-4.5	BFRP	400	133	4.5	29.6	3.01	0.111	2	365	4067	239	34.7
C-C1-4.5	CFRP	400	133	4.5	29.6	3.01	0.111	1	365	4067	239	34.7

C-C2-4.5	CFRP	400	133	4.5	29.6	3.01	0.111	2	365	4067	239	34.7
C-B1-6.0	BFRP	400	133	6.0	22.2	3.01	0.111	1	365	4067	239	34.7
C-B2-6.0	BFRP	400	133	6.0	22.2	3.01	0.111	2	365	4067	239	34.7
C-C1-6.0	CFRP	400	133	6.0	22.2	3.01	0.111	1	365	4067	239	34.7
C-C2-6.0	CFRP	400	133	6.0	22.2	3.01	0.111	2	365	4067	239	34.7
C-B1-7.5	CFRP	400	133	7.5	17.7	3.01	0.111	1	365	4067	239	34.7
C-B2-7.5	CFRP	400	133	7.5	17.7	3.01	0.111	2	365	4067	239	34.7
C-C1-7.5	CFRP	400	133	7.5	17.7	3.01	0.111	1	365	4067	239	34.7
C-C2-7.5	CFRP	400	133	7.5	17.7	3.01	0.111	2	365	4067	239	34.7
Ding et *al*. (2018)												
C3ST1-A	CFRP	900	299	3.7	79.7	3.01	0.167	1	311	3481	245	39.3
C3ST1-B	CFRP	900	305	3.7	80.9	2.95	0.167	1	311	3481	245	39.3
C3ST2-A	CFRP	900	300	3.6	81.7	3.00	0.167	2	311	3481	245	39.3
C3ST2-B	CFRP	900	299	3.7	80.8	3.01	0.167	2	311	3481	245	39.3
C5ST1-B	CFRP	900	300	3.7	80.4	3.00	0.167	1	311	3481	245	57.4
C5ST2-A	CFRP	900	299	3.7	79.9	3.01	0.167	2	311	3481	245	57.4
C5ST2-B	CFRP	900	300	3.6	81.5	3.00	0.167	2	311	3481	245	57.4
Na et *al*. (2018)												
2C-3.5	CFRP	588	168	6.0	28.0	3.50	0.111	2	243	3550	250	38.0
2C-6	CFRP	1008	168	6.0	28.0	6.00	0.111	2	243	3550	250	38.0
2C-8	CFRP	1344	168	6.0	28.0	8.00	0.111	2	243	3550	250	38.0
2C-12	CFRP	2016	168	6.0	28.0	12.0	0.111	2	243	3550	250	38.0
2C-16	CFRP	2688	168	6.0	28.0	16.0	0.111	2	243	3550	250	38.0

V.3. 3D FINITE ELEMENT SIMULATION

In structural engineering research, three-dimensional (3D) finite element (FE) simulations play a pivotal role in interpreting experimental data and understanding the behavior of concrete compression members reinforced with FRP and steel tube materials. Accurate numerical models can predict the initiation and propagation of cracks, identify various failure modes, assess the influence of key governing parameters, and provide explanations for experimental observations that are difficult or impossible to measure directly. Realistic and reliable models must capture the complex behavior of concrete, including its nonlinear compressive response, post-cracking tensile behavior, and the bond-slip interactions at the FRP-steel-concrete interfaces. The primary objective of this chapter is to develop a 3D nonlinear finite element model capable of predicting the behavior of CFST columns externally strengthened with FRP wraps under axial compression. To achieve this goal,

commercial finite element analysis (FEA) software ABAQUS was employed. In this context, A detailed 3D model was developed, incorporating the column's geometry, material properties, and boundary conditions. Experimentally obtained stress–strain relationships for FRP-wrapped CFST columns were incorporated into the model to ensure realistic material behavior under different loading conditions. The simulation was carefully designed to replicate the actual performance of the columns under axial loading. This analysis provided key insights into the structural behavior, including the ultimate axial capacity and the axial load–strain response, as reported by Thai et *al*. (2014) and Mansour et *al*. (2024).

V.3.1. Types of elements and meshing strategy

The behavior of FRP-confined CFST columns under axial compression loads was simulated using a finite element model developed in ABAQUS. The concrete core was simulated by 8-node linear brick elements (C3D8R), while the steel tubes and FRP wraps were simulated using 4-node doubly curved thin shell elements (S4R) Hassanein et *al*. (2018) and Mansour et *al*. (2024). The interaction between the inner steel tube surface and the outer concrete surface was modeled in ABAQUS using a surface-to-surface contact approach (Mansour et *al.* 2024). For the normal direction, a hard contact condition was applied to ensure complete transfer of compressive forces while preventing tensile stress transmission across the interface. The tangential behavior was defined using Coulomb friction, with a coefficient of 0.6, following the recommendations of Tao et *al*. (2013), Tam et *al*. (2023), and Mansour et *al*. (2024). Experimental observations indicated no debonding between the FRP strengthening sheets and the steel tube surfaces; therefore, a perfect bond (tie) interaction was used to connect the FRP to the steel, designating the steel as the master surface and the FRP as the slave surface.

The performance of the proposed model, as well as the required computational time, strongly depends on the selection of the element type for each component of the FRP-strengthened CFST columns. Moreover, an appropriate mesh size setting helps resolve convergence issues that could prevent the completion of the model and ensures effective load transfer Mansour et *al*. (2024). In the present model, the mesh size was set to approximately 1/15 of the diameter of the CFST tubular column, in accordance with the recommendations of Tao et *al*. (2013) and Mansour et *al*. (2022). Details regarding the element types, mesh size, and boundary conditions are shown in Figure V.1. Additionally, the bottom surface of the column was fully restrained, preventing any translation or rotation to properly define the boundary conditions. The displacement at the reference point (RP2) was allowed only in the direction of axial loading, while displacements along the X and Y axes and all rotational degrees of freedom (URx, URy, URz) were fixed at zero; the axial displacement (Uz) remained free to vary. Using a displacement-controlled approach, a concentrically applied axial compressive force was introduced through the upper reference point (RP1). To ensure

uniform compression, this reference point was linked to the top surface of the uppermost tube. The axial displacement load was applied along the Z-axis at the reference point.

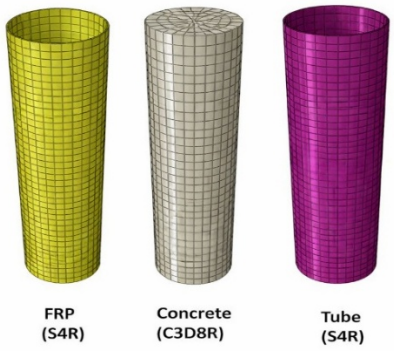

a) Concrete, steel and FRP elements

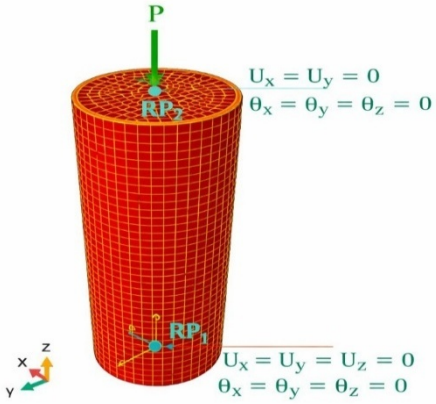

c) Boundary condition and loading

Figure V.1: Detail of FE simulation of FRP-confined CFST columns.

V.3.2. Material Modeling

V.3.2.1. Confined concrete

In CFST columns strengthened externally with FRP wraps, the concrete core must be simulated as confined concrete since it is restrained simultaneously by the combined effect of steel tube and the FRP wraps as seen in Figure V.2.

The confined concrete stress–strain behavior was modeled following the approach proposed by Tao et *al.* (2011, 2013). To accurately capture the response of confined concrete, three distinct regions were defined, as illustrated in Figure V.2. The first region represents the linear elastic stage, corresponding to the initial elastic stress range from point O to point A. Within this stage, the concrete's modulus of elasticity (E_c) and Poisson's ratio (υ) must be specified. The value of E_c was calculated using Eq. (V.1) in accordance with the ACI guidelines (ACI 2008), while υ was taken as 0.20, consistent with the findings of Tao et *al.* (2013).

$$E_c = 4700\sqrt{f_{co}} \tag{V.1}$$

Where $f_{co}(MPa)$ is the compressive strength of concrete cylinder.

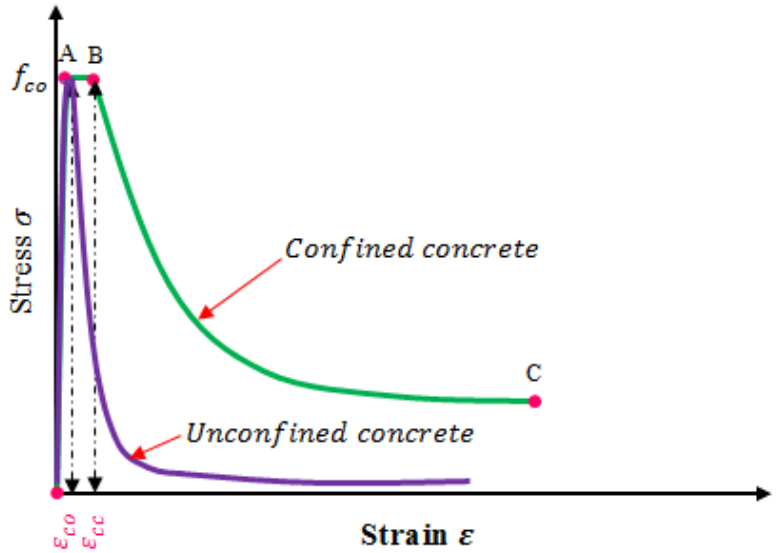

Figure V.2: confined concrete behavior

In addition, within the first region, the confining influence of the steel tube and FRP wrap on the concrete was neglected, so the core concrete exhibited behavior similar to that of unconfined concrete. Accordingly, the ascending portion of the stress–strain curve, was defined using the model proposed by Samani and Attard (2012) (Eq. V.2).

$$\frac{f}{f_{co}} = f_o \left(\frac{\left(\frac{\varepsilon_x}{\varepsilon_0}\right) r}{r - 1 + \left(\frac{\varepsilon_x}{\varepsilon_0}\right)^r} \right) \tag{V.2}$$

$$r = \frac{E_c}{E_c - \left(\frac{f_o}{\varepsilon_0}\right)} \tag{V.3}$$

Where, f is the compressive stress corresponding to compressive strain ε_x; f_o and ε_c represent the peak stress of the confined concrete, and ε_o represent the peak strain of concrete under uniaxial compression for circular FRP-confined CFST columns, determined using the expression of (Nicolo et *al*. 1994):

$$\varepsilon_o = 0.00076 + \sqrt{(0.626 f_{co} - 4.33) \times 10^{-7}} \tag{V.4}$$

After reaching the peak compressive stress (f_{co}) at point A, the plateau stage (AB), the second zone, will be initiated. The plateau zone defines the plastic progress of the core concrete after reaching peak stress. Then, the stain continues to increase until the core concrete's lateral expansion was stopped by steel tube and FRP wraps. At point (B), the strain is determined using the expression given by Eq (V.5) suggested by Samani and Attard (2012)

$$\frac{\varepsilon_{cc}}{\varepsilon_{co}} = e^{k}\,, \quad k = (2.9224 - 0.00367 f_{co}) \left(\frac{f_B}{f_{co}}\right)^{0.3124+0.002 f_{co}} \tag{V.5}$$

At point B, f_B represents the confining stress acting on the concrete core due to the combined effects of the FRP wraps and the steel tube. Tao et *al*. (2013) provided the following equation to calculate the confining stress of the core concrete (f_B)

$$f_B = \frac{\left(1 + 0.027 f_y\right) e^{-0.02\frac{D}{t}}}{1 + 1.6 e^{-10 f_{co}^{4.8}}} \tag{V.6}$$

After point B, the core concrete enters the softening phase, corresponding to the third region BC, as illustrated in Figure V.2. The stress–strain relationship in this stage is represented by an exponential function, following the formulation proposed by Binici (2005) and expressed as follows:

$$\sigma = f_r + (f_{co} - f_r) exp\left[-\left(\frac{\varepsilon_x - \varepsilon_{cc}}{\alpha}\right)^{\beta}\right] \qquad \varepsilon \geq \varepsilon_{cc} \tag{V.7}$$

In this context, f_r denotes the residual stress, while α and β are parameters that characterize defining the descending portion of the third region (BC).

According to Tao et *al*. (2013), β is taken as 1.2, and the values of f_r, α, ξ_c are determined using the expressions below:

$$f_r = 0.7\left(1 - e^{-1.38\xi_c}\right) f_{co} \leq 0.25 f_{co} \tag{V.8}$$

$$\alpha = 0.04 - \frac{0.036}{1 + e^{6.08\xi_c - 3.49}} \tag{V.9}$$

$$\xi_c = (f_{frp} A_{frp} + f_{ys} A_s) / f_{co} A_c \tag{V.10}$$

Here, ξ_c represents the confinement factor, f_{frp} and A_{frp} correspond to the tensile strength and cross-sectional area of the FRP, f_{ys} and A_s denote the yield strength and cross-sectional area of the steel tube, and A_c is the cross-sectional area of the concrete core.

In ABAQUS, the behavior of the confined concrete was represented using the Concrete Damage Plasticity (CDP) model. The parameters necessary for defining the CDP model are listed in the following Table.

Table V.2: Concrete damage plasticity parameters (Mansour et *al*. 2024).

Dilation angle	Eccentricity	Bi-axial to uniaxial compressive stress	Shape factor	Viscosoty parameter
40	0.1	1.277	0.667	0.0005

In addition, the tensile response of the confined concrete was described using the fracture energy approach. According to this criterion, the concrete's fracture energy (G_f) and its corresponding tensile strength (f_t) were determined using Eq. (V.11) (Tang et *al*. 2020) and Eq. (V.11) (ACI 2008), respectively.

$$G_f = 2.5(10^{-3})\alpha(0.10f_{co})^{0.70} \tag{V.11}$$

$$f_t = 0.33\sqrt{f_{co}} \tag{V.12}$$

where $= 1.25dmax + 10$, and d_{max} is the diameter of coarse aggregate in the concrete.

The analysis of the stress-strain relationship of confined concrete subjected to tension was conducted utilizing the tensile constitutive model. This was achieved through the application of the following equation.

$$\sigma_t = f_t\left(\frac{\varepsilon_{ct}}{\varepsilon_x}\right)^{0.85} \tag{V.13}$$

$$\varepsilon_{ct} = \frac{f_t}{E_c} \quad \text{and} \quad f_t = 0.26(1.25f_{co})^{2/3} \tag{V.14}$$

V.3.2.2. Steel tube Modeling

To propose a steel stress-strain model, an elastic-plastic behavior characterized by multilinear hardening and a four-stage stress-strain relationship was employed, as proposed by Tao et *al*. (2013), and depicted in Figure V.3. This relationship is applicable to steel exhibiting yield strengths (f_{ys}) between 200 MPa and 800 MPa. The elastic constants, which include the modulus of elasticity (E_s) and Poisson's ratio, were specified as 2.1 GPa and 0.3, respectively. The elastic and plastic regions were identified using the following equations.

$$\sigma = \begin{cases} E_s\varepsilon & 0 \le \varepsilon < \varepsilon_y \\ f_y & \varepsilon_y \le \varepsilon < \varepsilon_p \\ f_u - (f_u - f_y)\left(\dfrac{\varepsilon_u - \varepsilon}{\varepsilon_u - \varepsilon_p}\right)^p & \varepsilon_p \le \varepsilon < \varepsilon_u \\ f_u & \varepsilon \ge \varepsilon_u \end{cases} \tag{V.15}$$

In which f_u is the ultimate strength; ε_y is the yield strain, $\varepsilon_y = f_y/E_s$; ε_p is the strain at the onset of strain hardening; ε_u is the ultimate strain corresponding to the ultimate strength; p is the strain-hardening exponent, which can be determined by

$$p = E_p\left(\frac{\varepsilon_u - \varepsilon_p}{f_u - f_y}\right) \tag{V.16}$$

In which E_p is the initial modulus of elasticity at the onset of strain-hardening, and can be taken as $0.02E_s$. ε_p and ε_u are determined using Eqs. (V.17) and (V.18), respectively.

$$\varepsilon_p = \begin{cases} 15\varepsilon_y & f_y \le 300MPa \\ \left[15 - 0.018\left(f_y - 300\right)\right]\varepsilon_y & 300MPa \le f_y \le 800MPa \end{cases} \tag{V.17}$$

$$\varepsilon_u = \begin{cases} 100\varepsilon_y & f_y \le 300MPa \\ \left[100 - 0.15\left(f_y - 300\right)\right]\varepsilon_y & 300MPa \le f_y \le 800MPa \end{cases} \tag{V.18}$$

A simplified illustration of this material model is provided in Figure V.3. As shown, the complete stress–strain response can be defined using only three fundamental parameters: the yield strength (f_y), the ultimate strength (f_u), and the elastic modulus (E_s). When the elastic modulus E_s was not specified for a given specimen, a default value of 200,000 MPa was adopted in the numerical model. Similarly, in cases where the ultimate tensile strength f_u was not provided, it was estimated from the yield strength f_y using the relationship proposed by Tao et *al*. (2013).

$$f_u = \begin{cases} \left[1.6 - 2 \times 10^{-3}\left(f_y - 200\right)\right]f_y & 200MPa \le f_y \le 400MPa \\ \left[1.2 - 3.75 \times 10^{-4}\left(f_y - 400\right)\right]f_y & 300MPa \le f_y \le 800MPa \end{cases} \tag{V.19}$$

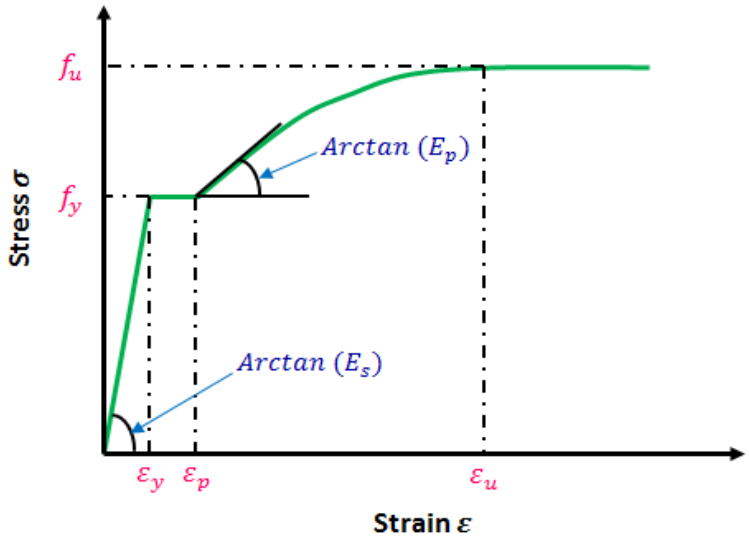

Figure V.3: Stress–strain behavior for structural steel as suggested by Tao et *al*. (2013).

V.3.2.3. FRP Modeling

In this FE analysis, the FRP jackets were modeled as an orthotropic material. Their substantial tensile capacity along the fiber direction was accounted for, while their compressive behavior was intentionally omitted. Consequently, the LAMINA material formulation was employed to specify the elastic modulus, shear modulus, and Poisson's ratio of the FRP layers, using the mechanical properties reported in the experimental programs adopted for model validation (Mansour et *al*. 2024). Since experimental studies consistently showed that FRP jackets failed by tensile rupture, it was essential to incorporate appropriate damage parameters into the FE model. The degradation of the FRP material was characterized using its elastic modulus (E_f), tensile capacity (f_f), and the associated failure criteria. The directional strengths of the FRP both along and across the fibers were introduced based on manufacturer data and implemented using the Hashin failure model. According to Mansour et *al*. 2024, The corresponding damage evolution parameters adopted for the FRP layers are provided in Table V.3, following the recommendations of Hany et *al*. (2016) and Shi et *al.* (2012).

Table V.3: Damage evolution of the FRP composites (Mansour et *al*. 2024).

Longitudinal tensile fracture energy (N mm/mm²)	Longitudinal compressive fracture energy (N mm/mm²)	Transverse tensile fracture energy (N mm/mm²)	Transverse compressive fracture energy (N mm/mm²)
91.6	79.9	0.22	1.1

V.3.3. Validation of FEM with test specimens

To assess the accuracy of the developed finite element model (FEM) via the ABAQUS software, an exhaustive validation investigation is performed through a comparative analysis

of simulation outcomes against experimental findings of five distinct research work namely; Gu et *al*. (2004), Che et *al*. (2012), Wei et *al*. (2014), Ding et *al*. (2018), and Na et *al*. (2018). All selected specimens were strengthened with FRP-steel tube and subjected to axial compression loads. The detail information of each experimental test was presented in Table V.1. The primary indices of performance for validation proceedings are the axial load bearing-capacity and the axial strain of the FRP-confined CFST columns. Table V.2 presents the calculated deviation for each FRP-confined CFST column, FEMs against experimental data in (Gu et *al*. 2004, Che et *al*. 2012, Wei et *al*. 2014, Ding et *al*. 2018, and Na et *al*. 2018) works. In general, the deviations in axial load predictions remain within a reasonable range, often below 5%, indicating good agreement between simulation and experimental results. Some specimens, such as CSC A-2 (10.22%), C-C2-3.0 (14.65%), and C5ST2-A (7.00%), show relatively higher deviations, which may be attributed to localized failure mechanisms or boundary conditions not fully captured by the FEM model. On the other hand, specimens like C-B1-4.5 (0.24%) and C-C2-6.0 (0.17%) display minimal discrepancies, confirming the FEM model's high accuracy in predicting peak axial capacity in specific configurations.

For the axial strain results, the findings show more variation, with several specimens exhibiting deviations exceeding 10%. Examples include 1-1.5 (17.58%), CSC A-2 (21.01%), and C-C1-4.5 (27.21%). These differences are likely due to complexities in strain distribution, confinement effects, and the inability of the numerical model to fully replicate material damage and post-peak deformation behavior. Nevertheless, many cases show acceptable agreement in strain predictions, such as C3ST2-A (0.10%) and 2C-12 (1.13%), reflecting the model’s ability to capture deformation characteristics under certain conditions.

Specifically, in the study by Gu et *al*. (2004), FEM results correlate well with experimental data, especially for axial load with most deviations under 4%. However, strain deviations such as 20.76% in specimen 1-3.5 indicate challenges in accurately simulating ductility and post-peak responses. In Che et *al.* (2012), the FEM slightly overestimated axial load in CSC A-2 and CSC B-2 with around 10% deviation, while strain deviations also indicated some sensitivity to composite interaction modeling. Wei et *al*. (2014) demonstrated consistent results between experimental and FEM data in most specimens. Yet, higher deviations in some cases, such as C-C2-3.0 and C-C1-4.5, suggest the need for improved confinement and material modeling in strain simulations. For Ding et *al.* (2018), FEM predictions are notably accurate for both axial load and strain, with deviations typically under 7%. This highlights the model’s robustness for thick-walled and highly confined CFST columns. Similarly, Na et *al*. (2018) showed a strong correlation between FEM and experimental outcomes in both axial load and strain, with deviations generally below 4%. Higher deviations in strain, such as in 2C-16 (17.58%), could be due to localized effects such as buckling not fully represented in the simulations.

Table V.4: Ultimate axial load and axial strain for FRP confined CFST columns.

xperimental study	Specimen designation	Experimental result		FEM result		Deviation (%)	
		Axial load (kN)	Axial strain x 10^3	Axial load (kN)	Axial strain x 10^3	Axial load	Axial strain
Gu et *al*. (2004)	1-1.5	1095.02	10.01	1112.27	8.25	1.58	17.58
	1-2.5	1313.43	12.96	1346.90	14.43	2.55	11.34
	1-3.5	1329.59	11.32	1282.09	8.97	3.57	20.76
	1-4.5	1682.71	16.44	1739.32	16.61	3.36	1.03
	2-1.5	1285.33	16.49	1248.00	15.60	2.90	5.40
	2-2.5	1531.98	17.34	1543.33	15.89	0.74	8.36
	2-3.5	1573.74	16.45	1586.72	15.73	0.82	4.37
	2-4.5	1798.80	19.59	1834.70	19.65	1.99	0.3
Che et *al*.	CSC B-1	1333.80	11.47	1294.44	10.91	2.95	4.88
	CSC A-2	1395.48	13.04	1538.09	15.78	10.22	21.01
	CSC B-2	1535.66	16.49	1685.12	16.74	9.73	1.52
	CSC C-2	1869.03	14.53	2000.68	16.29	7.04	12.11
Wei et *al*.	C-B1-3.0	1174.74	14.48	1189.48	14.16	1.25	2.21
	C-B2-3.0	1390.88	21.50	1374.86	20.11	1.15	6.47
	C-C1-3.0	1447.07	17.86	1418.98	20.10	1.94	12.54
	C-C2-3.0	1548.56	17.21	1775.48	18.60	14.65	8.08
	C-B1-4.5	1670.41	16.18	1666.47	13.49	0.24	16.63
	C-B2-4.5	1929.11	23.89	2036.54	26.35	5.57	10.30
	C-C1-4.5	1785.46	11.98	1870.27	15.24	4.75	27.21
	C-C2-4.5	1954.68	15.57	2050.84	18.93	4.92	21.58
	C-B1-6.0	2025.27	22.12	1989.90	20.75	1.75	6.19
	C-B2-6.0	2174.61	23.40	2095.22	19.63	3.65	16.11
	C-C1-6.0	1858.96	14.21	1882.47	12.25	1.26	13.79
	C-C2-6.0	2302.23	19.93	2306.05	18.30	0.17	8.18
	C-B1-7.5	2156.69	20.00	2185.56	20.48	1.34	2.40
	C-B2-7.5	2257.07	25.48	2271.62	25.90	0.64	1.65
	C-C1-7.5	2085.67	23.50	2209.31	19.30	5.93	17.87
	C-C2-7.5	2348.57	19.50	2329.91	18.04	0.79	7.49
Ding et *al*.	C3ST1-A	4497.85	7.02	4642.53	6.20	3.22	11.68
	C3ST1-B	4506.11	6.15	4642.53	6.20	3.03	0.81
	C3ST2-A	5526.51	10.13	5679.64	10.14	2.77	0.10
	C3ST2-B	5543.24	9.55	5679.64	10.14	2.46	6.18
	C5ST1-B	5849.83	9.57	5595.16	11.09	4.35	15.88
	C5ST2-A	6872.66	10.72	7353.42	9.36	7.00	12.69
	C5ST2-B	6892.41	8.52	7353.42	9.36	6.69	9.86
Na et *al*. (2018)	2C-3.5	2358.31	17.44	2382.22	16.78	0.45	2.97
	2C-6	2165.97	18.36	2162.12	17.39	0.33	5.91
	2C-8	2012.92	16.73	2038.99	16.77	2.12	1.37
	2C-12	1805.35	11.31	1909.95	11.61	3.77	1.13
	2C-16	1513.04	2.88	1487.40	2.87	1.58	17.58

V.3.4. Comparison of finite element model simulation with experimental results of Gu et *al.*

Figure V.4(a-d) compares the experimental axial load-axial strain results with those obtained through the FEA (finite element analysis) models for eight concrete specimens confined by both steel tubes and fiber-reinforced polymer (FRP) wraps (FRP-CFST), subjected to concentric axial loading, as tested by Gu et *al*. (2004). The continuous lines represent the experimental results, while the dashed lines indicate the FEM model predictions. The test parameters include column diameters (D) of 127, 129, 131, and 133 mm, steel tube thicknesses (t_s) of 1.5, 2.5, 3.5, and 4.5 mm, FRP wrap thickness (t_{frp}) of 0.167 mm, and the compressive strength of unconfined concrete (f_c') of 40.15 MPa. The designation "1" refers to specimens wrapped with a single layer of FRP (e.g., 1-1.5), while "2" corresponds to specimens wrapped with two layers of FRP (e.g., 2-1.5).

The comparison of the results shows that increasing the number of FRP layers significantly enhances the axial load-carrying capacity, as evidenced by the higher peak load observed in the two-layer specimens compared to those with a single layer. This improvement is well captured by the FEM model, which closely matches the experimentally observed peak loads. Moreover, the post-peak behavior indicates improved ductility with two FRP layers, as both the experimental and numerical curves exhibit a more gradual load decline, reflecting better energy dissipation capacity.

The FEM results also show good agreement in terms of initial stiffness and overall axial load-axial strain behavior. However, slight deviations are observed in the early inelastic region, likely due to the idealized assumptions of the numerical model. Overall, the FEM model accurately predicts both the strength and ductility of FRP-confined CFST columns, confirming its effectiveness for simulating and analyzing such composite systems.

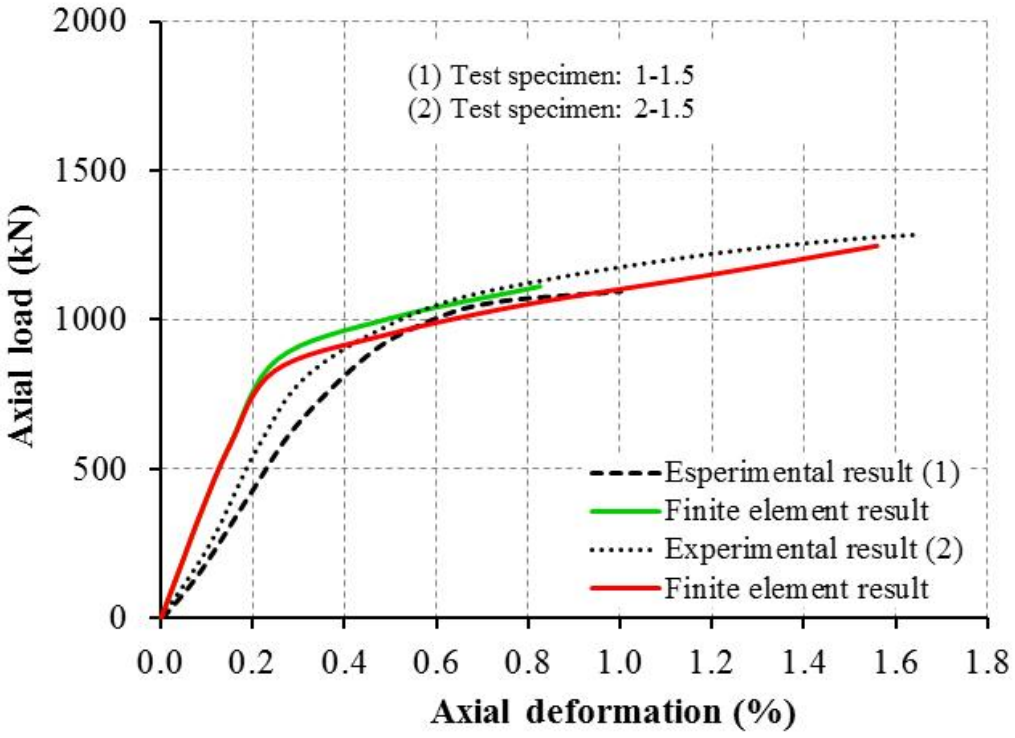

(a)- $D = 127\ mm, t_s = 1.5\ mm$

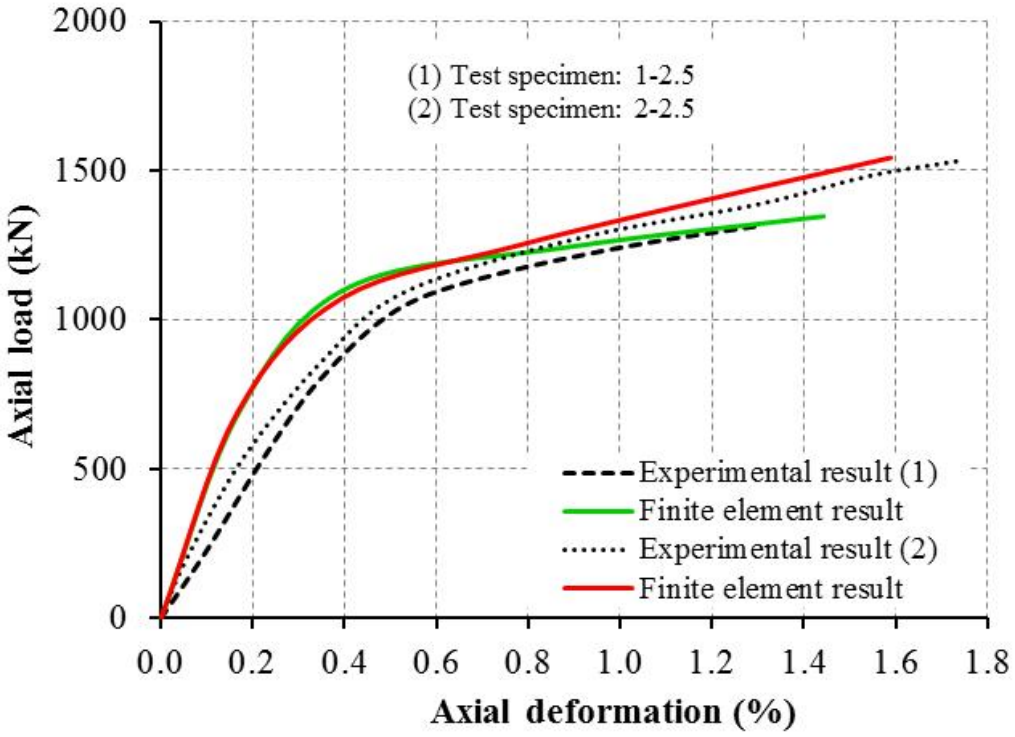

(b)- $D = 129\ mm, t_s = 2.5\ mm$

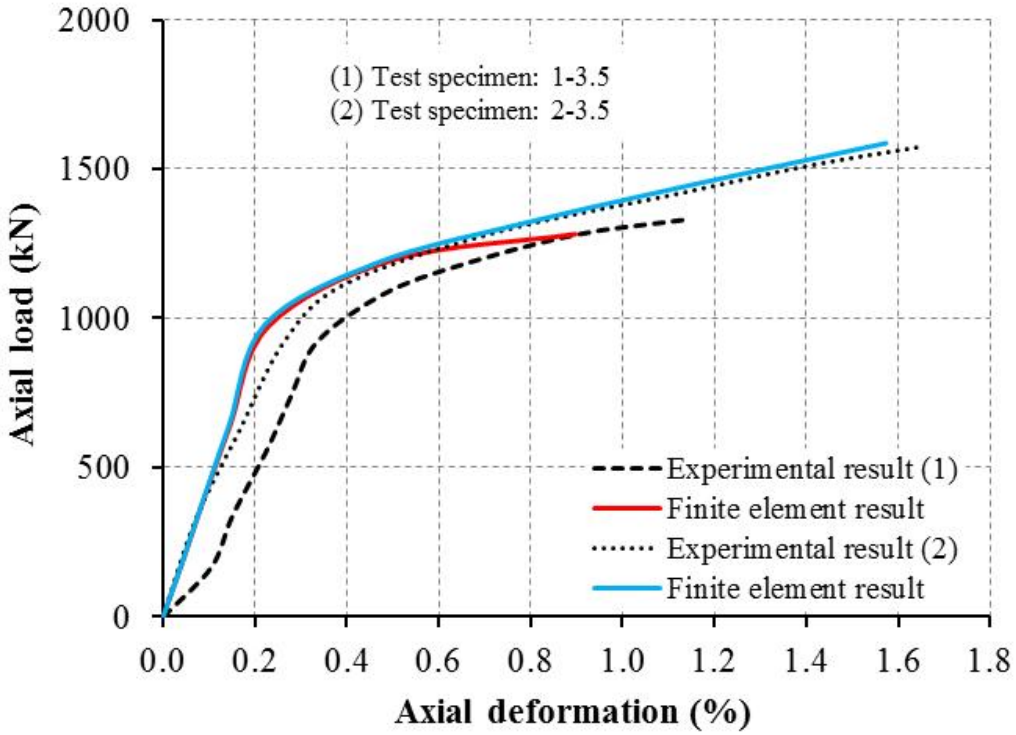

(c)- $D = 131\ mm, t_s = 3.5\ mm$

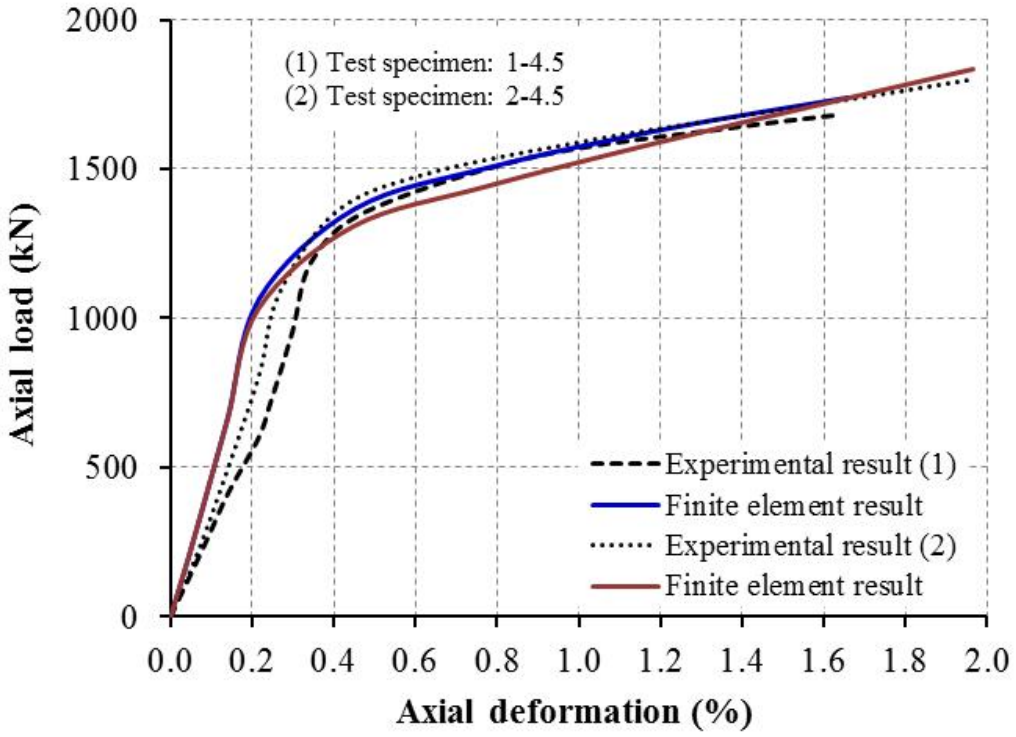

(d)- $D = 133\ mm, t_s = 4.5\ mm$

Figure V.4: Axial load-axial deformation verification FEMs and Gu et *al*. (2004).tests results with ($t_f = 0.167\ mm, f_c' = 40.15MPa$).

V.3.5. Comparison of finite element model simulation with experimental results of Che et *al.*

The Figure V.5(a-d) illustrates a comparative analysis between experimental results and Finite Element Method (FEM) predictions for FRP-confined concrete-filled steel tube (FRP-CFST) specimens under concentric axial loading, and tested by Che et *al*. (2012). The parameters in the figures include column diameter (D), steel tube thickness (t_s), FRP wrap thickness (t_{frp}), and compressive strength of unconfined concrete (f_c'). The labels "1" and "2" denote the number of FRP layers, representing one and two layers, respectively.

From the graphs, it is evident that the FEM results are in good agreement with the experimental curves in terms of both initial stiffness and peak load capacity. However, minor deviations are noticed in the post-peak region, particularly in the inelastic zone, likely due to idealized assumptions in the numerical modeling.

For Specimen CSC A-2 ($D = 127\,mm$, $t_s = 1.5\,mm$), the FEM prediction follows the experimental curve quite well up to the peak load. The divergence becomes slightly more noticeable in the post-peak regime, but the overall trend and deformation behavior are well captured by the FEM.

In Specimens CSC B-1 and B-2 ($D = 127\,mm$, $t_s = 2.5\,mm$), a more prominent difference is observed between one and two layers of FRP confinement. The specimen with two FRP layers (CSC B-2) exhibits significantly higher axial strength and enhanced ductility, indicated by a smoother post-peak decline and delayed failure. This clearly demonstrates the beneficial effect of additional FRP layers in improving the confinement efficiency and energy dissipation capacity.

The FEM results for both CSC B-1 and CSC B-2 closely follow the experimental curves, successfully predicting the relative increase in strength and ductility associated with the second FRP layer. The model accurately reflects the impact of increased confinement due to the thicker steel tube and additional FRP layer, validating its reliability in simulating FRP-CFST structural behavior.

The thicker steel tube ($t_s = 3.5\,mm$) in CSC C-2 provides stronger confinement, which improves the specimen's axial load capacity and ductility, as expected. However, the finite element model predicts more controlled behavior with a slower post-peak load decrease compared to the experimental results, where failure appears more abrupt. This discrepancy is likely due to factors like material imperfections, boundary effects, or localized instabilities that are difficult to capture in the idealized finite element model. In any case, the thicker steel tube should have contributed to better overall performance in CSC C-2, especially in terms of axial load-bearing capacity..

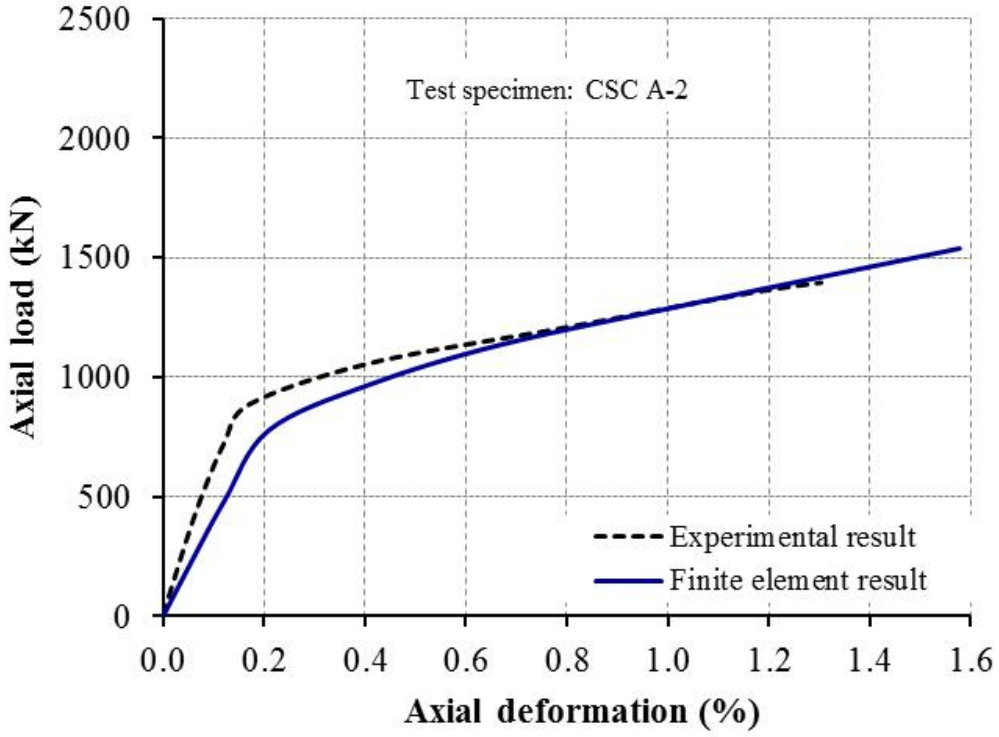

(a) CSC A-2 ($t_s = 1.5\ mm$)

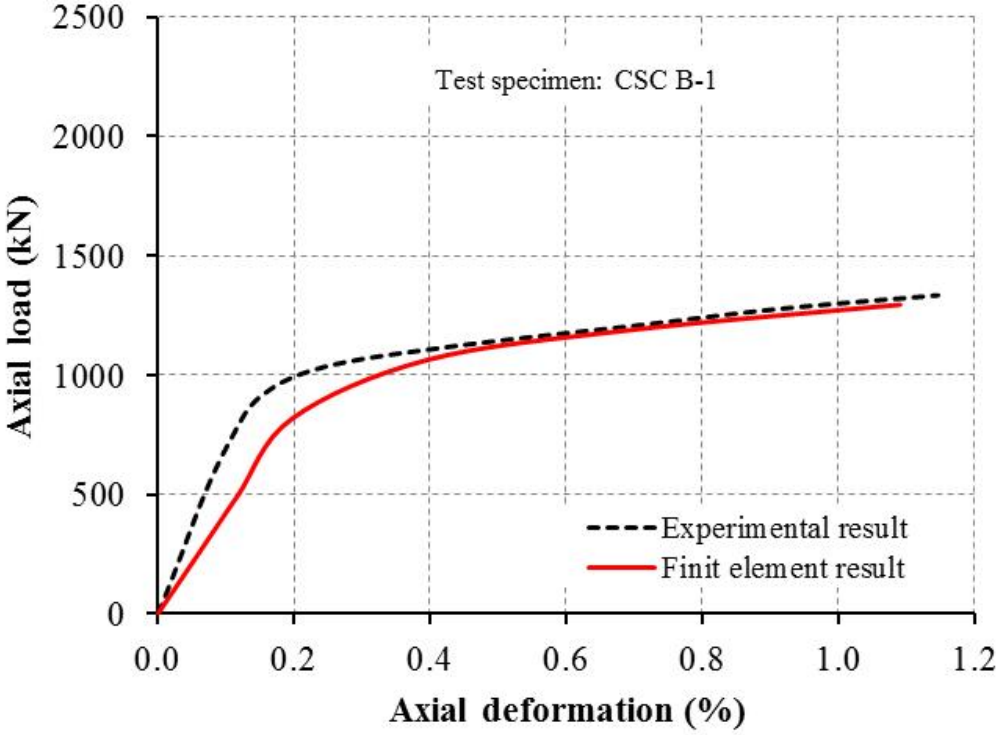

(b) CSC B-1 ($t_s = 2.5\ mm$)

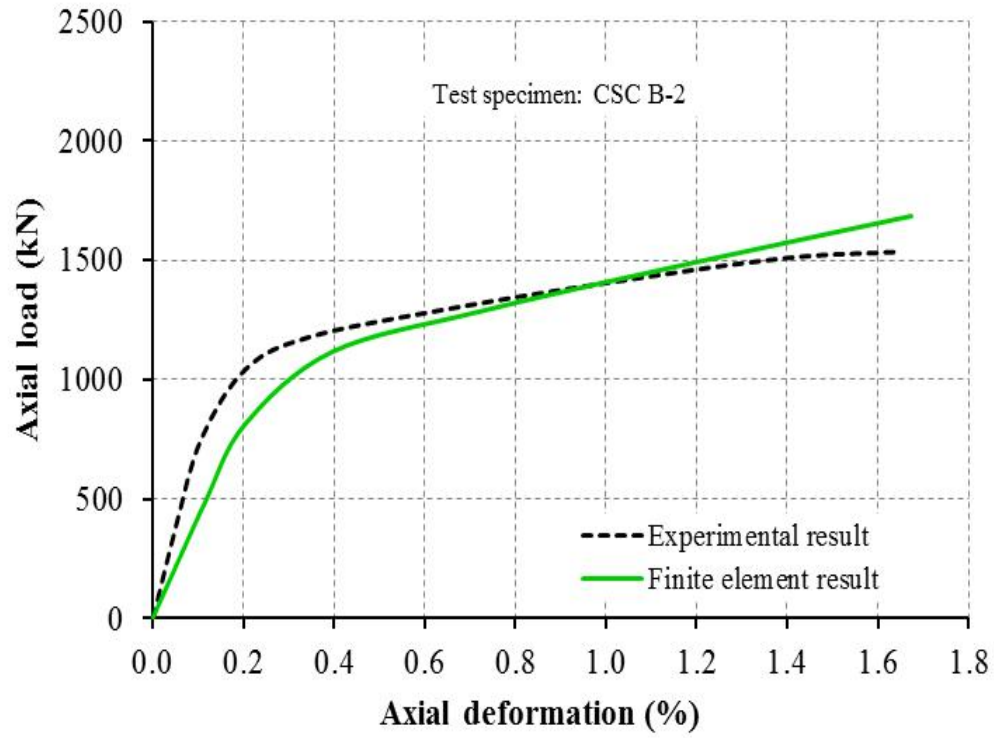

(c) CSC B-2 ($t_s = 2.5\ mm$)

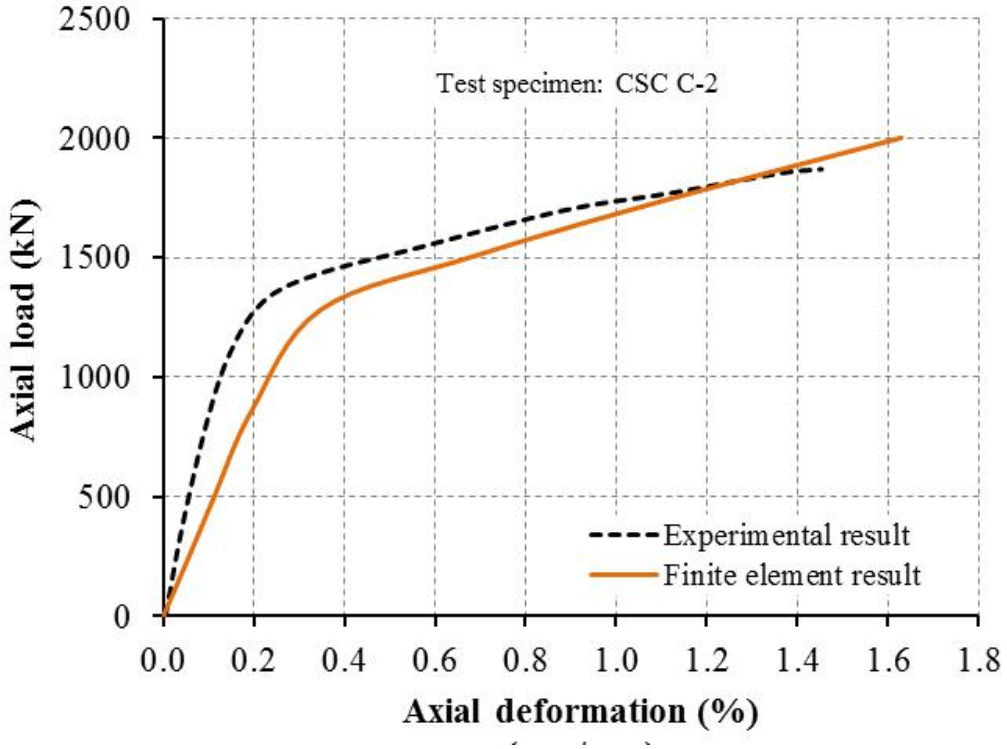

(d) CSC C-2 ($t_s = 3.5\ mm$)

Figure V.5: Axial load-axial deformation verification FEMs and Che et *al*. (2012) tests results with ($D = 127\ mm, t_f = 0.167\ mm, f'_c = 36.2\ MPa$)

V.3.6. Comparison of finite element model simulation with experimental results of Wei et *al.*

The presented Figure V.6(a-h) illustrates a comparison between experimental results of Wei et *al*. (2014) and finite element model (FEM) simulations. In these graphs, D represents the diameter of the specimens, t_s is the thickness of the steel tube, f_{frp} denotes the thickness of the FRP wraps, and f_c' indicates the compressive strength of unconfined concrete. Additionally, the numeral '1' corresponds to one layer of FRP wrap, whereas '2' denotes two layers.

In Figures V.6a and V.6b ($t_s = 3.00\,mm, f_c' = 31.2\,MPa$), it is evident that the FEM results closely follow the experimental curves in terms of initial stiffness and ultimate axial load. Increasing the number of FRP layers from one (C-B1-3.0) to two (C-B2-3.0) clearly enhances both load-carrying capacity and ductility. Similarly, specimens C-C1-3.0 and C-C2-3.0 demonstrate improved behavior with additional FRP confinement. Minor variations observed in the post-peak range can be attributed to idealizations in the FEM modeling process. However, with an increase in steel tube thickness to 4.5 mm (Figures V.6c and V.6d $t_s = 4.50\,mm, f_c' = 34.7\,MPa$), the specimens exhibit greater axial strength and stiffness. Specimens C-B2-4.5 and C-C2-4.5 with two layers of FRP wrap show a significant improvement in performance compared to their single-layer counterparts. FEM curves accurately capture this trend, validating the effectiveness of the numerical model in simulating enhanced confinement and post-peak behavior. Moreover, as the steel tube thickness increases further to 6.0 mm (Figures V.6e and V.6f $t_s = 6.00\,mm, f_c' = 34.7\,MPa$), the confinement effect provided by the steel becomes more dominant. However, the addition of FRP layers continues to contribute positively to load resistance and energy dissipation. The FEM predictions remain consistent with the experimental trends, showing enhanced performance in specimens with two FRP layers (C-B2-6.0, C-C2-6.0), though slight discrepancies are noted in the plastic deformation region. In addition, at the highest steel thickness of 7.5 mm (Figure Figures V.6g and V.6h $t_s = 7.50\,mm, f_c' = 34.7\,MPa$), all specimens demonstrate maximum axial load capacities. The role of FRP becomes more pronounced in enhancing ductility, as seen in the smoother and more gradual post-peak behavior in specimens with two layers of FRP (C-B2-7.5, C-C2-7.5). The FEM results align well with experimental curves, effectively reflecting the improved load capacity and deformation performance due to the combined confinement provided by steel and FRP. Consequently, the FEM simulation results show good agreement with experimental data across different steel tube thicknesses and FRP configurations. The axial load capacity and ductility are clearly influenced by the number of FRP layers and the thickness of the steel tube. Although slight deviations are observed in the post-peak region, FEM analysis proves to be a reliable tool for predicting the behavior of FRP-confined CFST columns under axial loading.

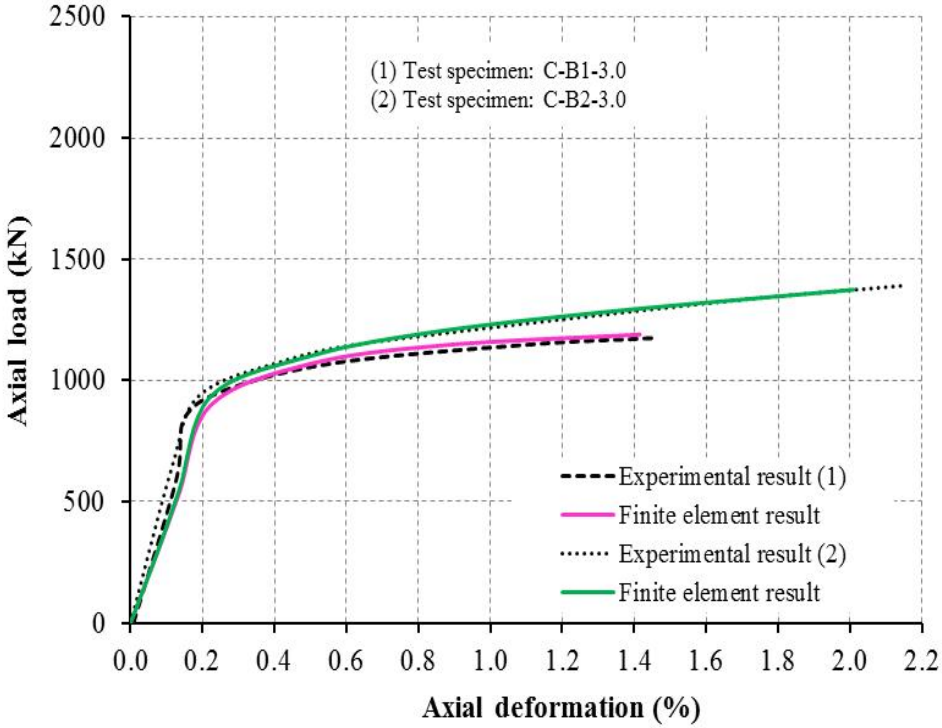

(a) C-B1-3.0 and C-B2-3.0 ($f_c' = 31.2\ MPa$)

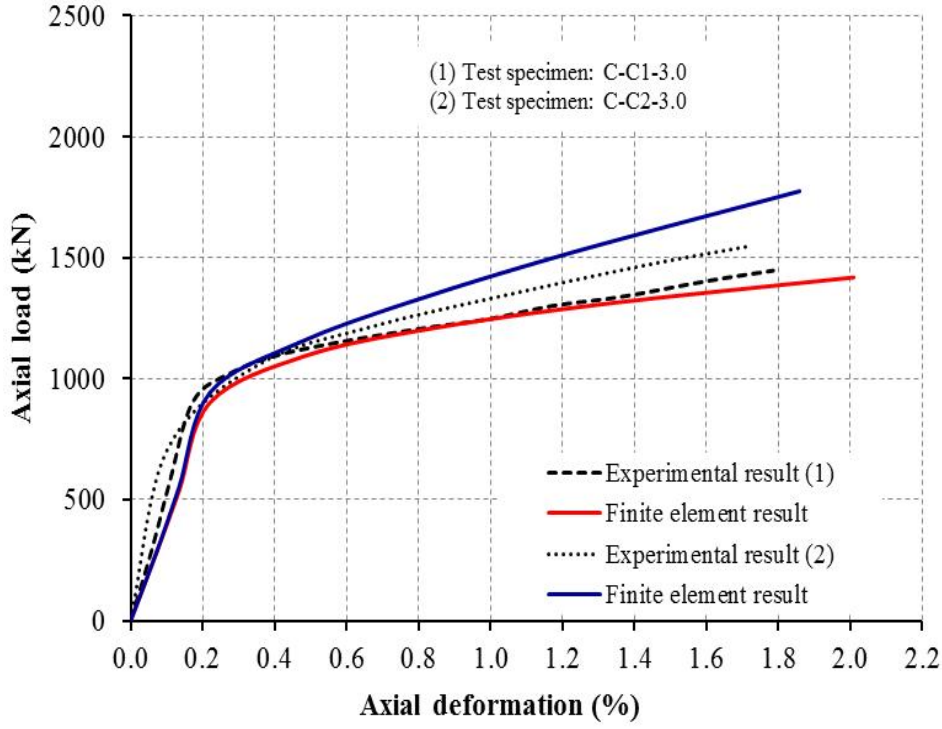

(b) C-C1-3.0 and C-C2-3.0 ($f_c' = 31.2\ MPa$)

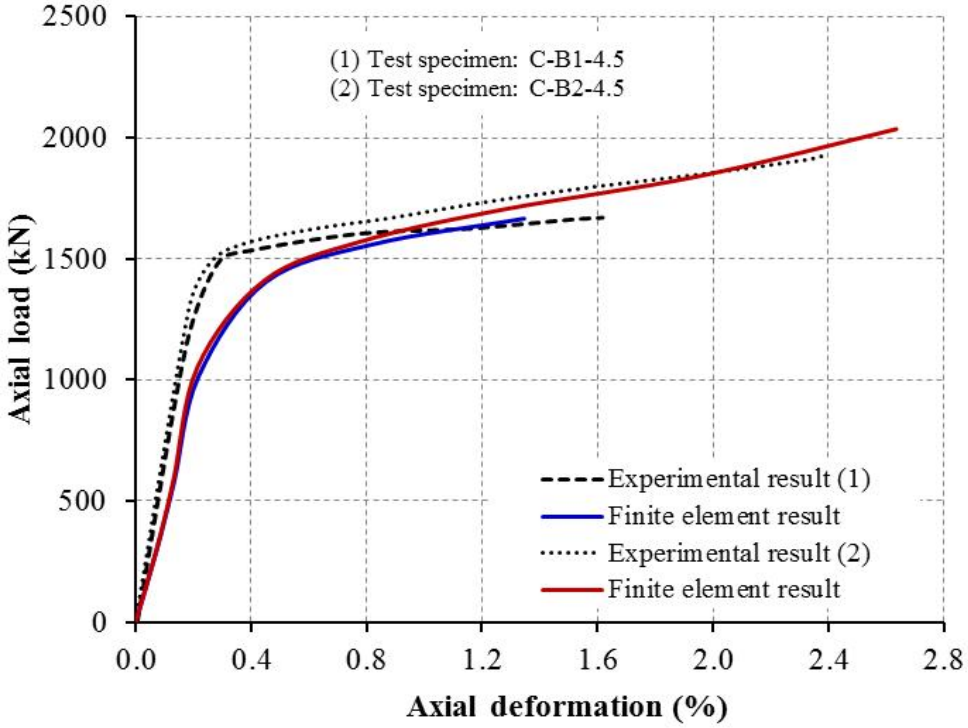

(c) C-B1-4.5 and C-B2-4.5 ($f_c' = 34.7\ MPa$)

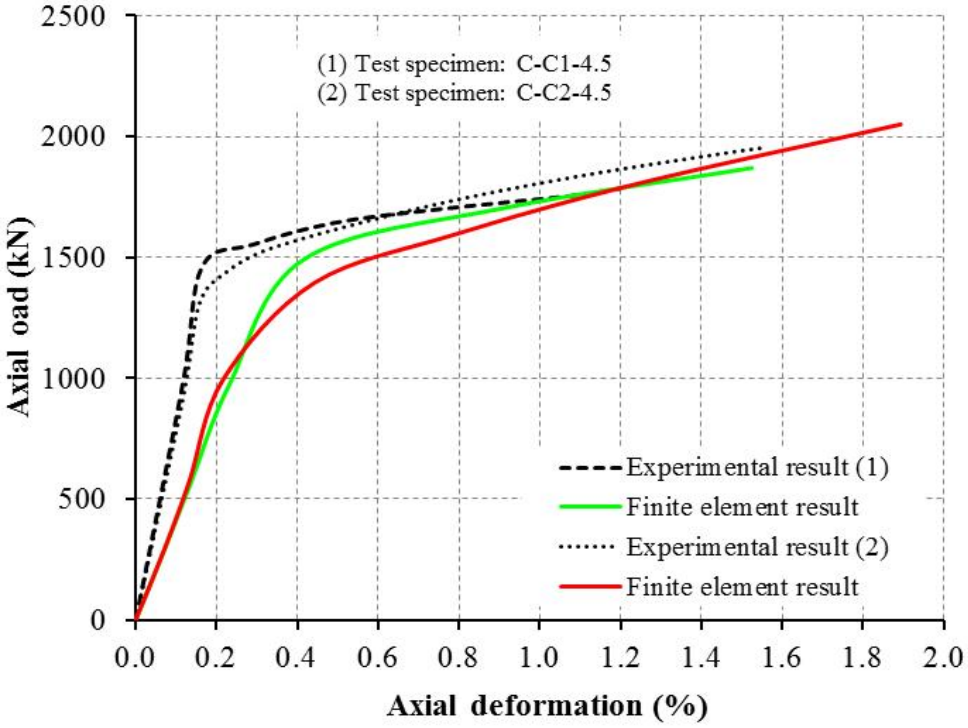

d) C-C1-4.5 and C-C2-4.5 ($f_c' = 34.7\ MPa$)

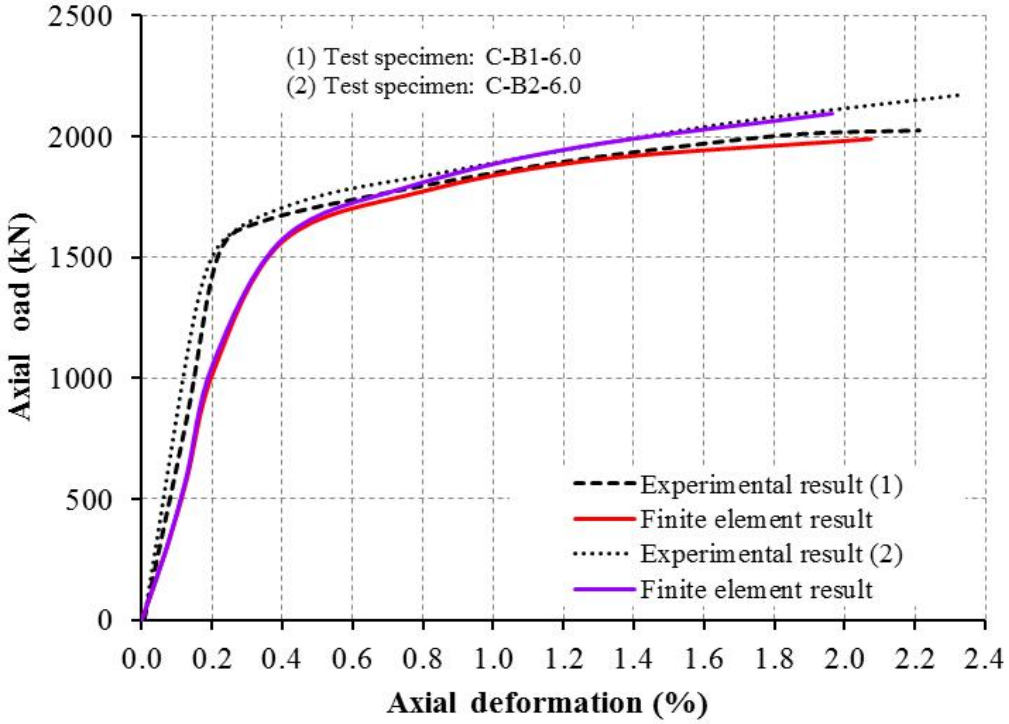

(e) C-B1-6 and C-B2-6 ($f_c' = 34.7\ MPa$)

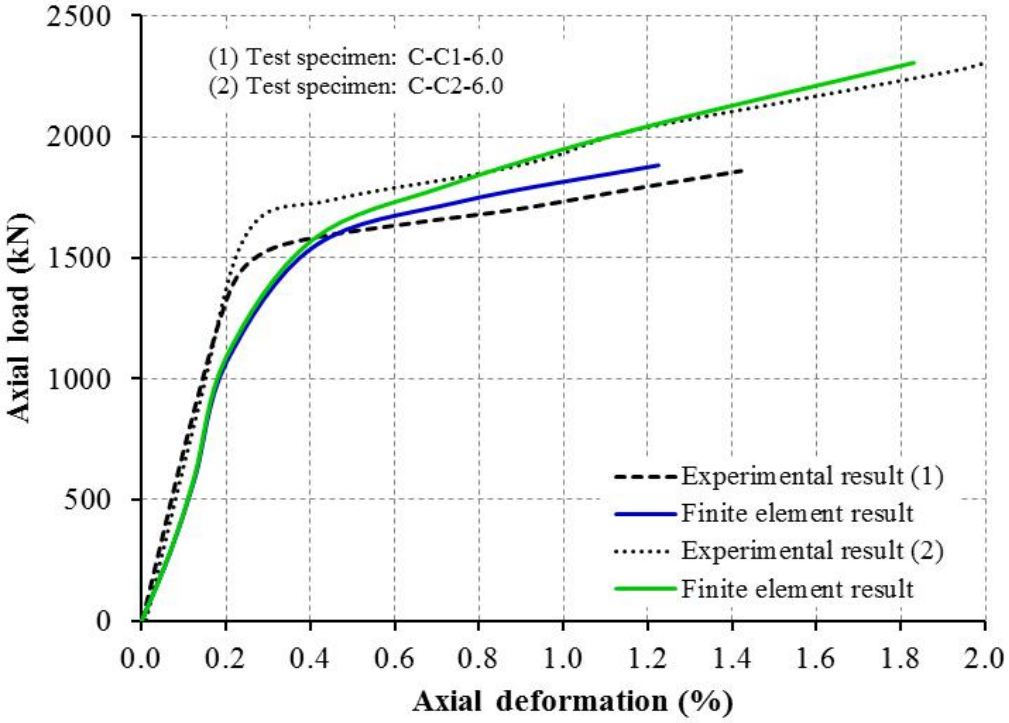

(f) C-C1-6 and C-C2-6 ($f_c' = 34.7\ MPa$)

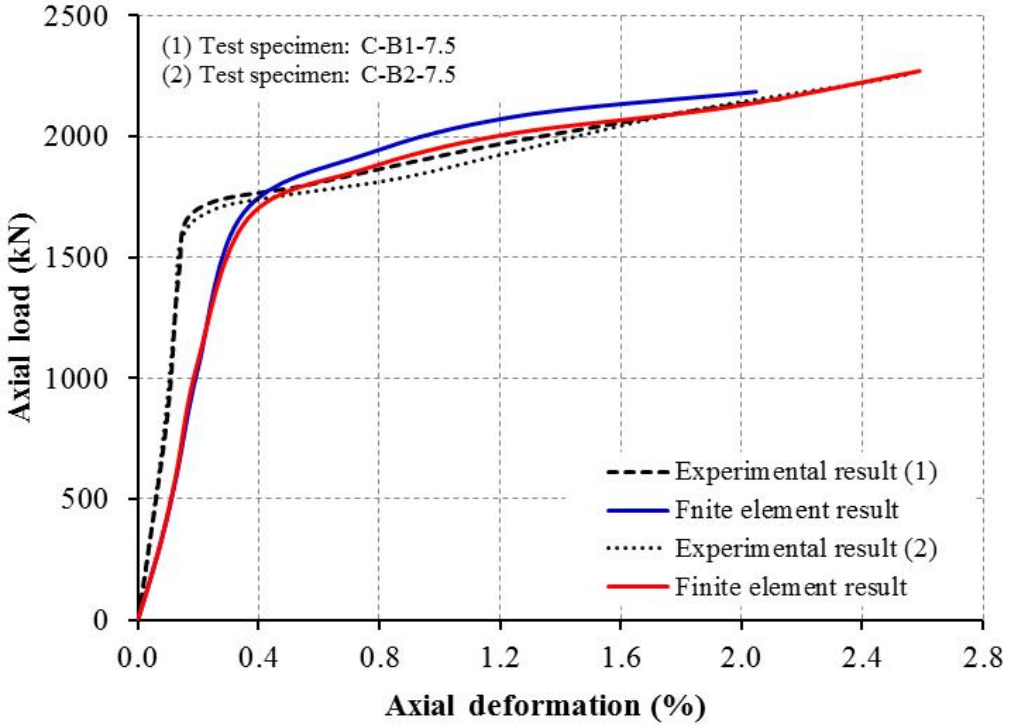

(d)

(g) C-B1-7.5 and C-B2-7.5 ($f_c' = 34.7\ MPa$)

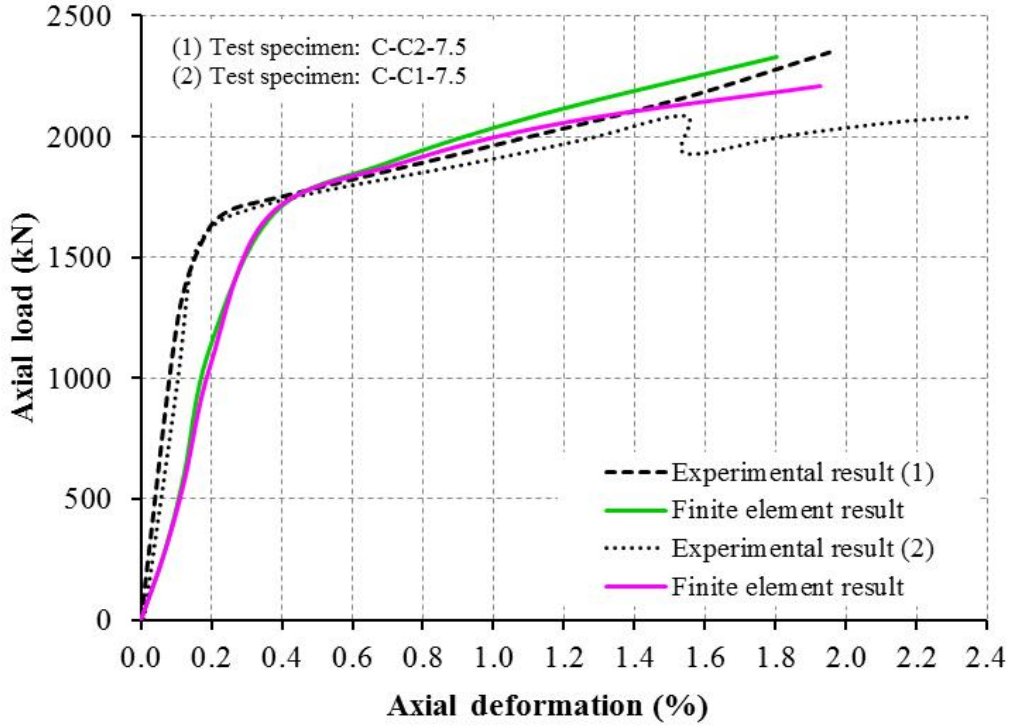

(h) C-C1-7.5 and C-C2-7.5 ($f_c' = 34.7\ MPa$)

Figure V.6: Axial load-axial deformation verification FEMs and Wei et *al.* (2014) tests results with ($D = 133\ mm, t_f = 0.111\ mm$)

V.3.7. Comparison of finite element model simulation with experimental results of Ding et *al.*

The Figure V.7(a-d) provides a comparative evaluation between the experimental outcomes of Ding et *al*. (2018) (solid lines) and the finite element method (FEM) simulations (dashed lines) for FRP-confined CFST specimens. The graphs reflect the axial load versus axial strain response for different configurations, where D, t_s, t_{frp} and f_c' denote the diameter of the specimens, thickness of the steel tube, thickness of the FRP wraps, and compressive strength of unconfined concrete. Additionally, '1' corresponds to one layer of FRP, while '2' denotes two layers.

In the Figure V.7a (C3ST1 series, $f_c' = 39.3\ MPa,\ t_s = 3.7\ mm$), both experimental and FEM curves show a good agreement in terms of initial stiffness and ultimate load. It is evident that the FEM model effectively replicates the peak load and general deformation trend. Slight differences occur in the post-peak softening phase, which could be attributed to the simplifications inherent in the numerical model. Specimens C3ST1-A and C3ST1-B (one layer of FRP) exhibit similar load-bearing capacities, with minor variations in ductility. However, in the Figure V.7b (C3ST2 series, $f_c' = 39.3\ MPa,\ t_s = 3.7\ mm$), the addition of a second layer of FRP wrap leads to noticeable improvements in axial strength and energy absorption. The FEM predictions closely follow the experimental trends, although a slightly stiffer response is observed in the post-peak region for FEM results. The overall performance enhancement due to the additional FRP confinement is well captured by the numerical simulations, validating the model's accuracy in assessing confinement effects. Moreover, in the Figure V.7c (C5ST1 series, $f_c' = 57.4\ MPa,\ t_s = 3.7\ mm$), the influence of higher concrete strength is evident. The axial load capacity increases substantially, and the FEM simulations again align well with the experimental results. Both curves demonstrate a higher peak load and increased stiffness. However, minor deviations are observed in the post-peak region, potentially due to the limitations of the constitutive material models used in FEM analysis. Despite this, the FEM still reliably predicts the load–strain behavior. In addition, in the Figure V.7d (C5ST2 series, $f_c' = 57.4\ MPa,\ t_s = 3.7\ mm$), the addition of a second layer of FRP wrap leads to noticeable improvements in axial strength and energy absorption. Consequently, the FEM results exhibit strong correlation with experimental data across varying FRP layers and concrete strengths. The increase in FRP layers enhances both load-carrying capacity and ductility, while higher concrete strength contributes significantly to the overall axial resistance. Although some differences are noted in the post-peak zone, the FEM model demonstrates its effectiveness in simulating the axial behavior of FRP-confined CFST specimens.

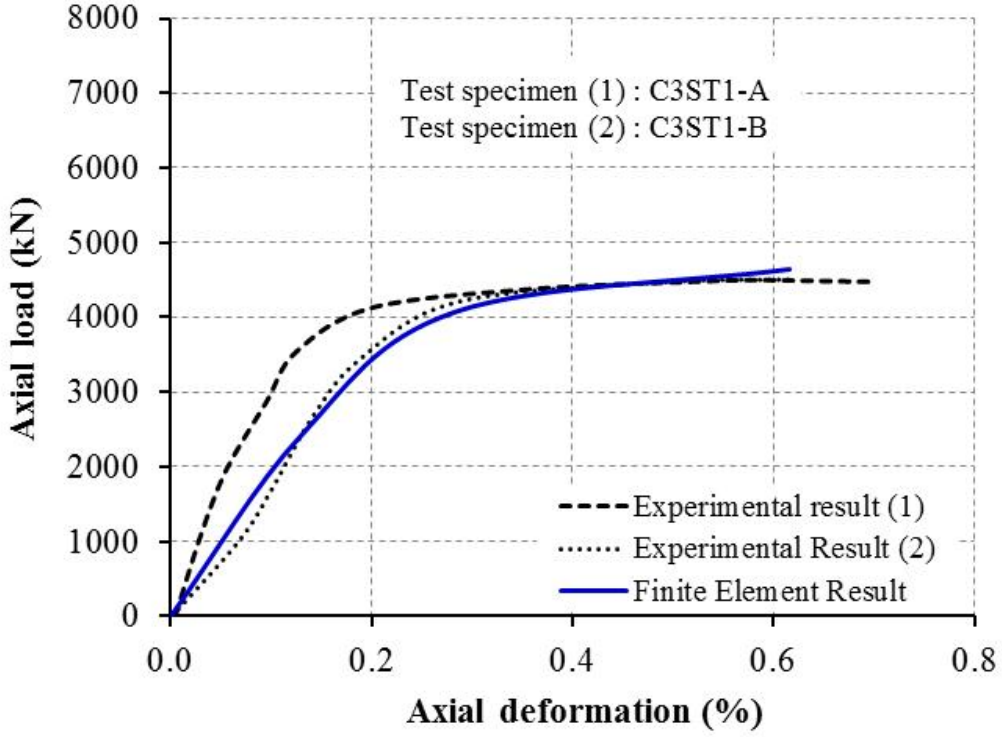

(a) $f'_c = 39.3\ MPa$

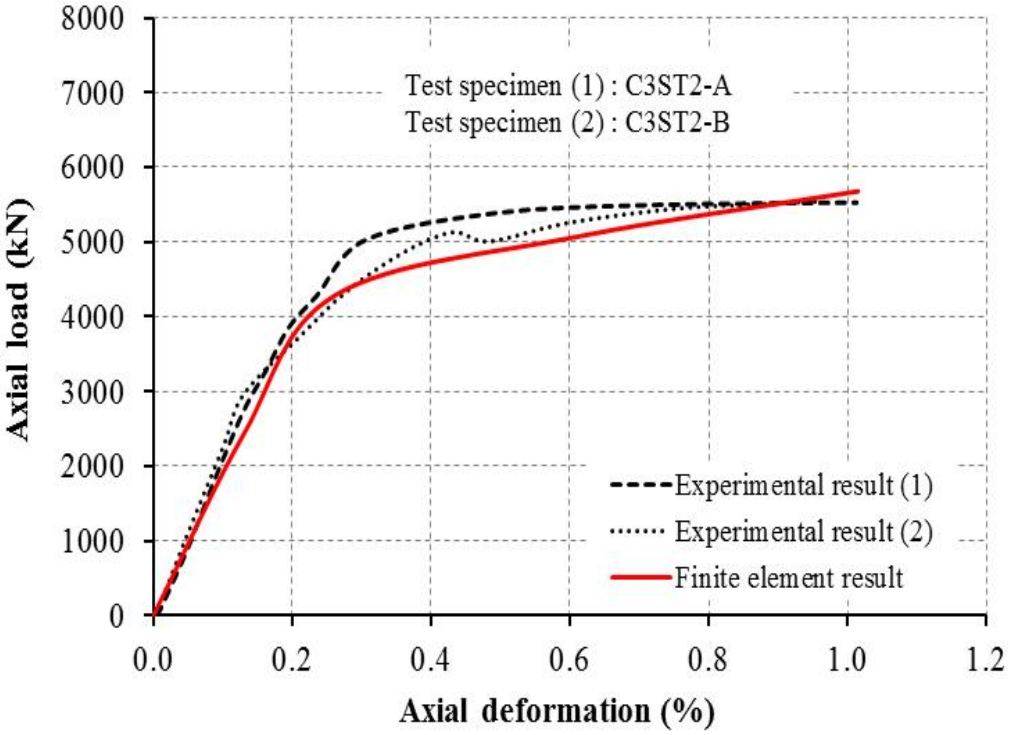

(b) $f'_c = 39.3\ MPa$

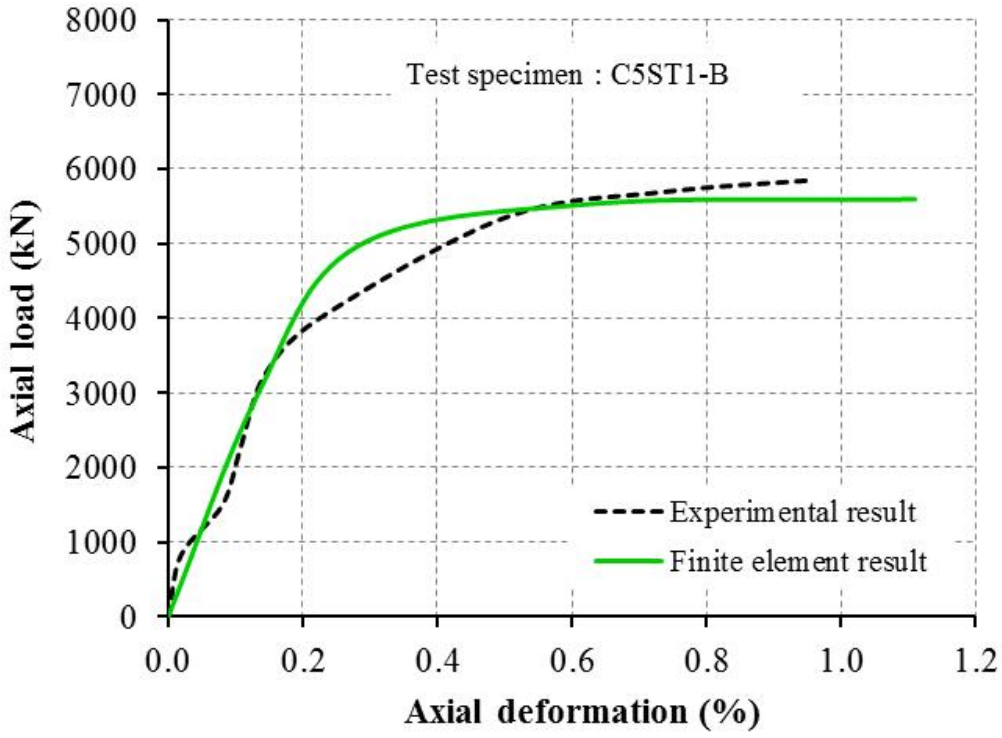

(c) $f'_c = 57.4\ MPa$

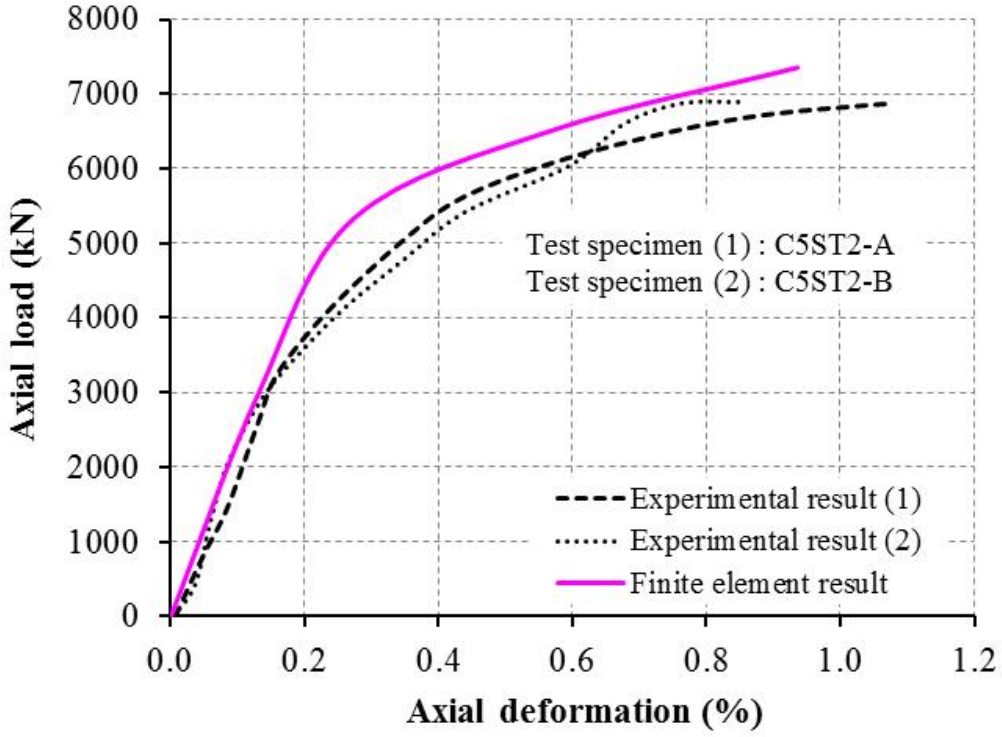

(d) $f'_c = 57.4\ MPa$

Figure V.7: Axial load-axial deformation verification FEMs and Ding et *al*. (2018) tests results with ($D = 300\ mm, t_s = 3.70\ mm, t_f = 0.167\ mm$).

V.3.8. Comparison of finite element model simulation with experimental results of Na et *al.*

The experimental and finite element analysis (FEA) results for the axial load–strain behavior of FRP-confined concrete-filled steel tube (CFST) specimens with varying H values are compared in Figure V.7 (a–e). The specimens correspond to the following confinement parameters: 2C-3.5 (H = 588 mm), 2C-6 (H = 1008 mm), 2C-8 (H = 1344 mm), 2C-12 (H = 2016 mm), and 2C-16 (H = 2688 mm). All specimens have a constant diameter of 168 mm and are confined with two layers of FRP wraps. The compressive strength of the unconfined concrete is 38 MPa, and the steel tube thickness and FRP wrap thickness are 6.0 mm and 0.111 mm, respectively.

The results indicate that both experimental and FEA data exhibit similar trends across all H levels, characterized by an initial linear elastic phase, followed by a nonlinear transition region, and finally a strain-hardening or plateau phase. In most cases, the experimental curves lie slightly above the FEA predictions, reflecting a slightly higher measured axial load capacity compared to the numerical model. This difference can be attributed to material heterogeneity, variations in bonding conditions, or conservative assumptions in the numerical simulation

For specimens with lower H values (2C-3.5, H = 588 mm and 2C-6, H = 1008 mm) (Figure V.7a and b), there is excellent agreement between experimental and FEA results, suggesting that the confinement effects of the FRP wraps and steel tube are well captured by the numerical model. As H increases (2C-8, H = 1344 mm and 2C-12, H = 2016 mm) (Figure V.7c and d), the experimental results generally show higher axial load capacities than FEA predictions, indicating that the interaction between the FRP confinement and the steel tube at higher H levels is not fully represented in the simulation

For the specimen with the highest H value (2C-16, H = 2688 mm) (Figure V.7e), both experimental and numerical results indicate a significant increase in axial load capacity; however, the axial strain at peak load is reduced relative to specimens with lower H values. This suggests that as H increases, the structural system becomes stiffer, and the contribution of FRP confinement to overall ductility diminishes, resulting in behavior that is increasingly dominated by the steel–concrete composite action.

Overall, the comparison demonstrates that the FEA model provides a reasonable prediction of axial behavior for CFST columns across different H levels, particularly for specimens with lower H values. While experimental results show slightly higher load capacities, the effectiveness of FRP confinement decreases as H increases, highlighting the importance of optimizing the confinement parameter H to achieve a balanced strength–ductility response in hybrid CFST columns.

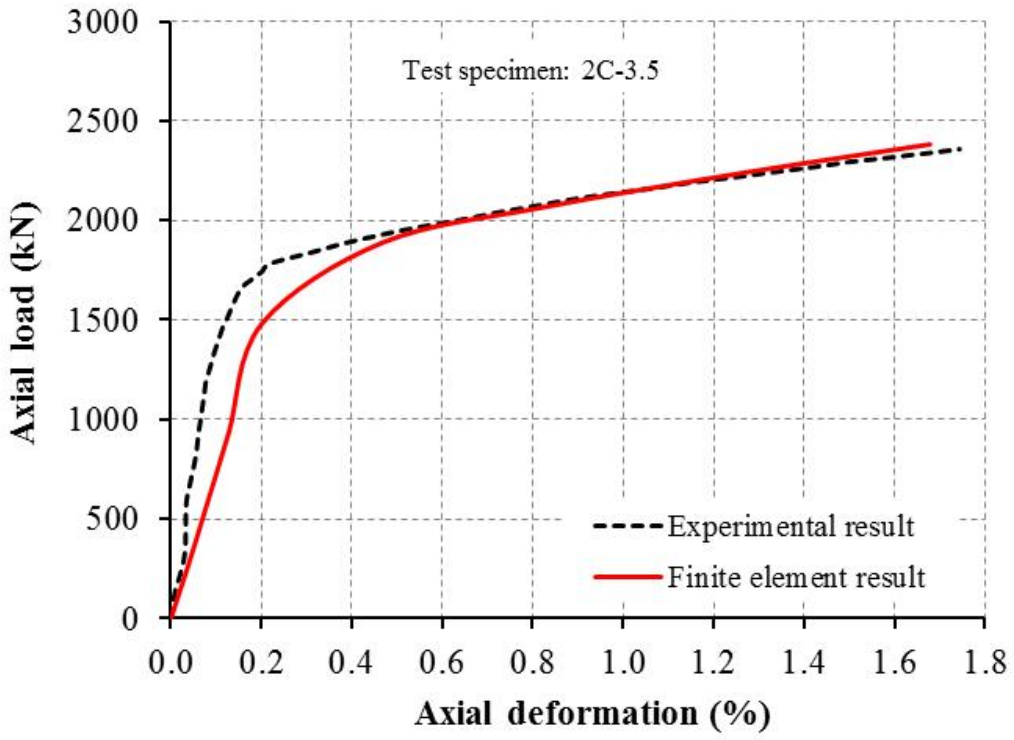

(a) 2C-3.5 ($H = 588\ mm$)

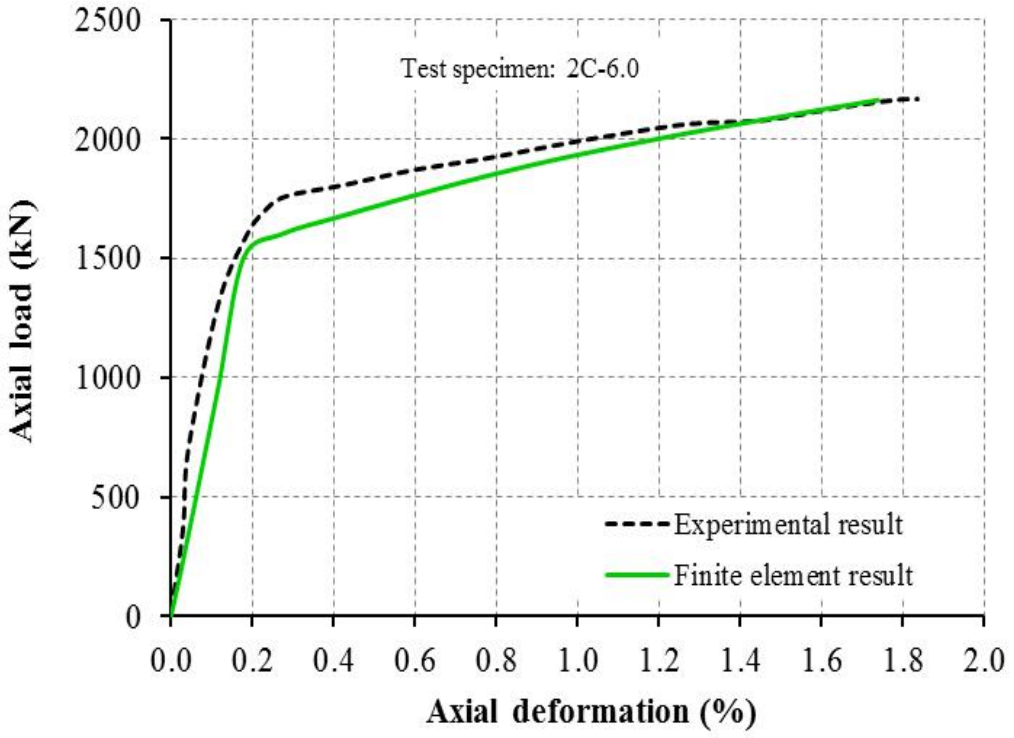

(b) 2C-6.0 ($H = 1008\ mm$)

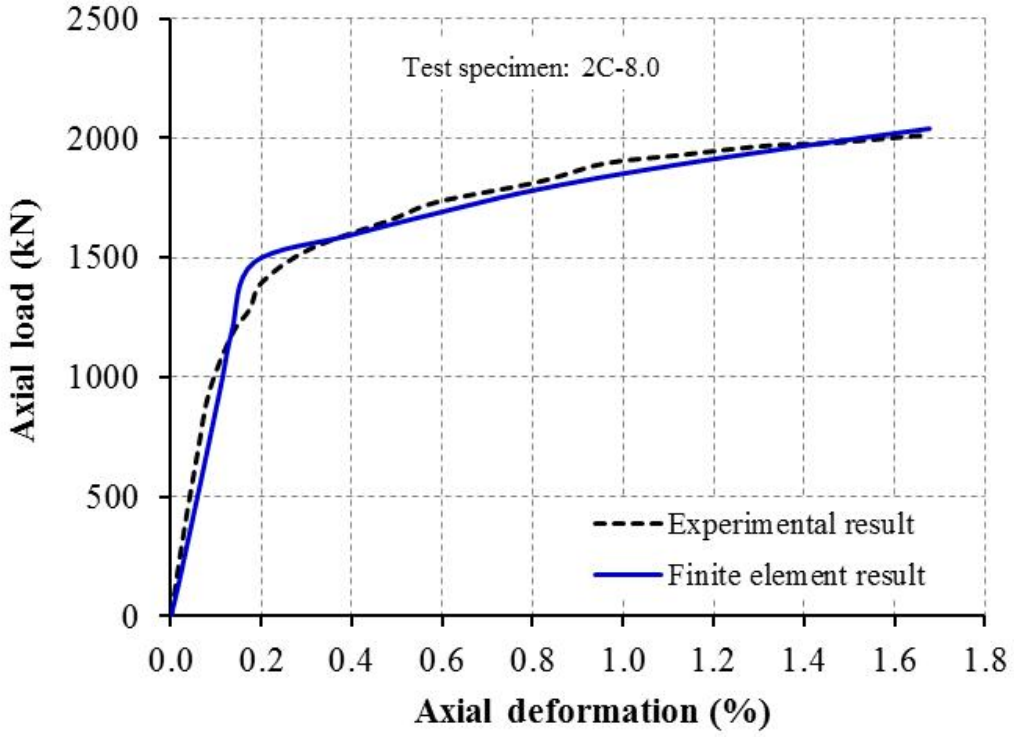

(c) 2C-8.0 ($H = 1344\ mm$)

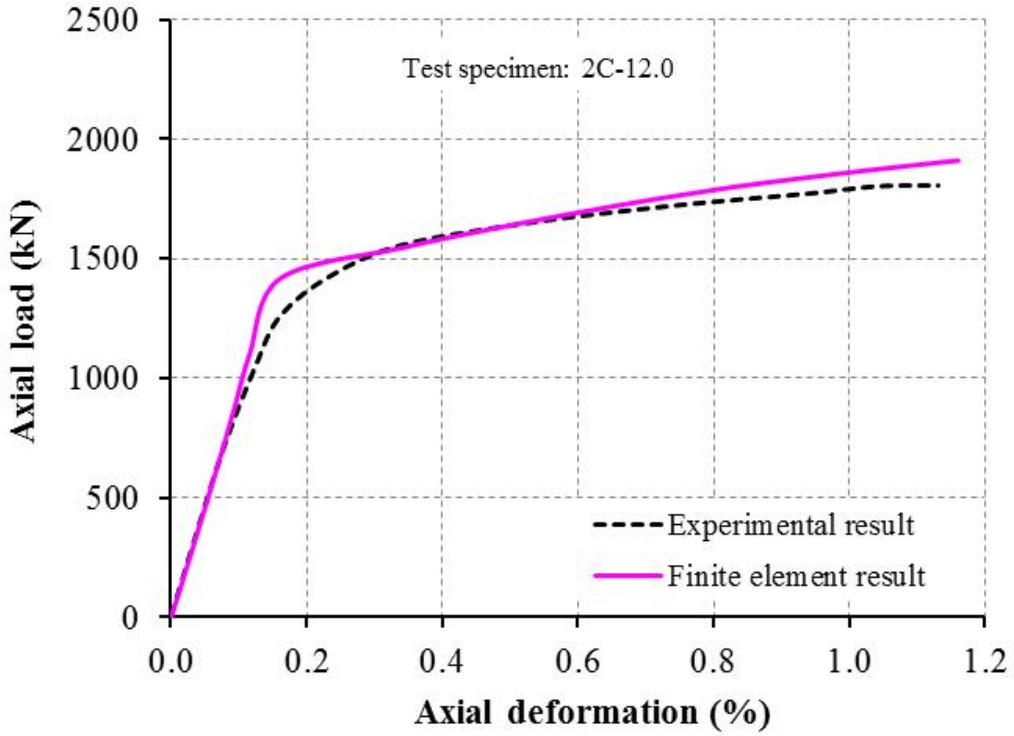

(d) 2C-12.0 ($H = 2016\ mm$)

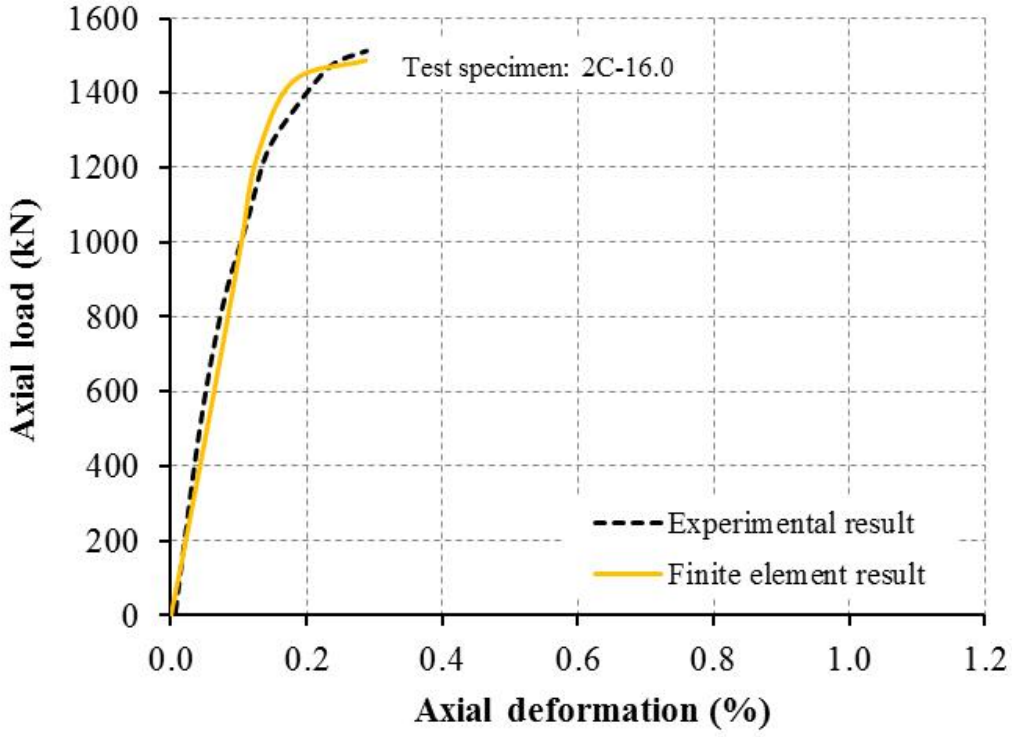

(e) 2C-16.0 ($H = 2688\ mm$)

Figure V.8: Axial load-axial deformation verification FEMs and Na et *al*. (2018) tests results with ($D = 168\ mm, t_S = 6.0\ mm, t_f = 0.111\ mm,\ \ f'_c = 38.0\ MPa$).

V.4. PARAMETRIC STUDY

The FEA parametric study involves systematically varying key parameters to analyze their effects on the structural behavior of FRP-CFST system. This investigation focuses specifically on the diameter-to-thickness ratio (D/t_s) and height-to-diameter ratio (H/D) in a parametric study. The aim is to understand how variation in these geometric ratios influences the structural performance of the FRP-confined CFST columns.

In this parametric study, the material properties such as yield strength of the steel tube, tensile strength, elastic modulus, thickness, number of layers of FRP wrap and the compressive strength of the unconfined concrete are kept constant, as utilized in validated FEA models. The focus is on varying the diameter-to-thickness ratio (D/t_s) and height-to-diameter ratio (H/D). By holding the material properties of FRP, steel and concrete fixed, this study isolates the effects of the geometric variations on the structural behavior FRP-confined CFST columns.

This parametric study allows for an understanding of how changes in the D/t_s and (H/D) ratios influence the column's load carrying capacity. The D/t_s ratio is varied to observe how different steel tube thicknesses impact the confinement effect of columns. Meanwhile, variations in the (H/D) ratio allow for the analysis of the column's slenderness and its susceptibility to global buckling. The result can offer deeper insights into how these specific geometric changes affect the performance of FRP-confined CFST columns while keeping key material properties strength consistence.

Table V.3 presents the geometric parameters used in a parametric study of FRP-confined CFST columns through FEA.

Table V.5: Geometric details of the samples investigated in the parametric study.

Specimen designation	FRP type	D/t_s	H/D	**Peak Axial Load (kN)**	**Peak axial strain $\times 10^3$**
2C-3.5	CFRP	28.0	3.50	2382.22	16.78
2C-6	CFRP	28.0	6.00	2162.12	17.39
2C-8	CFRP	28.0	8.00	2038.99	16.77
2C-12	CFRP	28.0	12.0	1909.95	11.61
2C-16	CFRP	28.0	16.0	1487.40	2.87
C-C1-3.0	CFRP	44.3	3.01	1418.98	20.10
C-C1-4.5	CFRP	29.6	3.01	1870.27	15.24
C-C1-6.0	CFRP	22.2	3.01	1882.47	12.25
C-C1-7.5	CFRP	17.7	3.01	2209.31	19.30

Figure V.9 illustrates the peak axial load of FRP-confined CFST samples. From this figure, it should be observed that for an D/t_s ratio equal to 44.3 (C-C1-3.0), the peak axial load is 1418.98 kN. As the D/t_s decrease to 29.6 (C-C1-4.5), the peak axial load increase to 1870.27 Kn. The decrease of the D/t_s ratio of structure leads to an increase in load-carrying capacity due to an increase of steel tube thickness to resist the buckling.

For D/t_s ratio equal 22.2 (C-C1-6.0), the peak axial load capacity further increase to 1882.47 kN. The hybrid FRP-CFST becomes even stiffer and provides better reinforcement. For D/t_s ratio of 17.7 (C-C1-7.5), the peak axial load decrease further to 2209.31 kN, which indicates a further increase compared to the D/t_s ratios 22.2, 29.6 and 44.3.

In conclusion, the thicker tubes provide better confinement for the concrete, enhancing the composite action between the FRP, steel and concrete.

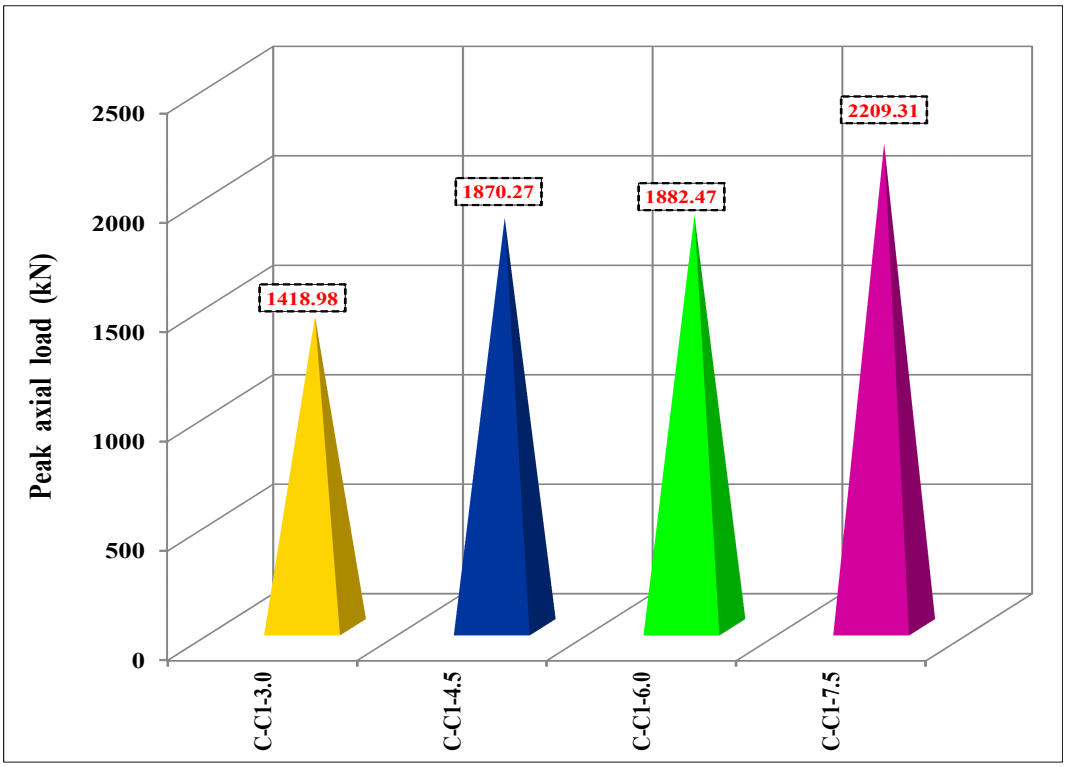

Figure V.9: Peak axial load of samples with varies D/t_s.

Figure V.10 illustrates the peak axial strain of FRP-confined CFST specimens. From this figure, it can be noted that for a specimen labeled C-C1-3.0 (D/t_s ratio of 44.3), the peak axial strain reaches 20.1. As the confinement level changes to C-C1-4.5 (D/t_s ratio of 29.6), the peak axial strain decreases to 15.24. Further reduction is seen in the C-C1-6.0 specimen (D/t_s ratio of 22.2), where the peak axial strain drops to 12.25. However, with the specimen C-C1-7.5 (D/t_s ratio of 17.7), the peak axial strain increases again to 19.3. This trend indicates that axial strain is highly influenced by the confinement configuration. The lower peak strain in C-C1-4.5 and C-C1-6.0 suggests a reduction in ductility, possibly due to less effective confinement. In contrast, the increased strain in C-C1-3.0 and C-C1-7.5 implies enhanced deformability and energy absorption capacity. The variation in peak axial strain values highlights the importance of optimizing confinement parameters to achieve the desired structural performance.

In conclusion, higher axial strain values generally correspond to better confinement efficiency, enhancing the ductility of the composite column system through improved interaction among FRP wrap, steel tube, and concrete core.

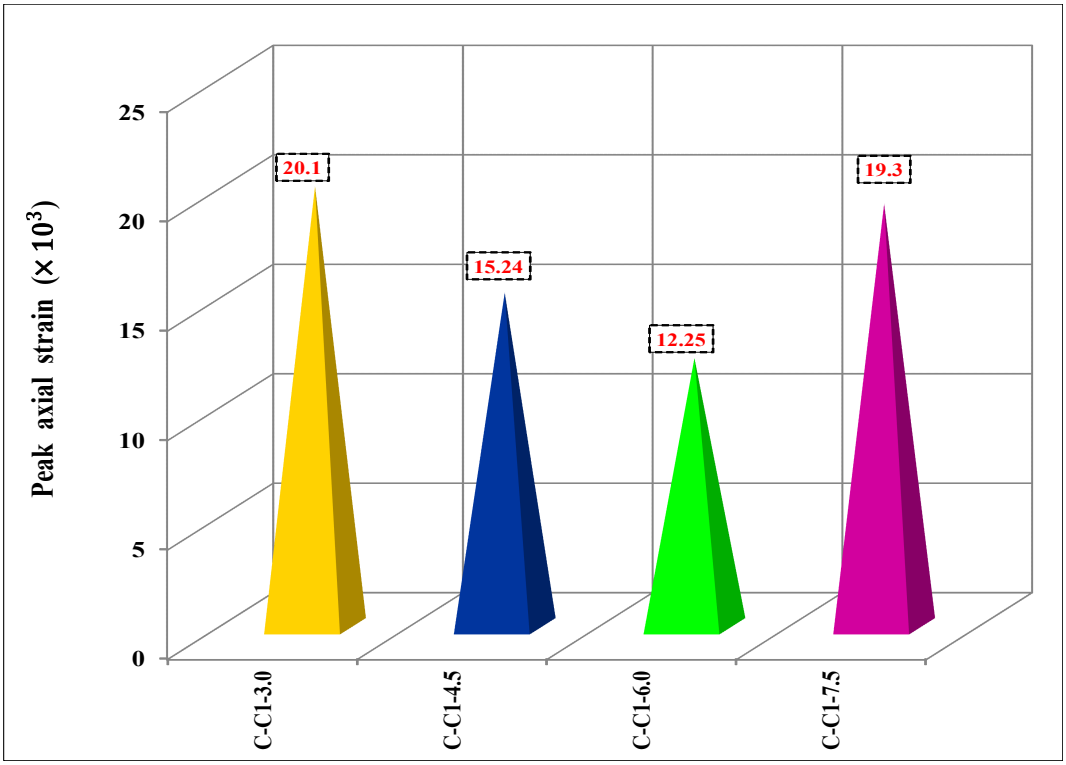

Figure V.10: Peak axial strain of samples with varies D/t_s.

Figure V.11 demonstrates the axial load–axial strain behavior of FRP-confined CFST columns with varying D/t_s ratios. The curves represent the mechanical response of specimens C-C1-3.0, C-C1-4.5, C-C1-6.0, and C-C1-7.5, each corresponding to different steel tube thicknesses, thereby altering the D/t_s ratios.

From the figure, it is evident that the axial load capacity increases as the D/t_s ratios decrease. For the specimen C-C1-3.0, which corresponds to the highest D/t_s ratios, the axial load capacity is the lowest among all, indicating relatively lower confinement efficiency. As the D/t_s ratios decrease in specimens C-C1-4.5 and C-C1-6.0, a significant enhancement in both axial load capacity and strain ductility is observed. This improvement is attributed to the increased wall thickness of the steel tube, which provides stronger confinement and delays local buckling.

Notably, the specimen C-C1-7.5, with the lowest D/t_s ratios, exhibits the highest axial load capacity and greater axial strain. This indicates superior composite action between the steel tube, FRP wrap, and concrete core. The enhanced confinement results in a more ductile response and higher energy absorption capability, improving the overall structural performance.

In summary, a lower D/t_s ratios, which corresponds to a thicker steel tube, significantly improves the load-bearing and deformation capacity of FRP-confined CFST columns. The increased confinement effectiveness enhances structural integrity, delay of local instability, and better composite action among the constituent materials.

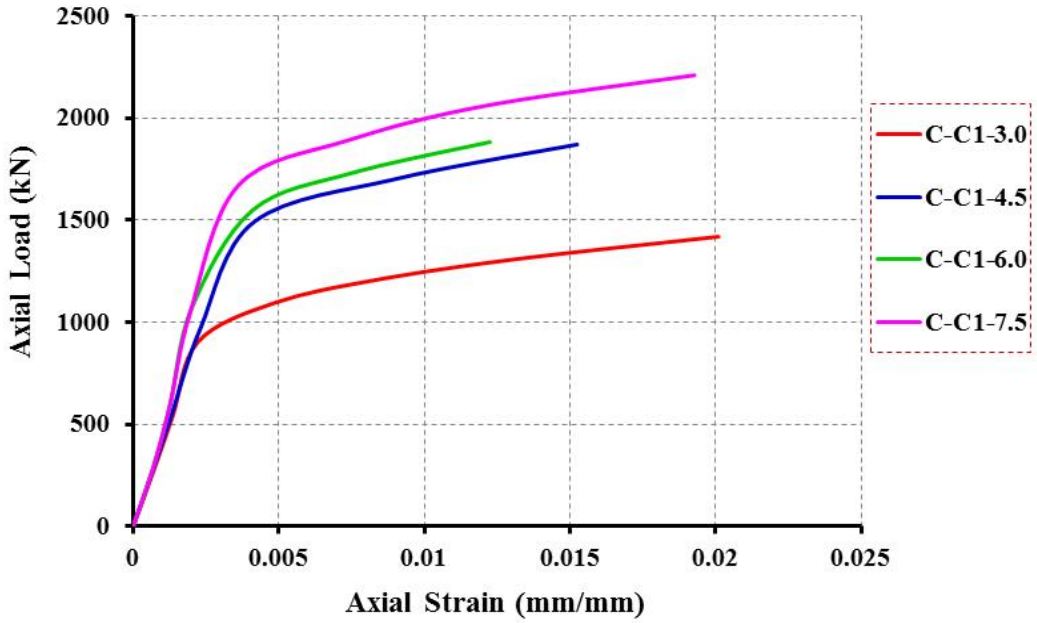

Figure V.11: Axial load versus axial stain performance of samples with varies D/t_s.

Figure V.12 illustrates the variation in peak axial load for FRP-confined CFST specimens with different H/D ratios. The specimens labeled 2C-3.5, 2C-6, 2C-8, 2C-12, and 2C-16 correspond to increasing H/D ratios, representing increasing column slenderness.

From the figure, it is evident that as the H/D ratio increases, the peak axial load capacity decreases significantly. The specimen 2C-3.5, which has the lowest H/D ratio, achieves the highest peak axial load of 2382.22 kN, indicating a strong confinement effect and superior load-bearing capacity due to its squat geometry. As the H/D ratio increases to 6 and 8, the peak axial load drops to 2162.12 kN and 2038.99 kN, respectively. This reduction is attributed to the transition from a stubby to a more slender column, which reduces the effectiveness of confinement and increases the risk of global instability.

Further increase in the H/D ratio to 12 and 16 results in a continued decline in peak axial load, reaching 1909.95 kN and 1487.4 kN, respectively. These results clearly demonstrate that slender columns exhibit lower axial load capacity, as their failure mode is more influenced by overall buckling rather than material crushing or confinement.

In conclusion, as the H/D ratio increases, the axial load-carrying capacity diminishes due to the reduced confinement efficiency and increased slenderness effects. Therefore, shorter CFST columns (lower H/D ratio) exhibit superior performance in terms of peak axial load, benefiting more from the synergistic confinement effect of FRP, steel tube, and concrete.

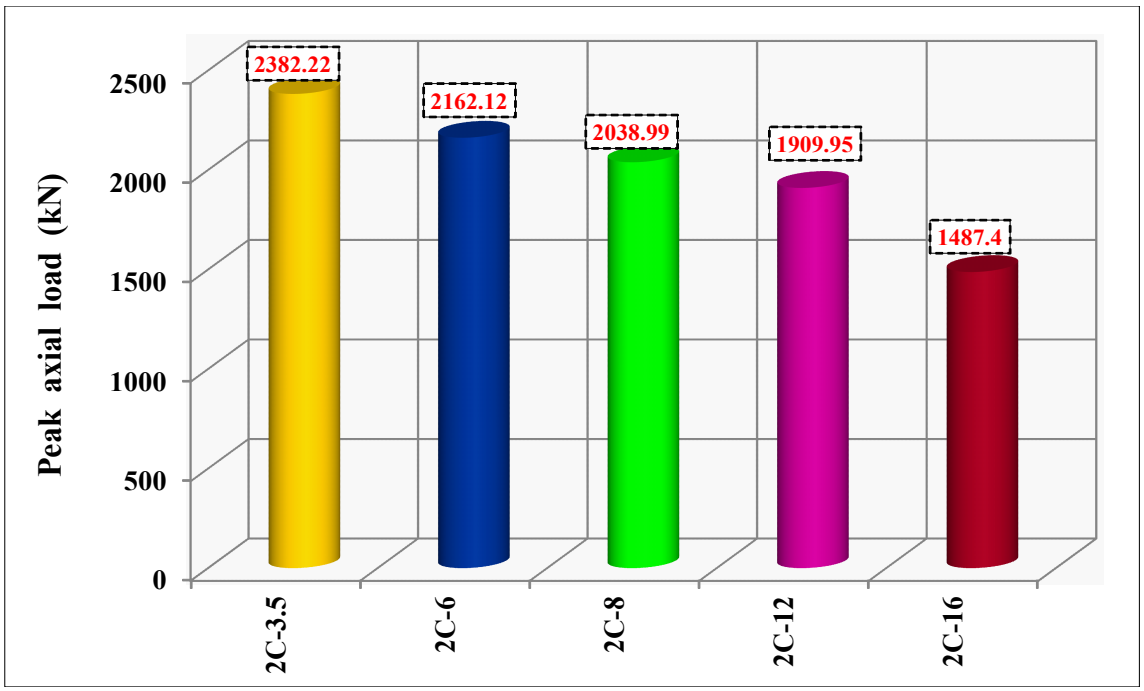

Figure V.12: Peak axial load of samples with varies H/D.

Figure V.13 presents the variation in peak axial strain for FRP-confined CFST columns with different H/D ratios, represented by specimens 2C-3.5, 2C-6, 2C-8, 2C-12, and 2C-16.

From the figure, it is observed that specimens with lower H/D ratios, such as 2C-3.5 (16.78) and 2C-6 (17.39), exhibit higher peak axial strain, indicating greater ductility and deformation capacity before failure. This reflects the beneficial effect of a stubby geometry, where confinement provided by the FRP and steel tube is more effective, allowing the column to undergo larger strains under axial loading.

As the H/D ratio increases, a clear decline in peak axial strain is observed. Although 2C-8 (16.77) still maintains relatively high strain capacity, a significant drop occurs for 2C-12 (11.61), and the lowest strain value is recorded for the most slender specimen, 2C-16 (2.87). This indicates that increased slenderness reduces ductility, leading to more brittle failure behavior due to global instability effects and reduced confinement effectiveness.

In summary, lower H/D ratios enhance the strain capacity of FRP-confined CFST columns, improving their ductility and energy absorption characteristics. On the other hand, higher H/D ratios result in reduced peak axial strain, highlighting the adverse impact of column slenderness on deformation performance.

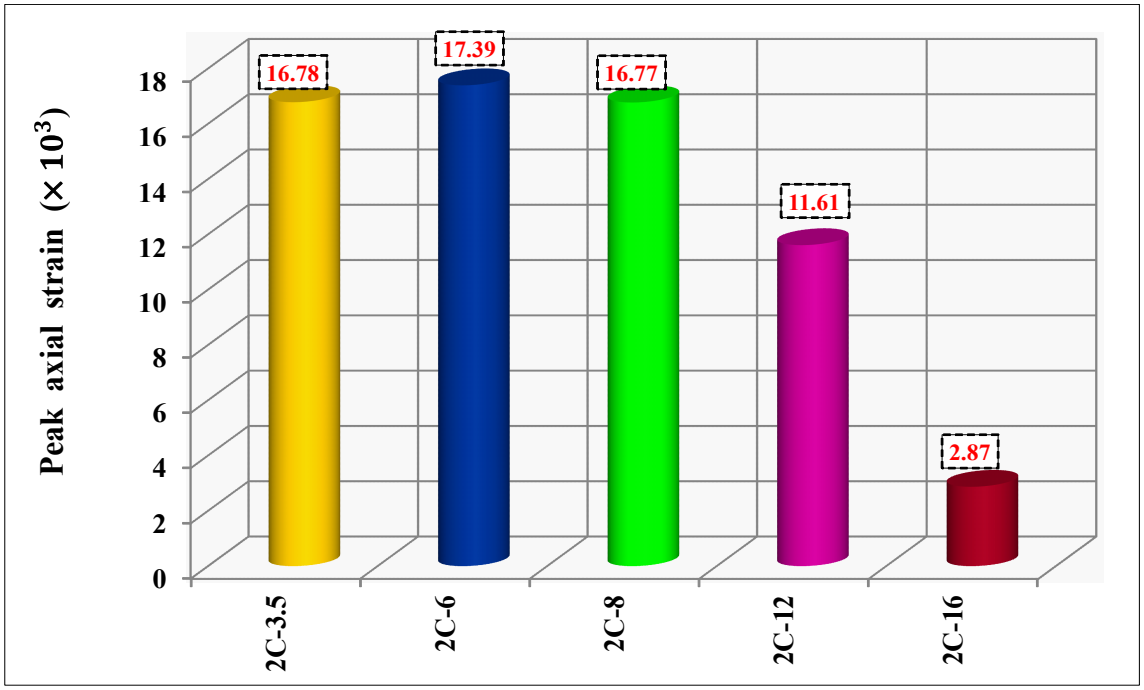

Figure V.13: Peak axial strain of samples with varies H/D.

Figure V.14 illustrates the axial load versus axial strain responses for FRP-confined CFST specimens with different H/D ratios, namely 2C-3.5, 2C-6.0, 2C-8.0, 2C-12, and 2C-16. The curves reflect the load-bearing capacity and deformation characteristics under axial compression.

From the figure, it is evident that as the H/D ratio decreases, the columns exhibit a more pronounced strain-hardening behavior and attain higher axial load capacity. The specimen with the smallest H/D ratio (2C-3.5) displays the highest load-carrying capacity and a gradual increase in load even at higher strains, indicating enhanced confinement and improved structural performance.

In contrast, as the H/D ratio increases, the peak axial load tends to decrease, and the curves become flatter, signifying reduced ductility and confinement effectiveness. Specimens 2C-12 and 2C-16, having higher slenderness ratios, demonstrate lower load capacity and earlier strain plateauing, which may indicate a transition toward global instability or buckling effects.

Furthermore, the post-peak behavior becomes less ductile with increasing H/D ratio. Slender columns experience a more brittle response, which compromises their energy absorption capacity under loading conditions. This behavior highlights the importance of geometric proportions in FRP-CFST design, where lower H/D ratios provide superior performance in both strength and deformation.

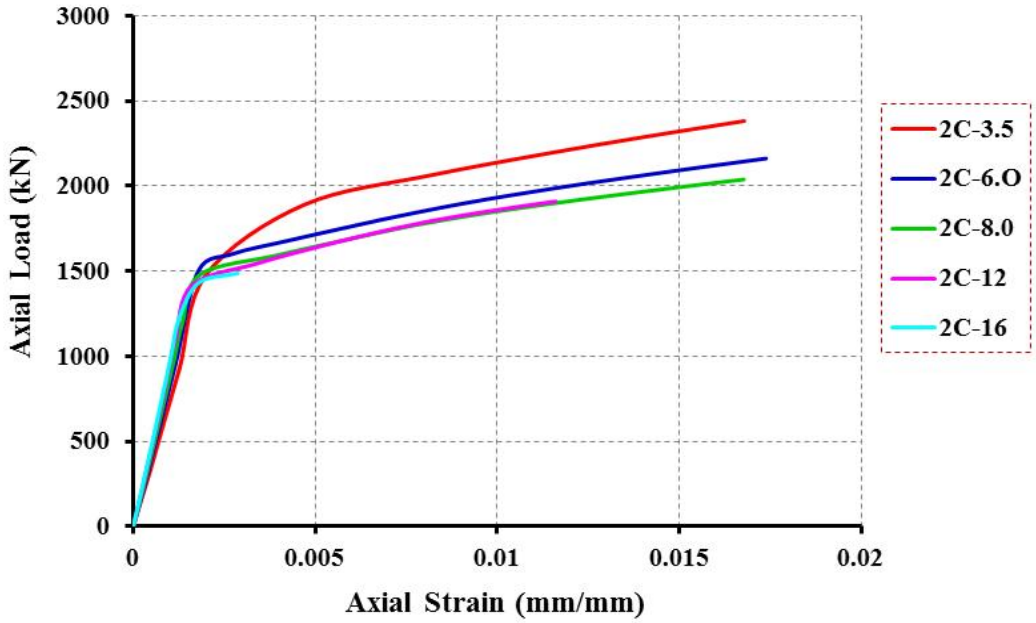

Figure V.14: Axial load versus axial stain performance of samples with varies H/D.

V.5. CONCLUSION

The behavior of forty columns was simulated using a nonlinear tree-dimensional finite element analysis (FEA) model. By comparing the FEA simulation results and axial load-axial strain curves to the experimental data, the generated FEA model is validated. The geometry properties, such as diameter-to-thickness of steel tube ratio, height-to-diameter ratio, and material properties, such as yield strength of steel tube, thickness, tensile strength, thickness, and elastic modulus of FRP wraps were all taken on into consideration when analyzing forty FRP-confined CFST columns. The findings of the experiment demonstrated that the FEA model agrees with them well. Moreover, the following points can be drawn from the analytical study:

1. The interaction between the FRP wraps, steel tube and concrete core improves load-carrying capacity , demonstrating the importance of hybrid confinement system (FRP-CFST);
2. In general, the deviations in axial load predictions remain within a reasonable range, often below 5%. While in axial strain predictions remain within a range, often below 10%, indicating good agreement between FEA model and experimental results. This suggests that the FEA model conservatively accurate, which is beneficial for design safety margins;
3. This study highlights the critical role material properties such as thickness of steel tube and number of FRP layer, compressive strength of unconfined concrete in predicting FRP-confined CFST column behavior. The model provides a reliable tool for understanding buckling and overall performance under axial load;
4. Lower D/t_s ratios, which corresponds to a thicker steel tube, significantly improves the load-bearing and deformation capacity of FRP-confined CFST columns. The increased confinement effectiveness enhances structural integrity, delay of local instability, and better composite action among the constituent materials;
5. The post-peak behavior becomes less ductile with increasing H/D ratio. Slender columns experience a more brittle response, which compromises their energy absorption capacity under loading conditions. This behavior highlights the importance of geometric proportions in FRP-CFST design, where lower H/D ratios provide superior performance in both strength and deformation.

Conclusions

This thesis has presented an analytical investigation and modeling of the structural behavior of FRP-reinforced concrete (FRP-RC) columns and FRP-confined concrete-filled steel tube (CFST) columns. Empirical and machine learning-based models for predicting axial load-carrying capacity of the FRP-RC concrete columns and hybrid deep learning-based models for predicting load-carrying capacity of FRP-confined CFST columns were also presented in this thesis. Furthermore, a finite element (FE) model for predicting the behavior of FRP-confined CFST columns was presented and verified with test results.

1. Axial load-carrying capacity of reinforced concrete (RC) columns reinforced with FRP bars

Chapter III presented the development of load-carrying capacity models of reinforced concrete (RC) columns reinforced with FRP bars at varying eccentricity levels, using both empirical modeling, eXtreme Gradient Boosting (XGBoost), and random forest (RF) algorithms. A comprehensive dataset comprising 308 test results on FRP-RC columns subjected to concentric and eccentric compression loads was analyzed. Utilizing this dataset, new empirical models, XGBoost, and RF algorithms were developed to predict the load-carrying capacity of FRP-RC columns. These models are applicable to cases with eccentricity ratios (e/h) ranging from 0 to 1. Based on these empirical and machine learning models, the following conclusions were drawn:

1. A statistical evaluation of 15 existing models for predicting axial load-carrying capacity (ALCC) in FRP-reinforced concrete columns revealed that these models tend to overestimate capacity compared to test results, showing conservative estimates. Additionally, the predictions from these models displayed significant variability, with low R^2 values ranging from 0.34 to 0.70 and high error rates. This discrepancy is likely due to the lack of consideration for eccentricity effects in the existing formulas;
2. A regression analysis was conducted to derive new, simplified equations for calculating ALCC in FRP-RC compressive members. Firstly, specific expression to members under concentric compression was developed, incorporating the impact of FRP bars' axial strain (ε_{frp}) and stiffness (E_{frp}). Subsequently, a unified expression for both concentric and eccentric compression loads (e/h from 0 to 1) was created, accounting for eccentricity effects;
3. The proposed empirical models demonstrated robust predictive performance over the test dataset. The first model, designed for concentric loading, achieved R^2 = 0.97, RMSE = 387.27 kN, MAE = 214.20 kN, AAE = 0.10, and SD = 0.15, indicating high precision and consistency. The second model, suitable for both concentric and eccentric loading, showed R^2 = 0.88, RMSE = 635.75 kN, MAE = 405.08 kN, AAE = 0.31, and SD = 0.52, highlighting its effective predictability across a wider range of load conditions;
4. The proposed XGBoost model exhibited exceptional predictive capability for the load-

carrying capacity of FRP-RC compressive members, achieving an R^2 value of 0.98 and low error values (RMSE = 259.05 kN, MAE = 144.36 kN, AAE = 0.11, SD = 0.14). This indicates the model's superior precision and reliability in comparison to empirical models;

5. When compared to existing formulas, the XGBoost model consistently outperformed empirical models in accuracy. This suggests that both the empirical and XGBoost models developed here offer reliable predictions for the load-carrying capacity of FRP-reinforced concrete compressive members under both concentric and eccentric loads, making them valuable tools for structural analysis and design applications;
6. This study also investigates whether machine learning, specifically Random Forest (RF) regression, could accurately predict the axial load-carrying capacity (ALCC) of FRP-reinforced concrete (FRP-RC) columns reinforced laterally with FRP ties or spirals, outperforming traditional empirical models. By analyzing a dataset of 308 records, the RF model used eleven key input variables to predict the ultimate capacity of these columns with high precision. The results affirmatively answer the research question: the RF model not only closely aligned with actual test data but also outperformed fifteen existing empirical formulas, achieving a robust R^2 of 0.98 and lower errors across multiple metrics (e.g., RMSE of 282.11 kN). These findings confirm that RF regression provides a reliable, more accurate approach to ALCC prediction, offering a practical tool for structural engineers and advocating for the broader integration of machine learning in civil engineering applications.

Our study contributes to a more nuanced understanding of the behavior of FRP-reinforced concrete (FRP-RC) compressive members by demonstrating the effectiveness of machine learning techniques, in predicting peak axial capacity. This predictive accuracy advances our understanding of FRP-RC behavior under varying eccentricity levels by providing reliable and data-driven estimates for complex structural scenarios that traditional empirical models may struggle to capture. The findings underscore the potential for machine learning to handle nonlinear relationships and variability in FRP-RC performance, offering insights that could lead to improved design codes and standards for FRP-reinforced members.

2. Axial load-carrying capacity of FRP-confined concrete-filled steel tube columns

A comprehensive investigation into the prediction of the axial load-carrying capacity (ALCC) of Fiber Reinforced Polymer (FRP)-confined Concrete-Filled Steel Tubes (CFST) under axial compression, using hybrid deep learning (HDL) approaches, has been presented in chapter IV. A large dataset comprising 255 experimental results of FRP-confined CFST samples subjected to axial compression loads was compiled from previous literature. Based on this database, two deep learning models were developed: a hybrid CNN-BiLSTM model and a traditional BiLSTM model to predict the ALCC of strengthened columns with a hybrid confinement system (FRP wraps–steel tube). Based on deep learning modeling, the following conclusions were drawn:

1. The deep learning models, particularly the CNN-BiLSTM, outperformed the traditional BiLSTM model, demonstrating significant improvements in prediction accuracy. The CNN-BiLSTM model achieved the lowest root-mean-square error (an RMSE) of 204.555 and a mean absolute error (an MAE) of 150.589, indicating its superior predictive capability compared to empirical models. For example, CNN-BiLSTM outperformed empirical models such as that proposed by Tao et al. (2007), which reported an RMSE of 949.523 and an MAE of 874.451. This highlights the advantage of advanced deep learning models in addressing complex prediction tasks;
2. Empirical models, while valuable, exhibited greater deviations compared to deep learning models. For example, the model proposed by Park et al. (2011) (Eq. (8)) provided more accurate predictions than other empirical approaches but still fell short when compared to the CNN-BiLSTM results.

3. Finite element (FE) modeling of the behavior of FRP-confined concrete-filled steel tube columns

Chapter V presents the FE simulation of forty FRP-confined concrete-filled steel tube (CFST) columns. The generated FEA model was validated by comparing the FEA simulation results, specifically axial load-axial strain curves, with the experimental data. The geometry properties, such as the diameter-to-thickness ratio and the height-to-diameter ratio of the steel tube, and the material properties, such as the yield strength and the thickness of the steel tube, and tensile strength, thickness, and elastic modulus of FRP wraps, were all taken into consideration when analyzing the forty FRP-confined CFST columns. The experimental findings demonstrated good agreement with the FEA model. Moreover, the following points can be drawn from the analytical study:

1. The interaction between the FRP wraps, steel tube and concrete core improves load-carrying capacity , demonstrating the importance of hybrid confinement system (FRP-CFST);
2. In general, the deviations in axial load predictions remain within a reasonable range, often below 5%. While in axial strain predictions remain within a reasonable range, often below 10%, this indicates good agreement between the FEA model and experimental results. This suggests that the FEA model is conservatively accurate, which is beneficial for design safety margins;
3. This study highlights the critical role of material properties such as the thickness of the steel tube and the number of FRP layer, the compressive strength of unconfined concrete in predicting FRP-confined CFST column behavior. The model provides a reliable tool for understanding buckling and the overall performance under axial load;
4. Lower D/t_s ratios**,** which corresponds to a thicker steel tube, significantly improves the load-bearing and deformation capacity of FRP-confined CFST

columns. The increased confinement effectiveness enhances structural integrity, delay of local instability, and better composite action among the constituent materials;

5. The post-peak behavior becomes less ductile with increasing H/D ratio. Slender columns experience a more brittle response, which compromises their energy absorption capacity under loading conditions. This behavior highlights the importance of geometric proportions in FRP-CFST design, where lower H/D ratios provide superior performance in both strength and deformation.

4. Further Research

Considering the limitation of the proposed models, the input parameters are acceptable within the range provided in the databases. Future works are recommended to:

1. Develop explainable machine learning and deep learning-based predictions of axial capacity of FRP-reinforced self-compacting geopolymer concrete compressive members.
2. Develop analytical model for predicting the behavior of FRP-confined concrete-filled steel tube columns under combined axial compression and monotonic or cyclic lateral loading.
3. Conduct an experimental investigation into the behavior of damaged concrete columns confined with both FRP wraps and bars under axial compression loads.

References

REFERENCES

Abdelazim, W., Mohamed, HM. and Benmokrane, B. (2020), "Inelastic second-order analysis for slender GFRP-reinforced concrete columns: Experimental investigations and theoretical study", *J of Compos for Constr.*, **24**(3), 04020016. https://doi.org/10.1061/(ASCE)CC.1943-5614.0001019

Abdelrahman, A. (2023), "Strengthening of concrete structures: unified design approach, numerical examples and case studies", *Springer Nature*. https://doi.org/10.1007/978-981-19-8076-3

Abdulazeez, A., Salim, B., Zeebaree, D. and Doghramachi, D (2020), "Comparison of VPN protocols at network layer focusing on WireGuard protocol".

Abunassar, N., Alas, M. and Ali, Sia. (2023), "Prediction of compressive strength in self-compacting concrete containing fly ash and silica fume using ANN and SVM", *Arab J. for Sci. and Eng.*, **48**(4), 5171–5184.

ACI (2015), "American Concrete Institute, Guide for the Design and Construction of Concrete Reinforced with FRP Bars", In: ACI 4401R-15, ACI, Farmington Hills, MI.

ACI 318. (2011), "Building code requirements for structural concrete and commentary", American Concrete Institute; Farmington Hills, MI, U.S.A, 436 pp.

ACI (2008), "Building code requirements for structural concrete and commentary", In: ACI 318-08, American Concrete Institute, Farmington Hills, MI, U.S.A.

Afaq, A., Bahrami, A., Alajarmeh, O., Chairman, N. and Yaqub, M. (2023), "Investigation of circular hollow concrete columns reinforced with GFRP bars and spirals", *Build.*, **13**(4), 1056. https://doi.org/10.3390/buildings13041056

Afifi, M. M. Z. M. (2013), "Behavior of circular concrete columns reinforced with FRP bars and stirrups [Doctoral dissertation, Université de Sherbrooke]. Université de Sherbrooke Institutional Repository.

Afifi, M.Z., Mohamed, H.M. and Benmokrane, B. (2014), "Axial capacity of circular concrete columns reinforced with GFRP bars and spirals", *J of Compos for Constr.*, **18**(1), 04013017. https://doi.org/10.1061/(ASCE)CC.1943-5614.0000438

Afifi, M.Z., Mohamed, H.M. and Benmokrane, B. (2014), "Strength and axial behavior of circular concrete columns reinforced with CFRP bars and spirals", *J of Compos for Constr*, 18(2), 04013035. https://doi.org/10.1061/(ASCE)CC.1943-5614.0000430

Ahmad, A., Ahmad, W., Aslam, F. and Joyklad, P. (2022), "Compressive strength prediction of fly ash-based geopolymer concrete via advanced machine learning techniques", *Case. Stu. in Const. Mater*, **16**, e00840.

Alatshan, F., Ding, Y. and Zhang, L. (2020), "Stiffened concrete-filled steel tubes: A systematic review", *Thin-Wall. Struct.*, **148**, 106590. https://doi.org/10.1016/j.tws.2019.106590

Alatshan, F., Osman, S. A., Hamid, R. and Mashiri, F. (2020), "Stiffened concrete-filled steel tubes: A systematic review", Thin-Wall. Struct., **148**, 106590. https://doi.org/10.1016/j.tws.2019.106590

Al-Haddad, D. B. and Jokhio, G. A. (2024), "Durability Design Approach and Exposure Conditions in Eurocode, British Standard and ISO 13823 Standards: A Review", In BUiD Doctoral Research Conference 2023: Multidisciplinary Studies, 203-213.

Ali, M.A. and El-Salakawy, E. (2016), "Seismic performance of GFRP-reinforced concrete rectangular columns", *J of Compos for Constr.,* **20**(3), 04015074. https://doi.org/10.1061/(ASCE)CC.1943-5614.0000637

Alnemrawi, B.R. and Al-Rousan, R. (2024), "The Detailed Axial Compression Behavior of CFST Columns Infilled by Lightweight Concrete", *Build*., **14**(9), 2844. https://doi.org/10.3390/buildings14092844

Al-Rousan, R.Z. and Sawalha, H.M. (2024), "The behavior of concrete filled steel tubular columns infilled with high-strength geopolymer recycled aggregate concrete", *Steel and Comp. Struct*., **51**(6), 661-678. https://doi.org/10.12989/scs.2024.51.6.661

Al-Rousan, R.Z., Bara'A R. Alnemrawi, B.R. and Sawalha, H.M. (2024), "The ultimate capacity of geopolymer recycled aggregate concrete filled steel tubular columns: Numerical and theoretical study", *J. of Build. Eng*., **96**, 110365. https://doi.org/10.1016/j.jobe.2024.110365

Alzubaidi, L., Zhang, J., Humaidi, A.J., Al-Dujaili, A., Duan, Y., Al-Shamma, O., Santamaría, J., Fadhel, M.A., Al-Amidie, M. and Farhan, L. (2021), "Review of deep learning: Concepts, CNN architectures, challenges, applications, future directions", *Journal of Big Data*, **8**(1), 53, 2021. https://doi.org/10.1186/s40537-021-00444-8 .

American Concrete Institute (ACI) (1996), "State-of-the-art report on fiber reinforced plastic (FRP) reinforcement for concrete structures", ACI 440R-96 Committee 440.

Andrade, C. and Alonso, C. (2001), "On-site measurements of corrosion rate of reinforcements", Constr. and Build. Mater., **15**(2-3), 141-145. https://doi.org/10.1016/S0950-0618(00)00063-5

Arabshahi, A., Gharaei-Moghaddam, N. and Tavakkolizadeh, M. (2019), "Proposition of new applicable strength models for concrete columns confined with fiber reinforced polymers", *SN Appl. Sci*., **1**(12), 1-28. https://doi.org/10.1007/s42452-019-1643-5

AS 3600. (2018), "Concrete Structures", Standards Australia: Sydney, Australia.

Association CS. (2012), "Design and construction of building structures with fibre-reinforced polymer", CAN/CSA S806-12. Toronto, ON, Canada.

Bakouregui, A.S., Mohamed, H.M., Yahia, A. and Benmokrane, B. (2021), "Explainable extreme gradient boosting tree-based prediction of axial capacity of FRP-RC columns", *Eng Struct*, **245**, 112836. https://doi.org/10.1016/j.engstruct.2021.112836

Balaguru, P., Nanni, A. and Giancaspro, J. (2008), "FRP composites for reinforced and prestressed concrete structures: a guide to fundamentals and design for repair and retrofit", CRC Press.

Barua, S. and El-Salakawy, E. (2020), "Performance of GFRP-reinforced concrete circular short columns under concentric, eccentric, and flexural loads", *J of Compos for Constr*, **24**(5), 04020044. https://doi.org/10.1061/(ASCE)CC.1943-5614.0001058

Bentéjac, C., Csörgő, A. and Martínez-Muñoz, G (2021), "A comparative analysis of gradient boosting algorithms", Artific. Intellig.e Rev., **54**, 1937–1967.

Berhane, K., Hauptmann, M. and Langholz, B. (2008), "Using tensor product splines in modeling exposure–time–response relationships: Application to the Colorado Plateau Uranium Miners cohort", Statis. Medic., **27**, 5484–5496.

Berradia, M. and Kassoul, A. (2018), "Ultimate strength and strain models proposed for CFRP confined concrete cylinders", *Steel and Compos. Struct*., **29**(4), 465–481.

Berradia, M., Azab, M., Ahmad, Z., Accouche, O., Raza, A. and Alashker, Y. (2022), "Data-driven prediction of compressive strength of FRP-confined concrete members: An application of machine learning models", *Struct Eng and Mech*., **83**(4), 515-535. https://doi.org/10.12989/sem.2022.83.4.515

Berradia, M., El Ouni, M.H., Liaqat, A., Raza, A. and Ali, B. (2021), "Data-oriented analysis of axial capacity of externally CFRP-confined concrete columns transversely reinforced

with steel hoops or spirals", *Mech of Adv Mater and Struct*., **28**(19), 1-14. https://doi.org/10.1080/15376494.2021.1980928

Berradia, M., Meziane, E.H, Raza, A., Ahmed, M., Zaman Khan, Q. and Shabbir, F. (2023), "Prediction of ultimate strain and strength of CFRP-wrapped normal and high-strength concrete compressive members using ANN approach", *Mech of Adv Mater and struct*., https://doi.org/10.1080/15376494.2023.22

Berradia, M., Meziane, E.H., Raza, A., El Ouni, M.H. and Shabbir, F. (2023), "A GMDH-based estimation model for axial load capacity of GFRP-RC circular columns", *Steel and Compos Struct*., **49**(2), 161-180. https://doi.org/10.12989/scs.2023.49.2.161

Bett, B. J., Klingner, R. E. and Jirsa, J. O. (1988), "Lateral load response of strengthened and repaired reinforced concrete columns", *Struct. J*., **85**(5), 499-508.

Binici, B. (2005), "An analytical model for stress-strain behavior of confined concrete", *Eng Struct*., **27**(7), 1040-1051. https://doi.org/10.1016/j.engstruct.2005.03.002

Bournas, D. A. (2018), "Concurrent seismic and energy retrofitting of RC and masonry building envelopes using inorganic textile-based composites combined with insulation materials", *Compos; Part B: Eng*;, **148**, 195-205. https://doi.org/10.1016/j.compositesb.2018.04.002

Breiman, L. (2001), "Random forests", Machine Learning, 45, 5–32.

Broomfield, J.P. (2007), "Corrosion of steel in concrete: Understanding, investigation and repair", (2nd ed.), Taylor & Francis.

CAN/CSA S806-02, (2006), "Design and Construction of Building Structures with Fibre-Reinforced Polymers", Canadian Standards Association: Toronto, ON, Canada,.

Cañete-Sifuentes, L., Monroy, R. and Medina-Pérez, M.A (2021), "A review and experimental comparison of multivariate decision trees", IEEE Access, 9, 110451–110479.

Cao, M., Alkayem, N.F., Pan, L. and Novák, D. (2016), "Advanced methods in neural networks-based sensitivity analysis with their applications in civil engineering", Artificial Neural Networks – Models and Applications. *InTech*, 335–353.

Cao, S., Wu, C. and Wang, W. (2020), "Behavior of FRP confined UHPFRC-filled steel tube columns under axial compressive loading", *J Build Eng*., **32**, 101511. https://doi.org/10.1016/j.jobe.2020.101511

Chakra F.A. (2016), "Renforcement des poteaux en béton armé au moyen de polymère renforcé par fibre de carbone : comparaison des codes", Matériaux composites et construction, HAL archives-ouvertes.fr.

Chambers, J.M. and Hastie, T.J. (1992), "Statistical Models in S. Pacific Grove, CA: Wadsworth and Brooks/Cole".

Che, Y., Wang, Q.L. and Shao, Y.B. (2012), "Compressive performances of the concrete-filled circular CFRP-steel Tube (C-CFRP-CFST)", *Adv Steel Constr*., **8**, 331-358. https://doi.org/10.18057/IJASC.2012.8.4.2

Chen, T. and Guestrin, C (2016), "XGBoost: A scalable tree boosting system", Proceedings of the 22nd ACM SIGKDD International Conference on Knowledge Discovery and Data Mining, 785–794.

Chen, T. and Guestrin, C. (2016), "XGBoost: A Scalable Tree Boosting System", In: Proceedings of the 22nd ACM SIGKDD International Conference on Knowledge Discovery and Data Mining, 785-94. https://doi.org/10.1145/2939672.2939785

Chen, Z., Pang, Y., Xu, R., Zhou, J. and Xu, W. (2022), "Mechanical performance of ocean concrete-filled circular CFRP-steel tube columns under axial compression", *J Constr Steel Res*., **198**, 107514. https://doi.org/10.1016/j.jcsr.2022.107514

Cozmanciuc, C., Oltean, R. and Munteanu, V. (2009), "Strengthening techniques of RC columns using fibre reinforced polymeric materials", Bulet. Institutului Politechnic din lasi. Sectia Constructii, Arhitectura, **55**(3), 85.

Das, S., Tariq, A., Santos, T., Kantareddy, S.S. and Banerjee, I. (2023), "Recurrent neural networks (RNNs): Architectures, training tricks, and introduction to influential research", Colliot, O., ed. *Mach. Learn. for Brain Disord*., **197**, 117–138. https://doi.org/10.1007/978-1-0716-3195-9_4 .

Dassault Systemes Corp. (2012), "Abaqus: Standard user's manual, version 6.12", Providence, RI (USA).

De Luca, A., Matta, F. and Nanni, A. (2010), "Behavior of full-scale glass fiber-reinforced polymer reinforced concrete columns under axial load", *ACI struct J*, **107**(5), 589-96. https://doi.org/10.14359/51663912

Deng, J., Zheng, Y.F., Yi, W., Liu, T.H. and Li, H. (2017), "Study on axial compressive capacity of FRP confined concrete-filled steel tubes and its comparisons with other composite structural systems", *Int J Polym Sci*., 1-7. https://doi.org/10.1155/2017/6272754

Di Sarno, L., Elnashai, A. S. and Nethercot, D. A. (2006), "Seismic retrofitting of framed structures with stainless steel", J. of Constr. Steel Res., **62**(1–2), 93–104. https://doi.org/10.1016/j.jcsr.2005.05.007

Diboune, N., Benzaid, R. and Berradia, M. (2022), "New strength–strain model and stress–strain relationship for square and rectangular concrete columns confined with CFRP wraps", *Mech of Adv Mater and struct*., **30**(14), 2971-2994. https://doi.org/10.1080/15376494.2022.2067604

Diboune, N., Benzaid, R. and Berradia, M. (2022), "New strength–strain model and stress–strain relationship for square and rectangular concrete columns confined with CFRP wraps", *Mech. of Adv. Mater. and Struct*., **30**(14), 2971–2994. https://doi.org/10.1080/15376494.2022.2067604

Dimiduk, D.M., Holm, E.A. and Niezgoda, S.R. (2018), "Perspectives on the impact of machine learning, deep learning, and artificial intelligence on materials, processes, and structures engineering", *Integ. Mater. and Manuf. Innov*., **7**, 157–172.

Ding, F.X., Lu, D.R., Bai, Y., Gong, Y.Z., Yu, Z.W. and Ni, M. (2018), "Behaviour of CFRP confined concrete-filled circular steel tube stub columns under axial loading", *Thin-Wall. Struct.,* **125**, 107-118. https://doi.org/10.1016/j.tws.2018.01.015

Ding, L.N., Liu, X., Wang, X., Huang, H.J. and Wu, Z.S. (2018), "Mechanical properties of pultruded basalt fiber-reinforced polymer tube under axial tension and compression", *Constr. Build. Mater.,* **176**, 629-637. https://doi.org/10.1016/j.conbuildmat.2018.05.036

Djafar-Henni, I. and Kassoul, A. (2018), "Stress–strain model of confined concrete with Aramid FRP wraps", Constr. and Build. Mater., **186**, 1016–1030.

Dong, C.X., Kwan, A.K.H. and Ho, J.C.M. (2017), "Effects of external confinement on structural performance of concrete-filled steel tubes", *J Constr Steel Res*., **132**, 72-82. https://doi.org/10.1016/j.jcsr.2016.12.024

Dong, M., Elchalakani, M., Karrech, A., Pham, T.M. and Yang, B. (2019), "Glass fibre-reinforced polymer circular alkali-activated fly ash/slag concrete members under combined loading", *Eng Struct*., 199, 109598. https://doi.org/10.1016/j.engstruct.2019.109598

Eduardo, F. L., Julio, M., Branco, F. A., and Silva, V. D. (2005), "Structural rehabilitation of columns with reinforced concrete jacketing", ACI Struct. J., **102**(5), 676–684.

Elchalakani, M. and Ma, G. (2017), "Tests of glass fibre reinforced polymer rectangular concrete columns subjected to concentric and eccentric axial loading", *Eng Struct*., **151**, 93-104. https://doi.org/10.1016/j.engstruct.2017.08.023

Elchalakani, M., Dong, M., Karrech, A., Li, G., Mohamed Ali, M. and Yang, B. (2019), "Experimental investigation of rectangular air-cured geopolymer concrete columns reinforced with GFRP bars and stirrups", *J of Compos for Constr*., **23**(3), 04019011. https://doi.org/10.1061/(ASCE)CC.1943-5614.0000938

Elchalakani, M., Dong, M., Karrech, A., Mohamed Ali, M.S. and Huo, J.S. (2020), "Circular concrete columns and beams reinforced with GFRP bars and spirals under axial, eccentric, and flexural loading", *J of Compos for Constr.*, **24**(3), 04020008. https://doi.org/10.1061/(ASCE)CC.1943-5614.0001008

Elchalakani, M., Ma, G., Aslani, F. and Duan, W. (2017), "Design of GFRP-reinforced rectangular concrete columns under eccentric axial loading", *Magaz of Concr Res.*, 69(17), 865-77. https://doi.org/10.1680/jmacr.16.00437

El-Gamala, S. and AlShareedahb, O. (2020), "Behavior of axially loaded low strength concrete columns reinforced with GFRP bars and spirals", *Eng Struct.*, 216, 110732. https://doi.org/10.1016/j.engstruct.2020.110732

Elmesalami, N., El Refai, A. and Abed, F. (2019), "Fiber-reinforced polymers bars for compression reinforcement: A promising alternative to steel bars", *Constr and Build Mater.*, **209**(1), 725-737. https://doi.org/10.1016/j.conbuildmat.2019.03.105

ElMessalami, N., Abed, F. and El Refai, A. (2021), "Response of concrete columns reinforced with longitudinal and transverse BFRP bars under concentric and eccentric loading", *Compos. Struct.*, **255**, 113057. https://doi.org/10.1016/j.compstruct.2020.113057

ELMESSALAMI, N., ABED, F. and EL REFAI, A. (2021), "Response of concrete columns reinforced with longitudinal and transverse BFRP bars under concentric and eccentric loading", Compos. Struct., **255**, 113057. https://doi.org/10.1016/j.compstruct.2020.113057

Ersoy, U., Tankut, T., & Ozcebe, G. (1993), "Behavior of jacketed columns under axial load and lateral cyclic load", ACI Struct. J., **90**(5), 542–553.

Esfandiari, S. and Esfandiari, J. (2016), "Simulation of the behaviour of RC columns strengthen with CFRP under rapid loading", *Adv in Concr Constr.*, **4**(4), 319-332. https://doi.org/10.12989/acc.2017.4.4.319

Fakharifar, M., Chen, G., Wu, C., Shamsabadi, A., ElGawady, M. A. and Dalvand, A. (2016), "Rapid repair of earthquake-damaged RC columns with prestressed steel jackets". J. of Bridg. Eng., **21**(4), 04015075. https://doi.org/10.1061/(ASCE)BE.1943-5592.0000840

Fang, Y. (2024), "Study on mechanical properties and application of FRP confined concrete-filled steel tube columns", Trans. on Eng. and Techn. Res., **4**. https://creativecommons.org/licenses/by-nc/4.0/

Freund, Y. and Schapire, R.E (1997), "A decision-theoretic generalization of on-line learning and an application to boosting", J. of Comput. and Syst. Scien., **55**, 119–139.

Freund, Y. and Schapire, R.E. (1996), "Experiments with a new boosting algorithm", Proceedings of the 13th International Conference on Machine Learning, 148–156.

Friedman, J.H. (2001), "Greedy function approximation: A gradient boosting machine", Annals of Statistics, 29, 1189–1232.

Gandhi, N., Patel, J., Sisodiya, R., Doshi, N. and Mishra, S. (2021), "A CNN-BiLSTM based approach for detection of SQL injection attacks", *Int Conf Comput Intell Knowl Econ (ICCIKE)*, 378-383. https://doi.org/10.1109/ICCIKE51210.2021.9410675

Ghani, M. U., Ahmad, N., Abraha, K. G., Manj, R. Z. A., Sharif, M. H. and Wei, L. (2024), "Review and assessment of material, method, and predictive modeling for Fiber-Reinforced Polymer (FRP) partially confined concrete columns", *Polymers*, **16**(10), 1367.

Ghobarah, A., Biddah, A. and Mahcoub, M. (1997), "Rehabilitation of reinforced concrete columns using corrugated steel jacketing", J. of Earth. Eng., **1**(4), 651–673. https://doi.org/10.1080/13632469708962382

Gianey, H.K. and Choudhary, R. (2017), "Comprehensive review on supervised machine learning algorithms", International Conference on Machine Learning and Data Science, Noida, India.

Gkournelos, P., Bournas, D. A. and Triantafillou, T. C. (2021), "Seismic upgrading of existing reinforced concrete buildings: A state-of-the-art review", Eng. Struct., **244**, 112812. https://doi.org/10.1016/j.engstruct.2021.112812

Gu, W., Guan, C.W., Zhao, Y.H. and Cao, H. (2004), "Experimental study on concentrically-compressed circular concrete-filled CFRP-steel composite tubular short columns", *J Shenyang Archit Civ Eng Inst.,* **20**, 118-120.

Guo, D., Duan, P., Yang, Z., Zhang, X. and Su, Y. (2024), "Convolutional Neural Network and Bidirectional Long Short-Term Memory (CNN-BiLSTM)-Attention-Based Prediction of the Amount of Silica Powder Moving in and out of a Warehouse", *Energies*, **17**(15), 3757. https://doi.org/10.3390/en17153757

Hadhood, A., Mohamed, H.M. and Benmokrane, B. (2017), "Axial load–moment interaction diagram of circular concrete columns reinforced with CFRP bars and spirals: Experimental and theoretical investigations", *J Compos for Constr.*, **21**(2), 04016092. https://doi.org/10.1061/(ASCE)CC.1943-5614.0000748

Hadhood, A., Mohamed, H.M. and Benmokrane, B. (2017), "Strength of circular HSC columns reinforced internally with carbon-fiberreinforced polymer bars under axial and eccentric loads", *Constr and Build Mater.*, **141**(6), 366-378. https://doi.org/10.1016/j.conbuildmat.2017.02.117

Hadhood, A., Mohamed, H.M. and Benmokrane, B. (2017), "Strength of circular HSC columns reinforced internally with carbon-fiber-reinforced polymer bars under axial and eccentric loads", *Constr and Build Mater.*, **141**, 366-78. https://doi.org/10.1016/j.conbuildmat.2017.02.117

Hadhood, A., Mohamed, H.M. and Benmokrane, B. (2018), "Assessing stress-block parameters in designing circular high-strength concrete members reinforced with FRP bars", *J of Struct Eng.*, **144**(10), 04018182. https://doi.org/10.1061/(ASCE)ST.1943-541X.0002173

Hadhood, A., Mohamed, H.M. and Benmokrane, B. (2018), "Flexural stiffness of GFRP-and CFRP-RC circular members under eccentric loads based on experimental and curvature analysis", *ACI Struct J.*, **115**(4), 1185-98. https://doi.org/10.14359/51702235

Hadhood, A., Mohamed, H.M., Ghrib, F. and Benmokrane, B. (2017), "Efficiency of glass-fiber reinforced-polymer (GFRP) discrete hoops and bars in concrete columns under combined axial and flexural loads", *Compos Part B: Eng.*, **114**, 223-36. https://doi.org/10.1016/j.compositesb.2017.01.063

Hadi, M.N. and Youssef, J. (2016), "Experimental investigation of GFRP-reinforced and GFRP-encased square concrete samples under axial and eccentric load, and four-point bending test", *J of Compos for Constr.*, **20**(5), 04016020. https://doi.org/10.1061/(ASCE)CC.1943-5614.0000675

Hadi, M.N., Hasan, H.A. and Sheikh, M.N. (2017), "Experimental investigation of circular high-strength concrete columns reinforced with glass fiber-reinforced polymer bars and helices under different loading conditions", *J of Compos for Constr.*, **21**(4), 04017005. https://doi.org/10.1061/(ASCE)CC.1943-5614.0000784

Hadi, M.N., Karim, H. and Sheikh, M.N. (2016), "Experimental investigations on circular concrete columns reinforced with GFRP bars and helices under different loading conditions", *J of Compos for Constr.*, **20**(4), 04016009. https://doi.org/10.1061/(ASCE)CC.1943-5614.0000670

Hales, T.A., Pantelides, C.P. and Reaveley, L.D. (2016), "Experimental evaluation of slender high-strength concrete columns with GFRP and hybrid reinforcement", *J of Compos for Constr.*, **20**(6), 04016050. https://doi.org/10.1061/(ASCE)CC.1943-5614.0000709

Han, L.H. and Yao, G.H. (2004), "Experimental behaviour of thin-walled hollow structural steel (HSS) columns filled with self-consolidating concrete (SCC)", *Thin-Walled Struct.*, **42**, 1357-1377. https://doi.org/10.1016/j.tws.2004.03.016

Hany, N.F., Hantouche, E.G. and Harajli, M.H. (2016), "Finite element modeling of FRP-confined concrete using modified concrete damaged plasticity", *Eng. Struct.*, **125**, 1–14.

Hassanein, M. F., Hamed, A. Y., Cashell, K. A. and Shao, Y. B. (2023), "Confinement-based direct design method for fibre reinforced polymer confined CFST short columns", *Thin-Walled. Struct.*, **192**, 111207.

Hassanein, M.F., Hamed, A.Y., Cashell, K.A. and Shao, Y.B. (2023), "Confinement-based direct design of fibre reinforced polymer confined normal and high-strength CFST short columns", *Thin-Walled Struct.*, **192**, 111207. https://doi.org/10.1016/j.tws.2023.111207

Hassanein, M.F., Hamed, A.Y., Shao, Y.B. and Silvest, N. (2023), "Confinement-based direct design of circular steel tube confined concrete (STCC) short columns", *J Constr Steel Res.*, **204**, 107871. https://doi.org/10.1016/j.jcsr.2023.107871

Hassanein, M.F., Elchalakani, M., Karrech, A., Patel, V.I. and Daher, E. (2018), "Finite element modelling of concrete-filled double-skin short compression members with CHS outer and SHS inner tubes", *Mar. Struct.*, **61**, 85–99. https://doi.org/10.1016/j.marstruc.2018.05.002

Hewamalage, H., Bergmeir, C. and Bandara, K. (2020), "Recurrent neural networks for time series forecasting: Current status and future directions", International J. of Forecas., **37**(1), 388–427.

Hilloulin, B., Lagrange, M., Duvillard, M. and G.G., C. (2022), "ε–greedy automated indentation of cementitious materials for phase mechanical properties determination", *Cem. and Concr. Compos.*, **129**, 104465.

Hollaway, L. C. and Cadei, J. (2002), "Progress in the technique of upgrading metallic structures with advanced polymer composites", Progress in Struct. Eng. and Mater., **4**(2), 131-148.

Hosseinpour, F. and Abbasnia, R. (2014), "Experimental investigation of the stress-strain behavior of FRP confined concrete prisms", *Adv in Concr Constr.*, **2**(3), 177-192. https://doi.org/10.12989/acc.2014.2.3.177

Hu, W., Li, Y. And Yuan, H. (2020), "Review of experimental studies on application of FRP for strengthening of bridge structures", *Adv. in Mater. Scien. and Eng.*, 8682163. https://doi.org/10.1155/2020/8682163

HU, Y.-M, (2011), "Behaviour and modelling of FRP-confined hollow and concrete-filled steel tubular columns", Ph.D. Thesis, The Hong Kong Polytechnic University, Department of Civil and Structural Engineering.

Hu, Y.M., Yu, T. and Teng, J.G. (2011), "FRP-confined circular concrete-filled thin steel tubes under axial compression", *J Compos Constr.*, **15**, 850-860. https://doi.org/10.1061/(ASCE)CC.1943-5614.0000217

Isleem, H.F., Qiong, T., Chukka, N.R., Kumar, R., Nagaraju, T.V. and Hamed, A.Y. (2024), "Machine learning and nonlinear finite element analysis of fiber-reinforced polymer confined concrete-steel double-skin tubular columns under axial compression", *Struct Concr.*, https://doi.org/10.1002/suco.202300835

Isleem, H.F., Tayeh, B.A., Abid, M., Iqbal, M., Mohamed, A.M. and El Sherbiny, M.G. (2022), "Finite Element and Artificial Neural Network Modeling of FRP-RC Columns Under Axial Compression Loading", *Struct Mater.*, **9**. https://doi.org/10.3389/fmats.2022.888909

Jabbar, S.A. and Farid, S.B. (2018), "Replacement of steel rebars by GFRP rebars in the concrete structures", *Karb Inter J of Moder Sci.*, **4**(2), 216-227. https://doi.org/10.1016/j.kijoms.2018.02.002

Jalota, S. and Suthar, M (2024), "Machine learning models to predict mechanical performance properties of modified bituminous mixes: A comprehensive review", *Asian J. of Civ. Eng.*, **25** (7), 5581–5598.

Jiang, Y., Kim, H., Asnani, H., Kannan, S., Oh, S. and Viswanath, P. (2020), "Learn codes: Inventing low-latency codes via recurrent neural networks", *IEEE J. on Selec. Areas in Inf. Theory.*, **1**(1), 207–216.

John, R.A., Acharya, J., Zhu, C., Surendran, A., Bose, S.K., Chaturvedi, A., Tiwari, N., Gao, Y., He, Y. and Zhang, K.K. (2020), "Optogenetics inspired transition metal dichalcogenide neuristors for in-memory deep recurrent neural networks", *Nat. Commun.*, **11**(1), 1–9.

Kam, W.Y. and Pampanin, S. (2008), "Selective weakening techniques for the seismic retrofit of RC buildings", *Bull. of the New Zealand Society for Earth. Eng.*, **41**(2), 73-85.

Ke, G., Meng, Q., Finley, T., Wang, T., Chen, W. and Ma, W. (2017), "LightGBM: A highly efficient gradient boosting decision tree", Proceedings of the 31st International Conference on Neural Information Processing Systems, 3149–3157.

Khan, Q.S., Sheikh, M.N. and Hadi, M.N. (2016), "Axial-flexural interactions of GFRP-CFFT columns with and without reinforcing GFRP bars", *J of Compos for Constr.*, **21**(3), 04016109. https://doi.org/10.1061/(ASCE)CC.1943-5614.0000771

Khorramian, K. and Sadeghian, P. (2017), "Experimental and analytical behavior of short concrete columns reinforced with GFRP bars under eccentric loading", *Eng Struct.*, **151**, 761-73. https://doi.org/10.1016/j.engstruct.2017.08.064

Khorramian, K. AND Sadeghian, P. (2020), "Experimental investigation of short and slender rectangular concrete columns reinforced with GFRP bars under eccentric axial loads", *J of Compos for Constr.,* **24**(6), 04020072. https://doi.org/10.1061/(ASCE)CC.1943-5614.0001088

Lam, L. and Teng, G. (2002), "Strength models for fiber-reinforced plastic-confined concrete", *J Struct Eng*, **128**(5), 612-623. https://doi.org/10.1061/(ASCE)0733-9445(2002)128:5(612)

Liu, J.P., Xu, T.X., Wang, Y.H. and Guo, Y. (2018), "Axial behaviour of circular steel tubed concrete stub columns confined by CFRP materials", *Constr Build Mater.*, **168**, 221-231. https://doi.org/10.1016/j.conbuildmat.2018.02.131

Liu, L. and Lu, Y. (2010), "Axial bearing capacity of short FRP confined concrete-filled steel tubular columns", *J Wuhan Univ Technol-Mater Sci Ed.*, **25**, 455-485. https://doi.org/10.1007/s11595-010-0022-2

Liu, L. and Lu, Y. (2010), "Axial bearing capacity of short FRP confined concrete-filled steel tubular columns", *J Wuhan Univ Technol-Mater.*, **25**(3), 454-458. https://doi.org/10.1007/s11595-010-0022-2

Lu, W., Li, J., Wang, J. and Qin, L. (2021), "A CNN-BiLSTM-AM method for stock price prediction", *Neural Comput Appl.*, **33**(10), 4741-4753. https://doi.org/10.1007/s00521-020-05532-z

Lu, Y.Y., Li, N. and Li, S. (2014), "Behavior of FRP-confined concrete-filled steel tube columns", *Polym Bull.*, **6**, 1333-1349. https://doi.org/10.3390/polym6051333

Ma, H., Bai, H., Zhao, Y., Liu, Y. and Zhang, P. (2020), " Compressive performance of RAC filled GFRP tube-profile steel composite columns under axial loads ", *Adv in Concr Constr.*, **10**(2), 319-332. https://doi.org/10.12989/acc.2020.10.2.151

Ma, L., Zhou, C., Lee, D. and Zhang, J. (2022), "Prediction of axial compressive capacity of CFRP-confined concrete-filled steel tubular short columns based on XGBoost algorithm", *Eng Struct.*, **260**, 114239. https://doi.org/10.1016/j.engstruct.2022.114239

Ma, L., Zhou, C., Lee, D. and Zhang, J. (2022), "Prediction of axial compressive capacity of CFRP-confined concrete-filled steel tubular short columns based on XGBoost algorithm", *Eng Struct.*, **260**, 114239. https://doi.org/10.1016/j.engstruct.2022.114239

Ma, Y., Che, Y., & Gong, J. (2012), "Behavior of corrosion damaged circular reinforced concrete columns under cyclic loading", *Constr. and Build. Mater.*, **29**, 548-556. https://doi.org/10.1016/j.conbuildmat.2011.11.00

Ma, Y., Ma, K., Han, X. and Yao, T. (2023), "Experimental investigation of FRP-confined HSC-filled steel tube stub columns under axial compression", *Eng Struct.*, **280**, 115670. https://doi.org/10.1016/j.engstruct.2023.115670

MacGregor, J. G. and Wight, J. K. (2016), "Reinforced concrete: Mechanics and design", (7th ed.). Pearson.

Mahmoudabad, N.S., Bahrami, A., Saghir, S., Ahmed, A., Iqbal, M., Elchalakini, M. and Özkılıç, Y.O. (2024), "Effects of eccentric loading on performance of concrete columns reinforced with glass fiber‑reinforced polymer bars", *Sci Rep.*, **14**(1), 1890. https://doi.org/10.1038/s41598-023-47609-4

Mander, J. and Priestley, M. (1988), "Theoretical stress-strain model for confined concrete", J *Struct Eng.*, **114**, 1804-1826. https://doi.org/10.1061/(ASCE)0733-9445(1988)114:8(1804)

Mander, J. B., Priestley, M. J. and Park, R. (1988), "Theoretical stress-strain model for confined concrete", *J. of struct. Eng.*, **114**(8), 1804-1826.

Mansour, W., Osama, B., Li, W., Wang, P. and Sobuz, H.R. (2024), "Numerical response of concrete-filled steel tubular (CFST) columns externally strengthened with FRP composites subjected to cyclic loading", *Int. J. Concr. Struct. Mater.*, **18**(82). https://doi.org/10.1186/s40069-024-00716-6

Maranan, G., Manalo, A., Benmokrane, B., Karunasena, W. and Mendis, P. (2018), "Behavior of concentrically loaded geopolymer-concrete circular columns reinforced longitudinally and transversely with GFRP bars", *Eng Struct.*, **117**, 422-36. https://doi.org/10.1016/j.engstruct.2016.03.036

Matiyas, S., Workeluel, N., Mohanty, T. and Saha, P. (2023), "Review of different analysis and strengthening techniques of soft story buildings", Mater. Today: Proc., https://doi.org/10.1016/j.matpr.2023.04.231

Méndez, M., Merayo, M.G. and Núñez, M. (2023), "Long-term traffic flow forecasting using a hybrid CNN-BiLSTM model", *Eng Appl Artif Intell.*, **121**, 106041. https://doi.org/10.1016/j.engappai.2023.106041

Mesbah, H.A. and Benzaid, R. (2017), "Damage-based stress-strain model of RC cylinders wrapped with CFRP composites ", *Adv in Concr Constr.*, **5**(5), 539-561. https://doi.org/10.12989/acc.2017.5.5.539

Mienyea, I.D., Suna, Y. and Wang, Z. (2019.), "Prediction performance of improved decision tree-based algorithms: A review", 2nd International Conference on Sustainable Materials Processing and Manufacturing.

Miladirad, K., Golafshani, E.M., Safehian, M. and Sarkar, A. (2022), "Application of machine learning methods for predicting the mechanical properties of rubbercrete", *Adv in Concr Constr.*, **14**(1), 15-34. OI: https://doi.org/10.12989/acc.2022.14.1.015

Mohamed Sayed, A., Mohamed Rashwan, M. and Emad Helmy, M. (2020) "Experimental Behavior of Cracked Reinforced Concrete Columns Strengthened with Reinforced Concrete Jacketing", *Mater.*, **13**(12), 2832. https://doi.org/10.3390/ma13122832

Mohamed, H. M. and Benmokrane, B. (2014), "Design and performance of reinforced concrete water chlorination tank totally reinforced with GFRP bars: Case study", J. of Compos. for Constr., **18**(1), 05013001.

Mohamed, H., Afifi, M. and Benmokrane, B. (2014), "Performance evaluation of concrete columns reinforced longitudinally with FRP bars and confined with FRP hoops and spirals under axial load", *J of Brid Eng.*, **19**(7), 04014020. https://doi.org/10.1061/(ASCE)BE.1943-5592.0000590

Mohammadi, M., Youssef-Namnoum, C., Robira, M. and Hilloulin, B. (2020), "Self-healing potential and phase evolution characterization of ternary cement blends", *Mater*., **13**(11), 2543.

Mohammed, N.N. and Abdulazeez, A.M. (2017.), "Evaluation of partitioning around medoids algorithm with various distances on microarray data", 2017 IEEE International Conference on Internet of Things (iThings), Green Computing and Communications (GreenCom), Cyber, Physical and Social Computing (CPSCom), and Smart Data (SmartData), 1011–1016.

Monti G. (2003), "Seismic upgrade of reinforced concrete columns with FRP", Technical report, Teheran, 29.

Moon, J., Kim, J. J., Lee, T. H. and Lee, H. E. (2014), "Prediction of axial load capacity of stub circular concrete-filled steel tube using fuzzy logic", *J. of Constr.l Steel Res*., **101**, 184-191.

Na, L., Yiyan, L., Shan, L. and Lan, L. (2018), "Slenderness effects on concrete-filled steel tube columns confined with CFRP", *J Constr Steel Res*, **143**, 110-118. https://doi.org/10.1016/j.jcsr.2017.12.014

Neville, A. M. and Brooks, J. J. (2010), Concrete technology (2nd ed.). Pearson.

Nicolo, B.D., Pani, L. and Pozzo, E. (1994), "Strain of concrete at peak compressive stress for a wide range of compressive strengths", *Mater Struct.*, **27**, 206-210. https://doi.org/10.1007/BF02473034

Nishino, T. and Furukawa, T. (2004), "Strength and deformation capacities of circular hollow section steel member reinforced with carbon fiber", Proceedings, Seventh Pacific Structural Steel Conference.

Nithurshan, M. and Elakneswaran, Y. (2023), "A systematic review and assessment of concrete strength prediction models", Case. Stud. in Constr. Mater., **18**, e01830.

Oreb, N. (2023), "Problem stabilnosti stupova [Undergraduate thesis]", University of Zagreb, Faculty of Civil Engineering. https://urn.nsk.hr/urn:nbn:hr:237:066641

Ortiz, J. D., Khedmatgozar Dolati, S. S., Malla, P., Mehrabi, A. And Nanni, A. (2023), "FRP-reinforced/strengthened concrete: State-of-the-art review on durability and mechanical effects", *Mater*., **16**(5), 1990. https://doi.org/10.3390/ma16051990

Othman, ZS. and Mohammad, AH. (2019), "Behaviour of eccentric concrete columns reinforced with carbon fibre-reinforced polymer bars", *Adv in civ eng*, **2019**, 1-13. https://doi.org/10.1155/2019/1769212

Park, J.W., Hong, Y.K., Hong, G.S. and Choi, S.M. (2009), "Experimental study on concrete steel circular tubes confined by carbon fiber sheet under axial compression loads", *J Earth. Eng Soc Korea*., **13**(5), 61-72. https://doi.org/10.5000/EESK.2009.13.5.061

Park, J.W., Hong, Y.K., Hong, G.S., Kim, J.H. and Ch, S.M. (2011), "Design formulas of concrete-filled circular steel tubes reinforced by carbon fiber reinforced plastic sheets", *Procedia Eng*., **14**, 2916-2922. https://doi.org/10.1016/j.proeng.2011.07.367

Parmar, A., Katariya, R. and Patel, V. (2018), "A review on random forest: An ensemble classifier", International Conference on Intelligent Data Communication Technologies and Internet of Things (ICICI) 2018. Lecture Notes on Data Engineering and Communications Technologies, 26.

Pascanu, R., Gulcehre, C., Cho, K. and Bengio, Y. (2014.), "How to construct deep recurrent neural networks", Proceedings of the Second International Conference on Learning Representations (ICLR).

Paultre, P., Calais, É., Proulx, J., Prépetit, C. and Ambroise, S. (2013), "Damage to engineered structures during the January 12, 2010, Haiti (Léogâne) earthquake", Canadian J. of Civ. Eng., **40**(8), 1–14. https://doi.org/10.1139/cjce-2012-0247

Pellizzer, G. P. and Leonel, E. D. (2020), "Probabilistic corrosion time initiation modelling in reinforced concrete structures using the BEM", *IBRACON Struct. and Mater. J.*, **13**(4), e13409. https://doi.org/10.1590/S1983-41952020000400009

Popovics, S. (1973), "A numerical approach to the complete stress-strain curve of concrete", *Cem. Concr. Res.*, **3**(5), 583-599. https://doi.org/10.1016/0008-8846(73)90096-3

Prachasaree, W., Piriyakootorn, S., Sangsrijun, A. and Limkatanyu, S. (2015), "Behavior and performance of GFRP reinforced concrete columns with various types of stirrups", *Inter J of Polym Sci.*, **2015**(3), 1-9. https://doi.org/10.1155/2015/237231

Prokhorenkova, L., Gusev, G., Vorobev, A., Dorogush, A.V. and Gulin, A. (2018), "CatBoost: Unbiased boosting with categorical features", Proceedings of the 32nd International Conference on Neural Information Processing Systems, 6639–6649.

Raza, A., El Ouni, M.H. and Baili, J. (2022), "Data-driven analysis on axial strength of GFRP-NSC columns based on practical artificial neural network tool", *Compos Struct.*, **291**, 115598. https://doi.org/10.1016/j.compstruct.2022.115598

Raza, A., Khan, Q.u.Z, and Ahmad, A. (2021), "Investigation of HFRC columns reinforced with GFRP bars and spirals under concentric and eccentric loadings", *Eng Struct*., **227**. https://doi.org/111461. 10.1016/j.engstruct.2020.111461

Raza, S., Khan, M. K. I., Menegon, S. J., Tsang, H.-H. and Wilson, J. L. (2019), "Strengthening and repair of reinforced concrete columns by jacketing: State-of-the-art review", *Sustainability*, **11**(11), 3208. https://doi.org/10.3390/su11113208

Razavi, S.V., Jumaat, M.Z., EI-Shafie, A.H. and Ronagh, H.R. (2015), "Load-deflection analysis prediction of CFRP strengthened RC slab using RNN", *Adv in Concr Constr.*, **3**(2), 091-102. https://doi.org/10.12989/acc.2015.3.2.091

Richart, F.E., Brandzaeg, A. and Brown, R.L. (1928), "A study of the failure of concrete under combined compressive stresses", University of Illinois, Engineering Experimental Station, Illinois, U.S.A.

Rivera-Lopez, R., Canul-Reich, J., Mezura-Montes, E. and Cruz-Chávez, M.A. (2022), "Induction of decision trees as classification models through metaheuristics", Swarm and Evolutionary Computation, 69, 101006.

Rodrigues, R., Gaboreau, S., Gance, J., Ignatiadis, I. and Betelu, S. (2020), "Reinforced concrete structures: A review of corrosion mechanisms and advances in electrical methods for corrosion monitoring", Constr. and Build. Mater., https://doi.org/10.1016/j.conbuildmat.2020.121240

Rodriguez, M., and Park, R. (1994), "Seismic load tests on reinforced concrete columns strengthened by jacketing", ACI Struct. J., **91**(2), 150–159.

Rosa, J.L.G. (2016), "Artificial Neural Networks – Models and Applications", InTech.

Rosa, J.L.G. (2016), "Artificial Neural Networks – Models and Applications", InTech.

Roziqin, M.C., Basuki, A. and Harsono, T. (2016), "A comparison of Monte Carlo linear and dynamic polynomial regression in predicting dengue fever case", 2016 International Conference on Knowledge Creation and Intelligent Computing (KCIC), 213–218.

Sak, H., Senior, A. and Beaufays, F. (2014), "Long short-term memory recurrent neural network architectures for large scale acoustic modeling", *Procee. of Interspeech*., 338–342.

Salah-Eldin, A., Mohamed, H.M. and Benmokrane, B. (2019), "Axial–flexural performance of high-strength-concrete bridge compression members reinforced with basalt-FRP bars and ties: Experimental and theoretical investigation", *J of Brid Eng*., **24**(7), 04019069. https://doi.org/10.1061/(ASCE)BE.1943-5592.0001448

Salah-Eldin, A., Mohamed, H.M. and Benmokrane, B. (2019), "Structural performance of high-strength-concrete columns reinforced with GFRP bars and ties subjected to eccentric loads", *Eng Struct*., **185**, 286-300. https://doi.org/10.1016/j.engstruct.2019.01.143

Samani, A.K. and Attard, M.M. (2012), "A stress–strain model for uniaxial and confined concrete under compression", *Eng Struct*., **41**, 335-349. https://doi.org/10.1016/j.engstruct.2012.03.027

Samra, R. M., Deeb, N. A. A. and Madi, U. R. (1996), "Transverse steel content in spiral concrete columns subject to eccentric loading", *ACI Struct. J*., **93**(4), 412–419. https://doi.org/10.14359/9700

Schapire, R.E. (1999), "A brief introduction to boosting", Proceedings of the 16th International Joint Conference on Artificial Intelligence, 2, 1401–1406.

Sharbatdar, M. K. (2003), "Concrete columns and beams reinforced with FRP bars and grids under monotonic and reversed cyclic loading", (Doctoral dissertation, University of Ottawa (Canada)).

Sharif, A.M., Al-Mekhlafi, G.M. and Al-Osta, M.A. (2019), "Structural performance of CFRP-strengthened concrete-filled stainless steel tubular short columns", *Eng Struct*., **183**, 94-109. https://doi.org/10.1016/j.engstruct.2019.01.011

Shen, Q., Wang, J., Wang, Y. and Wang, F. (2019), "Analytical modelling and design of partially CFRP wrapped thin-walled circular NCFST stub columns under axial compression", *Thin-Walled Struct*, **144**, 106276. https://doi.org/10.1016/j.tws.2019.106276

Shen, Q.H., Wang, J.H., Wang, J.X. and Ding, Z.D. (2019), "Axial compressive performance of circular CFST columns partially wrapped by carbon FRP", *J Constr Steel Res*., **155**, 90-106. https://doi.org/10.1016/j.jcsr.2018.12.017

Shi, Y., Swait, T. and Soutis, C. (2012), "Modelling damage evolution in composite laminates subjected to low velocity impact", *Compos. Struct*., **94**, 2902–2913.

Siami-Namini, S., Tavakoli, N. and Namin, A.S. (2019), "The performance of LSTM and BiLSTM in forecasting time series", *IEEE Int Conf Big Data (Big Data)*., 3285-3292. https://doi.org/10.1109/BigData47090.2019.9005997

Stefano, M. and Bini, A. (2018), "Artificial intelligence, machine learning, deep learning, and cognitive computing: what do these terms mean and how will they impact health care", *J. of Arthroplasty*, **33**, 2358–2361.

Stergiou, K., Ntakolia, C., Varytis, P., Koumoulos, E., Karlsson, P. and Moustakidis, S. (2023), "Enhancing property prediction and process optimization in building materials through machine learning: A review", *Comput. Mater. Sci*., **220**, 112031.

Suliman, A., Abed, F. and AlHamaydeh, M. (2013), "Behavior of CFSTs and CCFSTs under quasi-static axial compression", *J Constr Steel Res*, **90**, 235-244. https://doi.org/10.1016/j.jcsr.2013.08.007

Sun, L., Wei, M. and Zhang. N. (2017), "Experimental study on the behavior of GFRP reinforced concrete columns under eccentric axial load", *Constr and Build Mater*., **152**, 214-25. https://doi.org/10.1016/j.conbuildmat.2017.06.159

Sun, X., Liang, W., Zhou, C., Li, Y., Wang, G. and Yue, Y. (2024), "Short-Term Multi-Step Prediction of Process Industry Product Quality with CNN-BiLSTM Network Based on Parallel Attention Mechanisms", *IEEE Sens J.* https://doi.org/10.1109/JSEN.2024.3413990

Sun, Y. (2024), "Estimation of compressive strength for spiral stirrup-confined circular concrete column using optimized machine learning with interpretable techniques", *Mech of Adv Mater and Struct*., https://doi.org/10.1080/15376494.2023.2298232

Suna, H., Burton, H.V. and Huang, H. (2021), "Machine learning applications for building structural design and performance assessment: State-of-the-art review", J. of Build. Eng., **33**, 101816.

Tabatabaei, A., Eslami, A., Mohamed, H.M. and Benmokrane, B. (2018), "Strength of compression lap-spliced GFRP bars in concrete columns with different splice lengths",. Constr and Build Mater, 182, 657-69. https://doi.org/10.1016/j.conbuildmat.2018.06.154

Tang, H., Chen, J., Fan, L., Sun, X. and Peng, C. (2020), "Experimental investigation of FRP-confined concrete-filled stainless steel tube stub columns under axial compression", *Thin-Walled Struct*., **146**, 106483. https://doi.org/10.1016/j.tws.2019.106483

Tao, Z., Han, L.H. and Zhuang, J.P. (2006), "Axial loading behavior of CFRP strengthened concrete-filled steel tubular stub columns", *Adv Struct Eng.*, **10**, 37-46. https://doi.org/10.1260/136943307780150814

Tao, Z., Han, L.H. and Zhuang, J.P. (2007), "Axial loading behavior of CFRP strengthened concrete-filled steel tubular stub columns", *Adv Struct Eng*., **10**, 37-46. https://doi.org/10.1260/136943307780150814

Tao, Z., Wang, Z.B. and Yu, Q. (2013), "Finite element modelling of concrete-filled steel stub columns under axial compression", *J Constr Steel Res*., 89, 121-131.

Tapeh, A.T.G. and Naser, M.Z. (2023), "Artificial intelligence, machine learning, and deep learning in structural engineering: A scientometrics review of trends and best practices", Arch. of Comput. Meth. in Eng., **30**, 115–159.

Tarawneh, A.N., Dwairi, H.M., Almasabha, G.S. and Majdalawey, S.A. (2021), "Effect of fiber reinforced polymer-compression reinforcement in columns subjected to concentric and eccentric loading", *ACI struct J*., **118** (3), 187-197.

Tavassoli, A. and Sheikh, S.A. (2017), "Seismic resistance of circular columns reinforced with steel and GFRP", *J of Compos for Constr*., **21**(4), 04017002. https://doi.org/10.1061/(ASCE)CC.1943-5614.0000774

Tayeh, B. A., Abu Naja, M., Shihada, S. and Arafa, M. (2019), "Repairing and strengthening of damaged RC columns using thin concrete jacketing", Adv. in Civ. Eng., 1–16. https://doi.org/10.1155/2019/2987412

Teng, J. G., and Hu, Y. M. (2004), "Suppression of local buckling in steel tubes by FRP jacketing", In Proceedings, 2nd international conference on FRP composites in civil engineering, Adelaide, Australia, 8-10.

Teng, J. G., Jiang, T., Lam, L. and Luo, Y. Z. (2009), "Refinement of a design-oriented stress–strain model for FRP-confined concrete", J. of compos. for constr., **13**(4), 269-278.

Thai, H.T. (2018), "Finite element analysis of large diameter high strength octagonal CFST short columns", *Thin-Walled Struct*., **123**, 467-482. https://doi.org/10.1016/j.istruc.2018.04.006

Thai, H.T., Uy, B., Khan, M., Tao, Z. and Mashiri, F. (2014), "Numerical modelling of concrete-filled steel box columns incorporating high strength materials", *J Constr Steel Res.*, 102, 256-265. https://doi.org/10.1016/j.jcsr.2014.07.014

Tikka, T., Francis, M., and Teng, B., (2010), "Strength of Concrete Bearn Columns Reinforced with GFRP Bars", 2nd International Structures Specialty Conference, Winnipeg, Manitoba, 46, 1-10.

Tobbi, H., Farghaly, A.S. and Benmokrane, B. (2012), "Concrete Columns Reinforced Longitudinally and Transversally with Glass Fiber-Reinforced Polymer Bars", *ACI struct J*., **109**(4), 551-8. https://doi.org/10.14359/51683874

Tobbi, H., Farghaly, AS. and Benmokrane, B. (2014), "Behavior of Concentrically Loaded Fiber-Reinforced Polymer Reinforced Concrete Columns with Varying Reinforcement Types and Ratios", *ACI struct J*., **111**(2), 375-86. https://doi.org/10.14359/51686528

Tu, J., Gao, K., He, L. and Li, X. (2019), "Experimental study on the axial compression performance of GFRP-reinforced concrete square columns", *Adv in Struct Eng*., **22**(7), 1554-65. https://doi.org/10.1177/1369433218817988

Vu, N. S., and Li, B. (2017), "Seismic performance of reinforced concrete columns in corrosive environment", In High Tech Concrete: Where Technology and Engineering Meet: Proceedings of the 2017 fib Symposium, held in Maastricht, The Netherlands, (895-903).

Wang, D., Huang, L., Yu, T. and Wang, Z. (2017), "Seismic performance of CFRP-retrofitted large-scale square RC columns with high axial compression ratios", J. of Compos for Constr., **21**(5), 04017031. https://doi.org/10.1061/(ASCE)CC.1943-5614.0000813

Wang, J., Shen, Q., Wang, F. and Wang, W. (2018), "Experimental and analytical studies on CFRP strengthened circular thin-walled CFST stub columns under eccentric compression", *Thin-Walled Struct*, **127**, 102-119. https://doi.org/10.1016/j.tws.2018.01.039

Wang, J.F., Xiao, Q., Shen, Q.H. and Sheng, M.Y. (2021), "Analysis on the axial behavior of CFRP wrapped circular CFST stub columns with initial concrete imperfection", *Prog Steel Build Struct*, **23**, 44-53.

Wang, Y.H., Wang, Y.Y., Hou, C., Deng, R., Lan, Y.S. and Luo, W. (2020), "Torsional capacity of concrete-filled steel tube columns circumferentially confined by CFRP", *J Constr Steel Res*, **175**, 106320. https://doi.org/10.1016/j.jcsr.2020.106320

Wang, Z.B., Yu, Q. and Tao, Z. (2015), "Behaviour of CFRP externally-reinforced circular CFST members under combined tension and bending", *J Constr Steel Res.*, **106**, 122-137. https://doi.org/10.1016/j.jcsr.2014.12.007

Wei, Y., Bai, J., Zhang, Y., Miao, K. and Zheng, K. (2021), "Compressive performance of high-strength seawater and sea sand concrete-filled circular FRP-steel composite tube columns", *Eng Struct.*, **240**, 112357. https://doi.org/10.1016/j.engstruct.2021.112357

Wei, Y., Wu, G. and Li, G. (2014), "Performance of circular concrete-filled fiber-reinforced polymer-steel composite tube columns under axial compression", *J Reinf Plast Compos*., **33**, 1911-1928. https://doi.org/10.1177/0731684414550836

Wu, Y. F., Griffith, M. C. and Oehlers, D. J. (2003), "Improving the strength and ductility of rectangular reinforced concrete columns through composite partial interaction: Tests", *J. of Struct. Eng*., **129**(9), 1183–1190. https://doi.org/10.1061/(ASCE)0733-9445(2003)129:9(1183)

Wu, Z., Wu, Y. and Fahmy, M. F. (2020), "Structures strengthened with bonded composites".

www.quantity-takeoff.com

www.frp-expert.com

Xiao, Y., He, W. and Choi, K.K. (2005), "Confined concrete-filled tubular columns", *J Struct Eng, ASCE*., **131**(3), 488-497. https://doi.org/10.1061/(ASCE)0733-9445(2005)131:3(488)

Xiao, Y., He, W., and Choi, K. K. (2005), "Confined concrete-filled tubular columns", *J. of struct. Eng*., **131**(3), 488-497.

Xiaochun, F. and Zhang, M. (2016), "Behaviour of inorganic polymer concrete columns reinforced with basalt FRP bars under eccentric compression: An experimental study", *Compos Part B*., 104, 44-56. http://dx.doi.org/10.1016/j.compositesb.2016.08.020

Xing, L., Sun, S., Mei, K., Guo, Y. and Yang, Z. (2024), "Research progress on short-term mechanical properties of FRP bars and FRP-reinforced concrete beams", Journal of Traffic and Transportation Engineering (English Edition).

Xu, T., Liu, J., Wang, X., Guo, Y. and Chen, F. (2020), "Behaviour of short CFRP-steel composite tubed reinforced normal and high-strength concrete columns under eccentric compression", *Eng Struct*., **205**, 110096. https://doi.org/10.1016/j.engstruct.2019.110096

Xue, W., Peng, F. and Fang, Z. (2018), "Behavior and Design of Slender Rectangular Concrete Columns Longitudinally Reinforced with Fiber-Reinforced Polymer Bars", *ACI struct J*., **115**(2). https://doi.org/10.14359/51701131

Xue, W., Peng, F. and Fang, Z. (2018), "Behavior and Design of Slender Rectangular Concrete Columns Longitudinally Reinforced with Fiber-Reinforced Polymer Bars", *ACI struct J*., **115**(2), 311-322. https://doi.org/10.14359/51701131

Yang, J., Wang, J., Zhang, S. and Wang, Z. (2020), "Behavior of eccentrically loaded circular CFRP steel composite tubed steel-reinforced high-strength concrete columns", *J Constr Steel Res*., **170**, 106101. https://doi.org/10.1016/j.jcsr.2020.106101

Ye, Y.Y., Zhuge, Y., Smith, S.T., Zeng, J.J. and Bai, Y.L. (2022), "Behavior of GFRP-RC columns under axial compression: Assessment of existing models and a new axial load-strain model", *J of Build Eng*., **47**, 103782. https://doi.org/10.1016/j.jobe.2021.103782

Yu, F., Kong, Z., Li, D. and Vu, Q.V. (2020), " Experimental study on the stress-strain relation of PVC-CFRP confined reinforced concrete column subjected to eccentric compression ", *Adv in Concr Constr.*, **10**(2), 151-159. https://doi.org/10.12989/acc.2020.10.2.151

Yu, Q. (2002), "Behaviors of FRP-Confined Concrete Columns", New York: Harbin Institute of Technology.

Yüce, S. Z., Yüksel, E., Bingöl, Y., Taşkın, K. and Karadoğan, H. F. (2007), "Local thin jacketing for the retrofitting of reinforced concrete columns", *Struct. Eng. and Mech*., **27**(5), 589–607. https://doi.org/10.12989/sem.2007.27.5.589

Zeng, J.-J., Ye, Y.-Y., Li, Y., Zhang, Y.-F., Wang, Y. and Wang, Y. (2023), "Behaviour of FRP spiral-confined concrete and contribution of FRP longitudinal bars in FRP-RC columns under axial compression", *Eng. Struct*., **278**, 115747. https://doi.org/10.1016/j.engstruct.2023.115747

Zeng, J.J., Zheng, Y.W., Liu, F., Guo, Y.C. and Hou, C. (2021), "Behavior of FRP ring-confined CFST columns under axial compression", *Compos Struct*., **257**, 113166. https://doi.org/10.1016/j.compstruct.2020.113166

Zhai, C.L., Wei, Y. and Li, G.F. (2012), "Research on design and application of FRP-Steel composite pipe concrete pier", Highway 01, 83-87.

Zhang, S., Miao, K., Wei, Y., Xu, X., Luo, B. and Shi, W. (2023), "Experimental and theoretical study of concrete-filled steel tube columns strengthened by FRP/Steel strips under axial compression", *Int J Concr Struct Mater*., **17**. https://doi.org/10.1186/s40069-022-00556-2

Zhang, X. and Deng, Z. (2018), "Experimental study and theoretical analysis on axial compressive behavior of concrete columns reinforced with GFRP bars and PVA fibers", *Constr and Build Mater*, **172**, 519-32. https://doi.org/10.1016/j.conbuildmat.2018.03.237

Zhang, Y., Wei, Y., Bai, J., Wu, G. and Dong, Z. (2020), "A novel seawater and sea sand concrete-filled FRP-carbon steel composite tube column: Concept and behaviour", *Compos Struct*., **246**, 112421. https://doi.org/10.1016/j.compstruct.2020.112421

Zhang, Z., Li, Y., Li, L., Li, Z. and Liu, S. (2019), "Multiple linear regression for high efficiency video intra coding", IEEE International Conference on Acoustics, Speech and Signal Processing (ICASSP), 1832–1836.

Zhao, J.L., Xu, C.H., Sun, L.Z. and Wu, D.Y. (2020), "Behaviour of FRP-confined compound concrete–filled circular thin steel tubes under axial compression", *Adv Struct Eng*., **23**, 1772-1784. https://doi.org/10.1177/1369433219900941

Zhao, X. L. and Zhang, L. (2007), "State-of-the-art review on FRP strengthened steel structures", Eng. Struct., **29**(8), 1808-1823. https://doi.org/10.1016/j.engstruct.2006.10.006

Zhou, D.X. (2020), "Theory of deep convolutional neural networks: Downsampling", *Neural Networks*, **124**, 319–327.